

# Investigation of Multi Suppressive Layers under Impact Load

Sameh Yaken Aref Ahmed

A Thesis

In

The Department of  
Building, Civil and Environmental Engineering

Presented in Partial Fulfillment of the Requirements  
for the Degree of Doctor of Philosophy (Civil Engineering) at

**Concordia University**

Montréal, Québec, Canada

**August 2016**

© Sameh Yaken Aref Ahmed, 2016

**Concordia University**  
**School of Graduate Studies**

This is to certify that the thesis prepared

By: **Mr. Sameh Yaken Aref Ahmed**

Entitled: **Investigation of Multi Suppressive Layer under Impact Load**

and submitted in partial fulfillment of the requirements for the degree of

**Doctor of Philosophy (Building, Civil and Environmental Engineering)**

Complies with the regulations of this University and meets the accepted standards with respect to originality and quality.

Signed by the final examining committee:

\_\_\_\_\_ Chair  
Dr. G. Gouw

\_\_\_\_\_ External Examiner  
Dr. Ex A. El Damatty

\_\_\_\_\_ Examiner, External to Program  
Dr. R. Sedaghati

\_\_\_\_\_ Examiner  
Dr. A. Bagchi

\_\_\_\_\_ Examiner  
Dr. A. Bhowmick

\_\_\_\_\_ Supervisor  
Dr. K. Galal

Approved by: \_\_\_\_\_  
Fariborz Haghighat, Ph.D., P.Eng, Graduate Program Director  
Department of Building, Civil and Environmental Engineering

August 15, 2016

\_\_\_\_\_  
Dr. Amir Asif, Ph.D., PEng, Dean  
Faculty of Engineering and Computer Science

# **Abstract**

## **Investigation of Multi Suppressive Layers under Impact Load**

Sameh Yaken Aref Ahmed, Ph.D.

Concordia University, 2016

Recently, mitigation of blast effects has become one of the major challenges in structural engineering. In this regard, sandwich panels are considered attractive systems for blast mitigation applications. This is contributed to their considerable energy absorption capability compared to solid panels of the same weight. These sandwich panels can have different inner core configurations to provide adequate stiffness, strength, and energy absorption for resisting different blast loads.

This research evaluates numerically the effectiveness of using woven shapes as a new core topology in sandwich panels to act as a suppressive layer for resisting blast loads. The new shape has been studied for both fibre reinforced polymer (FRP) sandwich panels and metallic sandwich panels. The numerical models have been created using nonlinear explicit finite element simulation. Each model has been validated using available data in the literature that uses honeycomb and folded shapes. The results of proposed woven shapes have been compared to those of honeycomb and folded shapes to examine the effectiveness of using woven shape in blast mitigation.

Throughout the study, twelve FRP panels with different inner core configurations are proposed to enhance panels' performance by reducing their peak deformation and increasing their energy dissipation. A parametric study was conducted on the best performing inner core configurations to achieve the highest resistance for blast loads. Moreover, the study investigates the effect of filling the FRP sandwich panels with sand, polyurethane foam, and dytherm foam on the panels' blast resistance. In order to generalize the findings of this research, other panels with the new proposed inner core configurations are simulated using stainless steel instead of FRP. Finally, the effect of changing the outer layers' thickness, applying successive blast loads on the same sandwich panels, and changing scaled distance has been investigated for metallic sandwich panels. Comparing

woven shapes to honeycomb and folded shapes shows that using sandwich panels with woven shapes provides a better impulsive resistance.

*This dissertation is dedicated to the memory of my beloved father, Yaken Aref Ahmed, and to my beloved mother; they were and will always be my greatest support in life.*

# Acknowledgements

I would like to express my deep gratitude and appreciation to Professor Khaled Galal for being my supervisor and mentor throughout the planning and development of this thesis. Dr. Khaled has been keen on patiently providing ongoing support and encouragement. Without his endless constructive advice and guidance, this work could not have been completed. It has been an honor for me to be one of his Ph.D. students. Such experience has enriched my knowledge and is a remarkable success in my Academic journey. I sincerely wish Dr. Khaled Galal the best of luck and success in his life and professional endeavors.

I would also like to extend my thanks to the respectable committee members, Dr. Ramin Sedaghati, Dr. Ashutosh Bagchi, and Dr. Anjan Bhowmick for being part of my committee and for providing their valuable comments and feedback on the provided work.

I, lovingly, would like to dedicate this thesis to the memory of my dear father, Yaken Aref, who wished to see it happens and is in heaven now. Certainly, I am truly grateful to my mother. Without her love, dedication, endless support, and prayers, it would have been impossible to achieve so much in my life. Also, I would like to offer my special thanks to my dearest amazing sisters for their love and sincere support throughout my entire life. My utmost thanks and gratitude to my uncle, Ahmed Aref Ahmed, for being a great source of encouragement in my life and for putting me on the right path to follow. Last but not least, truly unbounded thanks are due to my dear wife, for her loving support, tolerance, and endless encouragement, which has been essential in bringing this work to reality.

Also, I would like to offer my sincere appreciation for my dear friends Omar Yagoub and Ashraf Osman for their true support throughout this journey and I wish them best of luck and success in their lives.

Finally, I am truly grateful for my Professor in Egypt, Dr. Mostafa Abdel Wahab, who has been a great supporter during my thesis and is still backing me up during my Ph.D. journey. Dr. Mostafa is always willing to transfer his deep knowledge and experiences to me whenever needed.

# Table of Contents

---

<b>LIST OF FIGURES .....</b>	<b>X</b>
<b>LIST OF TABLES .....</b>	<b>XVI</b>
<b>LIST OF ABBREVIATIONS.....</b>	<b>XVII</b>
<b>CHAPTER 1 INTRODUCTION .....</b>	<b>1</b>
1.1 RESEARCH SIGNIFICANCE .....	1
1.2 RESEARCH OBJECTIVES.....	3
1.3 SCOPE OF RESEARCH .....	3
1.4 CONTRIBUTIONS .....	4
1.5 RESEARCH OVERVIEW.....	5
1.6 DISSEMINATION OF THE WORK DESCRIBED IN THIS STUDY.....	6
<b>CHAPTER 2 LITERATURE REVIEW .....</b>	<b>7</b>
2.1 INTRODUCTION ON BLAST LOADING AND ITS EFFECTS ON STRUCTURES.....	7
2.2 FUNDAMENTALS OF BLAST LOADING .....	8
2.2.1 <i>Blast Wave Parameters</i> .....	11
2.2.2 <i>Scaling Laws</i> .....	13
2.2.3 <i>Trinitrotoluene (TNT) Equivalence</i> .....	15
2.2.4 <i>Blast Load Prediction</i> .....	16
2.3 BACKGROUND ON SANDWICH PANELS .....	21
2.4 EFFECTIVENESS OF USING SANDWICH PANELS .....	21
2.5 COMPOSITE SANDWICH PANELS TO RESIST BLAST LOADS .....	26
2.6 METALLIC SANDWICH PANELS TO RESIST BLAST LOADS .....	29
2.7 EFFECTIVENESS OF USING FILLING MATERIAL .....	39
<b>CHAPTER 3 BLAST MODELLING .....</b>	<b>43</b>
3.1 INTRODUCTION.....	43
3.2 EXPLICIT FINITE ELEMENT METHOD (FEM) .....	43
3.3 <i>LS-DYNA AND AUTODYN SOFTWARE</i> .....	45
3.3.1 <i>Lagrange Analysis</i> .....	46
3.3.2 <i>Euler Analysis</i> .....	47
3.3.3 <i>Smooth Particle Hydrodynamics (SPH) Analysis</i> .....	49

3.3.4	<i>Coupled Eulerian-Lagrangian Analysis for LS-DYNA versus AUTODYN</i> .....	50
3.4	MATERIAL MODELLING .....	51
3.4.1	<i>Trinitrotoluene (TNT)</i> .....	52
3.4.2	<i>Air</i> .....	52
3.4.3	<i>FRP</i> .....	53
3.4.4	<i>Sand</i> .....	53
3.4.5	<i>Steel</i> .....	53
3.5	MODELLING THE PROPAGATION OF THE BLAST WAVE.....	54
3.5.1	<i>Define Geometry Properties</i> .....	54
3.5.2	<i>The Remapping Method</i> .....	59
3.5.3	<i>Sensitivity Analysis</i> .....	61
3.5.4	<i>Boundary Conditions</i> .....	66
3.5.5	<i>Interaction and contact points</i> .....	68
3.6	SUMMARY.....	68
<b>CHAPTER 4 FRP SANDWICH PANELS .....</b>		<b>70</b>
4.1	FRP CORE GEOMETRY .....	70
4.2	MATERIAL PROPERTIES .....	72
4.3	NUMERICAL MODEL VALIDATION.....	76
4.3.1	<i>Experimental and Numerical Deflections</i> .....	78
4.3.2	<i>Failure Modes</i> .....	81
4.4	ENERGY DISSIPATION.....	84
4.5	EFFECT OF SAND FILLING ON THE BEHAVIOUR OF FRP SANDWICH PANELS .....	85
4.6	PROPOSED CORE CONFIGURATIONS OF FRP SANDWICH PANELS.....	88
4.6.1	<i>Analysis Results</i> .....	91
4.6.1.1	<i>Numerical Results of Group 1</i> .....	91
4.6.1.2	<i>Numerical Results of Group 2</i> .....	92
4.6.1.3	<i>Numerical Results of Group 3</i> .....	94
4.6.2	<i>Failure Modes</i> .....	95
4.7	PARAMETRIC STUDY .....	97
4.7.1	<i>Effect of Changing Length, Width and Height</i> .....	100
4.7.2	<i>Effect of Thickness</i> .....	102
4.7.3	<i>Constant Weight</i> .....	104
4.7.4	<i>Effect of Wave Peak Length</i> .....	106
4.8	FILLING MATERIAL .....	110
4.9	SUMMARY.....	115

<b>CHAPTER 5 METTALIC SANDWICH PANELS .....</b>	<b>117</b>
5.1 CORE TOPOLOGIES .....	117
5.2 MATERIAL PROPERTIES .....	122
5.3 MODEL VALIDATION.....	123
5.3.1 <i>Varying Back Layer</i> .....	124
5.3.2 <i>Varying Front Layer</i> .....	128
5.4 PROPOSED CORE CONFIGURATIONS.....	132
5.4.1 <i>Varying Back Layer</i> .....	132
5.4.2 <i>Varying Front Layer</i> .....	135
5.5 CHANGING OUTER LAYERS' THICKNESS .....	138
5.5.1 <i>Front Layer Deflection</i> .....	138
5.5.2 <i>Back Layer Deflection</i> .....	140
5.5.3 <i>Energy Dissipation</i> .....	142
5.6 SUCCESSIVE BLAST LOADS ON SAME SANDWICH PANEL.....	145
5.6.1 <i>Front Layer Deflection</i> .....	145
5.6.2 <i>Back Layer Deflection</i> .....	148
5.6.3 <i>Energy Dissipation</i> .....	151
5.7 CHANGING SCALED DISTANCE .....	153
5.7.1 <i>Scaled Distance of 1 m/kg<sup>1/3</sup></i> .....	153
5.7.2 <i>Scaled Distance of 0.87 m/kg<sup>1/3</sup></i> .....	161
5.7.3 <i>Scaled Distance of 0.79 m/kg<sup>1/3</sup></i> .....	169
5.8 PARAMETERS CHART OF DIFFERENT PANELS TOPOLOGIES.....	178
5.9 SUMMARY.....	181
<b>CHAPTER 6 CONCLUSION.....</b>	<b>182</b>
6.1 CONCLUSIONS.....	182
6.2 FUTURE WORK.....	186
<b>REFERENCES .....</b>	<b>188</b>

# List of Figures

---

<b>Figure 2.1</b> Explosion creation at different time steps (Bang, 2014).....	9
<b>Figure 2.2</b> Blast loading categories: a) free air burst, b) air burst, c) surface burst (Solomos, 2013) .....	10
<b>Figure 2.3</b> Blast pressure profile (Army, 1990) .....	11
<b>Figure 2.4</b> Mach stem creation (Army, 1990).....	13
<b>Figure 2.5</b> Hopkinson-Cranz scaling law (Army, 1990) .....	14
<b>Figure 2.6</b> Positive phase blast parameters for hemispherical TNT surface blast (DoD, 2008).....	17
<b>Figure 2.7</b> Positive phase blast parameters for spherical TNT surface blast (DoD, 2008).....	18
<b>Figure 2.8</b> Negative phase blast parameters for hemispherical TNT surface blast (DoD, 2002) .....	18
<b>Figure 2.9</b> Negative phase blast parameters for spherical TNT surface blast (DoD, 2002) .....	19
<b>Figure 2.10</b> Reflected pressure coefficient versus angle of incidence (DoD, 2008) .....	20
<b>Figure 2.11</b> Normalized reflected impulse versus angle of incidence (DoD, 2008) .....	20
<b>Figure 2.12</b> Honeycomb core (Meraghni et al., 1999) .....	22
<b>Figure 2.13</b> Bending behaviours of sandwich panel: (a) elastic deformation; (b) buckling and debonding; and (c) core shear (Fan et al., 2007) .....	24
<b>Figure 2.14</b> Corrugated-core sandwich panel and a panel unit (Chang et al., 2005).....	24
<b>Figure 2.15</b> Typical lattice truss topologies: (a) octet truss, (b) tetrahedral lattice truss, (c) lattice block, (d) pyramidal lattice truss, and (e) 3D kagome (Liu et al., 2006) .....	25
<b>Figure 2.16</b> Different inner core configurations (Hoemann, 2007).....	29
<b>Figure 2.17</b> The deformations predicted for the three cores (Liang et al., 2007) .....	32
<b>Figure 2.18</b> Dynamic core crushing of a cellular core sandwich panel (H. Wadley et al., 2008) .....	33
<b>Figure 2.19</b> Sketches of the (a) square honeycomb, (b) triangular honeycomb, (c) multi-layer pyramidal truss, (d) triangular corrugation, and (e) diamond corrugation sandwich cores (Dharmasena et al., 2010) .....	34
<b>Figure 2.20</b> Photographs of the dynamically tested sandwich panels for (a) square-honeycomb, (b) triangular honeycomb, (c) multi-layer pyramidal truss, (d) triangular corrugation and (e) diamond corrugation (Dharmasena et al., 2010) .....	35
<b>Figure 2.21</b> Folded and honeycomb core topologies (Alberdi et al., 2013) .....	37
<b>Figure 2.22</b> Orthotropic core topologies (Alberdi et al., 2013).....	37
<b>Figure 2.23</b> Core deformed shapes (Alberdi et al., 2013) .....	38
<b>Figure 2.24</b> Effect of increasing front layer thickness (P. Zhang et al., 2015).....	38
<b>Figure 2.25</b> Effect of increasing back layer thickness (P. Zhang et al., 2015) .....	39
<b>Figure 2.26</b> Empty and foam filled panels; (a) long beam empty, (b) long beam filled, (c) short beam empty, and (d) short beam filled (Yan et al., 2014).....	41

<b>Figure 2.27</b> High-speed images of unfilled corrugated steel core sandwich panel during shock loading (Yazici et al., 2014).....	41
<b>Figure 2.28</b> High-speed images of foam core sandwich specimen during shock loading (Yazici et al., 2014).....	42
<b>Figure 2.29</b> High-speed images of fully foam filled corrugated core sandwich specimen during shock loading (Yazici et al., 2014).....	42
<b>Figure 3.1</b> Grid deformation in a Lagrange analysis (Birnbaum et al., 1999).....	46
<b>Figure 3.2</b> A typical computation step in a Lagrange analysis (AUTODYN, 2014).....	47
<b>Figure 3.3</b> Material flow through a stationary grid in an Euler analysis (Birnbaum et al., 1999).....	48
<b>Figure 3.4</b> A typical computation step in an Euler analysis (AUTODYN, 2014).....	49
<b>Figure 3.5</b> A typical computation step in an SPH analysis (AUTODYN, 2014).....	50
<b>Figure 3.6</b> Field test schematic (adapted from Hoemann, 2007).....	54
<b>Figure 3.7</b> Schematic of the FRP finite element model.....	55
<b>Figure 3.8</b> Schematic of the metallic finite element model.....	56
<b>Figure 3.9</b> 1D initial expansion model of TNT.....	59
<b>Figure 3.10</b> 2D expansion model of TNT.....	60
<b>Figure 3.11</b> 3D expansion model of TNT for metallic model.....	60
<b>Figure 3.12</b> Schematic of wave propagation in FRP finite element model.....	61
<b>Figure 3.13</b> Incident pressure for different wedge categories of the FRP model.....	62
<b>Figure 3.14</b> Reflected pressure for different 3D air categories of FRP model.....	63
<b>Figure 3.15</b> Incident pressure for different wedge categories of the metallic model.....	64
<b>Figure 3.16</b> Reflected pressure for different 3D air categories of the metallic model.....	65
<b>Figure 3.17</b> Illustration of the solid mesh.....	66
<b>Figure 3.18</b> Boundary conditions for the FRP panels.....	67
<b>Figure 3.19</b> Boundary conditions for the metallic panels.....	67
<b>Figure 4.1</b> Inner core configurations of the FRP sandwich panels.....	71
<b>Figure 4.2</b> Experimental (Hoemann, 2007) and numerical (current study) pressure time histories.....	77
<b>Figure 4.3</b> Experimental and numerical deflection time histories for W1.....	79
<b>Figure 4.4</b> Experimental and numerical deflection time histories for W2.....	79
<b>Figure 4.5</b> Experimental and numerical deflection time histories for W3.....	80
<b>Figure 4.6</b> Experimental and numerical deflection time histories for W4.....	80
<b>Figure 4.7</b> Experimental panels failure of the TRW shape configuration (a) W1 and (b) W3 (Hoemann, 2007).....	82
<b>Figure 4.8</b> Experimental panels failure of the PW shape configuration (Hoemann, 2007).....	82
<b>Figure 4.9</b> Failure patterns of the simulated panel W1.....	82
<b>Figure 4.10</b> Failure patterns of the simulated panel W2.....	83
<b>Figure 4.11</b> Failure patterns of the simulated panel W3.....	83

<b>Figure 4.12</b> Failure patterns of the simulated panel W4 .....	84
<b>Figure 4.13</b> The distribution of energy dissipated between panel components .....	85
<b>Figure 4.14</b> Numerical deflection time history of W1 .....	86
<b>Figure 4.15</b> Numerical deflection time history of W2 .....	87
<b>Figure 4.16</b> Numerical deflection time history of W3 .....	87
<b>Figure 4.17</b> Numerical deflection time history of W4 .....	88
<b>Figure 4.18</b> Central point deflection time histories of Group 1 .....	92
<b>Figure 4.19</b> Central point deflection time histories of Group 2 .....	93
<b>Figure 4.20</b> Central point deflection time histories of Group 3 .....	94
<b>Figure 4.21</b> Failure patterns of RW panels (a) W5, and (b) W8 .....	96
<b>Figure 4.22</b> Failure patterns of WV2-1 panels (a) W6, and (b) W13 .....	96
<b>Figure 4.23</b> Inner core configurations of W16; (a) WV2-1 Strips and (b) RW Axis .....	98
<b>Figure 4.24</b> Failure pattern of the proposed panel W16 .....	99
<b>Figure 4.25</b> Woven core sandwich panel schematic .....	100
<b>Figure 4.26</b> Central point deflection time histories with changed parameters and h=50 mm .....	101
<b>Figure 4.27</b> Central point deflection time histories with changed parameters and h=30 mm .....	102
<b>Figure 4.28</b> Central point deflection time histories with changed parameters and h=110 mm .....	102
<b>Figure 4.29</b> Central point deflection time histories of W16 with different thickness .....	104
<b>Figure 4.30</b> Central point deflection time histories of W19 with different thickness .....	104
<b>Figure 4.31</b> Central point deflection time histories of panels with constant weight .....	106
<b>Figure 4.32</b> Schematic of a woven core sandwich panel with wave peak length $\geq 0$ .....	107
<b>Figure 4.33</b> Effect of peak length variations .....	108
<b>Figure 4.34</b> Compaction of sand .....	110
<b>Figure 4.35</b> Compaction of polyurethane and dytherm foams .....	111
<b>Figure 4.36</b> Deflection time history of W3 with different filling materials .....	112
<b>Figure 4.37</b> Deflection time history of W4 with different filling materials .....	113
<b>Figure 4.38</b> Deflection time history of W16 with different filling materials .....	113
<b>Figure 4.39</b> Deflection time history of W26 with different filling materials .....	114
<b>Figure 4.40</b> Deflection time history of W27 with different filling materials .....	114
<b>Figure 5.1</b> Honeycomb core topologies .....	119
<b>Figure 5.2</b> Folded core topologies .....	120
<b>Figure 5.3</b> Woven core topologies .....	121
<b>Figure 5.4</b> Effect of changing back layer thickness on front layer deflection for honeycomb shape using LS_DYNA (Alberdi et al., 2013) and AUTODYN (Current study) .....	125
<b>Figure 5.5</b> Effect of changing back layer thickness on front layer deflection for folded shape using LS_DYNA (Alberdi et al., 2013) and AUTODYN (Current study) .....	126

<b>Figure 5.6</b> Effect of changing back layer thickness on back layer deflection for honeycomb shape using LS_DYNA (Alberdi et al., 2013) and AUTODYN (Current study) .....	126
<b>Figure 5.7</b> Effect of changing back layer thickness on back layer deflection for folded shape using LS_DYNA (Alberdi et al., 2013) and AUTODYN (Current study) .....	127
<b>Figure 5.8</b> Effect of changing back layer thickness on energy dissipation for honeycomb shape using LS_DYNA (Alberdi et al., 2013) and AUTODYN (Current study) .....	127
<b>Figure 5.9</b> Effect of changing back layer thickness on energy dissipation for folded shape using LS_DYNA (Alberdi et al., 2013) and AUTODYN (Current study) .....	128
<b>Figure 5.10</b> Effect of changing front layer thickness on front layer deflection for honeycomb shape using LS_DYNA (Alberdi et al., 2013) and AUTODYN (Current study) .....	129
<b>Figure 5.11</b> Effect of changing front layer thickness on front layer deflection for folded shape using LS_DYNA (Alberdi et al., 2013) and AUTODYN (Current study) .....	130
<b>Figure 5.12</b> Effect of changing front layer thickness on back layer deflection for honeycomb shape using LS_DYNA (Alberdi et al., 2013) and AUTODYN (Current study) .....	130
<b>Figure 5.13</b> Effect of changing front layer thickness on back layer deflection for folded shape using LS_DYNA (Alberdi et al., 2013) and AUTODYN (Current study) .....	131
<b>Figure 5.14</b> Effect of changing front layer thickness on energy dissipation for honeycomb shape using LS_DYNA (Alberdi et al., 2013) and AUTODYN (Current study) .....	131
<b>Figure 5.15</b> Effect of changing front layer thickness on energy dissipation for folded shape using LS_DYNA (Alberdi et al., 2013) and AUTODYN (Current study) .....	132
<b>Figure 5.16</b> Effect of changing back layer thickness on front layer deflection for proposed panels.....	134
<b>Figure 5.17</b> Effect of changing back layer thickness on back layer deflection for proposed panels.....	134
<b>Figure 5.18</b> Effect of changing back layer thickness on energy dissipation for proposed panels .....	135
<b>Figure 5.19</b> Effect of changing front layer thickness on front layer deflection for proposed panels .....	137
<b>Figure 5.20</b> Effect of changing front layer thickness on back layer deflection for proposed panels.....	137
<b>Figure 5.21</b> Effect of changing front layer thickness on energy dissipation for proposed panels .....	138
<b>Figure 5.22</b> Effect of changing outer layers' thickness on front layer deflection for honeycomb panels...	139
<b>Figure 5.23</b> Effect of changing outer layers' thickness on front layer deflection for folded panels .....	140
<b>Figure 5.24</b> Effect of changing outer layers' thickness on front layer deflection for woven panels.....	140
<b>Figure 5.25</b> Effect of changing outer layers' thickness on back layer deflection for honeycomb panels...	141
<b>Figure 5.26</b> Effect of changing outer layers' thickness on back layer deflection for folded panels .....	142
<b>Figure 5.27</b> Effect of changing outer layers' thickness on back layer deflection for woven panels.....	142
<b>Figure 5.28</b> Effect of changing outer layers' thickness on energy dissipation for honeycomb panels .....	144
<b>Figure 5.29</b> Effect of changing outer layers' thickness on energy dissipation for folded panels.....	144
<b>Figure 5.30</b> Effect of changing outer layers' thickness on energy dissipation for woven panels .....	145
<b>Figure 5.31</b> Front layer deflection for honeycomb panels exposed to a second blast load .....	147
<b>Figure 5.32</b> Front layer deflection for folded panels exposed to a second blast load.....	147

<b>Figure 5.33</b> Front layer deflection for woven panels exposed to a second blast load .....	148
<b>Figure 5.34</b> Back layer deflection for honeycomb panels exposed to a second blast load.....	150
<b>Figure 5.35</b> Back layer deflection for folded panels exposed to a second blast load .....	150
<b>Figure 5.36</b> Back layer deflection for woven panels exposed to a second blast load.....	151
<b>Figure 5.37</b> Energy dissipation for honeycomb panels exposed to a second blast load .....	152
<b>Figure 5.38</b> Energy dissipation for folded panels exposed to a second blast load .....	153
<b>Figure 5.39</b> Energy dissipation for woven panels exposed to a second blast load .....	153
<b>Figure 5.40</b> Front layer deflection for honeycomb panels having scaled distance of $1 \text{ m/kg}^{1/3}$ .....	155
<b>Figure 5.41</b> Front layer deflection for folded panels having scaled distance of $1 \text{ m/kg}^{1/3}$ .....	155
<b>Figure 5.42</b> Front layer deflection for woven panels having scaled distance of $1 \text{ m/kg}^{1/3}$ .....	156
<b>Figure 5.43</b> Back layer deflection for honeycomb panels having scaled distance of $1 \text{ m/kg}^{1/3}$ .....	158
<b>Figure 5.44</b> Back layer deflection for folded panels having scaled distance of $1 \text{ m/kg}^{1/3}$ .....	158
<b>Figure 5.45</b> Back layer deflection for woven panels having scaled distance of $1 \text{ m/kg}^{1/3}$ .....	159
<b>Figure 5.46</b> Energy dissipation for honeycomb panels having scaled distance of $1 \text{ m/kg}^{1/3}$ .....	160
<b>Figure 5.47</b> Energy dissipation for folded panels having scaled distance of $1 \text{ m/kg}^{1/3}$ .....	160
<b>Figure 5.48</b> Energy dissipation for woven panels having scaled distance of $1 \text{ m/kg}^{1/3}$ .....	161
<b>Figure 5.49</b> Front layer deflection for honeycomb panels having scaled distance of $0.87 \text{ m/kg}^{1/3}$ .....	162
<b>Figure 5.50</b> Front layer deflection for folded panels having scaled distance of $0.87 \text{ m/kg}^{1/3}$ .....	163
<b>Figure 5.51</b> Front layer deflection for woven panels having scaled distance of $0.87 \text{ m/kg}^{1/3}$ .....	163
<b>Figure 5.52</b> Back layer deflection for honeycomb panels having scaled distance of $0.87 \text{ m/kg}^{1/3}$ .....	165
<b>Figure 5.53</b> Back layer deflection for folded panels having scaled distance of $0.87 \text{ m/kg}^{1/3}$ .....	166
<b>Figure 5.54</b> Back layer deflection for woven panels having scaled distance of $0.87 \text{ m/kg}^{1/3}$ .....	166
<b>Figure 5.55</b> Energy dissipation for honeycomb panels having scaled distance of $0.87 \text{ m/kg}^{1/3}$ .....	168
<b>Figure 5.56</b> Energy dissipation for folded panels having scaled distance of $0.87 \text{ m/kg}^{1/3}$ .....	168
<b>Figure 5.57</b> Energy dissipation for woven panels having scaled distance of $0.87 \text{ m/kg}^{1/3}$ .....	169
<b>Figure 5.58</b> Front layer deflection for honeycomb panels having scaled distance of $0.79 \text{ m/kg}^{1/3}$ .....	170
<b>Figure 5.59</b> Front layer deflection for folded panels having scaled distance of $0.79 \text{ m/kg}^{1/3}$ .....	171
<b>Figure 5.60</b> Front layer deflection for woven panels having scaled distance of $0.79 \text{ m/kg}^{1/3}$ .....	171
<b>Figure 5.61</b> Back layer deflection for honeycomb panels having scaled distance of $0.79 \text{ m/kg}^{1/3}$ .....	174
<b>Figure 5.62</b> Back layer deflection for folded panels having scaled distance of $0.79 \text{ m/kg}^{1/3}$ .....	175
<b>Figure 5.63</b> Back layer deflection for woven panels having scaled distance of $0.79 \text{ m/kg}^{1/3}$ .....	175
<b>Figure 5.64</b> Energy dissipation for honeycomb panels having scaled distance of $0.79 \text{ m/kg}^{1/3}$ .....	177
<b>Figure 5.65</b> Energy dissipation for folded panels having scaled distance of $0.79 \text{ m/kg}^{1/3}$ .....	178
<b>Figure 5.66</b> Energy dissipation for woven panels having scaled distance of $0.79 \text{ m/kg}^{1/3}$ .....	178
<b>Figure 5.67</b> Honeycomb topology parameters (back layer deflection, $\Delta$ , and energy dissipation, ED) versus scaled distance.....	179

<b>Figure 5.68</b> Folded topology parameters (back layer deflection, $\Delta$ , and energy dissipation, ED) versus scaled distance.....	180
<b>Figure 5.69</b> Woven topology parameters (back layer deflection, $\Delta$ , and energy dissipation, ED) versus scaled distance.....	180

# List of Tables

---

<b>Table 2.1</b> Equivalent TNT mass factors (Hyde, 1992).....	16
<b>Table 3.1</b> Material properties of Air .....	58
<b>Table 3.2</b> Material properties of TNT .....	58
<b>Table 3.3</b> Mesh sensitivity for the FRP model wedge .....	62
<b>Table 3.4</b> Mesh sensitivity for the 3D air domain of the FRP model.....	63
<b>Table 3.5</b> Mesh sensitivity of metallic model wedge.....	64
<b>Table 3.6</b> Mesh sensitivity for 3D air domain of the metallic model.....	65
<b>Table 4.1</b> Material properties of sand .....	72
<b>Table 4.2</b> Material properties of FRP.....	74
<b>Table 4.3</b> Description of FRP panels tested by Hoemann (2007).....	76
<b>Table 4.4</b> Summary of the blast pressure and impulse of the experimental tests of Hoemann (2007).....	76
<b>Table 4.5</b> The experimental (Hoemann, 2007) and numerical (current study) peak deflections .....	80
<b>Table 4.6</b> Effect of sand filling on panel deformations and energy dissipation .....	88
<b>Table 4.7</b> Description of the proposed FRP panels and their core configurations .....	90
<b>Table 4.8</b> Panel peak deflection and energy dissipation for Group 1.....	92
<b>Table 4.9</b> Panel peak deflection and energy dissipation for Group 2.....	93
<b>Table 4.10</b> Panel peak deflection and energy dissipation for Group 3.....	95
<b>Table 4.11</b> Effect of length, width, and height variations .....	101
<b>Table 4.12</b> Effect of thickness variations .....	103
<b>Table 4.13</b> Effect of changing sinusoidal dimensions with constant weight.....	105
<b>Table 4.14</b> Effect of changing wave peak length .....	109
<b>Table 4.15</b> Mechanical properties of polyurethane and dytherm foam.....	111
<b>Table 4.16</b> Effect of filling materials on panels' deformations and energy dissipation.....	115
<b>Table 4.17</b> Comparison between panels of different filling materials .....	115
<b>Table 5.1</b> Relative densities of different core topologies .....	122
<b>Table 5.2</b> Material properties of AISI 304 stainless steel .....	123

# List of Abbreviations

---

ALE	Arbitrary Lagrangian-Eulerian
EOS	Equation of State
Euler-FCT	Euler-Flux Corrected Transport
FE	Finite Element
FEM	Finite element method
FRP	Fibre Reinforced Polymer
GFRP	Glass Fibre Reinforced Polymer
JWL	Jones-Wilkins-Lee
PVC	Polyvinyl Chloride
SDOF	Single Degree of Freedom
SPH	Smooth Particle Hydrodynamics
TNT	Trinitrotoluene

## Chapter

# 1

## Introduction

Blast resistance structures are very important to minimize the risk to people and facilities from hazards arising from explosions. An explosion is defined as a large-scale, rapid and sudden release of energy. Explosions may be due to accidental explosions, terrorism, or military explosion. Many research studies nowadays have been conducted to investigate using sandwich panels in resisting blast effects. The current study investigates applications of Fibre Reinforced Polymer (FRP) sandwich panels and metallic sandwich panels to resist blast loads, where their light weight, fast installation and ease of handling, high-strength-to-weight ratio, and good thermal insulation properties are considered the main advantages of using these panels.

### 1.1 Research Significance

Recently, blast loads resulting from accidental or intentional events adversely affect different structures and threaten their occupants. Blast mitigation of structures has become an active area of research for governmental, industrial, and military organizations. In several industries, such as cement production, coal mining and petrochemical fields, the consequences of accidental explosions should be carefully considered. For example, in the petrochemical field, man-made accidents that occur in industrial facilities could trigger explosions that are accompanied by other phenomena such as fire and impact caused by explosion-borne missiles (Baker W.E., 1983). Accidental explosions can generate blast waves that threaten a structure's integrity. These structures are not usually designed to resist explosive actions, and hence they may be at great risk (Bulson, 2002).

Moreover, conventional structures are not designed to resist blast loads. Therefore, it is important to give due attention to the design and retrofit of structures against blast loads. Currently, the possibility of providing an adequate level of protection without changing people lifestyle and daily routine through building structures that are more similar to bunkers are one of the main controversial challenges facing researchers.

One of the solutions considered is using maneuverable blast walls to shield buildings and other structures against blast loads. Maneuverable walls act as a reflective surface for blast waves that reduces blast effect on the targeted building. During higher severity events, maneuverable walls are erected around structures as a first line of defense, increasing stand-off distance. The two main factors taken into consideration for designing maneuverable walls are the ease of assembly and portability. (X. Zhou & Hao, 2008) studied numerically the effectiveness of blast barriers in reducing blast effect. They stated that while placing a barrier between an explosion and a building, the peak reflected pressures and impulses created on the surface of a building are reduced, and the arrival time of blast wave is delayed.

Also, security has become a major concern for vital building facilities. Therefore, many facilities place blast-resistant checkpoints at the entrances or around the facility to control access. At higher levels of threat, the traditional way of reaching a higher protection level is to increase the stand-off distance by providing temporary checkpoints. Occupants of these temporary checkpoints will be at a great risk as these checkpoints are not usually designed against blast effects. Light weight sandwich panels are one of the solutions to provide temporary checkpoints that can be designed to resist blast load, while being moveable and easy to assemble. Moveable structures with such specifications can be also beneficial for temporary high-importance facilities such as barracks and hospitals (Hoemann, 2007). In addition, these temporary structures can be used in hazardous industrial fields that are vulnerable to blast.

Light-weight prefabricated moveable structures can provide a robust, durable and reliable replacement of the traditional sandbag bunkers used for temporary checkpoints. Sandwich panels are being used to manufacture light-weight moveable structures (Vinson, 2001). Sandwich panels are usually made of light-weight material. They typically consist of outer layers with a low-density core in between (Davies, 1993). The outer layers with the core layer form multi suppressive layers,

where the core material takes several forms such as honeycomb cores, corrugated cores, truss cores, Z-cores, C-cores, I-cores or solid foam cores.

## **1.2 Research Objectives**

The objective of this research is to conduct a thorough numerical study on the performance of composite and metallic sandwich panels under blast loading. Although this study is motivated by the use of sandwich walls to mitigate the blast effect, the findings can indeed be generalized and serve several other potential structural applications. These applications may include, but not limited to, flooring, decking, platforms and roofs. The study aims to change the inner core configuration of sandwich panels to reach the most effective core system that absorbs maximum energy with less damage level. In order to generalize the findings of this research, sandwich panels used have been once formed from FRP material and another time from stainless steel material.

Deflection and energy dissipation are the two factors that have been considered in this study against blast loads. The deflection can represent the failure that has occurred in the panels. Accordingly, the deflection is the primary factor that controls the design of panels, particularly, the deflection of the back layer as it is the last shield that protects occupants from blast (Kalny and Peterman, 2005). When addressing blast resistance, energy absorption is another important factor that should be taken into account. The target is to achieve maximum energy absorption with minimum failure level which is represented by deflection.

Several core topologies were used as suppressive layers of sandwich panels. The commonly used topologies are honeycomb and folded shapes for FRP sandwich panels. Whereas for metallic sandwich panels, the main topologies are honeycomb, folded, and lattice truss shapes. In this study, woven shapes have been proposed for both FRP and metallic sandwich panels. Also, the results of using woven sandwich panels versus that of folded and honeycomb sandwich panels have been compared, for both FRP and metallic materials.

## **1.3 Scope of Research**

Recently, an experiment study was carried out at Air Force Research Laboratory, Tyndall Air Force Base, in Florida by (Hoemann, 2007) to evaluate the use of FRP honeycomb composite panels for temporary structure applications under blast and fragmentation loading. In the current

research work, similar panels are simulated numerically to validate numerical results with experimental measurements. Other panels with different inner core configurations and different filling materials have been analyzed under blast loads. Deflection and energy absorption have been investigated. Furthermore, a geometric and material parametric study was conducted on the best performing core configurations, and the effect of changing filling material has been investigated. Throughout this research, sand, polyurethane foam, and dytherm foam are used as filling materials. Other panels with the new proposed inner core configurations are conducted using stainless steel instead of FRP. (Alberdi et al., 2013) studied metallic sandwich panels that are having folded and honeycomb shapes under blast effect. Similar panels have been simulated to validate the model. The proposed panels are modelled with the same dimension and boundary condition following the same approach of the work done by (Alberdi et al., 2013), by comparing the results of proposed panels with that of validated ones. Finally, the effect of changing the outer layers' thickness, applying successive blast loads on the same sandwich panel, and changing scaled distance has been investigated.

#### **1.4 Contributions**

The ability of sandwich panels to resist blast loads is better when compared with same aerial density monolithic metal plates (Shukla et al., 2010). In the current study, the newly proposed model with woven shape sandwich panel indicates that it can enhance the panels' performance under blast effects in terms of energy dissipation and deflection. It can reach up to twice the dissipation energy at a reduced level of deformation for FRP sandwich panels. On the other hand, for metallic sandwich panels, woven panels show better impulsive resistance than honeycomb and folded panels. Sandwich panels studied in this research work can be used in many applications such as:

- Maneuverable check points (instead of sand bags used nowadays),
- Protection wall panels which can be placed in front of any building that needs to be protected from blast effect,
- Moveable building which needs to be protected from blast effect like in gas and oil industry, and
- Military buildings like barracks and hospitals.

It is essential to mention that newly proposed core configurations that have been presented in this research can be studied to be used in other applications such as bridge decking, flooring, and roofing. In fact, these newly proposed core configurations can be studied to be used not only in structural engineering field but also in the mechanical engineering field (i.e., especially for the automotive, aerospace, and transportation applications).

## **1.5 Research Overview**

This study consists of 6 chapters including this introduction. Chapter 2 is the literature review, which provides a background on blast loading and its effects on structures. It also tackles the fundamentals of blast loading and the method used for determining blast parameters. Moreover, this chapter covers sandwich panels and tackles in more details the sandwich panels' performance in resisting blast loads and the effectiveness of using filling material. Chapter 3 represents more details on the models and methods of blast waves' generation. Moreover, a sensitivity analysis for the numerical model has been presented. In addition, the material models of materials used in this study and the boundary conditions are included in this chapter. Chapter 4 represents FRP sandwich panels. It includes the validation of numerical results with experimental measurements. Furthermore, the contribution of suppressive layers (front layer, inner core, and back layer) in energy dissipation has been studied. The influence of using sand as a filling material is investigated as well in this chapter. The chapter also studies the proposed panels with new core configurations and compares the obtained results with the results of validation models. Finally, results of the parametric study and effect of changing filling material have been discussed in this chapter. Chapter 5 discusses metallic sandwich panels. It starts with validating the model, then it introduces the proposed panels and studies their performance. This is in addition to studying the effect of changing the thickness of outer layers on the performance of metallic sandwich panels. This chapter also investigates the effect of successive blast loads on the same sandwich panel. Then, it tackles the effect of changing scaled distance on panel's performance. Finally, Chapter 6 includes the conclusions and represents the future work.

## 1.6 Dissemination of the Work Described in this study

During the current study, some of the findings have been prepared for dissemination and presentation in the following peer-reviewed journal and conference:

Ahmed, S., El-Sokkary, H, and Galal, K. (2016). Numerical Simulation of FRP Sandwich Panels under Blast Effects. *Journal of Performance of Constructed Facilities*, ASCE, in press, accepted April 2016.

Ahmed, S., and Galal, K. (2016). Effectiveness of FRP Sandwich Panels for Blast Resistance. *Journal of Composite Structures*, Elsevier. (Revised manuscript submitted July 2016)

Ahmed, S., and Galal, K. (2016). Metallic Sandwich Panels Response against Blast Loads. *Journal of Engineering Structures*, Elsevier. (Submitted August 2016)

Ahmed, S., and Galal, K. (2016). *Energy dissipation capacity of FRP sandwich panels subjected to blast loads*. Paper presented at the 7<sup>th</sup> International Conference on Advanced Composite Materials in Bridges and Structures, Vancouver, Canada, 10 pages.

# Chapter

# 2

## Literature Review

### 2.1 Introduction on Blast Loading and Its Effects on Structures

Nowadays, considerable attention has been given to the behaviour of structures against blast loading. Accordingly, the explosion phenomena and its effect have to be studied. During the last decades, several investigations had been done on the explosion phenomena especially in the military community.

Baker's *Explosions in Air* book (1973) covers the basics of air blast analysis, theoretical computational methods, and experimental blast analysis. It also covers the equipment used in air blast analysis and data gathering. A technical report by (Kingery & Bulmash, 1984) provides fitted functions within a Log-Log domain for determining the blast parameters. These functions are widely accepted as authoritative engineering predictions. The Army Technical Manual (1985) on the protective design of structures for conventional weapons effects, TM5-855-1, has essentially presented the methods found in Kingery and Bulmash for calculating blast loads, and accordingly has provided the designing guidelines that should be considered. Additionally, the Manual has achieved improvements in the structural aspects of blast events, the understanding of combustion and explosion phenomena, explosion characteristics, and many other effects were greatly improved. Finally, Bulson (2002) published a book on *The Explosive Loading of Engineering Structures* that discusses loads resulted from nuclear tests and smaller scale conventional explosives. This chapter provides a background on blast loading and discusses the effects of blast on structures in details.

## 2.2 Fundamentals of Blast Loading

An explosion can be categorized into physical, nuclear, or chemical event. Eruption of a volcano, catastrophic failure of pressure vessels or the violent mixing of liquids at different temperatures are examples of the physical explosions. A nuclear explosion may be caused by either fusion or fission reactions. In this study, the main point of focus is the chemical explosions.

Chemical explosions occur due to rapid oxidation reaction to fuel elements of an explosive compound. Rapid oxidation causes a reaction known as combustion. Most practical explosives are either formed as solid or liquid. Chemical explosions are known also as condensed explosives, and the molecules of the fuel elements contain the oxygen required to initiate combustion. During the reaction process, carbon and hydrogen atoms composing the fuel element of the explosive decompose violently, releasing heat and high pressure gas. When the velocity of the high pressure gas is significantly higher than the material sound speed, the explosive reaction is referred to as a detonation, and results in a high intensity shock wave known as a blast wave (Smith & Hetherington, 1994). Figure 2.1 illustrates the creation of explosion at different time steps.

To resist blast loads, it is important to understand the mechanics of blast loading. A blast load is generated when an explosion sets in motion a surrounding mass of air, creating a high speed shock wave that travels in radial directions from the detonation point. Blast loads cause pressures that are hundred times greater than the wind loads. Although blast loads have very high peak pressures, the durations are very short. The short blast loads durations reduce the effects of such high pressures on structures. A nearby building will be subjected to a short duration loading in the form of impulse (integral of pressure with respect to time). The intensity of such impulse depends on the following factors:

- Size of explosive material (typically expressed in the number of equivalent TNT)
- Distance from target (stand-off distance)
- Type of wave propagation
- Open or enclosed area
- Strength of cladding (assuming the structure has cladding) can influence the effective tributary area of loading
- Geometry of structure (an angle of incidence of  $0^\circ$  results in the highest load)

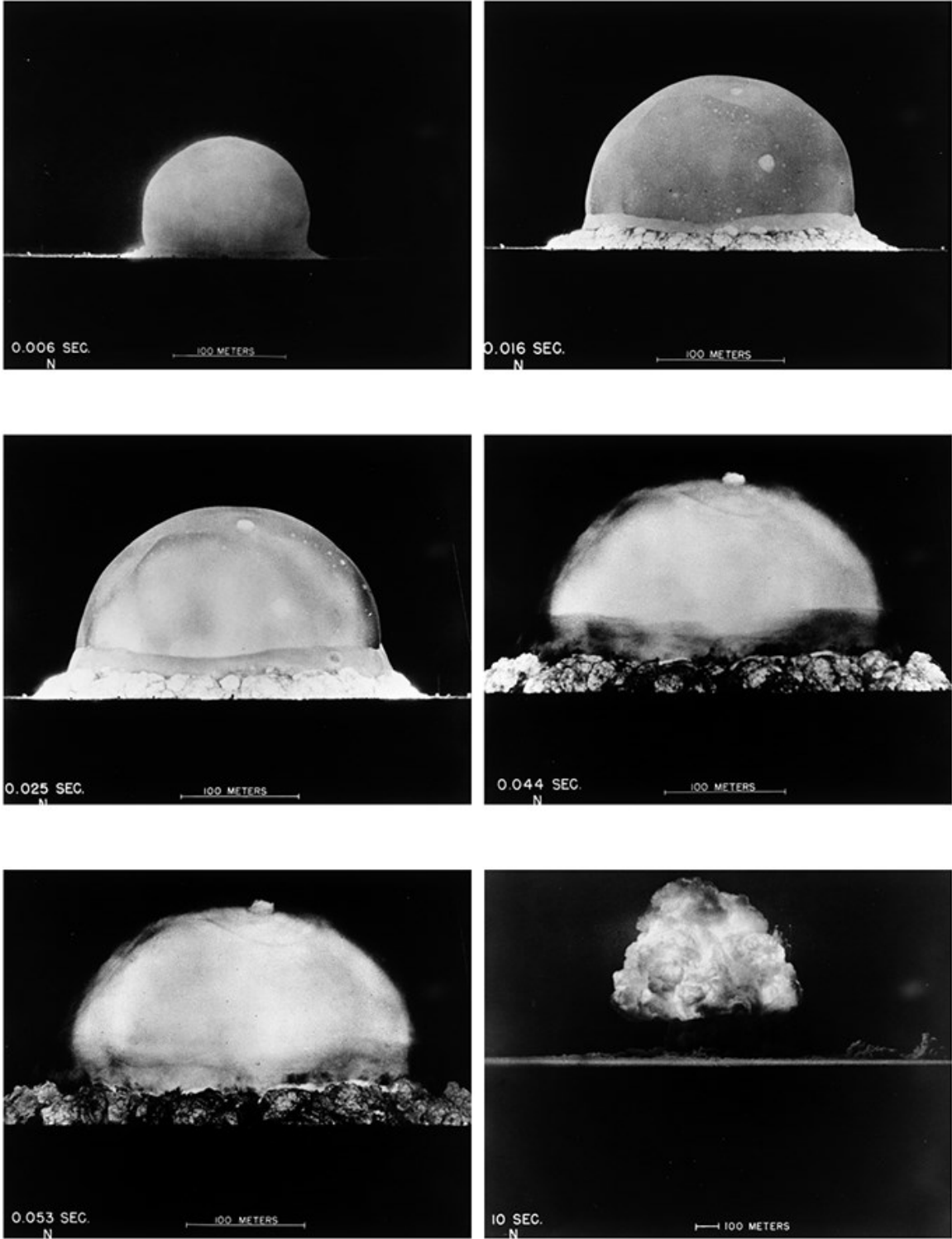


**Figure 2.1** Explosion creation at different time steps (Bang, 2014).

Blast loads are either confined (inside the structure) or unconfined (outside the structure). Confined blast load is divided into: fully vented, partially confined, and fully confined. Fully vented explosions occur when one or more surfaces are open to the atmosphere. Accordingly, no pressure occurs since blast waves are immediately sent into the atmosphere. In case of partially confined explosions, a limited opening is formulated, i.e. frangible surfaces that can contain the blast load for a limited amount of time before being released into the atmosphere. For the fully confined explosion, no opening is formulated. Blast waves are being reflected and amplified creating a gas pressure build-up (Conrath, 1999).

On the other hand, unconfined blast loads are divided into: free air burst, air burst (spherical surface burst), and surface burst (hemispherical surface burst). Unconfined explosions occur when blast waves propagate away from the source of explosion towards the structure due to the detonation of explosive in an open area. A free burst occurs when the shock wave produced by the detonation propagates away from the source and hits the structure directly before the reflection of the wave takes place. As for air burst explosion, the detonation occurs at a distance from the structure that allows blast wave reflection off the ground before reaching the structure. Finally, with surface burst explosions, detonation occurs near the ground and the initial shock wave is amplified at this point by the reflections of the shock wave out of the ground (Conrath, 1999). Figure 2.2 shows the three categories of unconfined blast loading: free airburst, airburst and surface burst. This study tackles in details the unconfined blast loads.

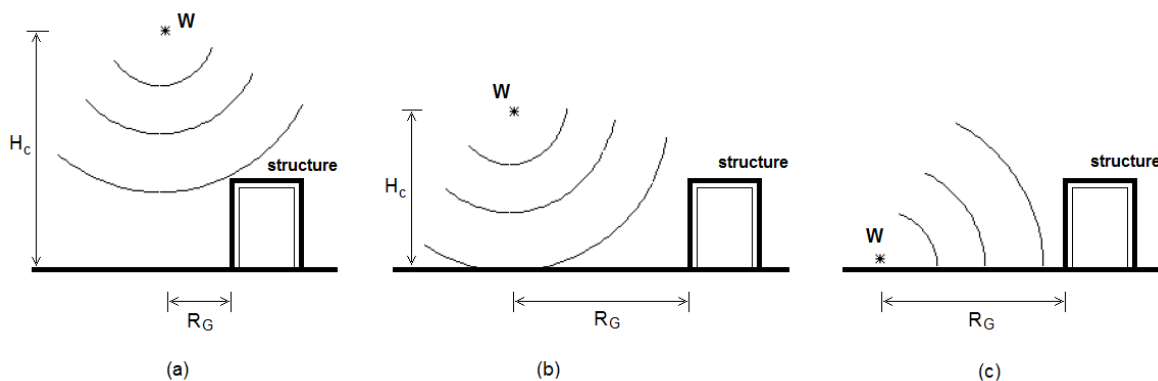


**Figure 2.2** Blast loading categories: a) free air burst, b) air burst, c) surface burst (Solomos, 2013)

During an explosion, hot gases under extremely high pressure are generated. The generated hot gases expand, forcing out the volume it occupies to travel at supersonic speed, creating a layer of compressed air called the shock front, and producing a sudden increase in pressure above the ambient atmospheric pressure (over-pressure). After a short time, the velocity of the shock front as well as the temperature decrease and the pressure drops below the ambient pressure. As a result of the dropped down pressure, a negative pressure region is then formed, creating a vacuum that sucked the air in. This phenomenon is called rarefaction.

### 2.2.1 Blast Wave Parameters

Blast loading are defined either by primary or secondary parameters. Overpressure, duration, and impulse are primary parameters for defining a blast loading. Whereas peak reflected pressure, peak dynamic pressure, shock front velocity, and blast wave length are considered secondary parameters. Secondary parameters are obtained from the primary parameters.

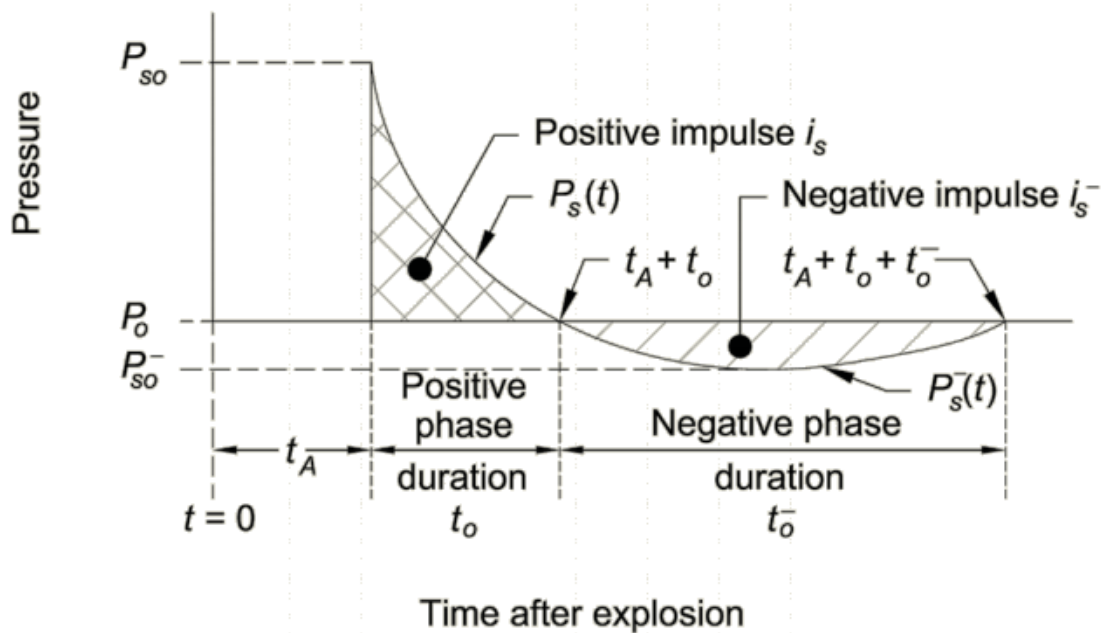


**Figure 2.3** Blast pressure profile (Army, 1990)

Figure 2.3 shows the pressure profile of a blast wave. This profile is a time history of a blast overpressure wave that impinges on a point in space, where there is a positive phase (over-pressure) and a negative phase (under-pressure) denoted by  $(t_d^+)$  and  $(t_d^-)$ , respectively. The time,

$t_a$ , represents the time of arrival which is the time that the shock wave takes to arrive at a recording station. The pressure,  $P_{SO}$ , represents the overpressure, or the peak incident pressure recorded at the station that is above the ambient atmospheric pressure ( $P_o$ ). The over-pressure is deemed more important than the under-pressure, and usually the effect of the under-pressure is neglected for the dynamic analysis of most structures.

The impulses are represented by the area under the pressure-time curve. The impulse,  $I_{SO}^+$ , represents the positive phase and can be computed from Equation 2.1, while the impulse,  $I_{SO}^-$ , represents the negative phase and can be computed from Equation 2.2 (Smith & Hetherington, 1994).

$$I_{SO}^+ = \int_{t_a}^{t_a+t_d^+} (P_{so}(t))dt \quad (2.1)$$

$$I_{SO}^- = \int_{t_a+t_d^+}^{t_a+t_d^++t_d^-} (P_{so}^-(t))dt \quad (2.2)$$

The pressure-time profile can be represented by the Friedlander equation, shown in Equation 2.3 (Smith & Hetherington, 1994).

$$P(t) = P_{SO} \left(1 - \frac{t}{t_d^+}\right) e^{\frac{bt}{t_d^+}} \quad (2.3)$$

In Equation 2.3,  $b$  is the decay coefficients that can be obtained from the following equation (Smith & Hetherington, 1994):

$$I_{SO}^+ = P_{SO} t_d^+ \left[ \frac{1}{b} - \frac{1}{b^2} (1 - e^{-b}) \right] \quad (2.4)$$

During shock waves propagation, upon encountering a denser medium, the reflection of shock waves occurs. Air molecules forming blast wave compress when it faces the reflecting surface due to the arrival of other incoming air molecules causing the overpressure to increase in magnitude. The angle of incidence between the plane shock front and the reflecting surface ( $\alpha_i$ ) controls the increase in pressure. This increasing pressure is more critical in designing blast resistant buildings and is known as reflected pressure ( $P_r$ ). Wave reflection can be normal ( $\alpha_i=90^\circ$ ), oblique ( $\alpha_i<90^\circ$ ), or Mach reflection. When spherical shock waves reach ground surface at a point directly under the

centre of detonation, Mach reflection is created. Shock waves are reflected and return back to the centre of detonation, and they are merged with other incoming waves forming a stronger shock front known as the Mach Stem. Figure 2.4 shows the incident wave, the reflected wave, the Mach Stem, and the triple point. The point at which Mach Stem, incident shock front, and reflected shock front are merged is called the triple point.

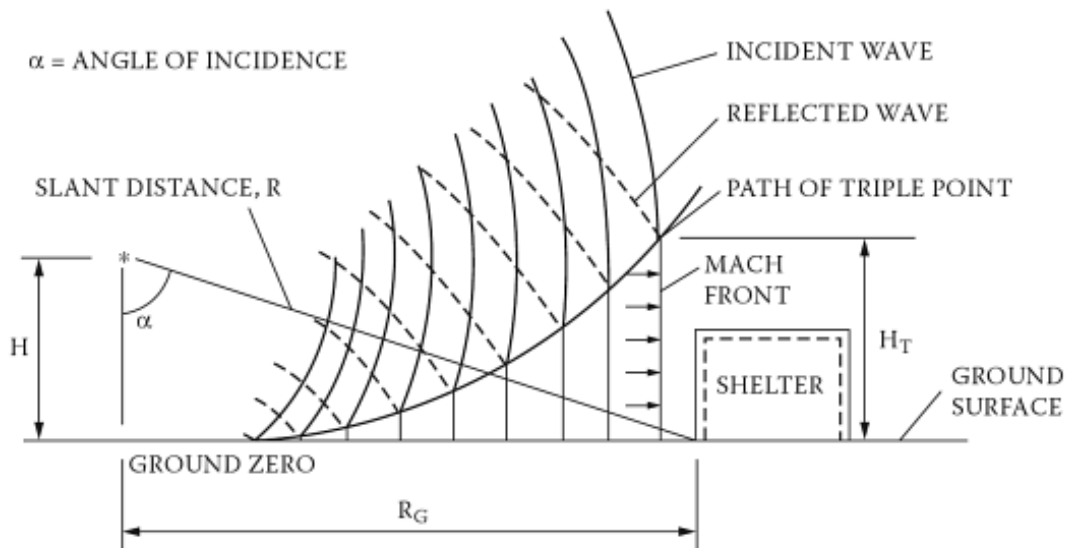


**Figure 2.4** Mach stem creation (Army, 1990)

## 2.2.2 Scaling Laws

In blast analysis, scaling laws are used to scale blast parameters. Results obtained from blast tests are generalized, and by changing one of the blast parameters, other parameters can be extrapolated. There are many different methods of scaling blast parameters but the most widely used is Hopkinson-Cranz scaling law. Hopkinson-Cranz scaling law was formulated by Hopkinson (1915) and is based on cube root scaling. It states that “Self-similar blast waves are produced at identical scaled distances when two explosive charges of similar geometry and of the same type of explosive, but of different sizes, are detonated in the same atmosphere” (Baker, 1973). In other words, if the charge weight,  $W$  (with “ $d$ ” diameter), is detonated at “ $R$ ” distance, the blast wave parameters: peak pressure ( $P_{SO}$ ), impulse ( $I_{SO}$ ), and duration of positive phase ( $t_d$ ), would be similar to an explosive charge weight ( $W_1$ ), with a diameter ( $\lambda d$ ), detonated at a distance ( $\lambda R$ ), with the same peak pressure ( $P_{SO}$ ), but with scaled duration ( $\lambda t_d$ ), and scaled impulse ( $\lambda I_{SO}$ ). For illustration, the Hopkinson-Cranz scaling law is shown in Figure 2.5.

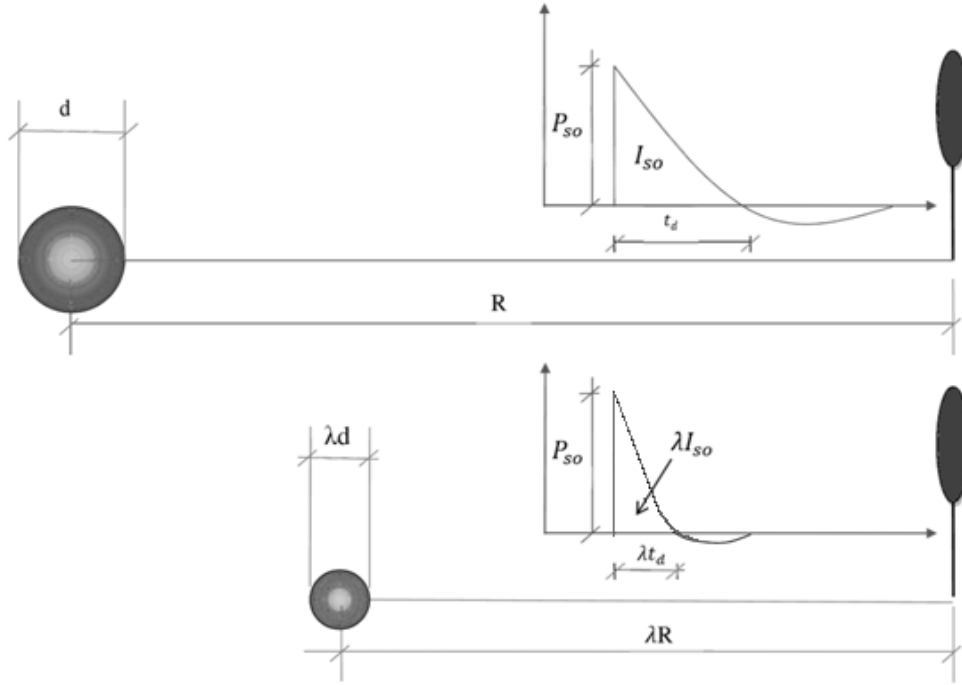


**Figure 2.5** Hopkinson-Cranz scaling law (Army, 1990)

The relationship between the two types of explosives can be expressed as follows:

$$W \propto d^3 \text{ and } W_1 \propto d_1^3 \quad (2.5)$$

Where  $d$  and  $d_1$  are the diameters of the spherically shaped explosive charges. From the above equation, the following relationship is obtained:

$$\frac{W}{W_1} = \left(\frac{d}{d_1}\right)^3 \text{ and } \frac{d}{d_1} = \left(\frac{W}{W_1}\right)^{\frac{1}{3}} \quad (2.6)$$

A dimensional scaled distance ( $Z$ ) is introduced as described by the following Equation, as the constant,  $Z$ , increases, the charge weight decreases resulting in a smaller incident pressure at the same stand-off distance.

$$\frac{R}{R_1} = \left(\frac{W}{W_1}\right)^{\frac{1}{3}} \Rightarrow \frac{R}{W^{1/3}} = \frac{R_1}{W_1^{1/3}} = \text{constant} = Z \quad (2.7)$$

Where  $R$  is the stand-off distance in meters (m) and  $W$  is the charge weight in kilograms (kg) of TNT.

### 2.2.3 Trinitrotoluene (TNT) Equivalence

The wide variety of explosives has led to the adoption of a universal quantity. TNT is chosen as a standard explosive for comparison purposes due to its availability, relative purity, safety of handling, and existence of test data. The mass of TNT needed to produce the same effect of a given explosive is called TNT equivalence and is expressed as:

$$TNT \text{ Equivalence} = \frac{W_E}{W_{EXP}} = \frac{H_{EXP}^d}{H_{TNT}^d} \quad (2.8)$$

Where  $W_E$  is the effective charge mass or TNT equivalent mass (kg);  $W_{EXP}$  is the mass of explosive (kg);  $H_{EXP}^d$  is the heat of explosion ( $J/kg$ ); and  $H_{TNT}^d$  is the heat of explosion of TNT ( $J/kg$ ).

Table 2.1 provides the equivalent TNT masses for the commonly used explosive materials. TNT equivalent mass varies slightly for pressure and impulse (Hyde, 1992).

**Table 2.1** Equivalent TNT mass factors (Hyde, 1992)

Explosive Type	Equivalent TNT Mass Factor	
	Pressure	Impulse
ANFO	0.82	0.82
A-3	1.09	1.07
B	1.11	0.98
C-3	1.08	1.01
C-4	1.37	1.19
H-6	1.38	1.15
HBX-1	1.17	1.16
Octal (75/25)	1.06	1.06
Pentolite	1.42	1.00
RDX	1.14	1.09
TNT	1.00	1.00
Tritonal	1.07	0.96

#### 2.2.4 Blast Load Prediction

Kingery-Bulmash charts are the widely accepted method used for determining the values of blast load parameters. These charts have been created due to experimental and theoretical researches on atmospheric conditions, based on TNT equivalent charge weights, for spherical and hemispherical detonations. These charts can be used to determine the peak reflected pressure ( $P_r$ ), peak incident overpressure, ( $P_{SO}$ ), reflected impulse, ( $I_r$ ), incident impulse, ( $I_{SO}$ ), time of arrival, ( $t_a$ ), shock front velocity ( $U$ ), duration of positive phase ( $t_d$ ) or ( $t_o$ ), and wave length ( $L_w$ ). A dimensional scaled distance ( $Z$ ) computed from Eqn. 2.7 is used to determine the blast parameters for a different type of explosive material, the mass of explosive should be converted to an equivalent mass of TNT by using conversion factors. Before determining the blast load parameters, it is important to determine whether the surface blast is spherical or hemispherical in nature.

Figures 2.6, 2.7, 2.8 and 2.9 show the Kingery-Bulmash charts for the different cases. For Figures 2.6 and 2.7, they show blast wave parameters of a positive phase for both cases; hemispherical and spherical TNT surface blast, respectively, whereas Figures 2.8 and 2.9 show blast wave parameters of a negative phase for both cases hemispherical and spherical TNT surface blast, respectively.

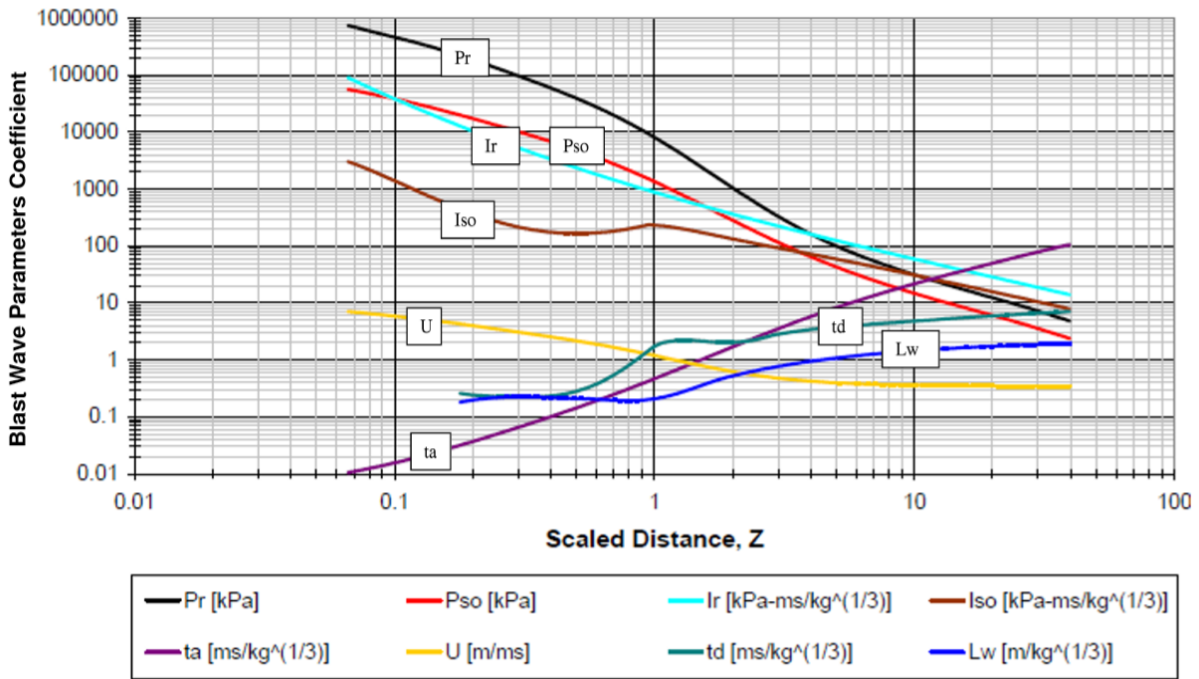


**Figure 2.6** Positive phase blast parameters for hemispherical TNT surface blast (DoD, 2008)

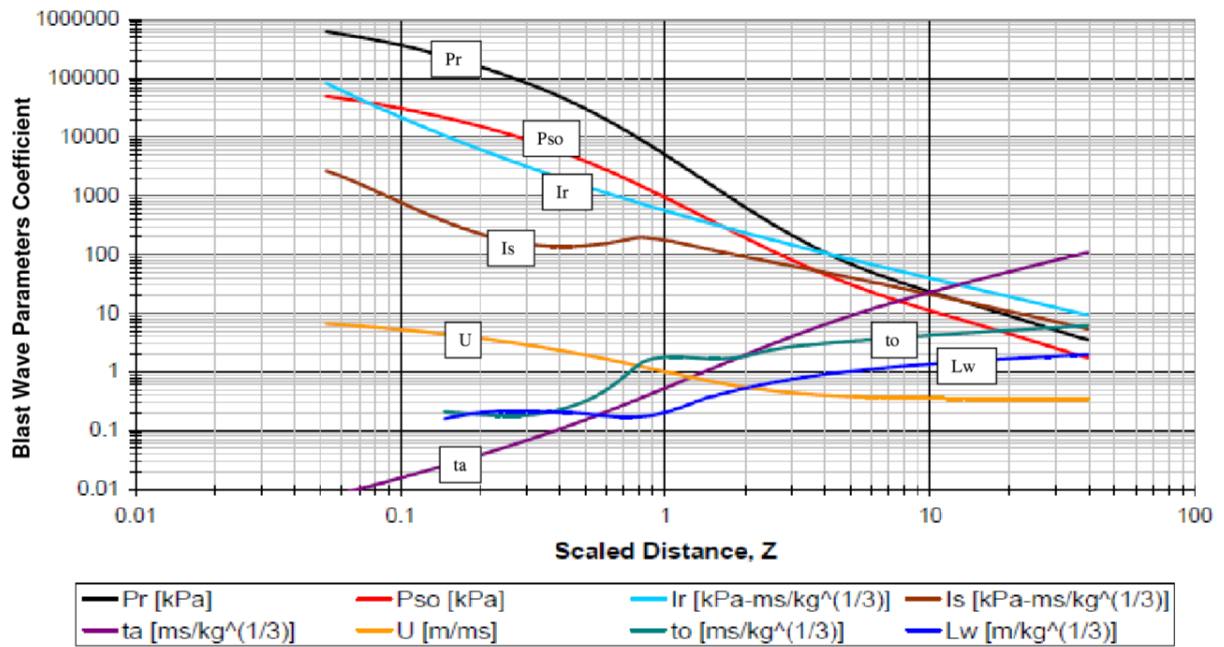


Figure 2.7 Positive phase blast parameters for spherical TNT surface blast (DoD, 2008)

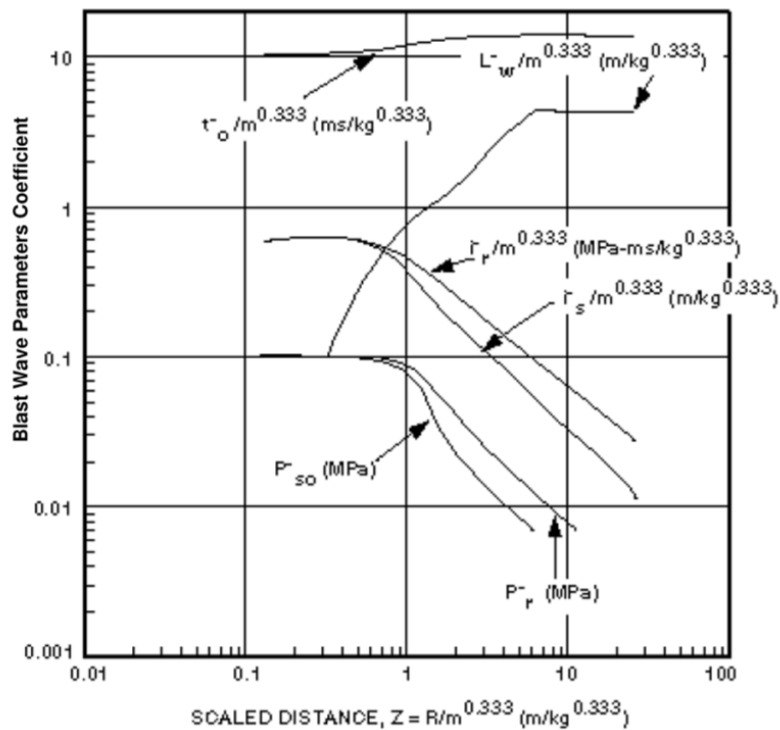
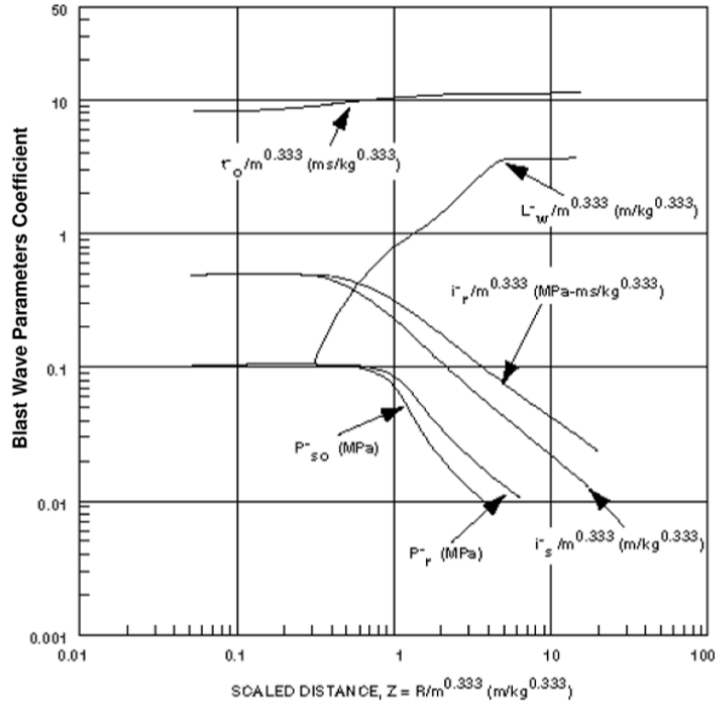


Figure 2.8 Negative phase blast parameters for hemispherical TNT surface blast (DoD, 2002)



**Figure 2.9** Negative phase blast parameters for spherical TNT surface blast (DoD, 2002)

The peak reflected pressure ( $P_r$ ) and impulse ( $I_r$ ) values determined from the curves are given when the angle of incidence ( $\alpha$ ) is  $0^\circ$ . Otherwise, the peak reflected pressure can be computed from the following equation:

$$P_r = C_R P_{S0} \quad (2.9)$$

Where  $C_R$  is a reflected pressure coefficient and  $P_{S0}$  is the peak incident overpressure.

Knowing the angle of incidence and interpolating for a specific incident pressure, the reflected pressure coefficient is obtained from the curves shown in Figure 2.10. The peak reflected pressure is then computed from Equation 2.9. While on using the curves shown in Figure 2.11, the peak reflected impulse is interpolated from the angle of incidence and the peak incident overpressure.

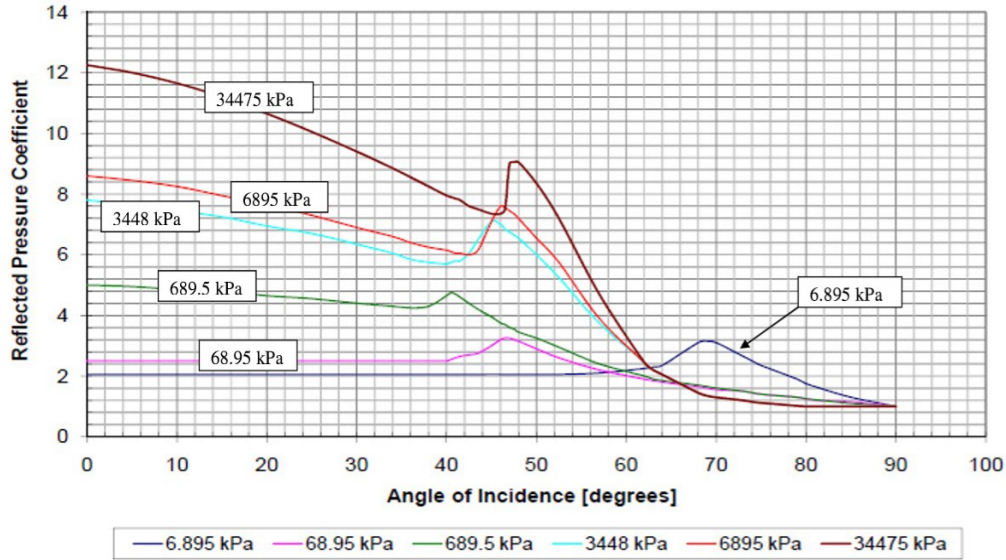


**Figure 2.10** Reflected pressure coefficient versus angle of incidence (DoD, 2008)

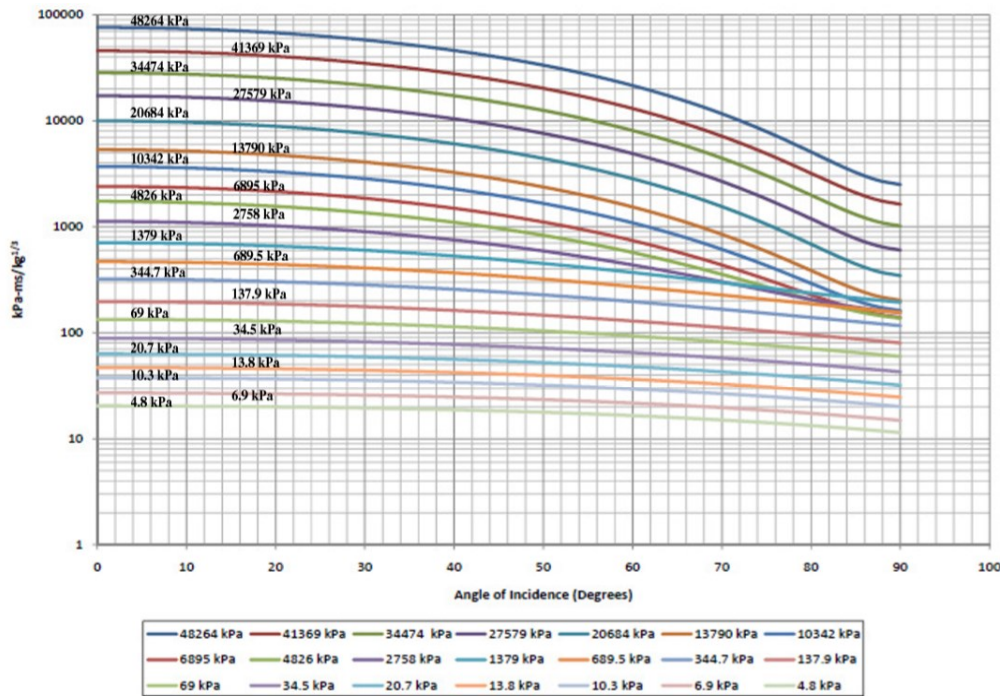


**Figure 2.11** Normalized reflected impulse versus angle of incidence (DoD, 2008)

For unconfined explosives and using these simple tools, blast wave parameters can be determined from the stand-off distance and TNT equivalent weight. Conversely, stand-off distance and TNT equivalent weight can be obtained from the blast wave parameters.

## **2.3 Background on Sandwich Panels**

In the last decade, sandwich panels have been used significantly to resist blast loads. The use of such panels goes back to few decades earlier since they have a great potential in many applications such as aerospace, automotive, transportation, and structural application. Typically, sandwich panels are composed of upper skin, lower skin, and core. The core may be a solid core or can take another shape like honeycomb cores, corrugated cores, truss cores, Z-shaped cores, C-shaped cores, and I-shaped cores. The skins and core materials may be metallic or polymeric. The concept behind sandwich structure is that the skins carry the in-plane compressive and tensile stresses resulting from the induced bending moment, while the main function of light-weight core is to keep the two skins apart, at a desired distance, and also to resist and transmit the induced shear forces to the supporting points.

Sandwich panels are being used in several structural engineering applications, especially after introducing FRP composite materials. These applications can be light-weight decking, flooring, or roofing and cladding panels for buildings.

## **2.4 Effectiveness of Using Sandwich Panels**

Sandwich panels are composite layers that maximize a section's potential to take advantage of the materials' strength-to-weight ratios. The earliest applications of sandwich panels in the 20th century have been applied in the aircraft industry (Allen, 1969). This was followed by an expansion of applications into the aerospace, automotive, and marine industries. The fundamental models of sandwich structures are presented by (Allen, 1969) and (Plantema, 1966), where the core is assumed to be incompressible in the out-of-plane direction and does not have any bending rigidity. On the other hand, the skins only have bending rigidity, while the core only has shear rigidity. (Meraghni et al., 1999) studied the tubular and honeycomb cores rigidities numerically, analytically, and experimentally as shown in Figure 2.12. The study showed that total thickness of the core is not as highly important on equivalent rigidities as wall thickness that has a great influence on rigidity.

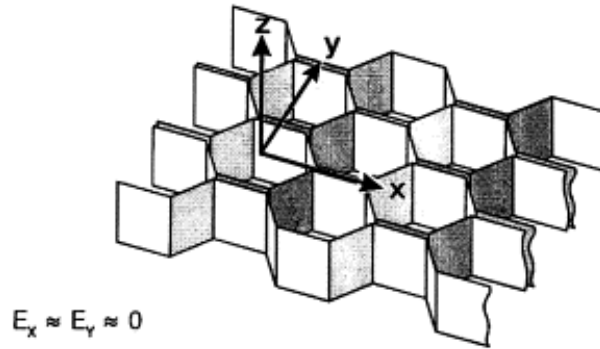


**Figure 2.12** Honeycomb core (Meraghni et al., 1999)

The use of composite GFRP-sandwich panels in building applications started in the 1970s (Pamla, 2007). (Thomsen & Frostig, 1997) studied experimentally and analytically the localized bending effects in sandwich beams having soft core subjected to loads under 3-point bending. The study showed that the high-order theory of sandwich panels provides accurate results compared with the experimental results. The mode of failure for honeycomb sandwich panels was studied by (Petras & Sutcliffe, 1999, 2000). The study showed that a failure happened in GFRP/Nomex honeycomb beams that were subjected to loads under 3-point bending. The contact pressure was assumed to be transferred directly to the core, which leads to core failure. The core failure load of panels can be predicted when applying a combination of compressive and shear stresses on the panels. (He & Hu, 2008) investigated the composite honeycomb sandwich panel structure. It was noticed that 50–66.7% of the whole honeycomb panel weight was considered the weight condition of honeycomb core, where the maximum flexural rigidity and bending strength of the sandwich panel are achieved.

(Fan et al., 2007) studied the mechanical behaviour of carbon fibre reinforced grids fabricated by the interlocked method. In this study, three experimental tests were considered; in-plane compression, out-of-plane compression, and 3-point bending tests. The conclusion of the study was that a high strength and stiffness can be achieved in comparison with other cellular materials. Moreover, the failure process in carbon fibre reinforced grids and the assembled sandwich panels could be ductile to some extent as shown in Figure 2.13. Finally, the main weakness of carbon fibre sandwich panels is the debonding occurrence, this usually happens in the adhesion area as it has lower strength than outer skins and inner core. (Reis & Rizkalla, 2008) investigated experimentally the material characteristics of 3D FRP sandwich panels with through-thickness

fibres passing through the core. It was noticed that the behaviour was independent of the presence and the amount of through-thickness fibres embedded in the face layer. The reduction in stiffness was approximately 33% for all face layers tested in this study. Increasing the amount of through-thickness fibre insertions from 1.25 to 2.5 per  $\text{cm}^2$  leads to a 25% decrease in tensile strength of the face layer. The study showed that thickness does not have any significant effect on the initial core shear modulus, however, increasing thickness reduces the shear strength considerably.

(Chang et al., 2005) investigated the bending behaviour of corrugated-core sandwich plates as shown in Figure 2.14. The effects of geometric parameters of corrugated-core sandwich plates with various boundary conditions on the plate behaviour and strength were numerically studied. The study established recommendations and guidance for the selection of geometric parameters of corrugated core sandwich plates. It showed that using lower ratios of some geometric parameters such as (full thickness / core thickness) and (core thickness / skin thickness) leads to achieving stronger plate. (Aviles & Carlsson, 2006) studied numerically a three-dimensional finite element buckling analysis of debonded sandwich panels. The study concluded that a buckling failure mode happened in the debonded face layer due to in-plane compressive loads. Moreover, it showed that the buckling load decreases with increased debonded size and reduced core modulus. (Tito Lívio Boni & Sérgio Frascino Müller de Almeida, 2008; Tito Lívio Boni & Sergio Frascino Müller de Almeida, 2008) investigated laterally supported sandwich panels subjected to large deflections. Experimental and numerical studies were conducted to predict the global behaviour of simply supported sandwich panels fixed by bolts on the two longitudinal edges or on all four edges. The study presented a good correlation for the observed displacement between experimental and numerical results.

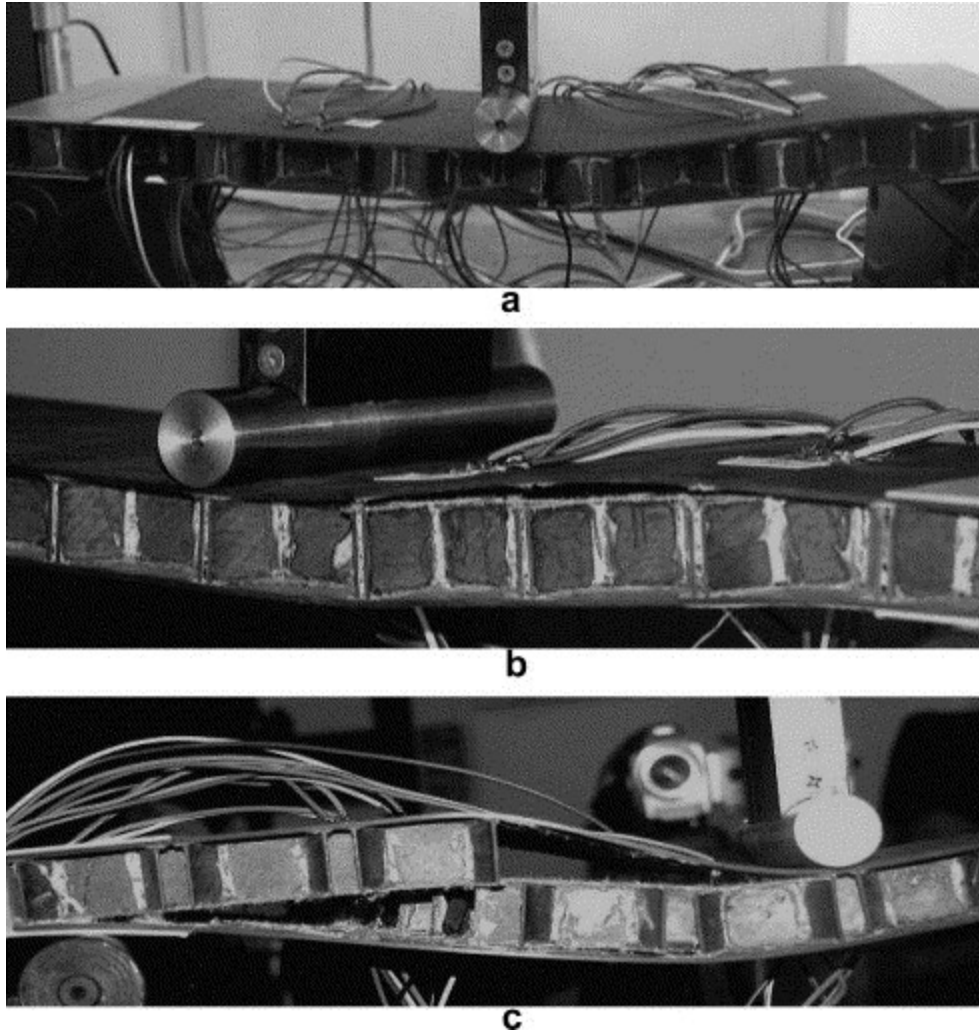


**Figure 2.13** Bending behaviours of sandwich panel: (a) elastic deformation; (b) buckling and debonding; and (c) core shear (Fan et al., 2007)

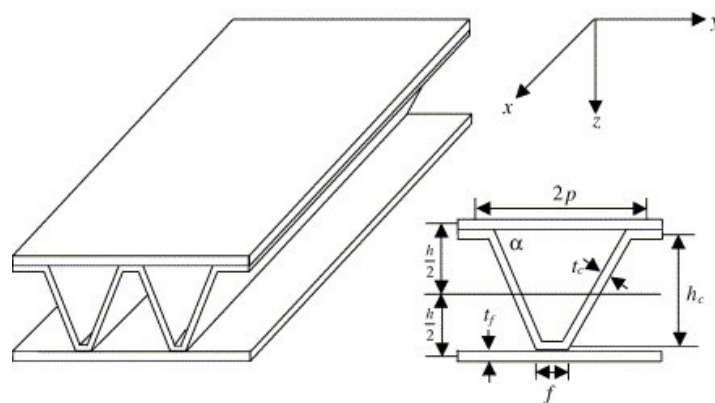


**Figure 2.14** Corrugated-core sandwich panel and a panel unit (Chang et al., 2005)

(Liu et al., 2006) studied the optimization of Lightweight metallic sandwich plates comprising periodic truss cores and solid face layers to achieve the same performance with minimizing the weight. Different core topologies were considered in this study as shown in Figure 2.15 and were applied to bending, transverse shear, and in-plan compression loads. The optimization was subjected to the constraints that no failure mechanism was active, including overall buckling, face layer buckling/wrinkling, face layer yielding, and core member yielding and buckling. For all core panels, the truss members were solid, except for pyramidal core panel where the truss members were hollow. The study presented that the out-of-plane behaviour for the 2D and 3D models was not in a good agreement, due to the fact that 2D homogenized model was based on the effective single layer sandwich approaches, which considers the in-plane deformations of face layers but ignores their out-of-plane deformations.

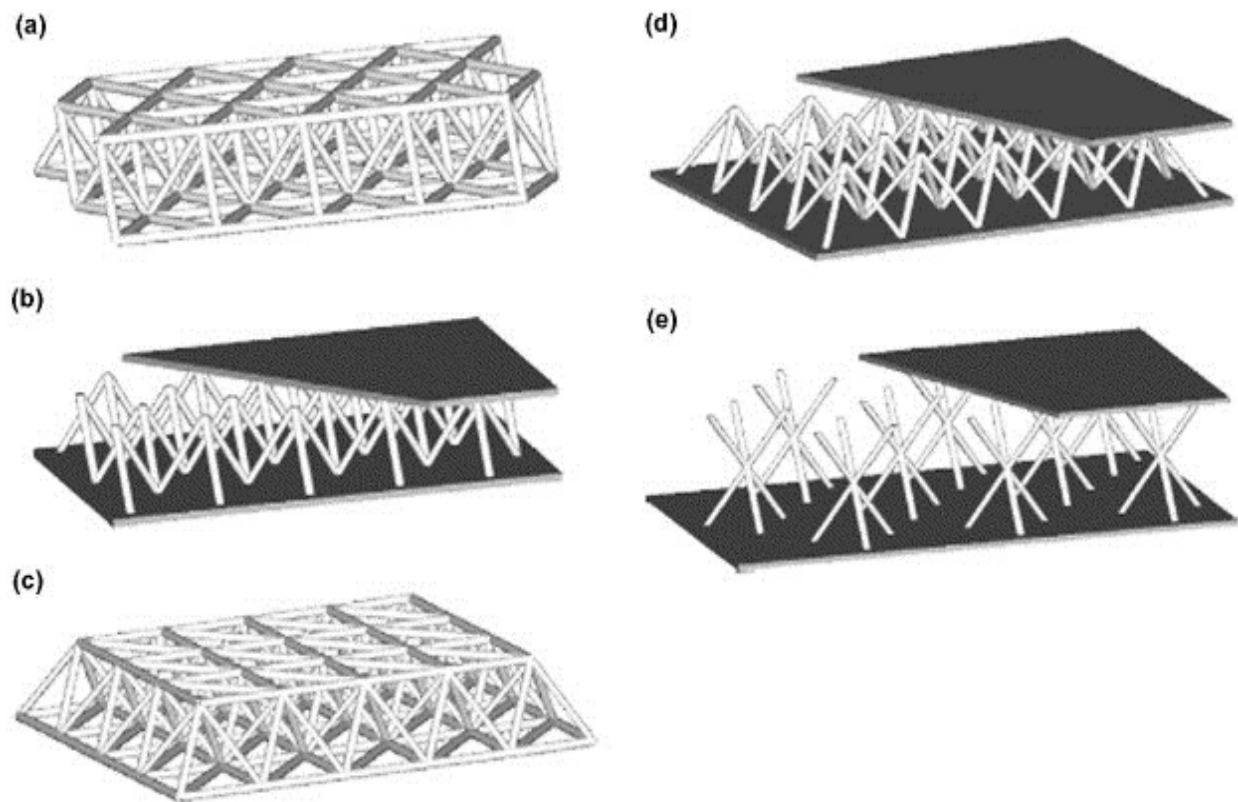


**Figure 2.15** Typical lattice truss topologies: (a) octet truss, (b) tetrahedral lattice truss, (c) lattice block, (d) pyramidal lattice truss, and (e) 3D kagome (Liu et al., 2006)

## 2.5 Composite Sandwich Panels To Resist Blast Loads

FRP composites have a great potential in manufacturing prefabricated panels that can be used for moveable structures. As for the skins, they are bonded to the core by means of an adhesive polymer such as epoxy resin. The high strength-to-weight ratio, resistance to corrosion, and ease of handling and fabrication are the basic advantages of FRP. In addition, FRP sandwich panels can be filled with a filling material to provide more energy absorption. The FRP skin carries in-plane compressive and tensile stresses resulting from bending, while the main function of the core is to keep the two FRP skins apart at the desired distance and to resist and transmit the induced shear forces to the supporting points. The core may also provide thermal insulation. (Steeves & Fleck, 2004) reported that a significant reduction in weight was achieved using glass FRP (GFRP) skins and polyvinyl chloride (PVC) or polyurethane cores. They also reported that the core material stiffness is the main factor controlling the sandwich panel's behaviour. (Chen & Davalos, 2003) reported that delamination of inner core from outer skins is the typical failure mode for sandwich panels.

Several studies have been conducted to examine the behaviour of FRP sandwich panels under static and blast loads. (Jacob et al., 2002) summarized the effect of changing FRP characteristics and their influence on energy absorption of panels. Also crushing modes and test methodologies in composite tubes were presented. They indicated that energy absorption increased when FRP tubes with less-density fibres, higher-strain capacity, or higher inter-laminar fracture toughness were used. (Dvorak & Bahei-El-Din, 2005) investigated the response of sandwich panels under blast load. A design modification was applied to control the delamination in the front layer and the core crushing. They concluded that, the modified designs increase panels' energy absorption, decrease panels' deflection, decrease panels' imparted kinetic energy, decrease the compression of the crushable core, and decrease the longitudinal strain in front layer. (G. Zhou et al., 2007) examined the effect of changing skin thickness, core density and type, indenter nose shape, and boundary conditions on the damage and energy absorption of honeycomb sandwich panels. They concluded that the variation of indenter nose shape changes the damage mechanisms and has the most significant effect on energy absorption, especially for panels with relatively thicker skins. The bigger skin thickness would lead to a significant increase in the initial threshold, ultimate load, and panel's energy absorption capacity. However, the core density increase led to a slight increase

in the panel's ultimate load and energy absorption capacity. (Hoemann, 2007) investigated experimentally the behaviour of FRP sandwich panels under blast load and fragmentation. As shown in Figure 2.16, different inner core configurations were used and four wall panels filled with sand and of different thicknesses and inner core configurations were tested. It was reported that the shear flow controls the overall performance of panels. While against fragmentation, fragments were stuck inside the panels and no complete penetration was observed. (Tekalur et al., 2009) demonstrated that increasing stitching density significantly reduces the damage occurred in sandwich panels. (Jackson & Shukla, 2011) experimentally studied blast performance of sandwich panels subjected to impact damage. Impact damage results from applying either high-velocity projectile or low-velocity drop weight to sandwich panels. This was followed by a secondary blast loading experiment that was performed on same panels to evaluate sandwich panels' performance under blast after being exposed to impact damage. They concluded that the performance of sandwich panels was controlled by the damage in front layer. Also, comparing the performance of sandwich panels in both cases; high-velocity impact and low-velocity impact, the performance of sandwich panels is superior in case of being previously subjected to high-velocity impact before blast load. (Su & McConnell, 2011) studied numerically the influence of material properties on energy dissipation capabilities of composite sandwich panels under blast loads. The study showed that density and tensile strength have the most significant effect on energy absorption capability of composite sandwich panels. Also, the failure of middle core increases energy absorption, so the failure in middle core is acceptable and, in fact, desirable. (Yang et al., 2011) Studied the dynamic response of four circular sandwich panel manufactures with different core configurations under blast loads. According to the study, a shear failure in the core started in the middle as a circle. Meanwhile, a failure circle appeared at the top and bottom surfaces. As dynamic loading increases, the failure circle spreads towards the centre resulting in a final failure. Moreover, using additional core layers and reducing kinetic and strain energy levels in the protected core improved the shear failure prevention of the core in both absolute and relative terms.

More recent studies have been conducted by (Langdon et al., 2012) who studied the response of sandwich panels to blast loading. According to their study, it was concluded that applying impulsive loads leads to front face layer delamination, core compression, back face layer delamination, fibre fracture, core fragmentation, plastic deformation, and back face layer debonding. However, no back face layer rupture was noticed upon applying impulsive loads.

Meanwhile, panels with denser cores exhibited lower levels of damage. Also, they stated that the energy absorption increase was due to delamination, core compression, and fibre fracture. (Arora et al., 2012) studied the blast resistance of GFRP sandwich panels that have various core thicknesses in both air and underwater environments. Also, the type of failure mode whether core crushing, core cracking, fibre breakage, or delamination has been investigated. The results showed that stiffness was significantly higher for thicker cores resulting in strong influence on the behaviour of panels against blast effect. In case of air blast, panels sustained blast loads without tearing or cracking. However, in case of underwater blast, panels suffered from crushing and fibre breakage. (Langdon et al., 2013) experimentally and numerically investigated the response of sandwich panels under blast loads. They reported that the lower transverse stiffness of the core and the smaller bending rigidity of the sandwich panel lead to a higher transverse velocity of the face layer causing larger deflections and, therefore, results in larger in-plane stresses in the face layer.

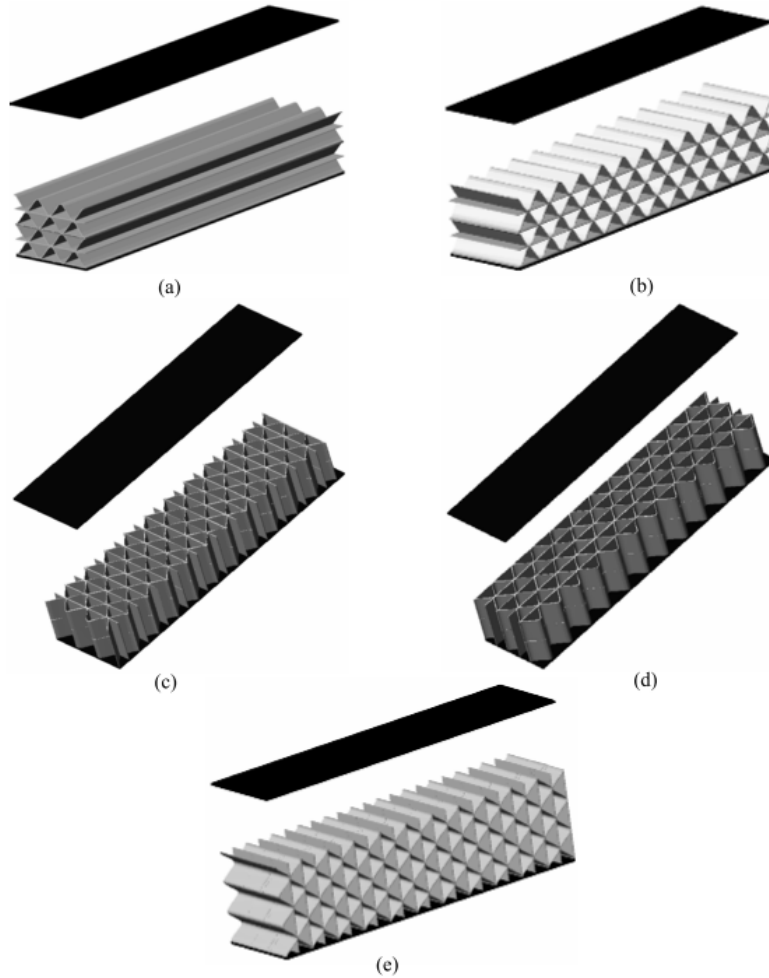


**Figure 2.16** Different inner core configurations (Hoemann, 2007)

## 2.6 Metallic Sandwich Panels to Resist Blast Loads

Several studies have been conducted to examine the behaviour of metallic sandwich panels under blast loads. (Xue & Hutchinson, 2003, 2004) investigated numerically the behaviour of sandwich panels when subjected to impulsive/blast loading. They concluded that a well-designed sandwich plate can resist more blast effect compared to a solid plate of the same weight and that the energy absorbed in core layers is due to the plastic deformation occurrence. Also, increasing the thickness of face layer increases the effectiveness of panels against blast loads. In this regard, (Rathbun et al., 2006) studied stainless steel square honeycomb core sandwich panels and solid monolithic beams. Stainless steel square honeycomb core sandwich panels and solid monolithic beams were subjected to high-pressure and short-duration impulses using shock simulation technique. All the measurements and simulations affirmed that when subjected to impulses load,

square honeycomb sandwich panels showed very small displacements than solid steel beams of the same mass. On the other hand, sandwich structures are noticeably beneficial at lower impulses as the core layers are stiff enough to prevent crushing. (Bahei-El-Din et al., 2006) studied sandwich panels under impulsive/blast loading and they proposed new designed panels. Two designed panels (conventional design and modified design) were conducted where the failure mode of panels resulted from having permanent crushing of foam core and an instant skin delamination. However, upon comparing conventional and modified designs, the modified design gives better result, as the damage, the total kinetic energy, and the stored and dissipated energy were reduced compared to the conventional design. (Mori et al., 2009) conducted an experimental study to quantify the performance and failure modes of sandwich structures under impulsive loading. Results confirmed that using sandwich structures is of high benefit as it enhances the performance up to 68% in terms of maximum panel's deflection. Based on the theoretical and computational analyses which were confirmed by the study, using soft cores enhances sandwich panels' performance under blast effect.

Sandwich panels consist of front, core, and back layers. The core can take several topologies. The main used topologies for the metallic sandwich panels are honeycomb, folded, and lattice truss shapes. Under these main topologies, many topologies are used to form the cores of sandwich panels to provide adequate stiffness and strength for structural load support. Although it showed the highest peak strength, honeycomb panels exhibit strong softening capability. On the other hand, truss and corrugated cores had significant lower strength but they acted as a metal foam. Relatively, they have a yield strength that can extend beyond a plastic strain by 60% (Dharmasena et al., 2010). (H. N. Wadley, 2006) stated that changing core configuration has significantly influenced the behaviour of sandwich panels. In this regard, (Fleck & Deshpande, 2004) studied different sandwich core topologies under the effect of both; air and water blast. They concluded that the best performance is obtained by diamond-celled core sandwich beam due to the longitudinal strength provided by the core. (Liang et al., 2007) studied metallic sandwich panels under blast load. Throughout the study, three topologies have been investigated which are square honeycomb, I core, and corrugated shapes. The performance of sandwich panels are studied under two scenarios; strong and weak core. The predicated deformation for the above mentioned topologies and scenarios are shown in Figure 2.17. They concluded that, soft core has better performance under blast effect. (H. Wadley et al., 2008) investigated the response of a multilayered pyramidal lattice structure constructed from stainless-steel. Using lattice shape resulting in

crushing of the core in a progressive manner by the sequential buckling of truss layers as shown in Figure 2.18. Also, using lattice shape resulted in reducing peak pressure transmitted to the back layer, dispersing pressure wave, and increasing waveform width. (Karagiozova et al., 2009) investigated numerically the behaviour of clamped sandwich panels under blast load. These panels were formed from front and back steel layer with aluminum honeycomb core in between. It was concluded that, the load transfer to the back layer is controlled by core thickness, load intensity, and flexibility of sandwich panels. (Theobald et al., 2010) studied experimentally the response of metallic sandwich panels under blast load. The performance of panels were studied once using hexagonal honeycomb core and another time when using aluminum foam core. It was concluded that, upon using thicker front layer, the performance was enhanced for the panels of honeycomb cores. (Dharmasena et al., 2010) investigated metallic sandwich panels under impulsive load. In the study, five core topologies were studied; square honeycomb, triangular honeycomb, multi-layer pyramidal truss, triangular corrugation, and diamond corrugation as shown in Figure 2.19. Figure 2.20 shows the core crushing for the five tested sandwich panels. They concluded that on comparing using crushable core with rigid core, the transmitted impulse was reduced by about 25%.

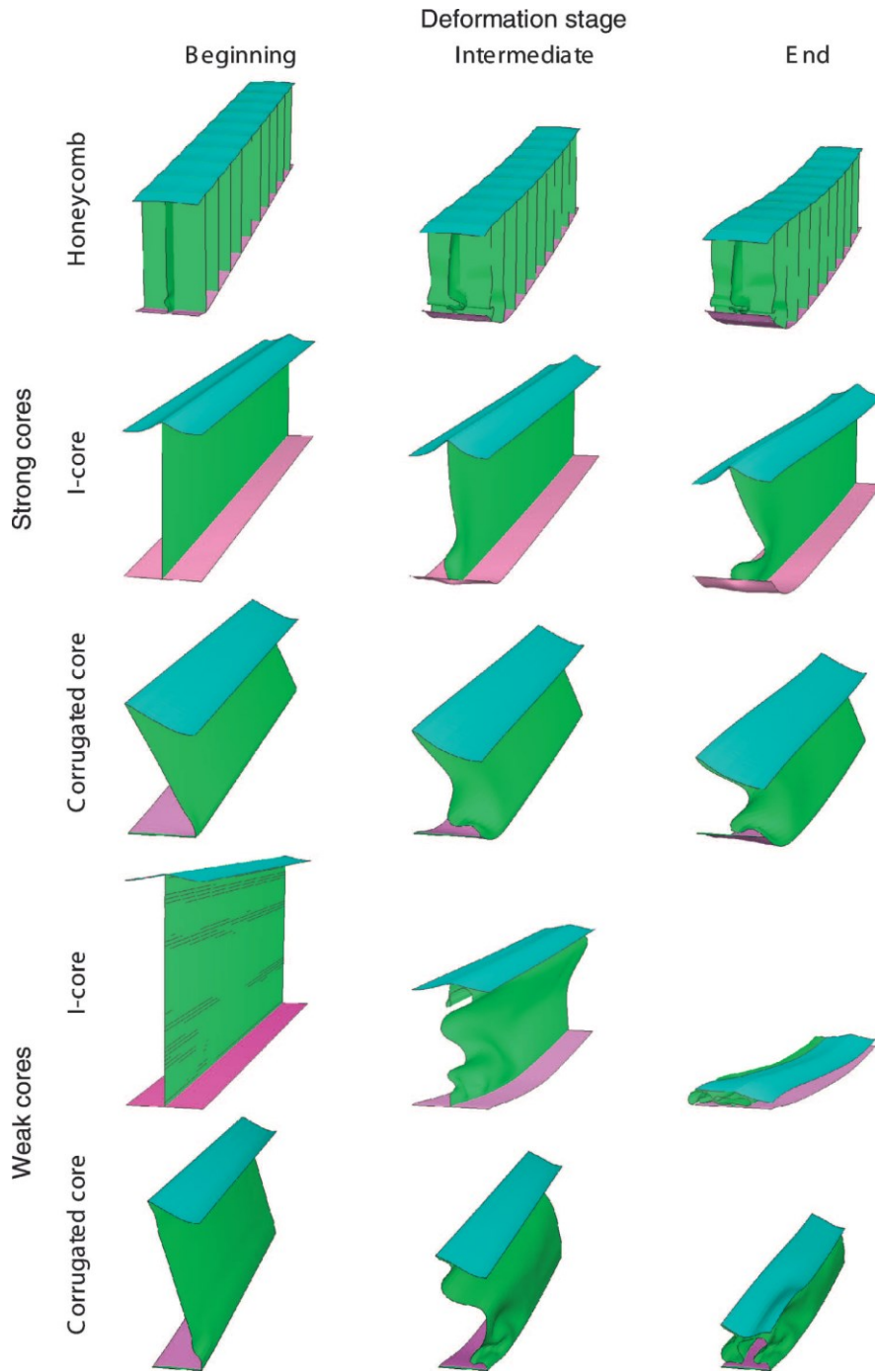


**Figure 2.17** The deformations predicted for the three cores (Liang et al., 2007)

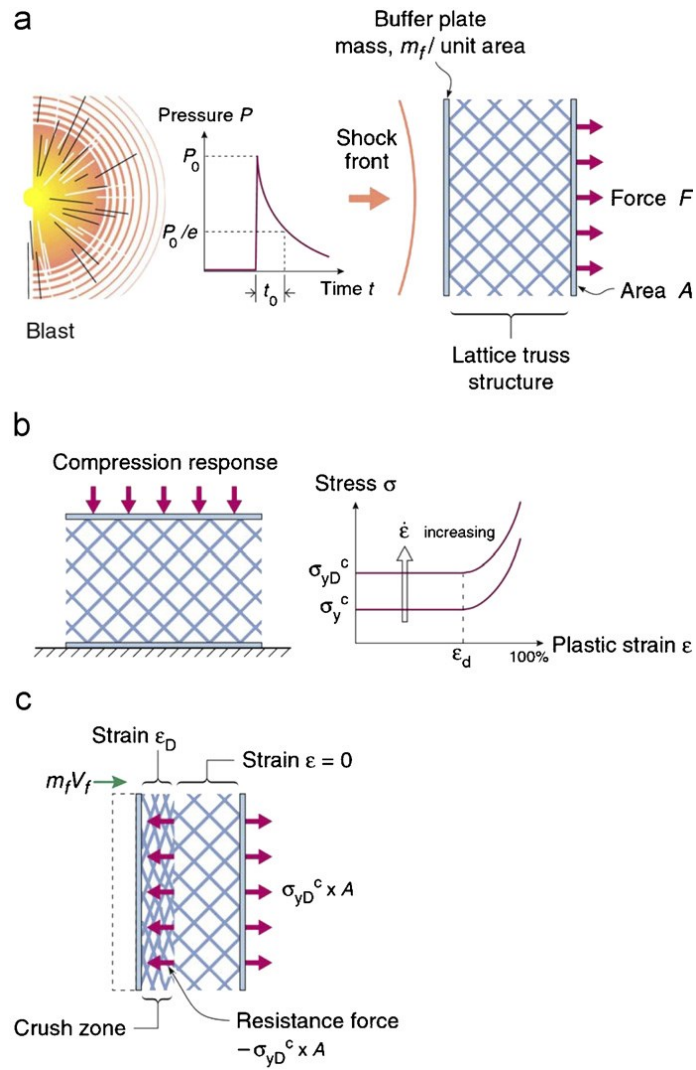


**Figure 2.18** Dynamic core crushing of a cellular core sandwich panel (H. Wadley et al., 2008)

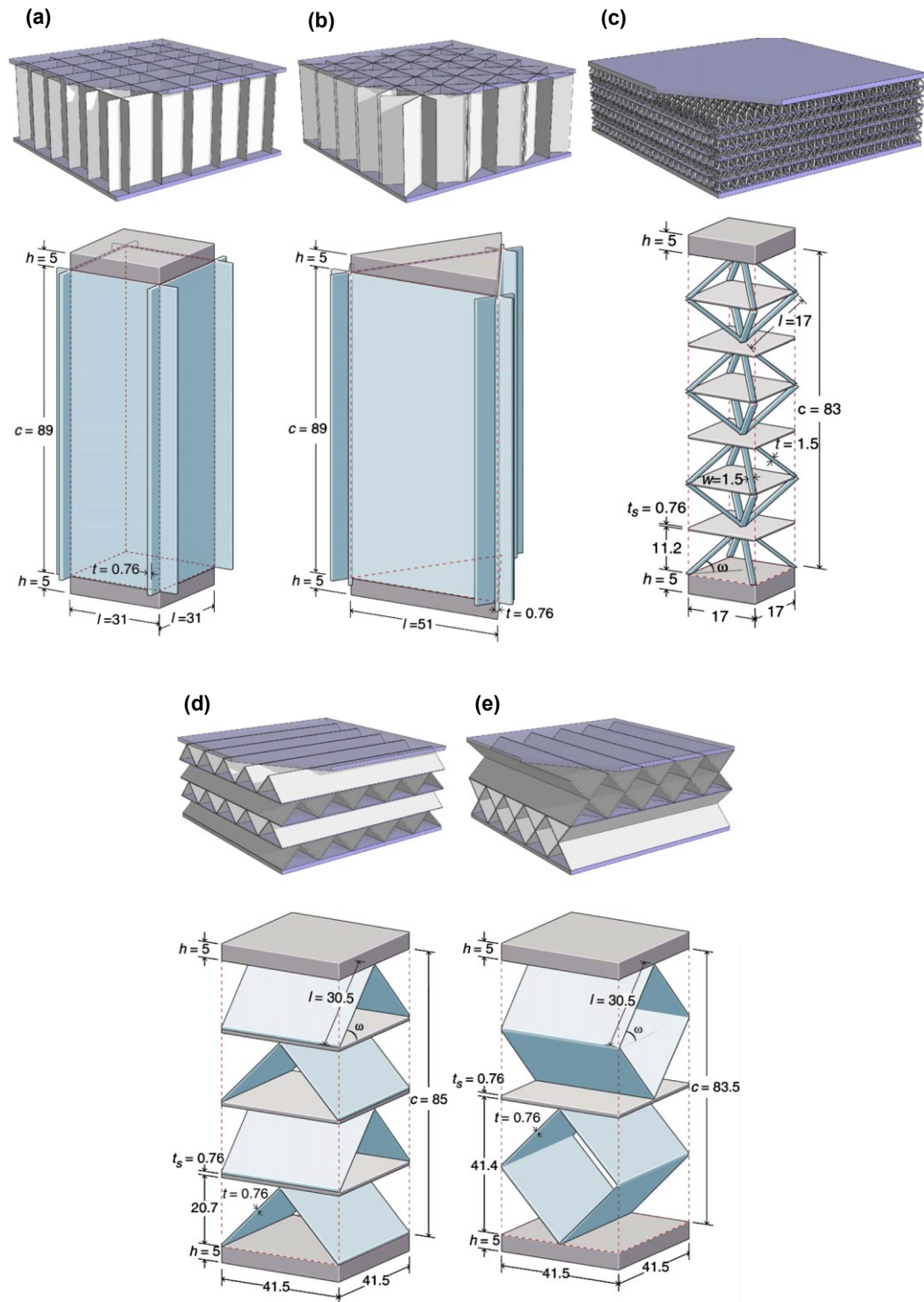


**Figure 2.19** Sketches of the (a) square honeycomb, (b) triangular honeycomb, (c) multi-layer pyramidal truss, (d) triangular corrugation, and (e) diamond corrugation sandwich cores (Dharmasena et al., 2010)

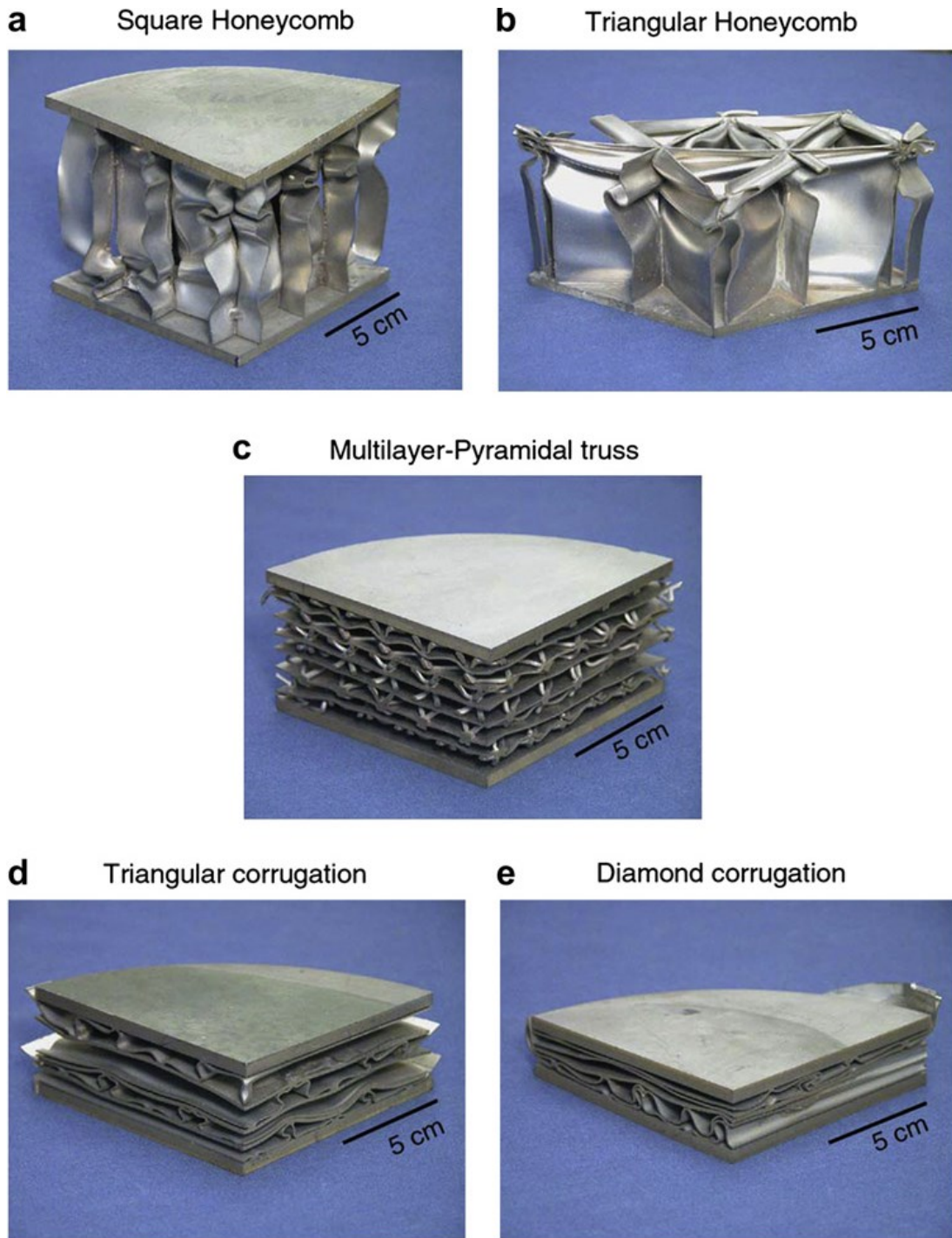


**Figure 2.20** Photographs of the dynamically tested sandwich panels for (a) square-honeycomb, (b) triangular honeycomb, (c) multi-layer pyramidal truss, (d) triangular corrugation and (e) diamond corrugation (Dharmasena et al., 2010)

More recent studies had been conducted. In this regard, (Cui et al., 2012) investigated experimentally the dynamic response of metallic lattice sandwich plates under impulsive blast load. Sandwich structures were composed of two face layers and tetrahedral lattice cores. From the experiment, the inconsistent deformation of front and back layers resulted in non-uniform compression deformation and shear deformation appeared in the tetrahedral lattice core. A comparison was conducted between maximum transverse deflections of tetrahedral lattice sandwich plates and that of hexagonal honeycomb manufactured from same materials and of core relative density. From the comparison, tetrahedral lattice sandwich structures showed better impulsive resistance than hexagonal honeycomb. (Nayak et al., 2013) conducted a study to minimize the blast effect on sandwich panel using optimization techniques. Results revealed that increasing front layer thickness realizes better load distribution in larger area of the core and hence back layer deflection decreases. (Alberdi et al., 2013) investigated numerically metallic sandwich panels having different core topologies under blast loads. The core topologies included folded and honeycomb shapes as shown in Figure 2.21, and it also included orthotropic topologies as shown in Figure 2.22. Panel's deflection, energy dissipation, and maximum force transferred were studied. They concluded that folded shapes dissipate more energy than honeycomb shapes. Also, front layer thickness controls the amount of energy dissipation, while back layer thickness has weak effect on energy dissipation. On the other hand, back layer deflections occurred in the opposite direction to the applied loads in some folded panels due to the overall performance of the panel as shown in Figure 2.23. In these configurations, the core topology, support conditions, and applied blast loads are factors affecting the performance of sandwich panels. However, orthogonal folded core topologies have the least back plate deflection of any topology at every charge level, they follow the same trend as folded topologies. (Li et al., 2014) investigated experimentally and numerically the dynamic response of corrugated sandwich panels under blast loading. From the deformation modes, it is noticed that face layers had high tensile strength that resulted in minor global deformation and small tearing. At high impulse levels, shear deformation and compressed region of core increased. Also, bending stiffness along longitudinal direction of corrugate core was higher than that along the transverse direction. (P. Zhang et al., 2015) investigated experimentally the performance of metallic trapezoidal corrugated core under blast load. The effect of stand-off distance, face layer thickness, core web thickness, and core height on sandwich panels was studied. It was concluded that on decreasing stand-off distance, the deflection and level of damage was

increased. The influence of front layer thickness is more important on panels' deflection than that of back layer thickness as shown in Figures 2.24 and 2.25. Blast performance of panel was enhanced on increasing the core web thickness and improving corrugation angle.

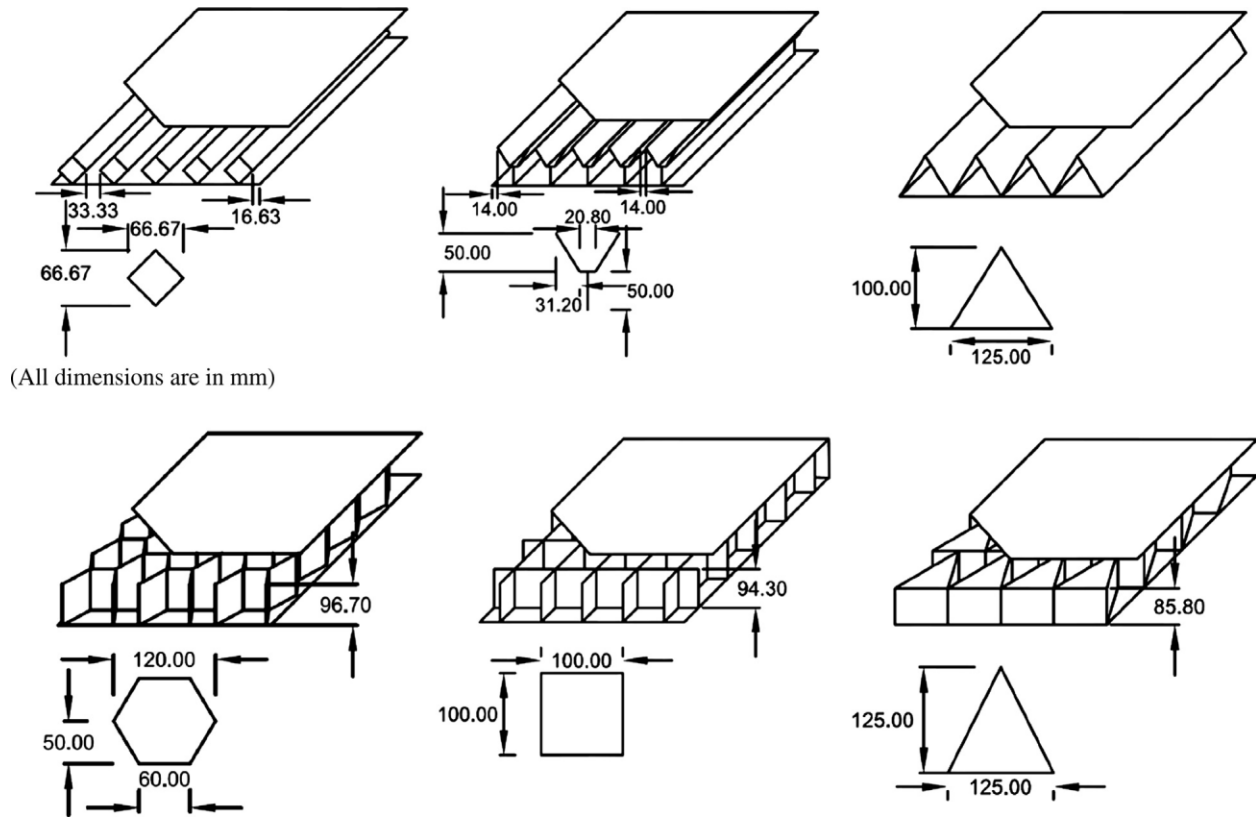


**Figure 2.21** Folded and honeycomb core topologies (Alberdi et al., 2013)

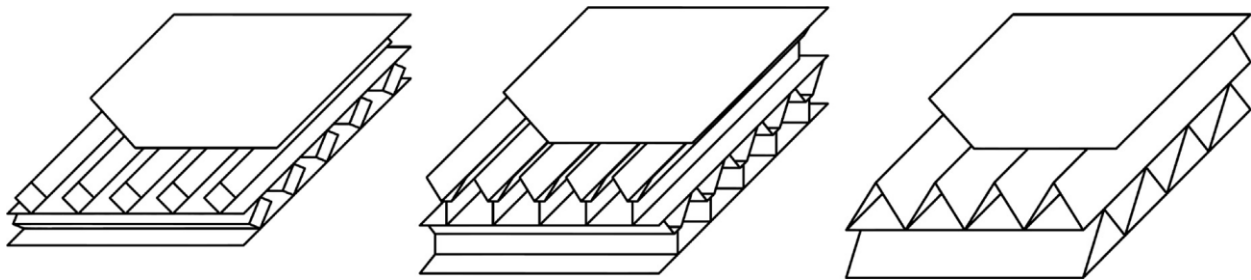


**Figure 2.22** Orthotropic core topologies (Alberdi et al., 2013)

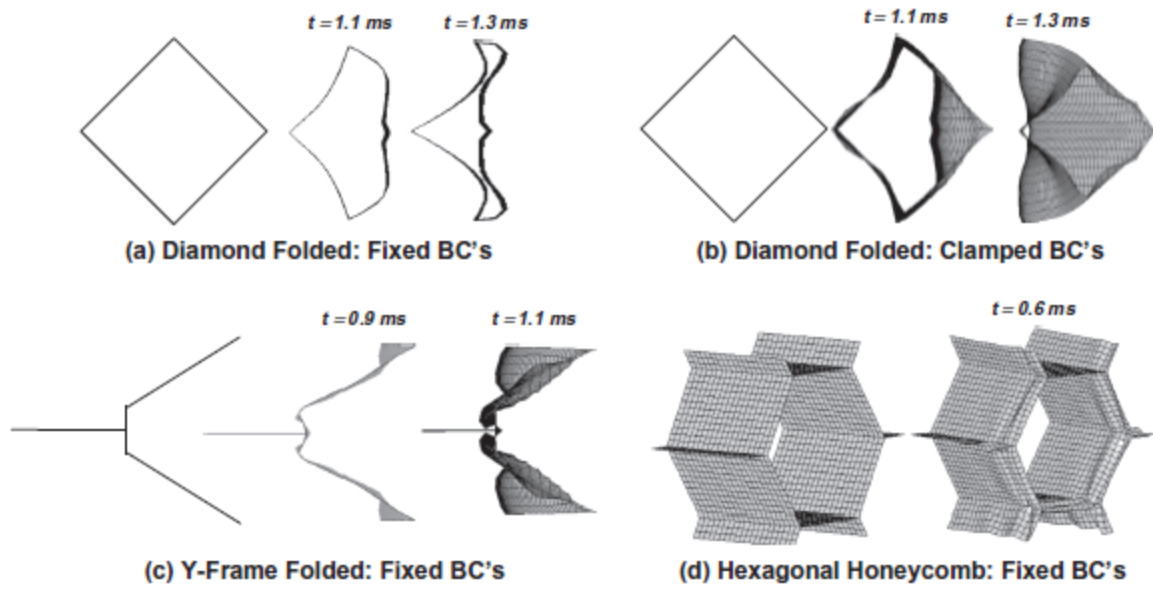


**Figure 2.23** Core deformed shapes (Alberdi et al., 2013)

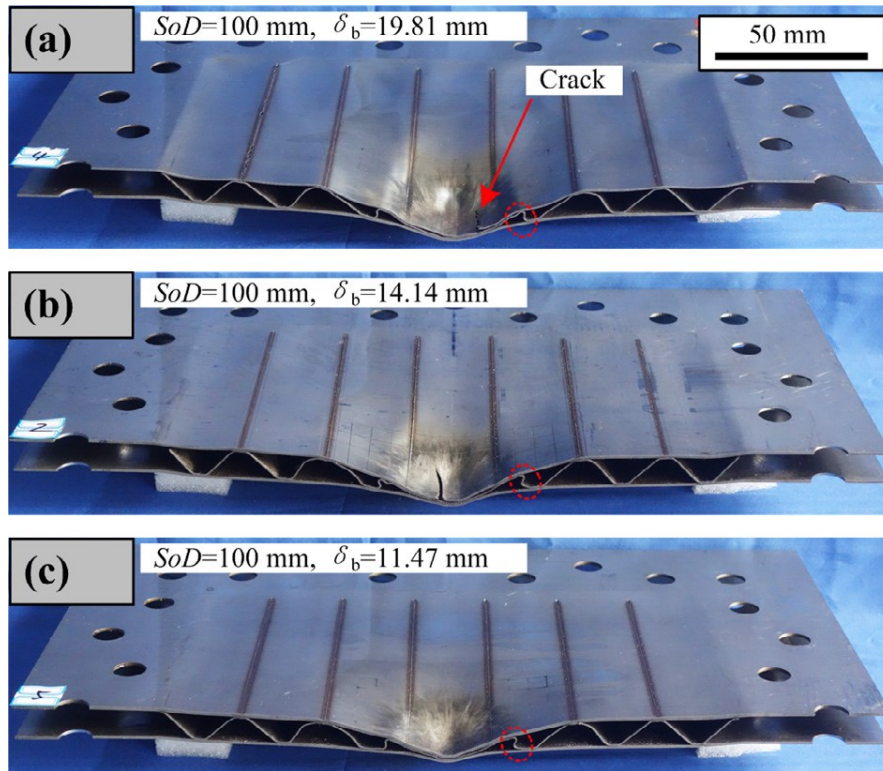


**Figure 2.24** Effect of increasing front layer thickness (P. Zhang et al., 2015)

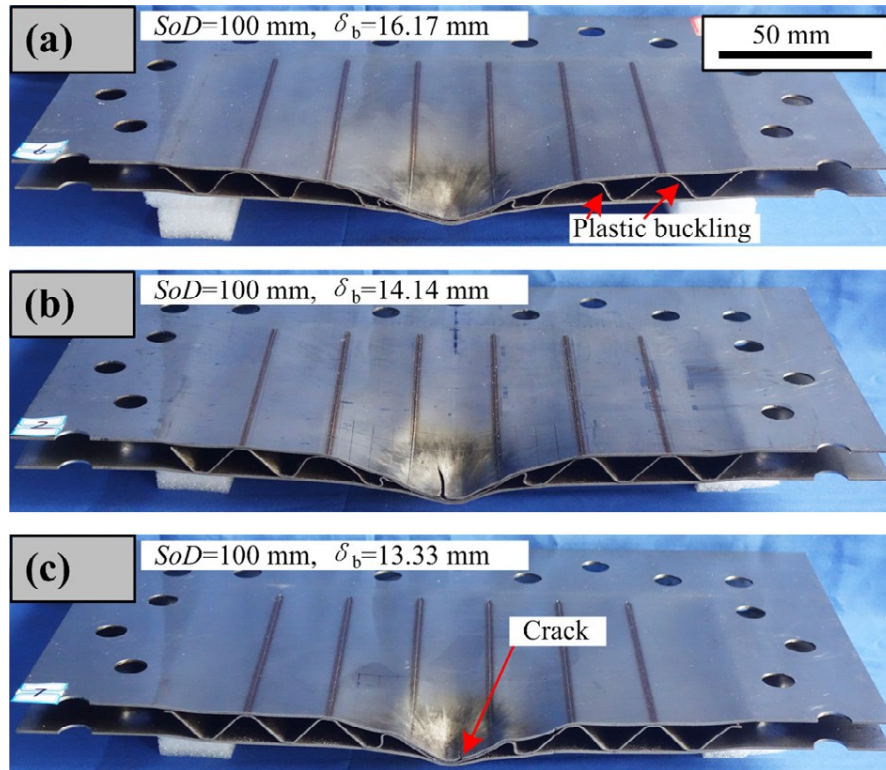


**Figure 2.25** Effect of increasing back layer thickness (P. Zhang et al., 2015)

## 2.7 Effectiveness of Using Filling Material

Using sandwich panels with filling materials improves their behaviour (Kujala & Klanac, 2005). In this regard, (Børvik et al., 2008) investigated aluminum panels to be used in protecting a 6 m (20 ft) ISO container. The results demonstrated that ballistic and blast load resistance were increased on using granular material as a filling material. (Goel et al., 2012) presented numerically foam sandwich panels under impulse loads. They reported that stiffened foam sandwich panels have the best performance against impulsive loads compared with the stiffened steel plate and foam sandwich panels. (J. Zhang et al., 2013) studied analytically and numerically the compressive strengths and dynamic response of corrugated sandwich plates with unfilled and foam-filled sinusoidal plate cores. They concluded that filled foams can significantly increase the normal compressive strengths of corrugated sinusoidal plate cores. However, the dynamic response of equal mass panels once while using foam-filled core and another time while using unfilled core is not as expected. (Yan et al., 2014) studied sandwich panels having metallic corrugated cores under three-point bending once without filling material and another time using foam filling as shown in figure 2.26. Bending stiffness, initial failure load, peak load, and sustained load-carrying capacity

after peak failure were increased upon using foams as filling material. The failure modes for empty and filled sandwich panels were observed. (Yazici et al., 2014) studied experimentally and numerically the influence of foam infill on blast resistivity of corrugated steel core sandwich panels. The experimental also studied the effect of panels with corrugated steel core, foam core, and foam filled corrugated core under shock loading as shown in Figures 2.27, 2.28, and 2.29. They concluded that using foam filling reduced front-face and back-face deflections by more than 50%, whereas the mass of the panel increased by only 2.30%. Foam filling reduced the deflection but its effect changed with face layer thickness, corrugated layer thickness, and boundary conditions. Hence, the benefits of using foam filling in sandwich structure were reduced when the thickness of face layer and corrugated layer was increased.

In this study, Polyurethane foam material has been one of the used filling materials, given the fact that it is one of the widely used as a core in sandwich panels. Polyurethane foam is distinguished for having low density and can be divided into two categories; flexible foam and rigid foam. Flexible polyurethane foam is used in bedding, while rigid polyurethane foam is used for thermal insulation. Additionally, polyurethane foams have unique cellular structure that can be exploited in engineering design. The foams have small cell size and low volume fraction which make them excellent thermal insulators for different usages starting from coffee cups to building cladding panels. Moreover, polyurethane foams are strong energy absorbers owing to their low compressive strength and high deformation capacity. This is the reason they are exploited in different packaging and protective padding. Finally, this type of foams with its low density makes it an ideal core material for light-weight structural sandwich panels (Gibson & Ashby, 1997).

Expanded Polystyrene is another material that has been used as a filling material. Using expanded polystyrene as a lightweight filling material has opened the opportunity for using it on a wider global scale and has introduced many different design applications. In addition to reduced vertical loads, using expanded polystyrene reduces horizontal loads, simplifies designs, and increases speed and ease of performing construction activities (Thompsett et al., 1995).

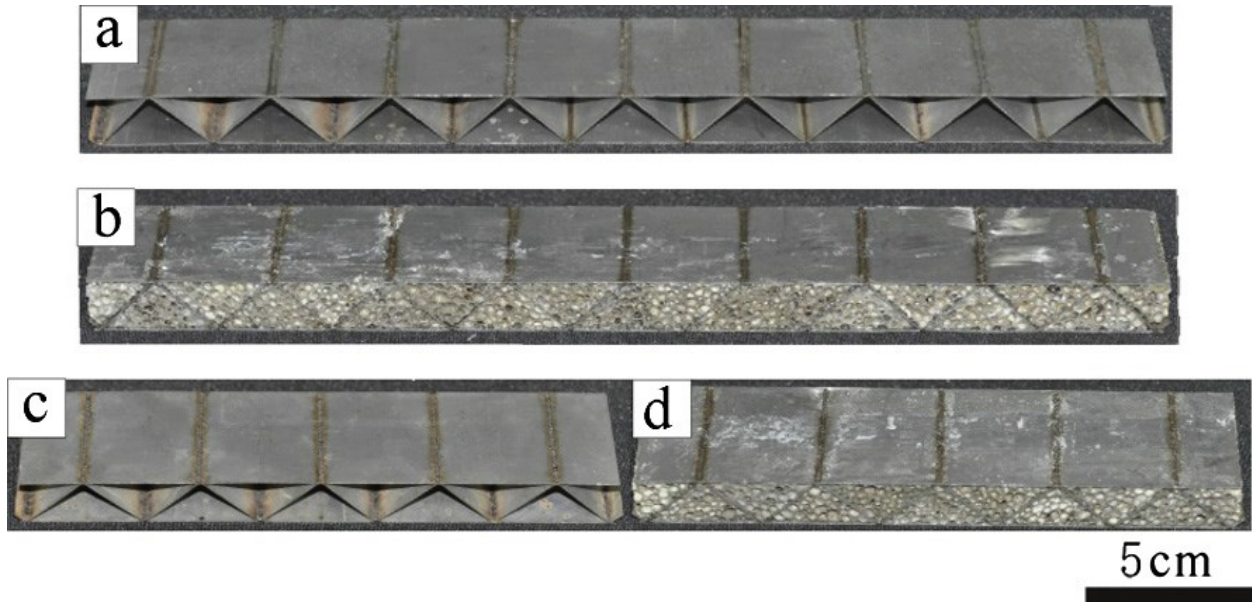


**Figure 2.26** Empty and foam filled panels; (a) long beam empty, (b) long beam filled, (c) short beam empty, and (d) short beam filled (Yan et al., 2014)

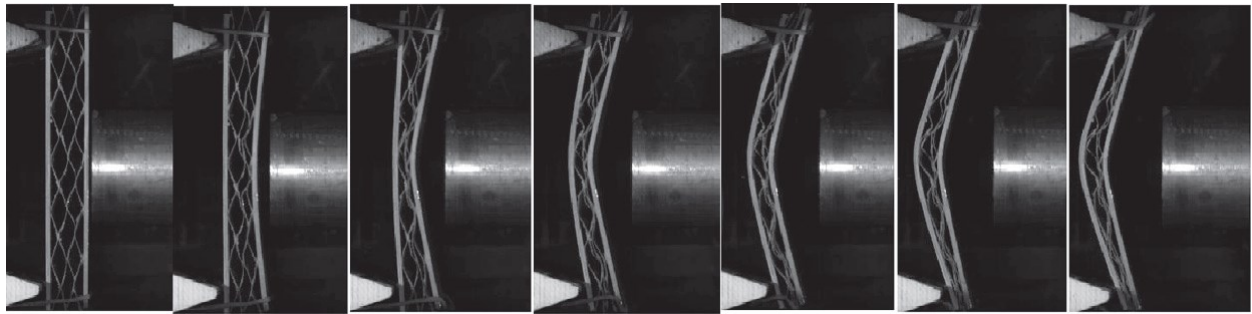


**Figure 2.27** High-speed images of unfilled corrugated steel core sandwich panel during shock loading (Yazici et al., 2014)

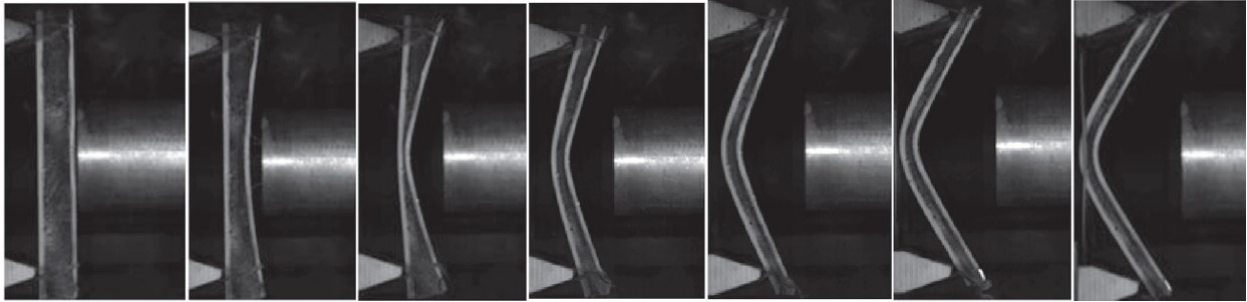


**Figure 2.28** High-speed images of foam core sandwich specimen during shock loading (Yazici et al., 2014)

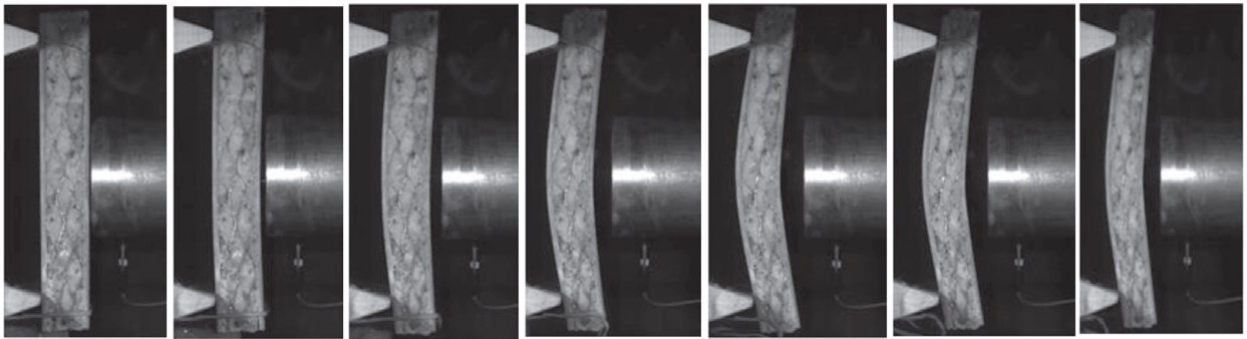


**Figure 2.29** High-speed images of fully foam filled corrugated core sandwich specimen during shock loading (Yazici et al., 2014)

## Chapter

# 3

## Blast Modelling

### 3.1 Introduction

For modelling the effect of blast loads on structures, many types of software using different techniques are used. These types of software can be classified into three categories: single degree of freedom (SDOF) systems, empirical programs, or hydrocodes. Many programs such as SPAN32 and WABEMST are based on SDOF analyses. SDOF systems are considered the fastest and the easiest technique that can generate global information about member performance. However, they may not be appropriate when more detailed information related to beam failure is required. Other programs like BlastX and ConWep are examples of the empirical programs. Empirical programs have the ability to incorporate a more detailed analysis of blast and structure interaction compared to SDOF systems. BlastX and ConWep are distributed through the governmentally controlled Defense Logistics Agency that monitors and controls access to the program due to the critical material that it contains. Software like *LS-DYNA* and *AUTODYN* are examples of hydrocode software. Hydrocodes are highly specialized numerical programs that are used to evaluate dynamic and shock events such as blasts or impacts. In this study, a brief explanation has been provided on *LS-DYNA* and *AUTODYN*.

### 3.2 Explicit finite element method (FEM)

The explicit dynamics was established to determine the dynamic response of a structure due to stress wave propagation, impact, or rapidly changing time-dependent loads. It is also used in other applications like underwater simulations, glass forming, sheet metal forming, failure analysis, and

earthquake engineering (LSTC, 2007). As for the implicit FEM, it is difficult to solve such problems where thousands of time steps must be taken because of the cost of inverting stiffness matrices to solve the large sets of nonlinear equations, especially for models with thousands of degrees of freedom or when nonlinearities are present. Whereas explicit FEM overcome this as it solves problems without forming a global stiffness matrix. The explicit approach is based on an element-by-element basis. Accordingly, the explicit approach can solve large three-dimensional models (thousands of degrees of freedom) with reasonable computational time. Moreover, the ease of implementation and the ability of modeling mechanical phenomena that are highly nonlinear are considered two other advantages. Nonlinearities may stem from the materials, (e.g. hyperelasticity, plastic flows, and failure), from contact (e.g. high speed collisions and impact), and from the geometric deformation (e.g. buckling and collapse). Although the explicit approach requires small time steps to be used, it is conditionally stable (LSTC, 2006). The time step used in an explicit dynamics analysis satisfies the CFL condition to maintain stability and consistency (AUTODYN, 2014).

$$\Delta t \leq \frac{d}{c} \quad (3.1)$$

Where  $d$  is a typical length of a zone and  $c$  is a local sound speed. Therefore, the time increment is proportional to the smallest element dimension in the model and inversely proportional to the sound speed in the materials used. This ensures that a disturbance does not propagate across a zone in a single time step.

Modeling the detonation process by the explicit approach is achieved by creating a physical finite element (FE) model of the explosive and the surrounding air. As a result, such modeling provides in detail the wave propagation through the explosive and also the subsequent passage of the shock wave through the surrounding air and resultant fluid-structure interactions, if any. Moreover, such modeling is conducted with no simplifying assumption. As in the modeling process, any charge shape, size, geometry, and point of detonation within the explosive can be defined resulting in accurate assessment of the blast overpressures. *LS-DYNA* and *AUTODYN* are two non-restricted codes used for modeling detonations. These two codes implement finite element, finite difference and/or finite volume techniques but differ in their solution methodology, modeling options, and usability.

### 3.3 *LS-DYNA* and *AUTODYN* Software

Livermore Software Technology Corporation (LSTC) developed the *LS-DYNA* explicit; a general purpose multi-physics finite element program. The program simulates highly complex real world problems and is suitable for modeling blast simulations. Whereas, ANSYS *AUTODYN* is an explicit analysis program designed for highly nonlinear dynamic problems using explicit finite difference, finite volume, and finite element techniques. *AUTODYN* is specifically designed for simulating dynamic impact whether in the form blast wave or a ballistic impact.

A finite difference method is one of the oldest methods where the domain discretized into a series of grid points and each node influences the subsequent results. Thus, the results obtained at the second node from adding or subtracting the quantities are computed at the first node. In this method, the properties of an element are only observed at the nodes and are considered constant through the element. Thus, one of the advantages of using this method is the easiness of implementation, whereas restriction to simple grids and failure to conserve momentum, energy, and mass on coarse grids are considered a disadvantage. Regarding the finite-volume method, it is mainly employed for the numerical solution of problems in fluid mechanics. The finite volume method uses the integral conservation equation that is applied to control volumes which subdivide the entire domain. Thus, the conserved variables are located within the volume element, and not at nodes or surfaces; and the boundary conditions can be applied noninvasively. One advantage of the finite volume method over finite difference method is that the former does not require a structured mesh (although a structured mesh can also be used). Finite volume methods are especially powerful on coarse non-uniform grids and in calculations where the mesh moves to track interfaces or shocks. Finally, the finite element method subdivides the whole domain into meshes, where the system matrices are used to simultaneously realize the desired output, such as strain, displacement, or stress at one or more integration points within each element. Interpolation functions are then used to determine the response of the element based on the output computed at integration points.

*LS-DYNA* and *AUTODYN* are able to use different solvers such as (i) Lagrange solver: used for solid continua and structures, (ii) Euler solver: used for gases, fluids and solids that undergo large deformations, and (iii) SPH solver: a Lagrange method that is gridless/meshless.

### 3.3.1 Lagrange Analysis

The Lagrange processors algorithms are based on the finite volume method, and it is typically used to solve structural dynamics problems. A slight modification has been done on the method in order to accommodate forces and masses at the nodes similar to explicit finite element method. In a Lagrange analysis, the mesh elements deform while no material movement would occur between two elements, i.e. the material in the element will remain within without any flow in or out of the element. Lagrange technique has the potential to be efficient and accurate for incorporating complex material model. The Lagrange method is best suited for modelling solid elements like structures (Zukas, 2004). In the Lagrange method, the coordinates  $x$ , velocities  $u$ , forces  $F$ , and masses  $m$ , in a mesh, are associated with the corner nodes, while stresses  $\alpha$ , strains  $\varepsilon$ , pressures  $p$ , energies  $e$ , and densities  $\rho$  are centred within the cells as shown in Figure 3.1 (Birnbbaum et al., 1999).

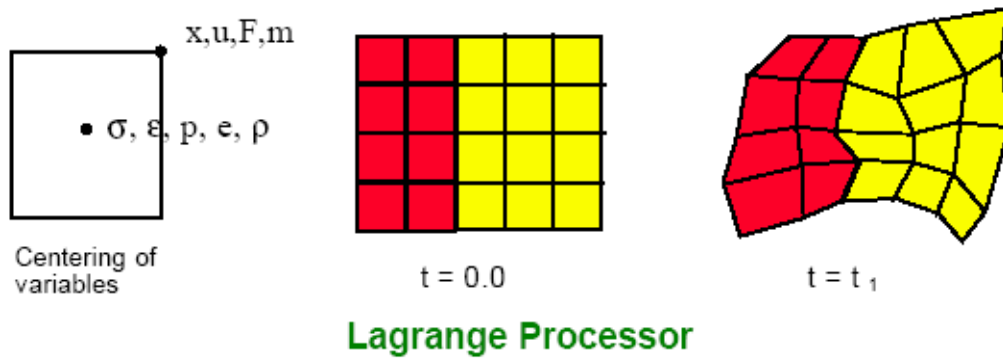


**Figure 3.1** Grid deformation in a Lagrange analysis (Birnbbaum et al., 1999)

Figure 3.2 shows a typical computation step in a Lagrange analysis where each time step must satisfy the CLF or Conart condition:

$$\Delta t < \frac{\Delta x}{c} \quad (3.2)$$

Where  $\Delta t$  is time step,  $\Delta x$  is the element size, and  $c$  is the local speed of sound. While, the factor of safety of two-thirds are then used. These limitations are conducted in order not to propagate a disturbance across an element in a single time step and to maintain the stability of the algorithm.

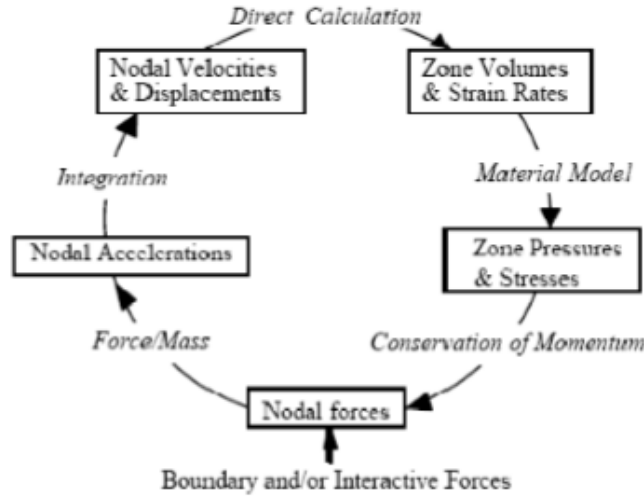


**Figure 3.2** A typical computation step in a Lagrange analysis (AUTODYN, 2014)

The main advantages of using the Lagrange processor in modelling are contributed to the fact that material boundaries and interfaces are clearly defined and do not mix, also, computations per cycle are good compared to other processors. Thus, Lagrange processor is well suited for modelling solid behaviour and strength. While, the main disadvantage of a Lagrange analysis is that it is used in problems which involve severe distortions that can lead to erroneous results or analysis termination. Severe element distortions lead to small time steps, and can lead to grid tangling causing the simulation to stop. This problem can be overcome by either using the erosion feature provided in *AUTODYN* or using the rezoning technique where the variables of a highly distorted mesh are conservatively remapped into an undistorted mesh, repairing the mesh and allowing the analysis to continue. Such techniques are described by (Zukas, 2004).

### 3.3.2 Euler Analysis

An Euler solver uses a control volume method to solve the governing conservative equations of mass, momentum and energy. The Euler – FCT processor is designed specifically to solve gas dynamics problems and in particular blast simulations. Contrary to the Lagrangian processor, the Euler processor involves a material movement between the mesh elements as shown in Figure 3.3. In an Euler solver, all variables are cell centred in a mesh, where  $x$  is the displacement,  $u$  is the velocity,  $F$  is the force,  $m$  is the mass,  $\sigma$  is the stress,  $\epsilon$  is the strain,  $p$  is the pressure,  $e$  is the internal energy, and  $\rho$  is the density. Defining the element properties at the cell centre helps to ease coupling with other solvers required to address fluid-structure interaction problems.

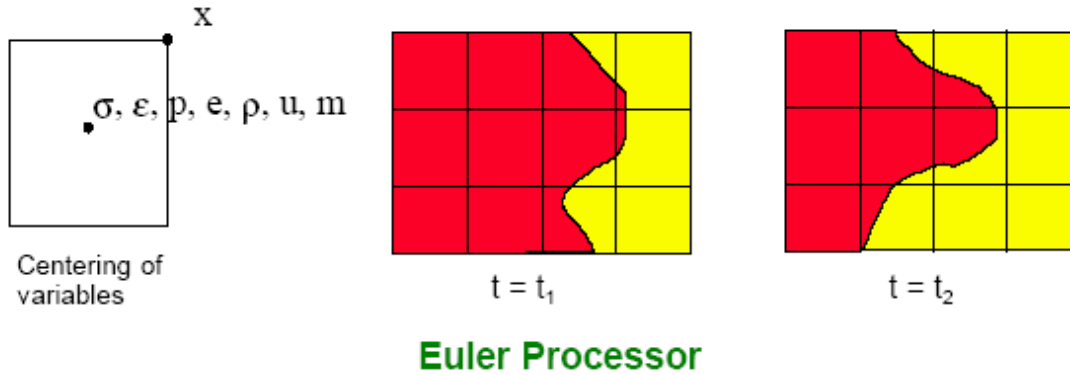


**Figure 3.3** Material flow through a stationary grid in an Euler analysis (Birnbbaum et al., 1999)

Figure 3.4 shows a typical computation step in an Euler analysis. Usually, Euler solvers use two-step procedure for every calculation time step. The first step is following the Lagrange analysis where the mesh moves with the fluid thereby conserving mass, and the nodal characteristics are updated after the mesh velocities and displacements are calculated. This process is repeated until the mesh deformation is acceptable or the mesh is not too distorted, after which a rezoning step is performed resulting in an undistorted mesh. Material is then advected from one element to another, which is determined by the amount of mesh rezoning. Thus, only the material moves from one location to another while the mesh remains stationary in each time step. Each time step must satisfy the CLF or Conart condition:

$$\Delta t < \frac{\Delta x}{(c + \|v\|)} \quad (3.3)$$

Where,  $\Delta t$  is time step,  $\Delta x$  is the element size,  $c$  is the local speed of sound, and  $v$  is the element velocity. While, factor of safety of two-thirds are then used. This limitation is conducted in order not to propagate a disturbance across an element in a single time step and to maintain stability of the algorithm.

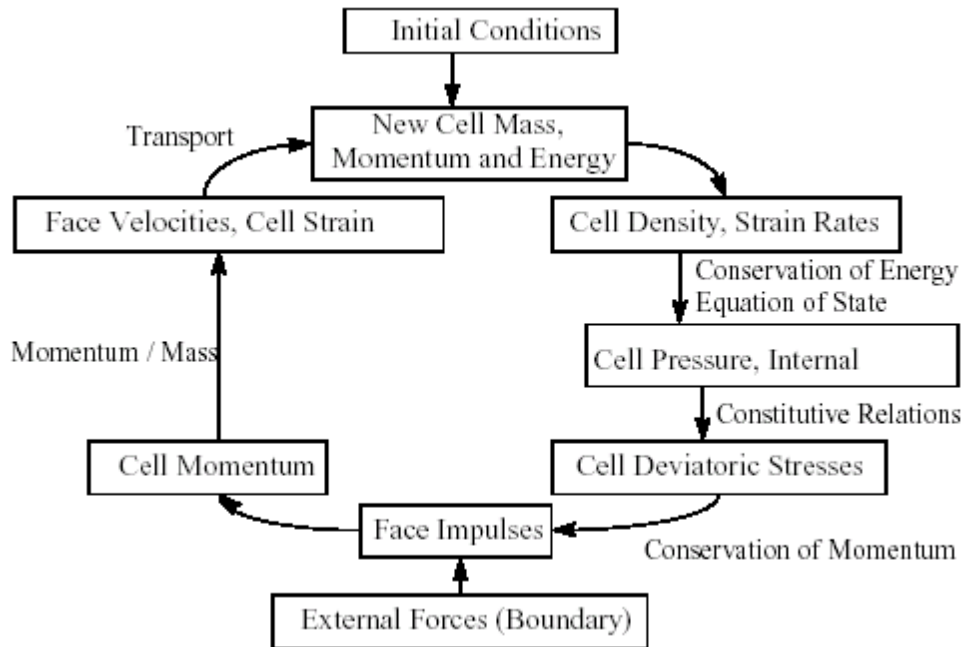


**Figure 3.4** A typical computation step in an Euler analysis (AUTODYN, 2014)

No grid distortions or tangling reducing time step or stopping the simulation are considered the main advantages of using the Euler processor in modelling. Also, Euler processor provides accurate and high-order method that is optimized for solving blast type problems. On the other hand, consuming more time for computations per cycle and assigning only one material are considered the disadvantages of using the Euler processor in modelling.

### 3.3.3 Smooth Particle Hydrodynamics (SPH) Analysis

SPH is a Lagrange technique but with the advantage of gridless “mesh free” method. The gridless method aids in solving computational continuum dynamics problems. SPH technique gives the ability to track the material deformation and trace history-dependent behaviour efficiently. Compared with Euler technique, SPH technique is more efficient since it needs only to model regions where the material exists not from where the material will flow, and complex constitutive models can be included more easily.

Figure 3.5 shows a typical computation step in an SPH analysis, which is similar to the Lagrange analysis, except for steps where a Kernel approximation is used. Kernel approximation is used “to compute forces from spatial derivatives of stress and spatial derivatives of velocity are

required to compute strain rates. In addition, SPH requires a sort of the particles at least once every cycle in order to locate current neighboring particles.” (Century Dynamics, 2005). In the SPH solver, the main advantages are preventing the grid tangling problems, and mesh degeneration so that a numerical erosion model is not needed.

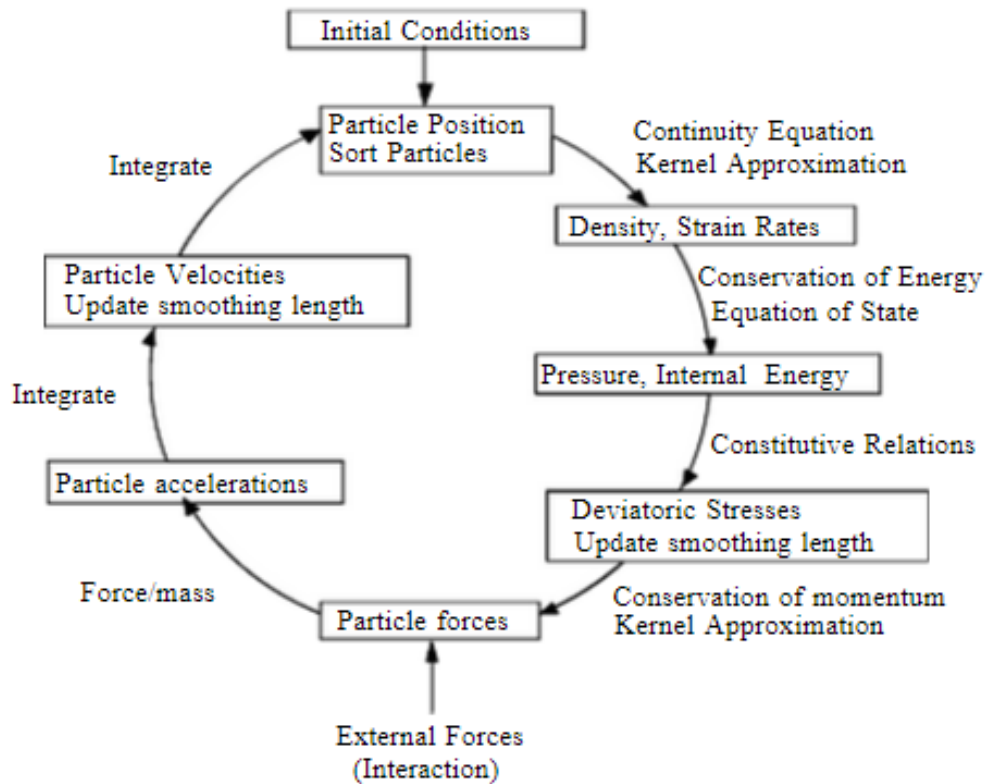


Figure 3.5 A typical computation step in an SPH analysis (AUTODYN, 2014)

### 3.3.4 Coupled Eulerian-Lagrangian Analysis for LS-DYNA versus AUTODYN

During blast wave propagation through the air, blast wave is reflected on hitting any solid surface. Accordingly, an interaction occurred between the structure and air, where the energy is transferred from the wave to the surface. For modeling this behaviour, the solvers must be coupled to capture air and structure responses. Such that energy, mass, and momentum are transferred from the Eulerian grid to Lagrangian grid and vice-versa. Such transfer is done in a form of boundary condition. In LS-DYNA, the interaction between air and the structure is done using an Arbitrary Lagrangian-Eulerian (ALE) solver for the air and a Lagrangian solver for the structure. ALE is a new solver that combines the features of Lagrangian and Eulerian solvers. Therefore, ALE has the

capability of addressing both the structural and fluid dynamics aspects of blast waves. Where the ALE solver rezones the nodes to an optimal position, contrary to Eulerian solver which rezones the nodes to their original location in a mesh. As the air mesh (ALE solver) is considered master mesh, whereas the structure mesh (Lagrangian solver) is considered slave mesh. In LS-DYNA, two coupling algorithms are available namely, constrained-based and penalty-based, which are well suited to simulate impact and blast. For the constrained based algorithm, it modifies the velocities and/or accelerations of solid element nodes and forces them to follow each other. Therefore, this coupling method conserves mass and momentum but not energy (LSTC, 2006). Whereas for the penalty-based algorithm, it tracks the relative motion between the nodes of the air (ALE) and structure (Lagrangian) meshes and applies penalty forces that resist the penetration of the ALE material through the Lagrangian mesh (LSTC, 2007).

The coupling method in AUTODYN is simpler than LS-DYNA. That is why AUTODYN software has been chosen to conduct this research. Euler-Lagrange coupling in AUTODYN considers a structure (Lagrangian) interface being cut through a fixed fluid (Eulerian) mesh in an arbitrary manner. The Eulerian elements intersected by the Lagrangian interface act as a pressure boundary for the Lagrangian mesh. Whereas, the Lagrangian mesh acts as a geometric boundary on the material flow in the Eulerian mesh. The Eulerian elements that are located adjacent to the Lagrangian interface boundary may be partially covered by the Lagrangian mesh, resulting in a continuous change in their control volumes and face areas. While in large-displacement problem, upon distortion of Lagrangian mesh, Eulerian elements that were not covered initially may be covered. Similarly, Eulerian elements that were initially covered may be uncovered. Upon distortion of Lagrangian mesh, some Eulerian cells will be covered and hence their control volumes can become very small and disappear when fully covered resulting in decreasing the obtained accuracy. In order to resolve this issue, the coupling method used in AUTODYN software combining the small control volume of an almost-covered cell to the control volume of the adjacent cell to form a single large control volume (AUTODYN, 2014).

### **3.4 Material Modelling**

To model a material in *AUTODYN*, the parameters of Equation of State (EOS) must be defined. While, the strength model and failure model are defined depending on the type of material.

**Equation of State (EOS)** describes the hydrodynamic response of a material where the relationship between the state variables (density, pressure and specific energy) is expressed. For liquids and gases, they cannot sustain shear and so this is the primary response of the material. For solids that have high deformation rate, this is considered also the primary response of the material.

**Material Strength Model** describes what happens to a material during the elastic-plastic phase.

**Material Failure Model** describes how the material would fail when subjected to excessive loads.

### 3.4.1 Trinitrotoluene (TNT)

For the Explosive material, the Jones-Wilkins-Lee (JWL) equation of state was used to model the rapid expansion of high explosive detonation products and has been used in the study. The pressure for the expanding gas is given by Equation (3.4).

$$P = A\left(1 - \frac{\overline{\omega}\eta}{R_1}\right)e^{-\frac{R_1}{\eta}} + B\left(1 - \frac{\overline{\omega}\eta}{R_2}\right)e^{-\frac{R_2}{\eta}} + \overline{\omega}\rho e \quad (3.4)$$

$$\eta = \rho/\rho_o \quad (3.5)$$

Where  $\rho$  is the density,  $\rho_o$  is the reference density,  $e$  is the specific internal energy, while  $A$ ,  $B$ ,  $R_1$ ,  $R_2$ , and  $\overline{\omega}$  are empirically derived constants.

The strength model parameter for TNT explosives was defined as Hydro (no strength) and there is no failure mode defined.

### 3.4.2 Air

For the Air material, the equation of state (Ideal gas) was used to model the Air material as in Equation (3.6).

$$P = (\gamma - 1)\rho e + P_{shift} \quad (3.6)$$

Where  $P$  is the pressure,  $\rho$  is the density,  $\gamma$  is the ideal gas constant,  $P_{shift}$  is the pressure shift (to define small initial pressures in a model), and  $e$  is the specific internal energy.

The strength model parameter for Air material was defined as Hydro (no strength) and there is no failure mode defined.

### 3.4.3 FRP

For the FRP material, the equation of state orthotropic is used. The incremental stress-strain relations are given by Equation (3.7).

$$[\sigma]^{n+1} = [\sigma]^n + [c][\dot{\epsilon}]\Delta t \quad (3.7)$$

Where  $[c]$  is the stiffness matrix,  $[\dot{\epsilon}]$  is the strain rate tensor, and  $\Delta t$  is the time step.

The strength model parameter used for FRP material is orthotropic yield. As for the failure model parameter, orthotropic softening was used.

### 3.4.4 Sand

For the sand material, the equation of state compaction is used. The elastic loading/unloading compaction curve comes from the density dependent bulk sound speed. The strength model parameter used for sand modelling is the granular strength model. The failure model parameter used is the hydro tensile limit as this is the minimum pressure at which the material can withstand continuous expansion.

### 3.4.5 Steel

For the steel material, a linear EOS for steel is used, see Equations (3.8 and 3.9). The pressure level is dependent on the bulk modulus  $K$  and the compression  $u$ .

$$P = K\mu = K\left(\frac{\rho}{\rho_0} - 1\right) \quad (3.8)$$

$$K = E/[3(1 - 2\mu)] \quad (3.9)$$

Where  $\rho$  is the density and  $E$  is the young's modulus.

The strength model parameter used for sand modelling is Johnson-Cook model. Whereas the failure model parameter used is plastic strain.

### 3.5 Modelling the Propagation of the Blast Wave

In this section, the propagation of the blast wave into the general model is presented. The remapping method has been used to simulate the blast wave.

#### 3.5.1 Define Geometry Properties

The FE model used in the current study has been created using a dynamic nonlinear explicit software *ANSYS AUTODYN*. Two scenarios have been studied, FRP sandwich panels and metallic sandwich panels. Regarding FRP sandwich panels, FE model is validated using the field experiments conducted by Hoemann (2007). Field experiments were designed based on a certain threat level of TNT located at 10.7 m from the test panels. The centre of the explosive charge was placed at 1.8 m above the ground level as shown in Figure 3.6, while Figure 3.7 shows the FE model of the FRP sandwich panels. The model consists of the explosive charge (TNT), the FRP sandwich panel (filled with a filling material if applicable), and the air domain. In the model, the TNT charge has been located at the corner of the FRP panel to simulate the field tests.

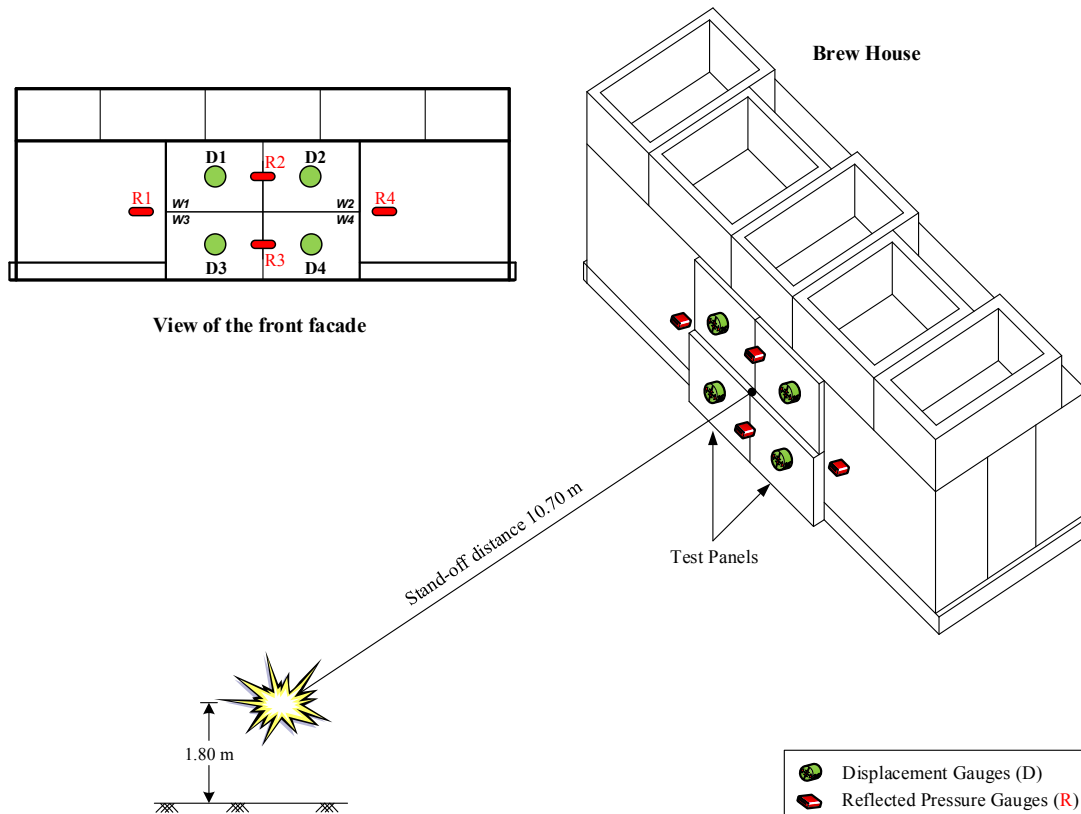
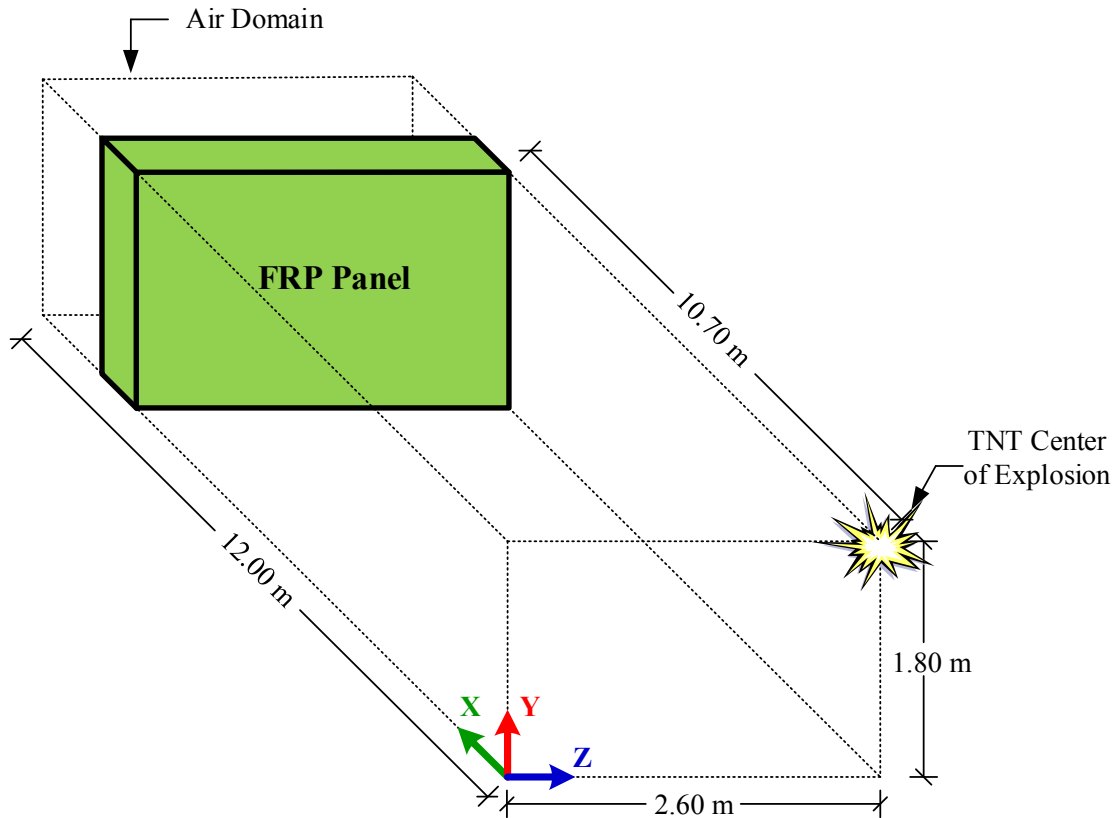
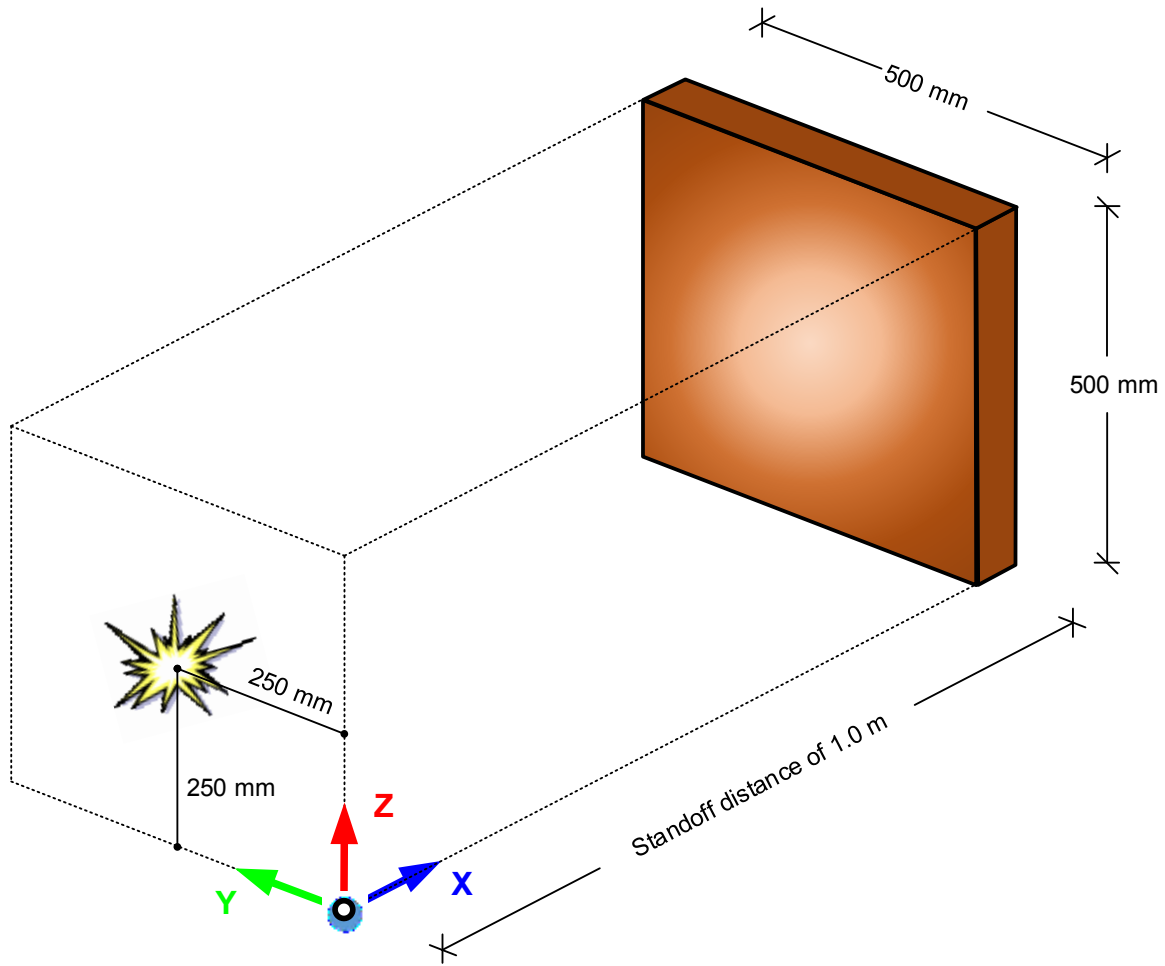


Figure 3.6 Field test schematic (adapted from Hoemann, 2007)



**Figure 3.7** Schematic of the FRP finite element model

As for the metallic sandwich panels, a numerical model has been simulated and validated based on the work conducted by Alberdi et al. (2013). Following Alberdi et al. (2013) work setup, the centre of explosion is 1 m from the simulated panel and elevated at 0.25 m from the ground surface. Figure 3.8 shows the FE model of the metallic sandwich panels.



**Figure 3.8** Schematic of the metallic finite element model

Using shell element for 1 mm thickness model is not appropriate due to the fact that shell formulation comes from the 2-dimensional approximation of 3-dimensional physics (Hahn 2005). Undoubtedly, shell model is not the appropriate model for providing good results for solid type structures. Although the common border ratio of thickness to length is 1/100, yet, this cannot be applied as a rule in actual finite element modeling. Some engineering software provide two different shell elements, a thick shell element and a thin shell element, for compensation. Previous research by Hahn and Kikuchi (2005) that studied the use of both shell and solid elements, indicated that it is still troublesome to determine specific guidelines for which each element should be used. In this study, since the FRP sandwich panels are of 10 mm thickness and the metallic sandwich panels reaches 1 mm thickness, the model is simulated as a solid element to obtain more precise results for both panels.

In the FE simulation, sandwich panels are defined as eight-node solid hexahedron Lagrange elements. As in the Lagrange analysis, the mesh elements would deform while no material movement between two elements occurred, i.e. the material remains within the element without any flow out of it. Lagrange technique has the potential to be efficient and accurate for complex material models. The Lagrange method is best suited for modelling solid elements like structures (Zukas, 2004). In this study, filling materials have been modeled as Smooth Particle Hydrodynamics (SPH) objects. SPH is a gridless technique that does not lead to grid tangling in case of large deformation problems and does not require using unphysical erosion algorithm (Hayhurst et al., 1996).

The air domain has been modeled as Euler-Flux Corrected Transport (Euler-FCT) sub-grid. Contrary to Lagrange analysis, Euler analysis involves material movement between mesh elements. The Euler-FCT processor is designed mainly to solve gas dynamics problems and, in particular, to be used for blast simulations. In the model, flowout boundary conditions of the air domain are applied along the box boundaries except at the bottom face which represents the ground surface.

For the purpose of material modelling using AUTODYN, the parameters of the material's equation of state (EOS) must be defined first. Then the strength and failure models are defined for each material. For the air, the Ideal Gas EOS was used. The strength model parameter is defined as a Hydro (i.e. no strength), while no failure mode has been defined. Whereas the material properties of the air are defined in Table 3.1. Regarding the TNT, the Jones-Wilkins-Lee (JWL) EOS was used. The strength model parameter is defined as a Hydro (i.e. no strength), while no failure mode was defined. Whereas the material properties of the air are defined in Table 3.2.

**Table 3.1** Material properties of Air

<b>Parameter</b>	<b>Value</b>
Density (g/cm <sup>3</sup> )	1.225e-03
Gamma	1.400
Reference temperature (K)	288.2
Specific heat (J/kgK)	717.600
Int. Energy (kJ/kg)	2.068e+05

**Table 3.2** Material properties of TNT

<b>Parameter</b>	<b>Value</b>
Density (g/cm <sup>3</sup> )	1.630
Parameter A (kPa)	3.738e+08
Parameter B (kPa)	3.747e+06
Parameter R1	4.150
Parameter R2	0.900
Parameter W	0.350
C-J Detonation velocity (m/s)	6.930e+03
C-J Energy / unit volume (kJ/m <sup>3</sup> )	6.000e+06
C-J Pressure (kPa)	2.100e+07

### 3.5.2 The Remapping Method

The explosion is simulated using the remap capability in *AUTODYN* (AUTODYN, 2014), where the output of a one-dimensional (1D) high-resolution initial detonation is remapped as initial conditions for the subsequent calculation stages. The remapping has been performed in three main steps:

1. Modelling of 1D detonation and initial expansion of TNT using a wedge model as shown in Figure 3.9
2. Remapping results of the 1D analysis into a 2D numerical model and then analyzing the model using a 2D code as shown in Figure 3.10
3. Remapping results of the 2D analysis into a 3D numerical model and then analyzing the model using a 3D code as shown in Figure 3.11

The aforementioned remapping steps are to be performed before any interaction with the ground or the FRP panel occurs.

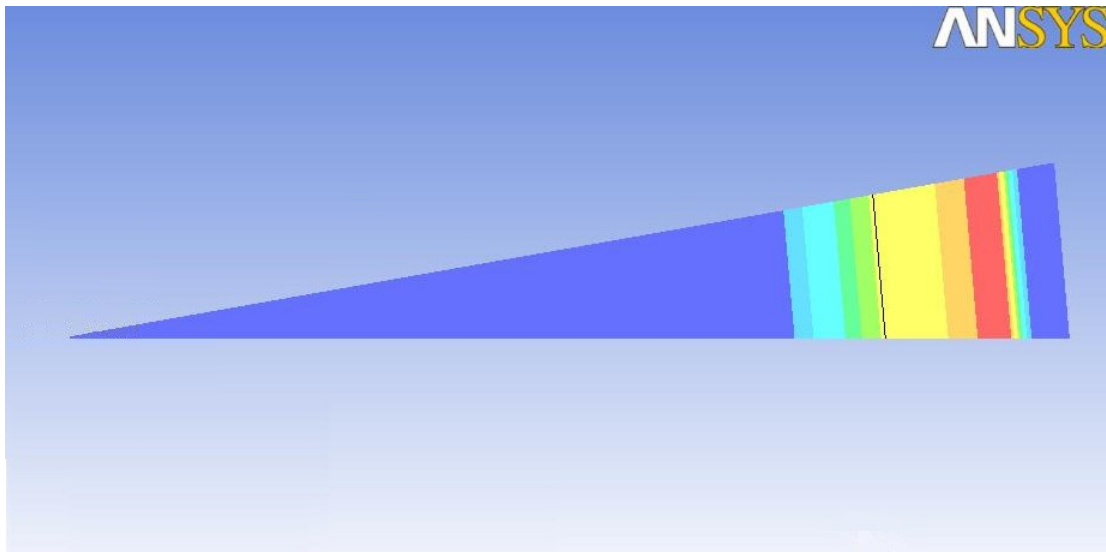


**Figure 3.9** 1D initial expansion model of TNT

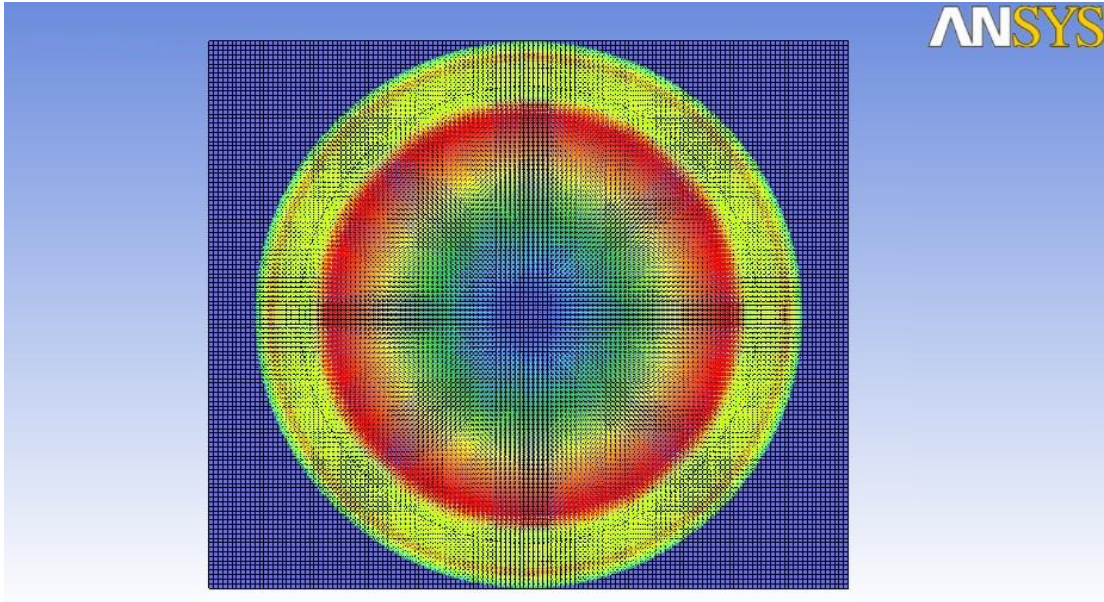


**Figure 3.10** 2D expansion model of TNT

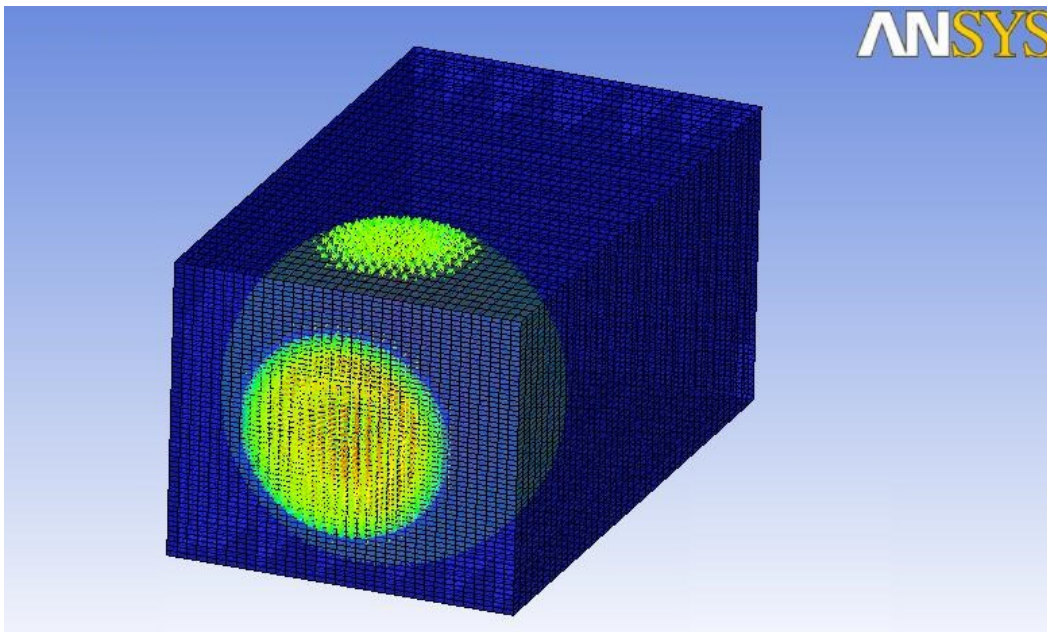


**Figure 3.11** 3D expansion model of TNT for metallic model

Modelling blast load using the remapping method enables the simulation of reflection and diffraction of blast wave. This represents the mutual interaction between the structure and the blast wave which cannot be ignored when structural displacement is large under the blast effect. Moreover, using 1D analysis helps calculating the initial pressure distribution with high accuracy

in minimum processing time. This can be achieved by using a fine mesh for the initial detonation wedge which is feasible compared to modelling the whole 3D domain using fine mesh size. Figure 3.12 shows the schematic of wave propagation and reflection waves. Reflection waves have occurred because the distance between explosions and ground is smaller than the stand-off distance.

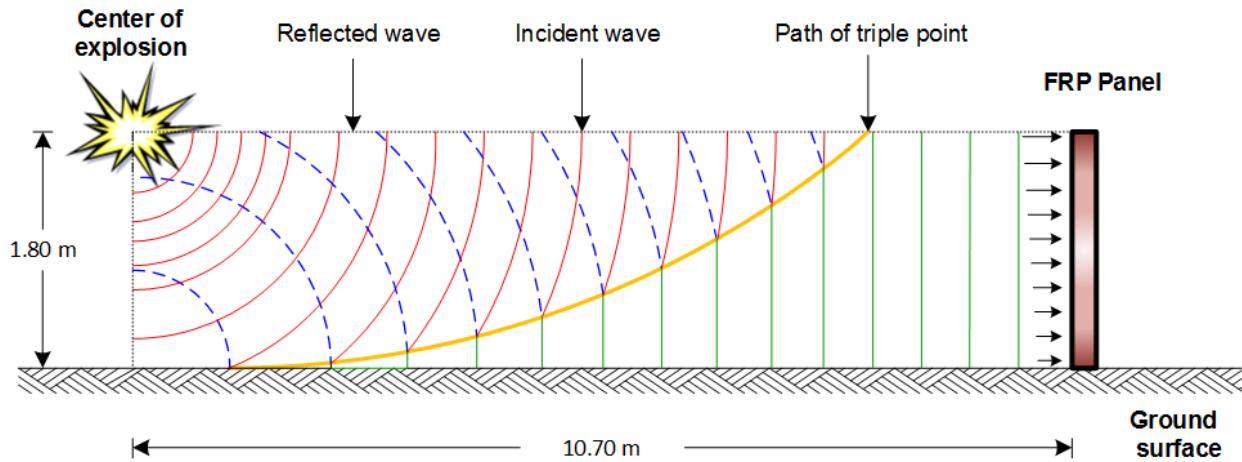


**Figure 3.12** Schematic of wave propagation in FRP finite element model

### 3.5.3 Sensitivity Analysis

For the FRP sandwich panel model, air domain was generated as a box with a length of 12 m in X direction, a height of 1.8 m in Y direction, and a width of 2.6 m in Z direction. Euler element size of: 15, 10, 5, 3, 2, 1, 0.5, 0.25, 0.125, and 0.0625 mm were used to perform mesh sensitivity analysis at a distance of 1.8 m – as it is the minimum distance before hitting a reflection surface. Table 3.3 classifies the considered wedge categories among the element size and the total number of elements in each category. Figure 3.13 shows the relation between wedge category and incident peak overpressure. As seen in the figure, the element size of 0.25 mm showed high level of accuracy, and hence was selected in the current study. Also, comparing numerical results (0.25 mm) with the results analytically obtained from the Kingery-Bulmash chart, a difference of 1.2% was realized.

**Table 3.3** Mesh sensitivity for the FRP model wedge

Wedge category	Element size (mm)	Total no. of elements
1	15	120
2	10	180
3	5	360
4	3	600
5	2	900
6	1	1,800
7	0.5	3,600
8	0.25	7,200
9	0.125	14,400
10	0.0625	28,800

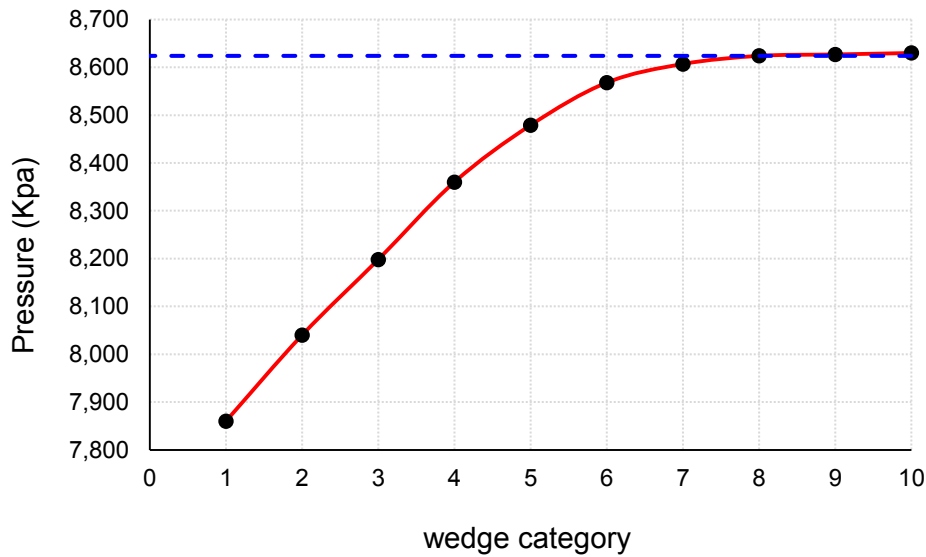


**Figure 3.13** Incident pressure for different wedge categories of the FRP model

For the 3D air domain with dimensions of  $12 \times 1.8 \times 2.6$  m, elements with aspect ratio of 1.0 and sizes of 50, 45, 40, 35, 30, 25, 20, and 15 mm were investigated. Table 3.4 classifies air domain categories as per the element size and the total number of elements in each category. Figure 3.14 shows the relationship between 3D air domain category and the peak reflected pressure measured at distance of 10.7 m. As seen in the figure, the element size of 30 mm showed an acceptable level

of accuracy (an error of less than 1.5 %), and hence it was selected in the current study. Comparing numerical results (30 mm) with these obtained analytically from Kingery-Bulmash chart, a difference of 3.9% was realized.

**Table 3.4** Mesh sensitivity for the 3D air domain of the FRP model

Category	Element size (mm)	Total no. of elements
1	50	449,280
2	45	619,440
3	40	877,500
4	35	1,294,482
5	30	2,064,000
6	25	3,594,240
7	20	7,020,000
8	15	16,608,000

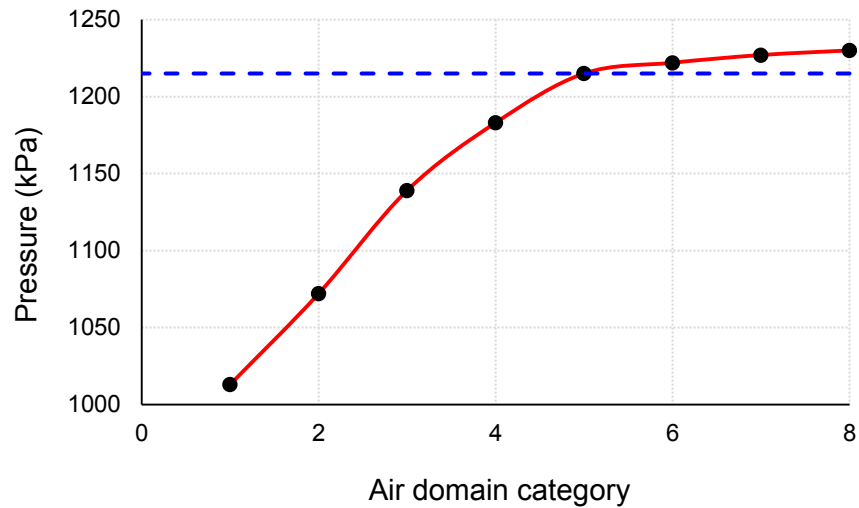


**Figure 3.14** Reflected pressure for different 3D air categories of FRP model

As for metallic sandwich panel model, the air domain has been generated as a box with a length of 1.2 m in X direction, a width of 0.5 m in Y direction, and a height of 0.5 m in Z direction. Euler element size of: 1, 0.8, 0.6, 0.4, 0.2, 0.1, 0.05, 0.025, and 0.0125 mm has been used to perform

mesh sensitivity analysis at a distance of 0.25 m – as it is the minimum distance before hitting a reflection surface. Table 3.5 classifies the considered wedge categories among the element size and the total number of elements in each category. Figure 3.15 shows the relation between the wedge category and the incident peak overpressure. As seen in the figure, the element size of 0.05 mm showed high level of accuracy, and hence was selected in the current study. Comparing the numerical results (0.05 mm) with these analytically obtained from Kingery-Bulmash chart, a difference of 5.2% was realized.

**Table 3.5** Mesh sensitivity of metallic model wedge

Wedge category	Element size (mm)	Total no. of elements
1	1	250
2	0.8	312
3	0.6	416
4	0.4	625
5	0.2	1,250
6	0.1	2,500
7	0.05	5,000
8	0.025	10,000
9	0.0125	20,000

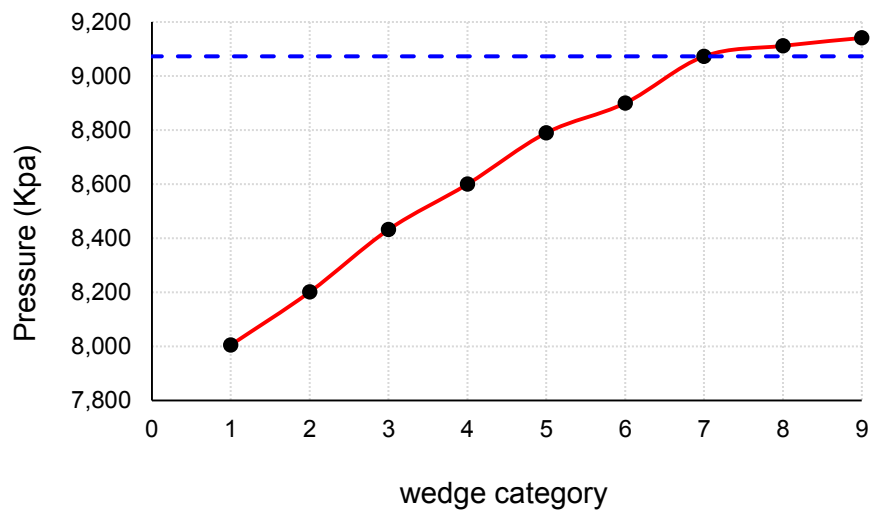


**Figure 3.15** Incident pressure for different wedge categories of the metallic model

For the 3D air domain with dimensions of  $1.2 \times 0.5 \times 0.5$  m, elements with aspect ratio of 1.0 and sizes of 30, 25, 20, 15, 10, and 5 mm were investigated. Table 3.6 classifies air domain categories as per the element size and the total number of elements in each category. Figure 3.16 shows the relationship between 3D air domain category and the peak of reflected pressure measured at distance of 1 m. As seen in the figure, element size of 15 mm showed an acceptable level of accuracy (an error of less than 3.1%), and hence it was selected in the current study. Also, comparing numerical results (15 mm) with these analytically obtained from Kingery-Bulmash chart, a difference of 9.8% was realized.

**Table 3.6** Mesh sensitivity for 3D air domain of the metallic model

Category	Element size (mm)	Total no. of elements
1	30	11,560
2	25	19,200
3	20	37,500
4	15	87,120
5	10	300,000
6	5	2,400,000

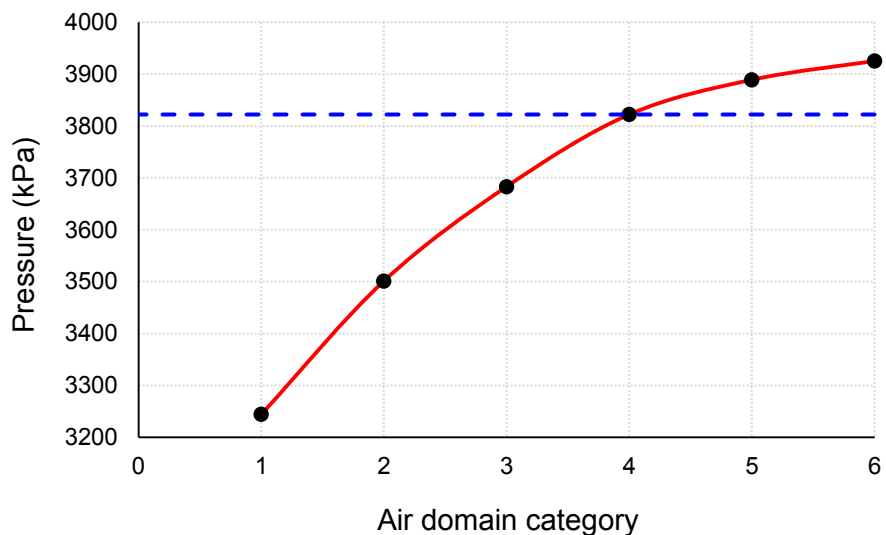


**Figure 3.16** Reflected pressure for different 3D air categories of the metallic model

Since the model is generated from several layers/strips, each layer/strip should be joined with the flat layers. In AUTODYN software, the nodes to be joined are required to be located within a small tolerance of one another. The mesh size are dictated by the smallest dimensions, which is the layers/strips thickness, while trying to keep the aspect ratio of the modeled mesh close to one. Figure 3.17 illustrates the mesh used throughout this research.

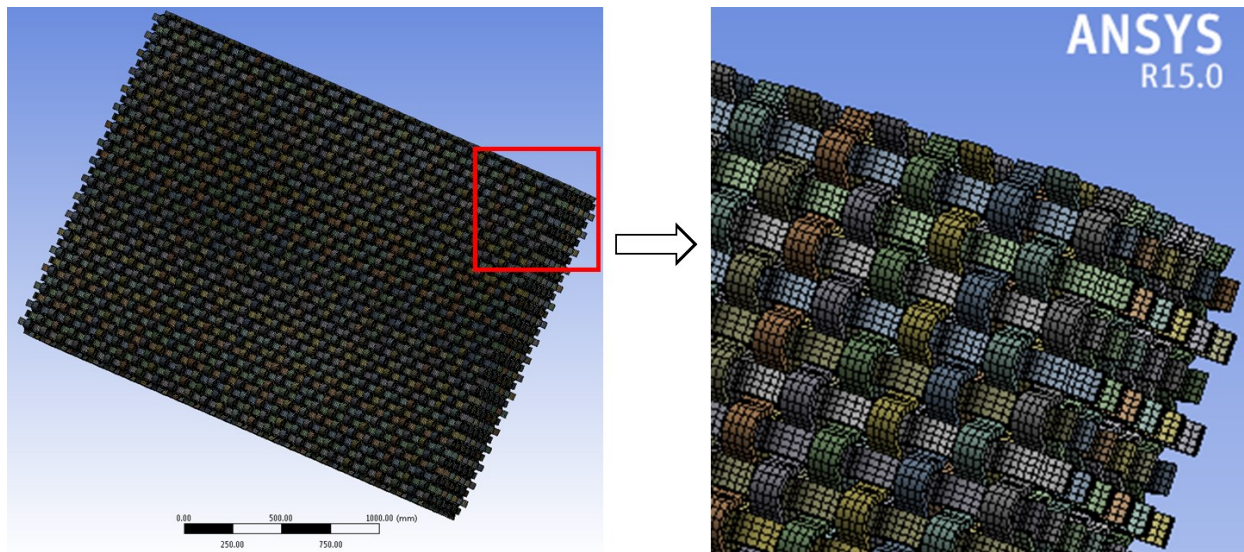


**Figure 3.17** Illustration of the solid mesh

### 3.5.4 Boundary Conditions

For FRP sandwich panel model, hinged boundary conditions are applied to the two vertical sides of FRP panel, while the top and bottom lines are free. It should be noted that in field tests, each vertical side of the four FRP panels was restrained by clamping anchorages along edges. These anchorages are fixed on the wall, in one side, and on the vertical interior column, centering the four panels on the other side. On the other hand, the two vertical sides of each panel were assumed to be hinged along the whole height as shown in Figure 3.18.

As for the metallic sandwich panel model, boundary conditions have been modeled as clamped boundary condition which has been applied along the perimeters of the modeled sandwich panels as shown in Figure 3.19.

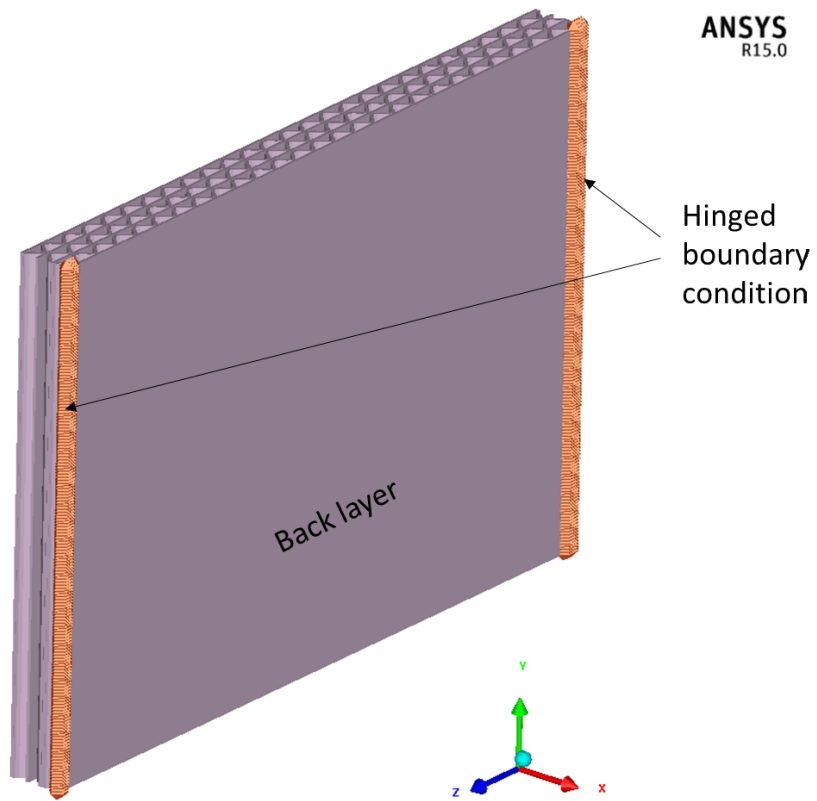


**Figure 3.18** Boundary conditions for the FRP panels

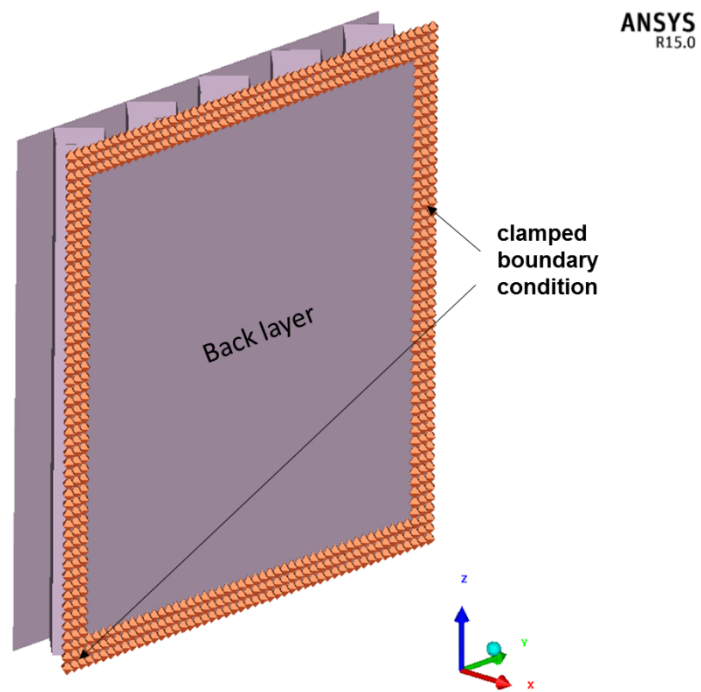


**Figure 3.19** Boundary conditions for the metallic panels

### 3.5.5 Interaction and contact points

Sandwich panels were defined as Lagrange elements, whereas air domain was simulated using Euler-FCT elements. Lagrange and Euler elements exchange impulses at their interfaces and both solvers must be coupled to simulate interaction between the structure and air domain. In coupling procedure, mass, energy, momentum, and forces are transferred from Euler mesh to the Lagrange and vice-versa. The interaction is defined as fully coupled where Lagrange elements interact dynamically with Euler elements (AUTODYN, 2014). This type of interaction is important specially when deflections occur, because the movement of the geometric constraint provided by the Lagrange mesh will influence pressure values (Yun & Park, 2013).

On the other hand, the interaction between the Lagrange FRP element and SPH filling materials is defined as gap contact, where the interaction follows conservation of angular and linear momentum. The gap contact algorithm uses a time step restriction to assure a stable interaction process. Such restriction assumes that during 1 computational time step, a surface node cannot travel more than 20% into the contact detection zone (AUTODYN, 2014).

$$\Delta t = 0.2 \frac{\delta}{V} \quad (3.10)$$

Where  $\delta$  is the gap size and  $V$  is the velocity of the penetrating node.

A bonded contact is used for joining the nodes of the FRP and metallic panels. By default, the bonded contact is unbreakable unless a stress failure criteria are defined (AUTODYN, 2014). In this study, stress failure criteria are defined for the FRP panels as the maximum normal stress limit is 9.6 MPa and the maximum shear stress limit is 36.4 MPa, as per the manufacturer data sheet (Cytec, 2016). Whereas no failure criteria is defined for the metallic sandwich panels.

## 3.6 Summary

This chapter provides a background on different software packages that can be used for modelling the effect of blast loads on structures. Also, it briefly introduces *AUTODYN* software that is used throughout the research. Throughout this chapter the geometry properties for both the FRP and metallic sandwich panels is defined. Moreover, it presents the approach used for modelling blast wave propagation for both the FRP and metallic sandwich panels, where a

remapping method was used. The remapping method using fine mesh for the initial detonation 1D wedge is of higher accuracy, has less processing time, and is more feasible than modelling the whole 3D domain modelling using fine mesh size. Accordingly, a mesh sensitivity analysis was applied for both the 1D wedge and 3D domain for the two models considered in this study; FRP and metallic model to better choose the best mesh size that will result in most acceptable accuracy level. Finally, the applied boundary conditions for each model are explained.

## Chapter

# 4

## FRP Sandwich Panels

### 4.1 FRP Core Geometry

Five different configurations of FRP panel inner core are considered in this study. Three configurations are available in the literature review and two other configurations are newly proposed. The effectiveness of each configuration is investigated using a dynamic nonlinear explicit FE model. The numerical model simulates the dynamic response of the FRP sandwich panel when subjected to an explosion.

Figure 4.1 shows the five FRP panel inner core configurations considered in the analyses. Configurations (a), (b), and (c) are the ones tested by Hoemann (2007). In these configurations, the standard sinusoidal honeycomb core layers were placed in different orientations. Configuration (a) represents the parallel weak (PW) axis, configuration (b) is a “turned” right-angle weak (TRW) axis, and configuration (c) is the right-angle weak (RW) axis. Configurations (d) WV2-1 and (e) WV2-2 are proposed in this study and they consist of strips that have been cut from the same sinusoidal honeycomb and are interlaced at a right angle forming the woven shape. WV2-1 consists of two sinusoidal honeycomb strips in the longitudinal direction and one transverse sinusoidal strip attached at every other peak of the longitudinal strips. For WV2-2, a transverse strip has been provided at every peak of the longitudinal strips as shown in the figure. It is worth mentioning that the woven shape WV2-1 has been designed so that the amount of FRP material used is the same amount used for PW, TRW, or RW shapes. While for the woven shape WV2-2, 33% more FRP material has been used compared to the other shapes.

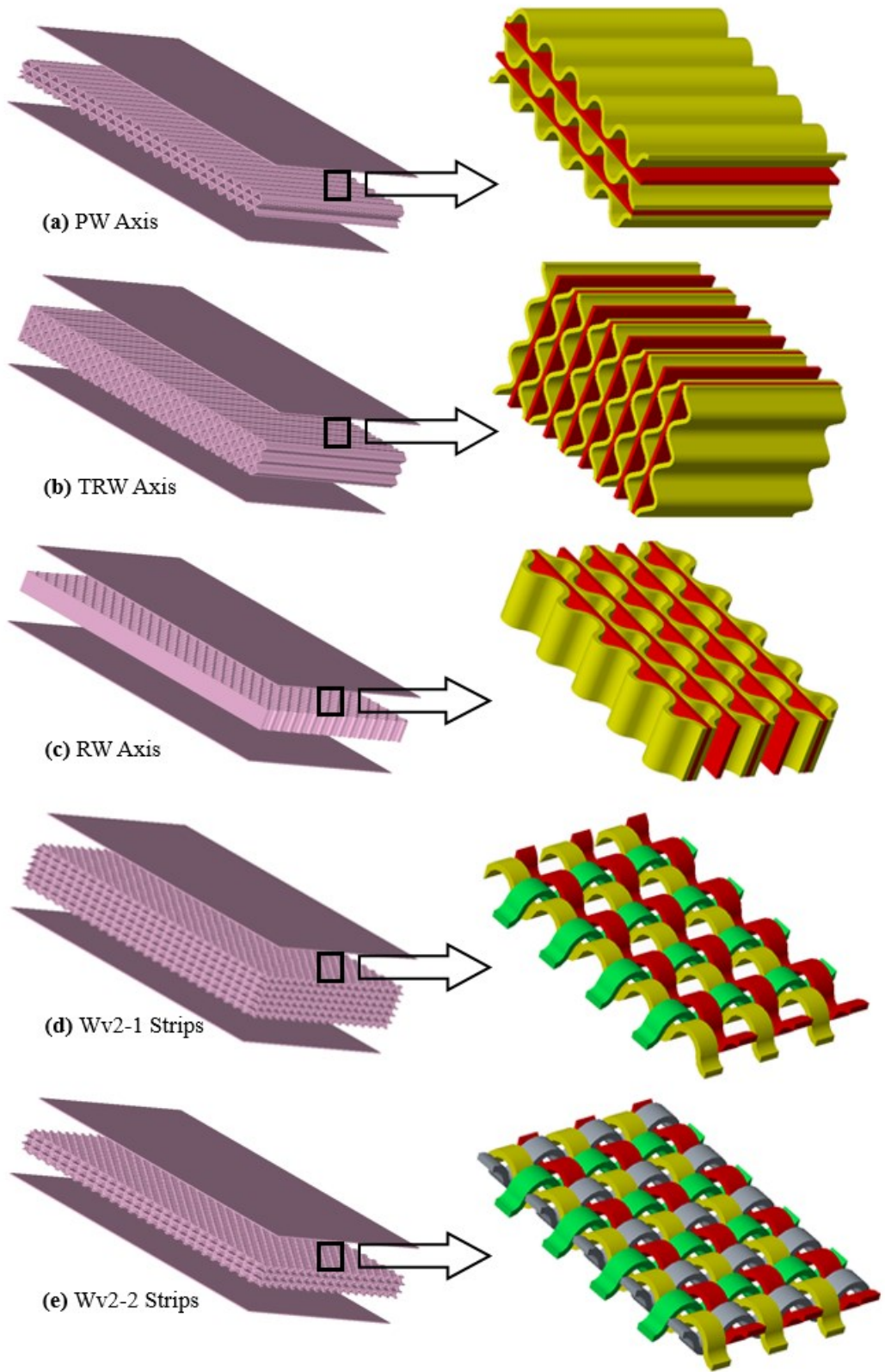


**Figure 4.1** Inner core configurations of the FRP sandwich panels

For each of the five configurations, every two sinusoidal honeycomb layers are bonded with a flat layer of similar material in between forming the core, where each two honeycomb layers are placed symmetrically around the flat layer as shown in the figure. Then the core is sandwiched between two FRP outer layers to form the honeycomb sandwich panels.

## 4.2 Material Properties

For the purpose of material modelling using AUTODYN (2014), the parameters of the material's equation of state (EOS) must be defined first. Then the strength and failure models are defined for each material. Regarding sand material, the compaction EOS was used, where the elastic loading/unloading compaction curve was obtained from the density-dependent bulk sound speed. The strength model parameter used for sand material is the Granular Strength model, while the failure model parameter used is the Hydro Tensile. The mechanical properties of sand material used in this study were defined according to Laine and Sandvik (2001). Table 4.1 lists the mechanical properties for the sand. For FRP material, the Orthotropic EOS has been used. The strength model parameter used is the Orthotropic Yield, while the failure model parameter used is the Orthotropic Softening. Table 4.2 lists the mechanical properties for the FRP composite material.

**Table 4.1** Material properties of sand

Parameter	Value	Parameter	Value
Density #1 (g/cm <sup>3</sup> )	1.674	Pressure #1 (kPa)	0.0
Density #2 (g/cm <sup>3</sup> )	1.739	Pressure #2 (kPa)	4.577e+03
Density #3 (g/cm <sup>3</sup> )	1.874	Pressure #3 (kPa)	1.498e+04
Density #4 (g/cm <sup>3</sup> )	1.997	Pressure #4 (kPa)	2.915e+04
Density #5 (g/cm <sup>3</sup> )	2.144	Pressure #5 (kPa)	5.918e+04
Density #6 (g/cm <sup>3</sup> )	2.250	Pressure #6 (kPa)	9.810e+04
Density #7 (g/cm <sup>3</sup> )	2.380	Pressure #7 (kPa)	1.794e+05
Density #8 (g/cm <sup>3</sup> )	2.485	Pressure #8 (kPa)	2.894e+05
Density #9 (g/cm <sup>3</sup> )	2.585	Pressure #9 (kPa)	4.502e+05
Density #10 (g/cm <sup>3</sup> )	2.671	Pressure #10 (kPa)	6.507e+05

Density #1 (g/cm <sup>3</sup> )	1.674	Soundspeed #1 (m/s)	265.2
Density #2 (g/cm <sup>3</sup> )	1.746	Soundspeed #2 (m/s)	852.1
Density #3 (g/cm <sup>3</sup> )	2.086	Soundspeed #3 (m/s)	1.722e+3
Density #4 (g/cm <sup>3</sup> )	2.147	Soundspeed #4 (m/s)	1.876e+3
Density #5 (g/cm <sup>3</sup> )	2.300	Soundspeed #5 (m/s)	2.265e+3
Density #6 (g/cm <sup>3</sup> )	2.572	Soundspeed #6 (m/s)	2.956e+3
Density #7 (g/cm <sup>3</sup> )	2.598	Soundspeed #7 (m/s)	3.112e+3
Density #8 (g/cm <sup>3</sup> )	2.635	Soundspeed #8 (m/s)	4.600e+3
Density #9 (g/cm <sup>3</sup> )	2.641	Soundspeed #9 (m/s)	4.634e+3
Density #10 (g/cm <sup>3</sup> )	2.800	Soundspeed #10 (m/s)	4.634e+3
Pressure (P-Y) #1 (kPa)	0.0	Yield stress (P-Y) #1 (kPa)	0.0
Pressure (P-Y) #2 (kPa)	3.401e+03	Yield stress (P-Y) #2 (kPa)	4.235e+03
Pressure (P-Y) #3 (kPa)	3.490e+04	Yield stress (P-Y) #3 (kPa)	4.469e+04
Pressure (P-Y) #4 (kPa)	1.013e+05	Yield stress (P-Y) #4 (kPa)	1.240e+05
Pressure (P-Y) #5 (kPa)	1.846e+05	Yield stress (P-Y) #5 (kPa)	2.260e+05
Pressure (P-Y) #6 (kPa)	5.000e+05	Yield stress (P-Y) #6 (kPa)	2.260e+05
Density (D-G) #1 (g/cm <sup>3</sup> )	1.674	Shear modulus (D-G) #1 (kPa)	7.690e+04
Density (D-G) #2 (g/cm <sup>3</sup> )	1.746	Shear modulus (D-G) #2 (kPa)	8.694e+05
Density (D-G) #3 (g/cm <sup>3</sup> )	2.086	Shear modulus (D-G) #3 (kPa)	4.032e+06
Density (D-G) #4 (g/cm <sup>3</sup> )	2.147	Shear modulus (D-G) #4 (kPa)	4.907e+06
Density (D-G) #5 (g/cm <sup>3</sup> )	2.300	Shear modulus (D-G) #5 (kPa)	7.769e+06
Density (D-G) #6 (g/cm <sup>3</sup> )	2.572	Shear modulus (D-G) #6 (kPa)	1.480e+07
Density (D-G) #7 (g/cm <sup>3</sup> )	2.598	Shear modulus (D-G) #7 (kPa)	1.657e+07
Density (D-G) #8 (g/cm <sup>3</sup> )	2.635	Shear modulus (D-G) #8 (kPa)	3.672e+07
Density (D-G) #9 (g/cm <sup>3</sup> )	2.641	Shear modulus (D-G) #9 (kPa)	3.735e+07
Density (D-G) #10 (g/cm <sup>3</sup> )	2.800	Shear modulus (D-G) #10 (kPa)	3.735e+07
Hydro tensile limit (kPa)	-1.00		

---

**Table 4.2** Material properties of FRP

<b>Parameter</b>	<b>Value</b>
Tensile strength (MPa)	460
$\nu_{12}$	0.216
$\nu_{23}$	0.3
$\nu_{31}$	0.216
$E_{11}$ (GPa)	21
$E_{22}$ (GPa)	7.9
$E_{33}$ (GPa)	7.9
$G_{12}$ (MPa)	1650
$G_{23}$ (MPa)	3040
$G_{31}$ (MPa)	1650
Bulk modulus A1 (GPa)	8.3
Parameter A2 (GPa)	50
Parameter T1 (GPa)	8.3
Reference temperature (K)	300
Specific heat (J/kgK)	1.42e3
A11	1.5
A22	1
A33	1
A12	-0.68
A13	-0.68
A23	-0.26

A44	4
A55	4
A66	4
Eff. Stress #1 (GPa)	0.155
Eff. Stress #2 (GPa)	0.155
Eff. Stress #3 (GPa)	0.167
Eff. Stress #4 (GPa)	0.178
Eff. Stress #5 (GPa)	0.187
Eff. Stress #6 (GPa)	0.192
Eff. Stress #7 (GPa)	0.210
Eff. Stress #8 (GPa)	0.235
Eff. Stress #9 (GPa)	0.252
Eff. Stress #10 (GPa)	0.316
Eff. Plastic strain #1	0.0
Eff. Plastic strain #2	9e-6
Eff. Plastic strain #3	6.19e-4
Eff. Plastic strain #4	1.24e-3
Eff. Plastic strain #5	1.86e-3
Eff. Plastic strain #6	2.4e-3
Eff. Plastic strain #7	5e-3
Eff. Plastic strain #8	8.8e-3
Eff. Plastic strain #9	12e-3
Eff. Plastic strain #10	25.7e-3

---

### 4.3 Numerical Model Validation

The numerical model has been validated using experimental results of the field tests conducted at Tyndall Air Force Base, Florida by Hoemann (2007). Four FRP sandwich panels have been constructed and tested under blast effects. Table 4.3 shows the dimensions of the tested FRP panels and their inner core configurations. Four pressure gauges have been installed as shown in Figure 3.6. Table 4.4 summarizes pressure gauge locations and their main readings during the experiment.

**Table 4.3** Description of FRP panels tested by Hoemann (2007)

Panel Name	Length (m)	Width (m)	Height (mm)	Core configuration	
				No. of layers	Core shape
W1	2.60	1.80	190	1	TRW
W2	2.60	1.80	190	3	PW
W3	2.60	1.80	360	1	TRW
W4	2.60	1.80	360	6	PW

**Table 4.4** Summary of the blast pressure and impulse of the experimental tests of Hoemann (2007)

Gauge name	Location	Elevation (m)	Peak pressure (kPa)	Impulse (kPa.ms)
R1	Left-side of the Brew House	2.13	1076	2061
R2	Centre of the Brew House	2.74	1224	2434
R3	Centre of the Brew House	0.91	Defective gauge	
R4	Right-side of the Brew House	2.13	1465	2420

In the numerical model, two types of gauges are used; fixed gauges and moving gauges. Fixed gauges are attached to their coordinates and they do not move throughout the simulation, while the moving ones move with the element during the simulation. Fixed gauges are suitable for capturing the pressure readings of the model, while the moving gauges are used to capture the deflection readings. In order to capture the pressure readings, air domain is simulated with 12 m length such that fixed gauges can be assigned to track pressure in front of and behind the modeled panels. Several pressure gauges have been assigned to track pressure change along the air domain. Figure 4.2 shows the pressure time history of the numerical pressure gauge located at the wall panel centre  $[(x, y, z) = (10.7, 0.9, 1.3) \text{ m}]$  plotted with the three pressure gauge readings of the field test. The peak value of the numerical pressure is 1215 kPa which is close to the average value of the three test gauge peak pressures.

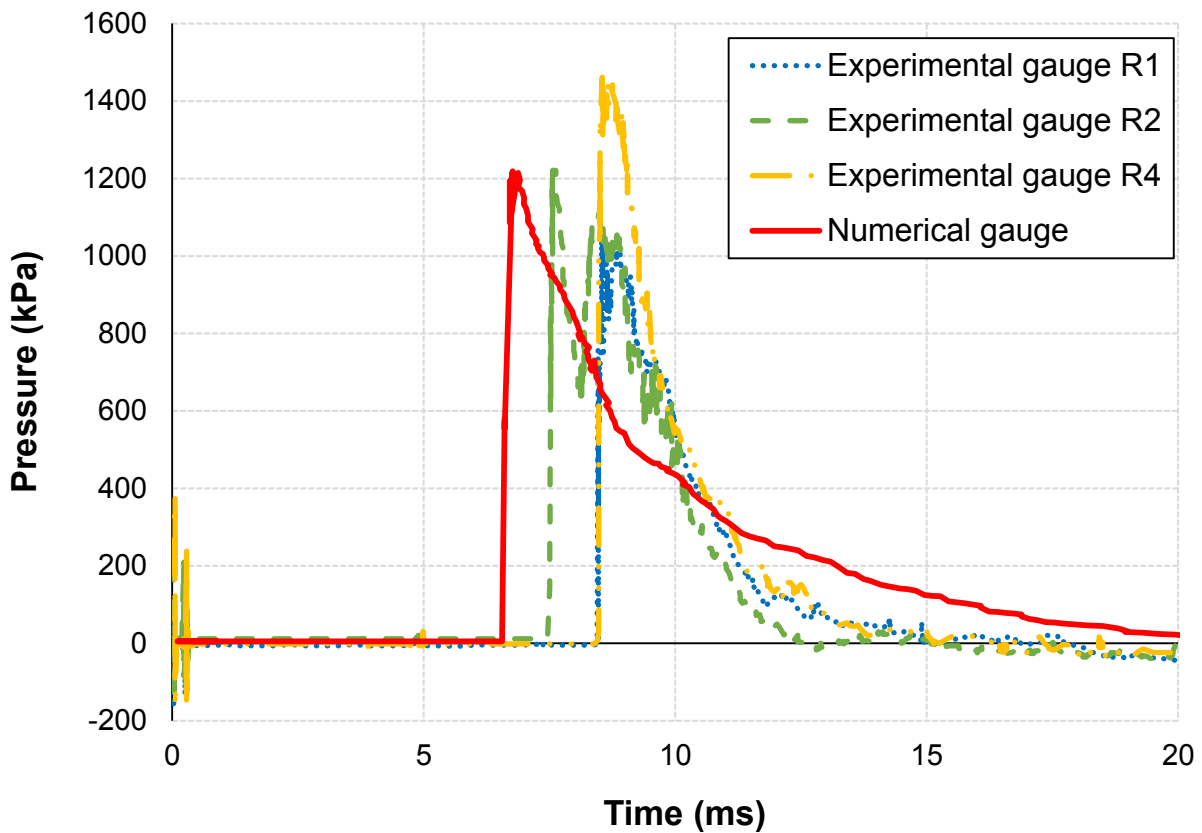


**Figure 4.2** Experimental (Hoemann, 2007) and numerical (current study) pressure time histories

### 4.3.1 Experimental and Numerical Deflections

Figures 4.3 to 4.6 show the experimental and numerical deflection time histories of the four panels considered (W1 to W4). The performance requirements of the blast resistance structures subjected to blast loads are often defined by response criteria. The response criteria considered in blast load analysis are essentially the maximum deflection of structural elements (Davidson et al., 2014) and (Dusenberry, 2010). Davalos et al. (2001), Kalny and Peterman (2005), Alagusundaramoorthy et al. (2006) and Ji et al. (2010) stated that deflection is the primary factor that controls the design of FRP panels, particularly, the deflection of back layer as it is the last shield that protects occupants from blast. In the numerical model, the panel's deflection has been determined using a moving gauge at the centre point of the back layer similar to the field tests. Table 4.5 shows the experimental and numerical peak deflections of the centre point of the panel's back layer. Figures and table show that the numerical model is able to predict the behaviour of tested panels under blast effects with a reasonable level of accuracy. The maximum deviation between experimental and numerical peak deflections of FRP panels is 18% as shown in the table. The figures show that the numerical model has been able to track the panels' behaviour with time efficiently for all panels except for panel W3. For this panel, the discrepancy between numerical and experimental deflection time histories is noticeable when the panel starts the rebound phase. This can be attributed to the fact that during the experimental test of W3, the panel has suffered an early rebound compared to other wall panels with a complete failure of the clamping anchorage joints. This major change in the panel's boundary conditions is not considered in the numerical model, where boundary conditions are assumed to remain the same during the analysis.

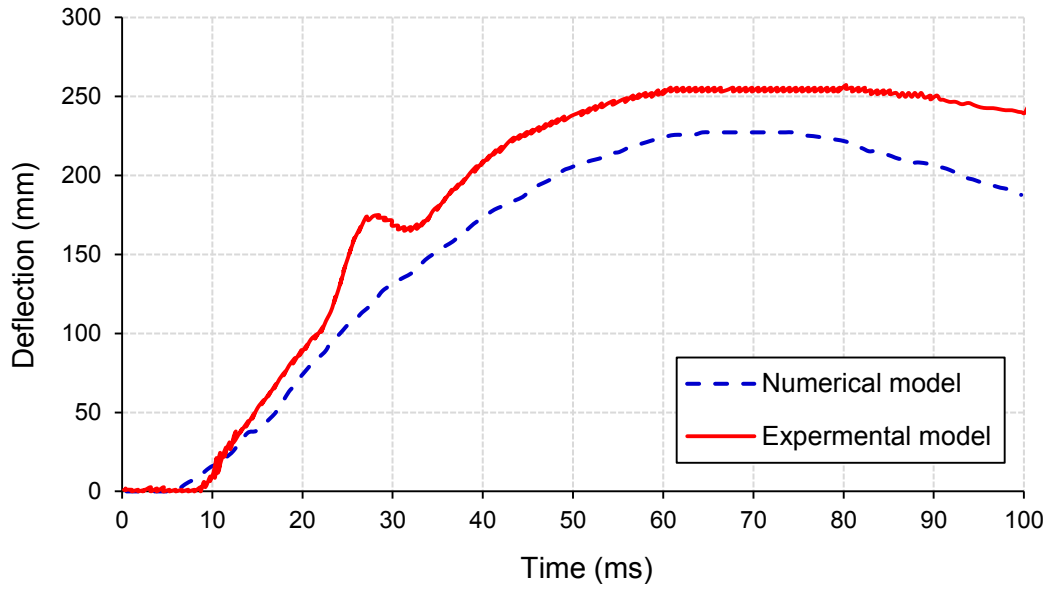


**Figure 4.3** Experimental and numerical deflection time histories for W1

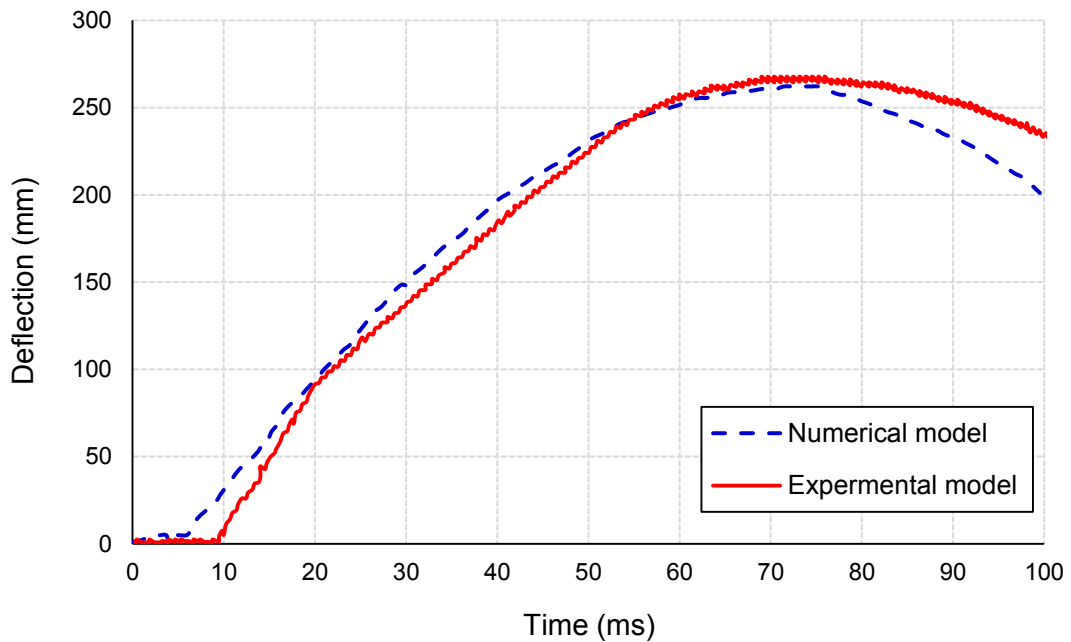


**Figure 4.4** Experimental and numerical deflection time histories for W2

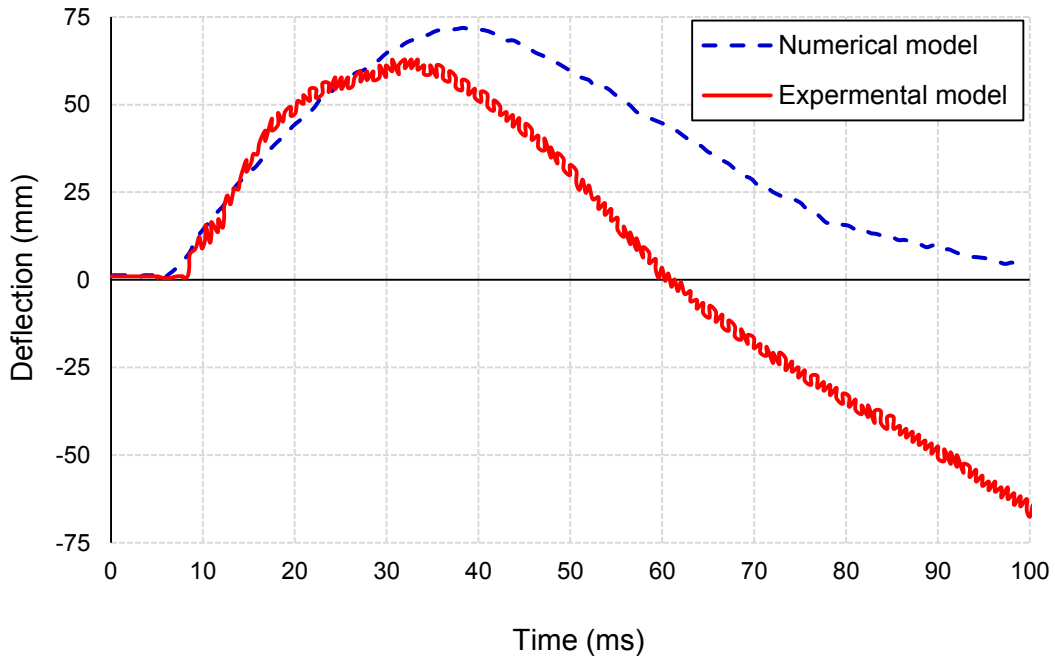


**Figure 4.5** Experimental and numerical deflection time histories for W3

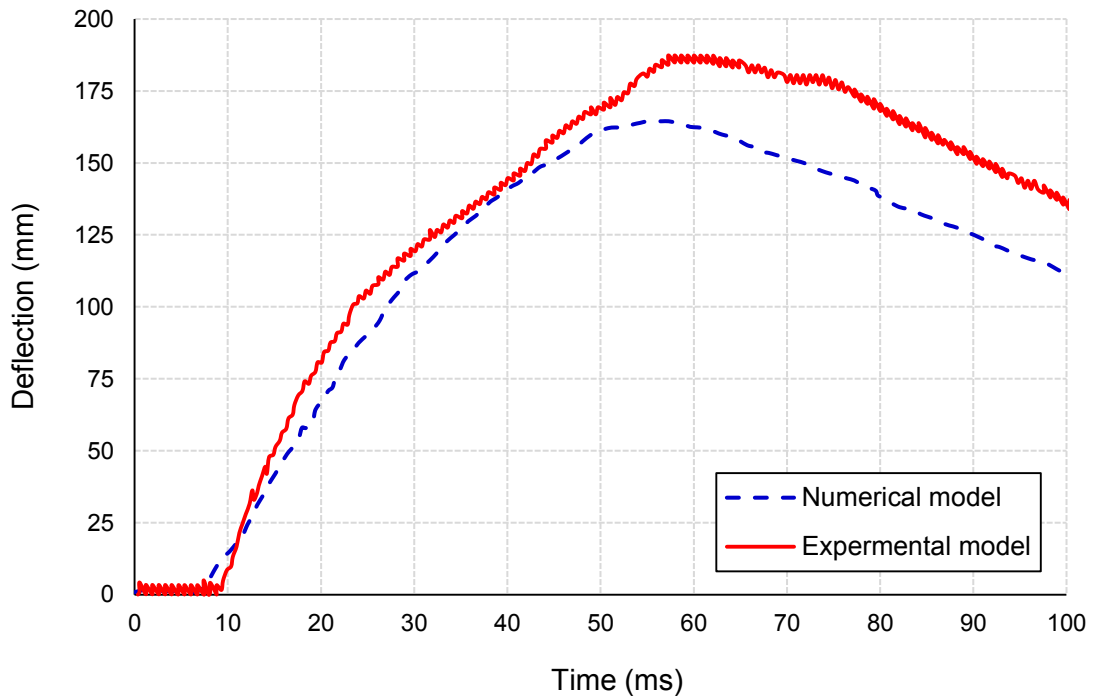


**Figure 4.6** Experimental and numerical deflection time histories for W4

**Table 4.5** The experimental (Hoemann, 2007) and numerical (current study) peak deflections

<b>Panel</b>	$\Delta_{\text{max.exp}}$ <b>(mm)</b>	$\Delta_{\text{max.Num}}$ <b>(mm)</b>	<b>% diff.</b>
W1	259	227	12
W2	269	262	3
W3	61	72	18
W4	190	163	14

### 4.3.2 Failure Modes

Figures 4.7 and 4.8 show the failure that happened in the experimental panels conducted by Hoemann (2007). The failure of the experimental panels occurred due to the shear failure of bond between the FRP layers. From the figures, it was noticed that all the panels suffered from a major bond failure except W3. While Figures 4.9 to 4.12 show the failure modes of the four panels considered in the analysis. Similar to the experimental observations, the failure of the test panels occurred due to the shear failure of bond between the FRP layers. For panel W1, the model is able to simulate complete bond failure and separation between core and outer layers as shown in the figure. While for panel W3, a partial bond failure between the front layer and the core is noticed. On the other hand, for panels W2 and W4, a complete bond failure and a separation occurs between sinusoidal and flat layers similar to what is observed during the experiment. By comparing numerical findings with experimental observations, it can be concluded that the Lagrange mesh was able to capture the level of damage occurred as well as the final failure pattern for each panel.



**Figure 4.7** Experimental panels failure of the TRW shape configuration (a) W1 and (b) W3 (Hoemann, 2007)



**Figure 4.8** Experimental panels failure of the PW shape configuration (Hoemann, 2007)

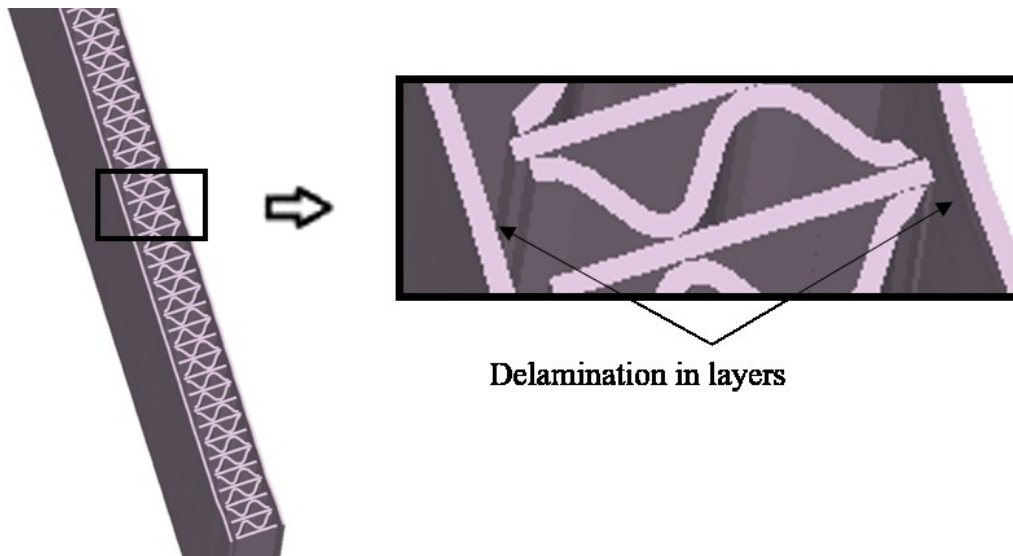


**Figure 4.9** Failure patterns of the simulated panel W1

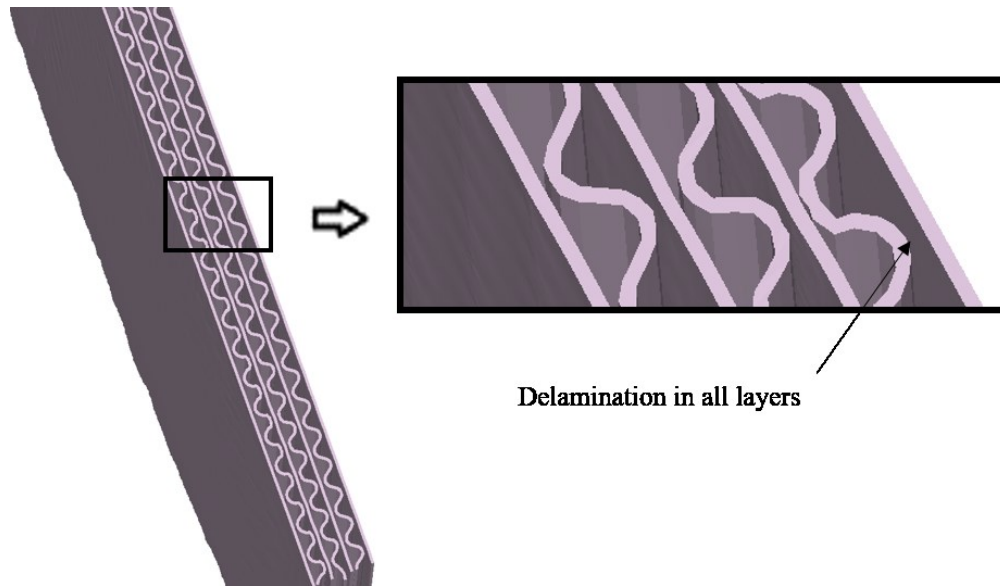


**Figure 4.10** Failure patterns of the simulated panel W2

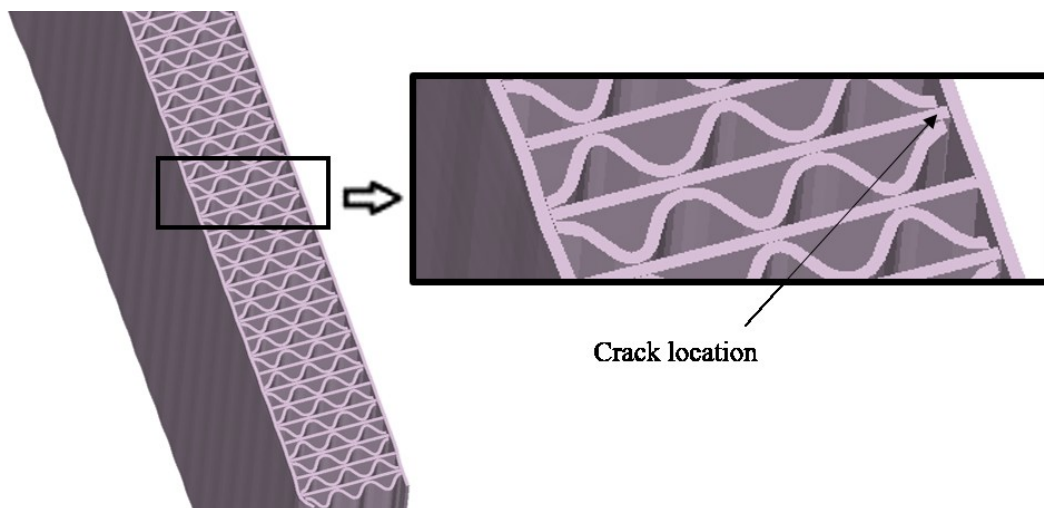


**Figure 4.11** Failure patterns of the simulated panel W3

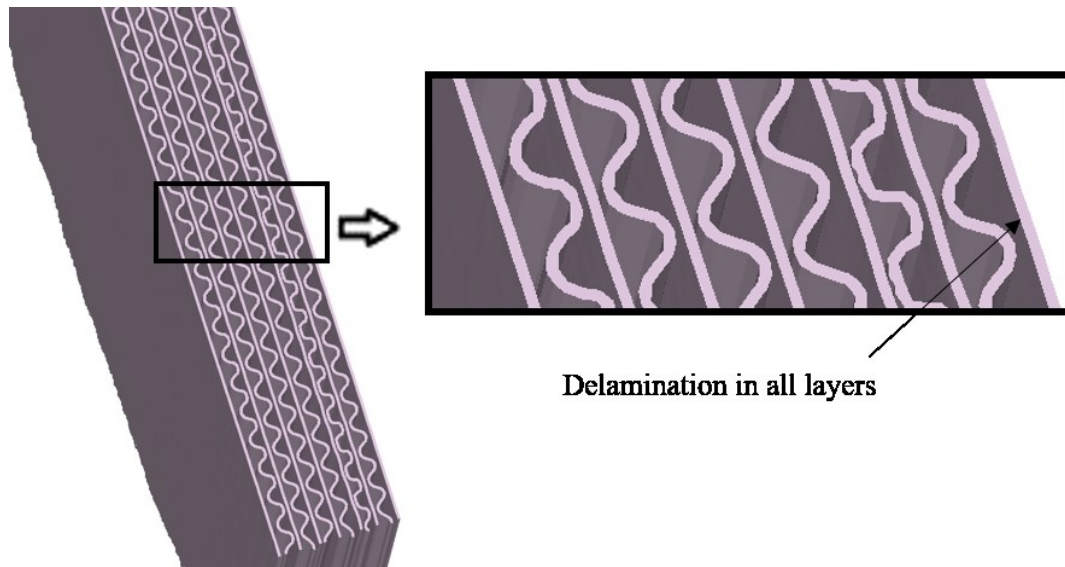


**Figure 4.12** Failure patterns of the simulated panel W4

#### **4.4 Energy Dissipation**

Due to the rapid decay of blast pressure, the blast wave transfers energy to the panels in a very short time, where the total energy will be transferred into kinetic energy. The kinetic energy reaches its peak value then starts to decay, and is transferred to internal energy. For the internal energy, upon reaching its peak value, the kinetic energy reaches its minimum value and the panel's deflection reaches its peak value. After reaching the peak deflection, the panels start to vibrate, which results in oscillating the energy between internal and kinetic energy. The response at this time is both elastic and inelastic response. The elastic strain energy will be transferred to kinetic energy, hence the internal energy is reduced until reaching its initial value. Lee and O'Toole (2004) indicated that the internal energy history can be used as the value of energy dissipation.

Energy dissipated by each component of the FRP panel has been obtained numerically and is shown in Figure 4.13. The figure highlights the contribution of suppressive layers (front layer, inner core, and back layer) in the energy dissipated by the panel as well as their percentages relative to the total energy.

From the figure, it can be noticed that the contribution of the back layer of W3 in the energy dissipation is considerable (even more than that of the front layer). This is attributed to the fact that W3 has experienced a minor damage which enables all the panel components to contribute to

the energy dissipation. On the other hand, the other panels have suffered a major level of damage which allows force and energy transfer from the core to the back layer.

It is worth noting that the energy-to-deflection ratios ( $E/\Delta$ ) of the analyzed panels are calculated as 0.88, 0.85, 1.68, and 1.64 for W1, W2, W3, and W4, respectively.  $E/\Delta$  ratio is defined as the total energy dissipated by the panel relative to the panel's maximum deflection at the centre point. The higher value of  $E/\Delta$  ratio indicates that the panel is able to absorb a higher amount of energy with less deformations and less amount of damage. Although W3 has shown the least amount of energy absorption between all panels, this panel has the highest  $E/\Delta$  ratio (which represents a smaller deflection). Therefore, in order to evaluate the performance of the FRP panels when subjected to blast loads, both deflection and  $E/\Delta$  ratio should be considered.

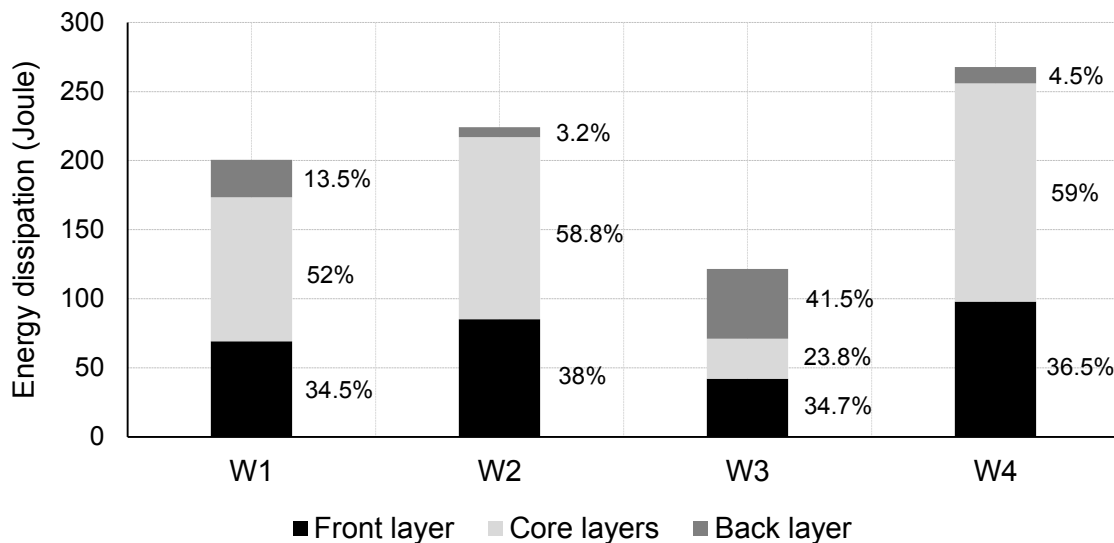


**Figure 4.13** The distribution of energy dissipated between panel components

#### 4.5 Effect of Sand Filling on the Behaviour of FRP Sandwich Panels

Figures 4.14 to 4.17 show the numerical centre point deflection time histories of the four test panels (W1 to W4) with or without sand filling. Table 4.6 illustrates the effect of sand filling on energy dissipated (ED) by the panel, maximum deflection of the panel, and the  $E/\Delta$  ratio. From the figures and the table, it can be seen that sand filling has led to a stiffer panel through the reduction of panel's maximum deformation. Adding sand to FRP panels reduces the panels' maximum deflection by up to 26% and increases the  $E/\Delta$  ratio by up to 76%. It is also noticed that

adding sand to panel W3 has not resulted in a significant enhancement in the panel's behaviour compared to other panels due to its high initial stiffness. Adding sand to other panels provides a higher shear resistance that helps delaying the shear failure of bond between the FRP layers, and thus increases energy absorption of the panels. Based on the results, it can be stated that filling FRP panels with sand material provides a damping environment that enhances the behaviour of FRP sandwich panels under blast loading. Moreover, the feasibility of using sand onsite and its cost efficiency are also two advantages of using it as a filling material.

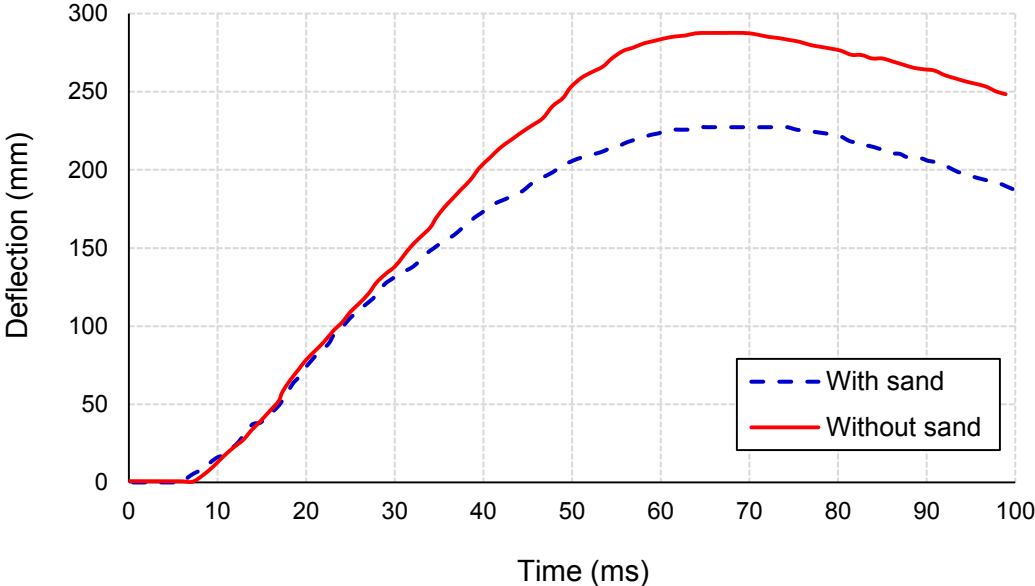


**Figure 4.14** Numerical deflection time history of W1

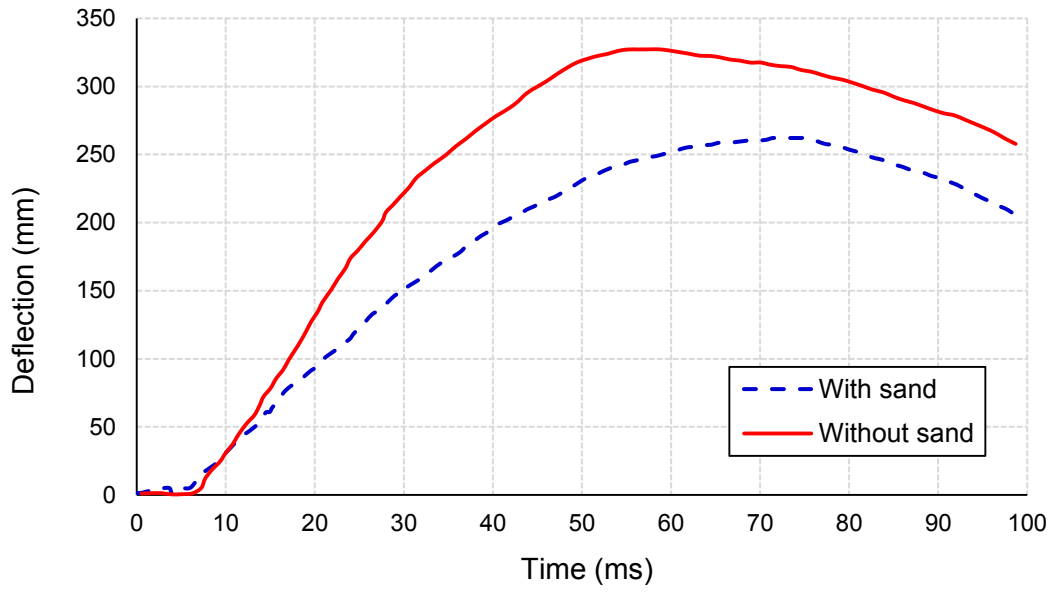


**Figure 4.15** Numerical deflection time history of W2

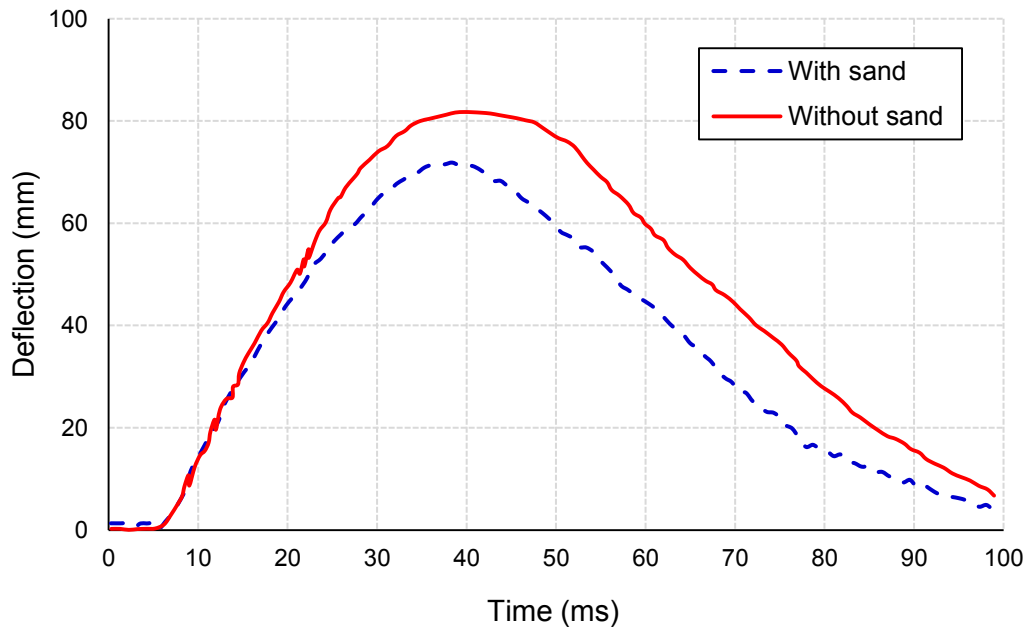


**Figure 4.16** Numerical deflection time history of W3

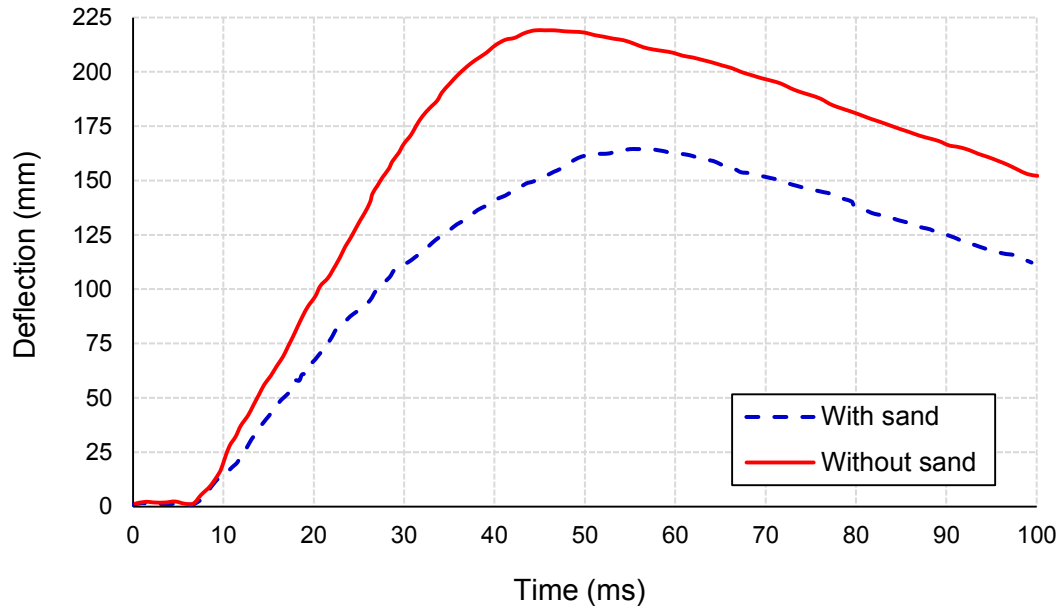


**Figure 4.17** Numerical deflection time history of W4

**Table 4.6** Effect of sand filling on panel deformations and energy dissipation

Panel	Without sand			With sand			% Difference		
	ED (J)	$\Delta_{max}$ (mm)	E/ $\Delta$	ED (J)	$\Delta_{max}$ (mm)	E/ $\Delta$	ED	$\Delta_{max}$	E/ $\Delta$
W1	164	287	0.57	200	227	0.88	22	-21	54
W2	180	328	0.55	224	262	0.85	24	-20	55
W3	103	82	1.25	121	72	1.68	17	-12	34
W4	205	219	0.93	268	163	1.64	31	-26	76

## 4.6 Proposed Core Configurations of FRP Sandwich Panels

Table 4.7 shows the description of the proposed FRP panels and their inner core configurations. Twelve panels with different inner core configurations have been proposed and analyzed. The table

shows panels' total thickness, number of core layers, and core shape used. The dimensions of the proposed panels are 1.8 m x 2.6 m similar to the experimental panels and they are categorized into three main groups. The first group includes three “thin panels” with a total thickness of 190 mm utilizing the core shapes RW, WV2-1, WV2-2 [Figure 4.1 (c-e)]. The second group includes five “thick panels” with a total thickness of 360 mm utilizing different combinations of core shapes PW and RW [Figure 4.1 (a and c)]. The third group includes four thick panels that consist of different combinations of core shapes RW, WV2-1, WV2-2. For each group, the panels are subjected to blast effect simulating experimental field test. The proposed configurations aim to enhance the behaviour of the FRP panel when subjected to blast loading through the increase of energy dissipated by the panel. The proposed configurations also intend to reduce the panel’s peak deflection which can represent the panel’s level of damage (Kalny & Peterman, 2005).

**Table 4.7** Description of the proposed FRP panels and their core configurations

Group no.	Panel name	Total thickness (mm)	Core configuration		
			No. of layers	Core shape	Thickness (mm)
1	W5	190	1	RW	$\frac{1}{2}$ T**
	W6	190	3	WV2-1	$\frac{1}{2}$ T
	W7	190	3	WV2-2	$\frac{1}{2}$ T
2	W8	360	1	RW	T
	W9	360	1	RW*	$\frac{1}{2}$ T
			3	PW	$\frac{1}{2}$ T
	W10	360	3	PW*	$\frac{1}{2}$ T
			1	RW	$\frac{1}{2}$ T
	W11	360	1	RW*	$\frac{1}{3}$ T
			2	PW	$\frac{1}{3}$ T
			1	RW	$\frac{1}{3}$ T
			2	PW*	$\frac{1}{3}$ T
			1	RW	$\frac{1}{3}$ T
W12	360	2	PW	$\frac{1}{3}$ T	
		1	RW	$\frac{1}{3}$ T	
		2	PW	$\frac{1}{3}$ T	
3	W13	360	6	WV2-1	T
	W14	360	6	WV2-2	T
	W15	360	1	RW*	$\frac{1}{3}$ T
			2	WV2-1	$\frac{1}{3}$ T
			1	RW	$\frac{1}{3}$ T
	W16	360	2	WV2-1*	$\frac{1}{3}$ T
			1	RW	$\frac{1}{3}$ T
2			WV2-1	$\frac{1}{3}$ T	

\* The first layer subjected to blast wave.

\*\* T = 340 mm.

## 4.6.1 Analysis Results

The following section presents the results of the explicit nonlinear dynamic analyses of the FRP panels with different core configurations when subjected to blast loading. Twelve FRP sandwich panels are simulated and classified into three main groups. The first group includes thin panels that are 190 mm thick, while the second and the third groups include thick panels that are 360 mm thick. The numerical modelling of the experimental test panels shows that, for thin panels, panel W1 has a higher energy-to-deflection ratio ( $E/\Delta$ ) than W2. Therefore, the behaviour of proposed FRP thin panels (Group 1) is compared to that of W1. Similarly, the behaviour of proposed thick panels (Groups 2 and 3) is compared to that of W3.

### 4.6.1.1 Numerical Results of Group 1

Figure 4.18 shows the time history of the central point deflection of the FRP panels of Group 1 along with the simulated test panels W1 and W2. Table 4.8 shows energy dissipated by the panels, panels' peak deflections, and energy-to-deflection ratios. In reference to Figure 4.18 and Table 4.8, it can be noted that panel W5 (with RW axis core configuration) has the same performance as W1 (TRW axis core configuration) with no enhancement in the behaviour. However, woven shapes represented by W6 and W7 show an enhancement in energy-to-deflection ratio by almost 24% compared to W1 (considering that W7 uses 33% more FRP material). Such minor enhancement can be attributed to the failure mode of the simulated panels of this group which is a complete bond failure between FRP layers. This high level of damage indicates that small thickness of these panels is insufficient to resist the blast level considered in this study.

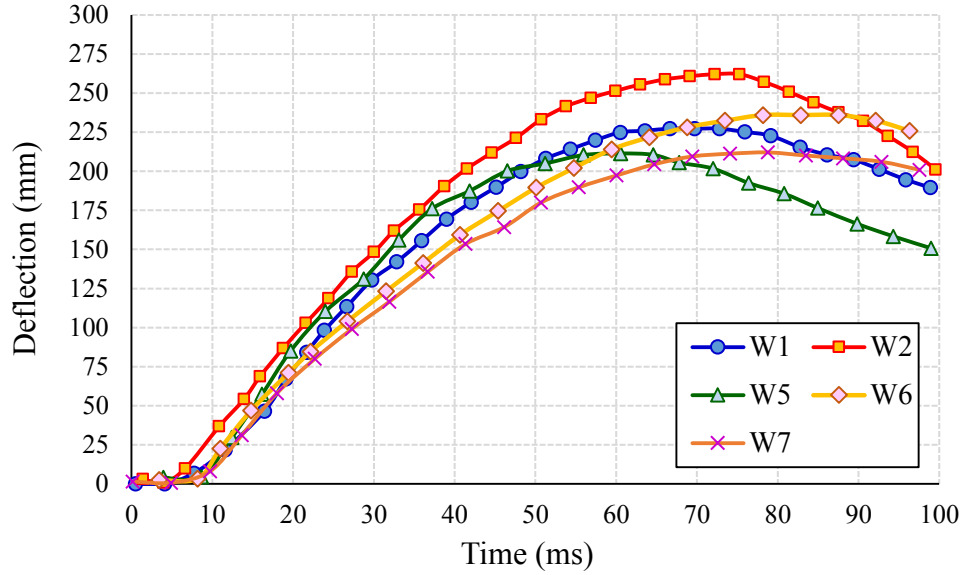


**Figure 4.18** Central point deflection time histories of Group 1

**Table 4.8** Panel peak deflection and energy dissipation for Group 1

Panel	ED (J)	$\Delta_{\max}$ (mm)	E/ $\Delta$	% E/ $\Delta$
W1	200	227	0.88	-
W5	182	210	0.87	-1
W6	258	236	1.09	24
W7	298	209	1.43	63

#### 4.6.1.2 Numerical Results of Group 2

Figure 4.19 and Table 4.9 illustrate the analysis results for the second group along with the simulated test panels W3 and W4. It is found that panel W8 (with RW axis core configuration) has the same behaviour as test panel W3 (TRW axis core configuration) which has been noticed earlier for Group 1. For other core configurations, panels W11 and W12 show the highest values of E/ $\Delta$  ratio within the group with an enhancement of up to 70% compared to W3. These panels dissipate up to 125% more energy compared to W3 accompanied by an increase in the panel's deflection by

up to 31%. Except for W8, the panels of this group exhibit a partial bond failure within the layers of the weak PW axis core.

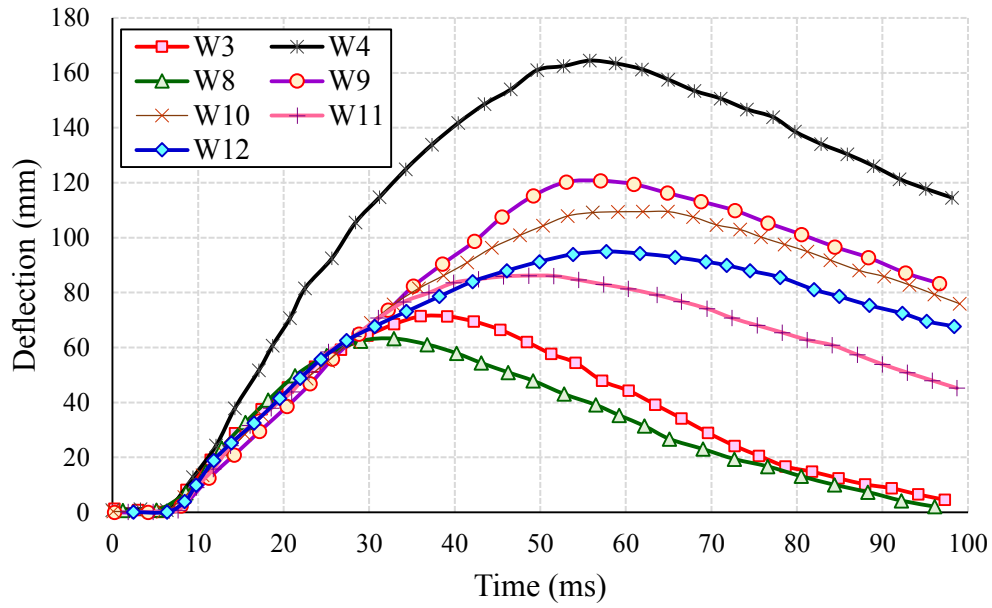


**Figure 4.19** Central point deflection time histories of Group 2

**Table 4.9** Panel peak deflection and energy dissipation for Group 2

Panel	ED (J)	$\Delta_{max}$ (mm)	E/ $\Delta$	% E/ $\Delta$
W3	121	72	1.68	-
W8	105	61	1.72	2
W9	257	121	2.12	25
W10	248	109	2.27	34
W11	236	86	2.74	62
W12	273	95	2.87	70

### 4.6.1.3 Numerical Results of Group 3

Figure 4.20 and Table 4.10 illustrate the analysis results of the third group along with the simulated test panels W3 and W4. Results indicate that a significant enhancement in the behaviour of FRP panels is achieved when woven shapes WV2-1 and WV2-2 are used. Panel W13 with the shape WV2-1 has been able to dissipate 113% more energy compared to W3 with a 5% more deflection only. Combining woven shape WV2-1 and RW axis (in W15 and W16) has resulted in a superior performance compared to the test panel W3. These panels are able to dissipate 111% more energy compared to W3 with even less deformations. Although using woven shape WV2-2 (panel W14) has resulted in the highest energy-to-deflection ratio (which represents the best behaviour among all panels), this core configuration uses about 33% more FRP material compared to other configurations. In addition, the difficulty associated with manufacturing this shape makes woven shape WV2-1 more practical and economical to use. Therefore, W16 can be considered to have the best performance among the thick panels (Groups 2 and 3) with the most effective utilization of FRP material.

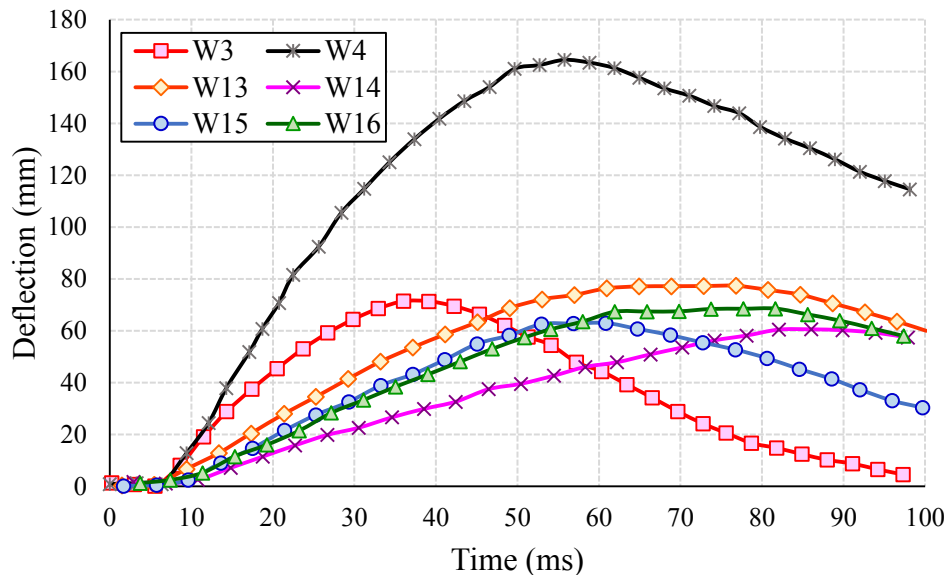


Figure 4.20 Central point deflection time histories of Group 3

**Table 4.10** Panel peak deflection and energy dissipation for Group 3

<b>Panel</b>	<b>ED (J)</b>	<b><math>\Delta_{\max}</math> (mm)</b>	<b>E/<math>\Delta</math></b>	<b>% E/<math>\Delta</math></b>
W3	121	72	1.68	-
W13	258	76	3.39	102
W14	298	60	4.97	196
W15	217	62	3.5	108
W16	256	67	3.8	126

#### 4.6.2 Failure Modes

Failure that has happened is due to shear failure of bond between FRP layers. Figure 4.21 shows failure mode of W5 and W8 with RW axis core configuration. It is noticed that the failure in the panel with this configuration is similar to what happened with the experimental panels W1 and W3 with TRW axis core configuration. For panel W5, a complete bond failure and a separation occurred between the core and the outer layers. While for panel W8, a partial bond failure between the front layer and the core is noticed at the edges at the maximum shear. Figure 4.22 shows the failure mode of W6 and W13 with the core configuration of woven shape WV2-1. For panel W6, a complete bond failure and separation occurred between sinusoidal strips and flat layers. While for panel W13, a bond failure has occurred between few nodes of sinusoidal strips and flat layers, especially in the nodes at the edges.

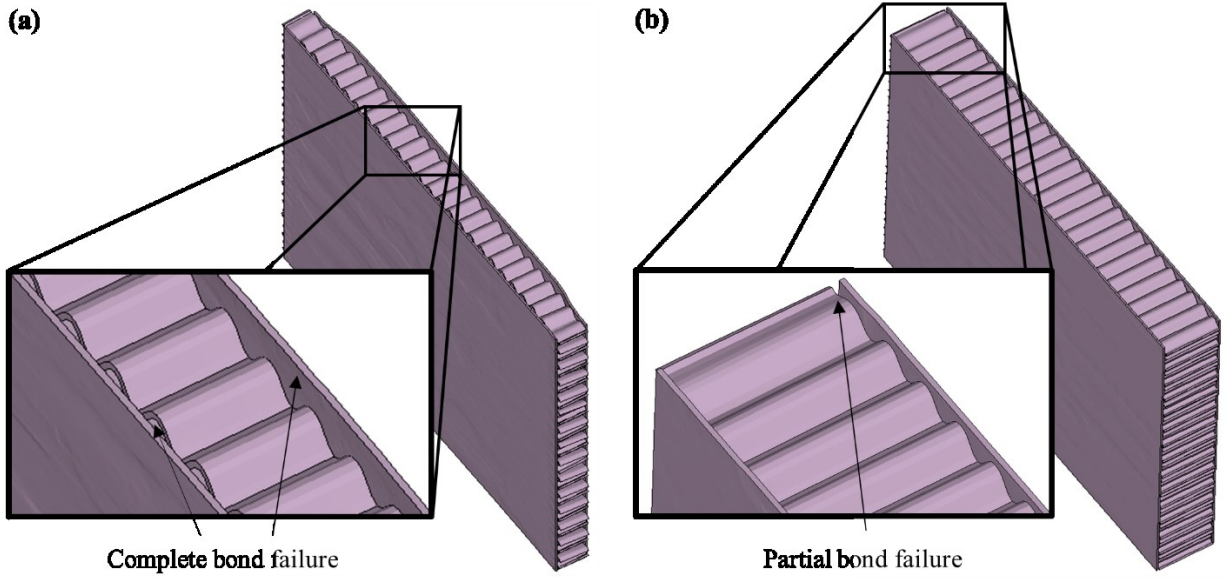


Figure 4.21 Failure patterns of RW panels (a) W5, and (b) W8

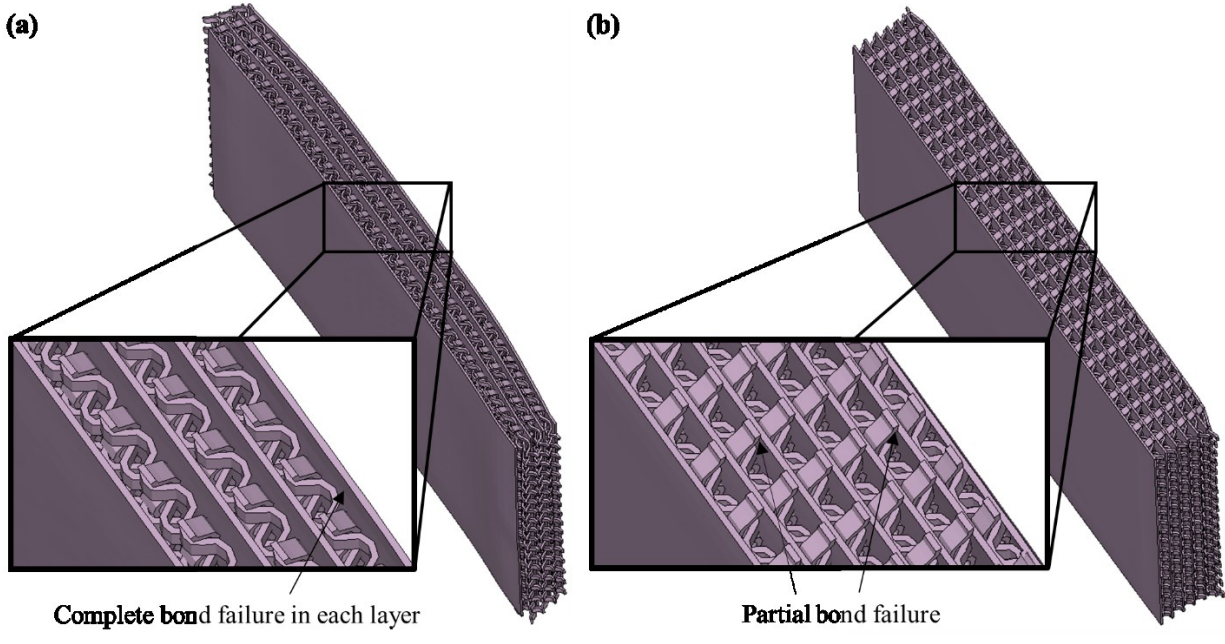
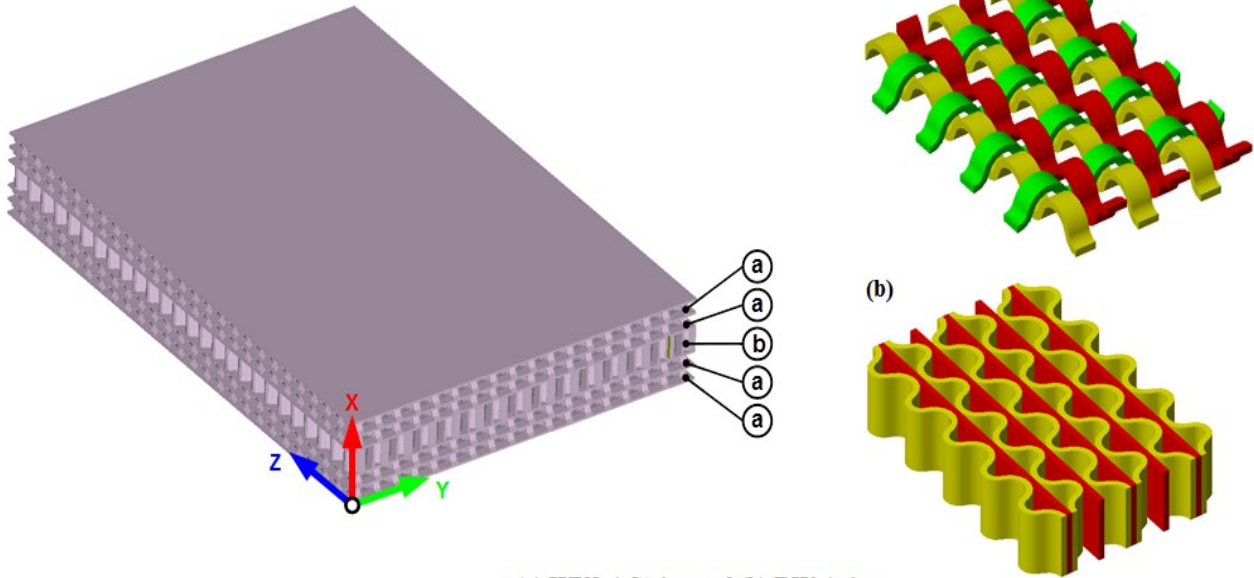


Figure 4.22 Failure patterns of WV2-1 panels (a) W6, and (b) W13

## 4.7 Parametric Study

From the twelve FRP sandwich panels, W16 has been chosen for parametric study application. This is due to the fact that W16 provides the best enhancement of FRP Panels' behaviour among all of the twelve panels. As shown in Figure 5.11, peak deflection of the proposed panel W16 is 67 mm reduced by 7% comparing to W3. Besides, an increased arrival time of peak deflection has been achieved. Whereas, under same conditions, it is noticed that energy dissipation of W16 is 256J; 111% increase and 4% decrease have been realized compared to W3 and W4, respectively. Therefore, W5 gets the advantage of having low-peak deflection as W3 and high-energy absorption as W4. W16 is formed of a new inner core configuration, which is formulated from a combination of woven and honeycomb shapes. In order to compare analyzed results, the same amount of FRP material used in W3 and W4 has been maintained. Also, modeled FRP panel has the same dimension and has been filled with sand as thick panels (W3 and W4). Sinusoidal core layers similar to the layers used in experimental panels (W1 to W4) form the inner core configuration. Sinusoidal core layers are used as layers for honeycomb shape or cutting strips for woven shape. Figure 4.23 illustrates FRP sandwich panel with the two main inner core configurations considered, woven and honeycomb shapes. Configuration (a) consists of perpendicularly interlaced strips that form the woven shape. “WV2-1 strips” represent Configuration (a). It consists of two strips from the sinusoidal layer in the longitudinal direction and one fill from the sinusoidal strip in the transverse direction. On the other hand, configuration (b) –represented by “RW axis”– is formed of sinusoidal layers that are separated by flat layers in between, forming a honeycomb shape. Inner core configurations are formed of four layers of WV2-1 and one layer of RW. Each two layers are separated with a flat layer. These four layers are divided into two layers at the top (TL) of 110 mm total thickness and other two layers at the bottom (BL) with the same total thickness. In between the TL and BL, the RW layer is placed with a thickness of 120 mm.

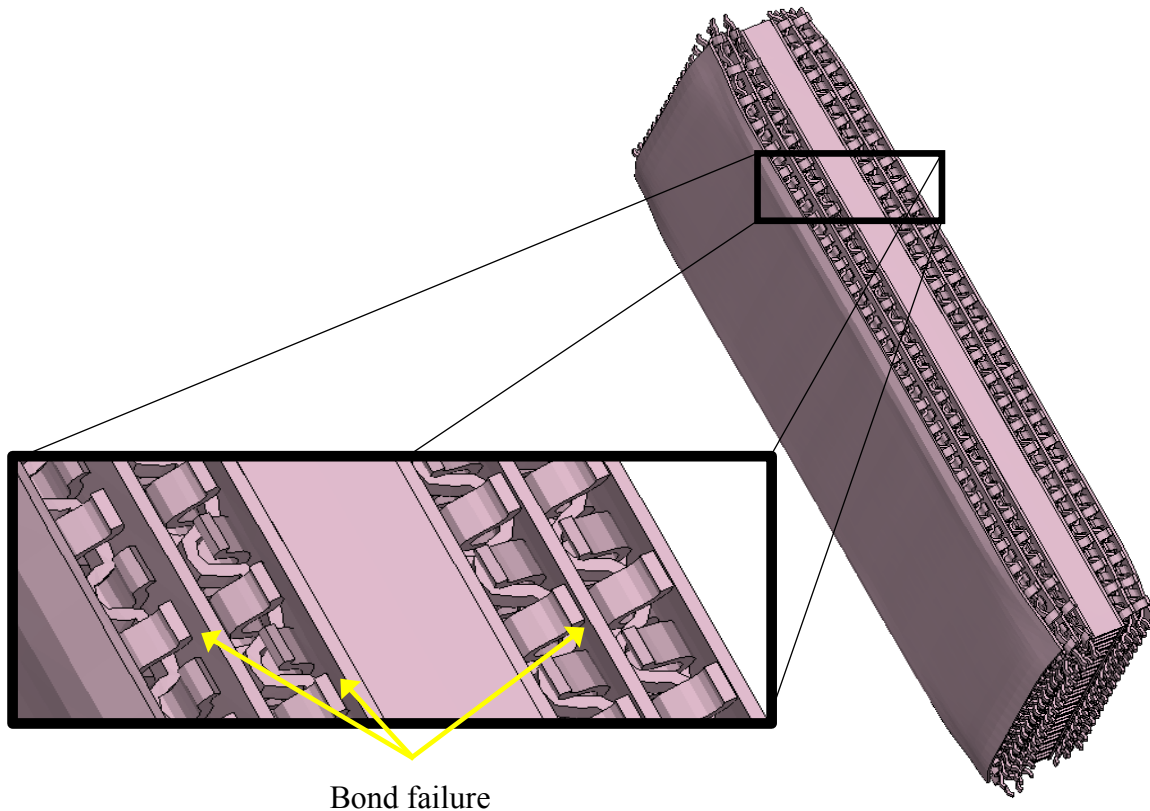
FRP Sandwich Panel



(a) WV2-1 Strips and (b) RW Axis

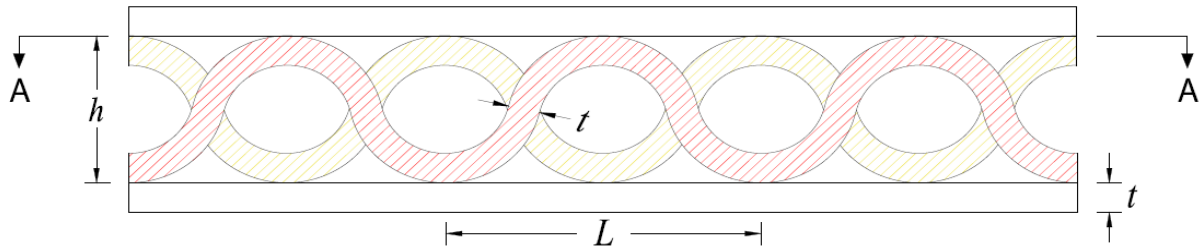
Figure 4.23 Inner core configurations of W16; (a) WV2-1 Strips and (b) RW Axis

Figure 4.24 shows the failure mode of W16. Failure that has happened in the panel is due to shear failure of bond between FRP layers. For WV2-1 layers, a complete bond failure has occurred between few nodes of sinusoidal strips and flat layers, especially in nodes at the edges. As for RW layer, a partial bond failure between the flat layer and the core has been noticed.



**Figure 4.24** Failure pattern of the proposed panel W16

Parametric analysis has been carried out on WV2-1 layers to better understand the performance of the proposed FRP panel against blast loads. During the study, the effect of changing parameters on energy dissipated by the panel, the maximum panel deflection, the maximum chord rotation, and the energy-to-deflection ratio ( $E/\Delta$ ) have been studied. The higher value of  $E/\Delta$  ratio is an indication for the panel's capability of absorbing a higher amount of energy with less deformations and less amount of damage. Figure 4.25 shows schematics of elevation and cross section of WV2-1 strips, where  $t$  is the thickness of sinusoidal and flat layers,  $h$  is the height of sinusoidal layer,  $L$  represents a single sinusoidal wave length, and  $W$  is the width of one strip. It is worth mentioning that W5 has the same sinusoidal and flat layers' dimensions and amount of material—as the thick experimental panels. Accordingly, all results obtained from the other analyzed panels and the amount of used materials are compared with W16.



Elevation



Section A-A

Figure 4.25 Woven core sandwich panel schematic

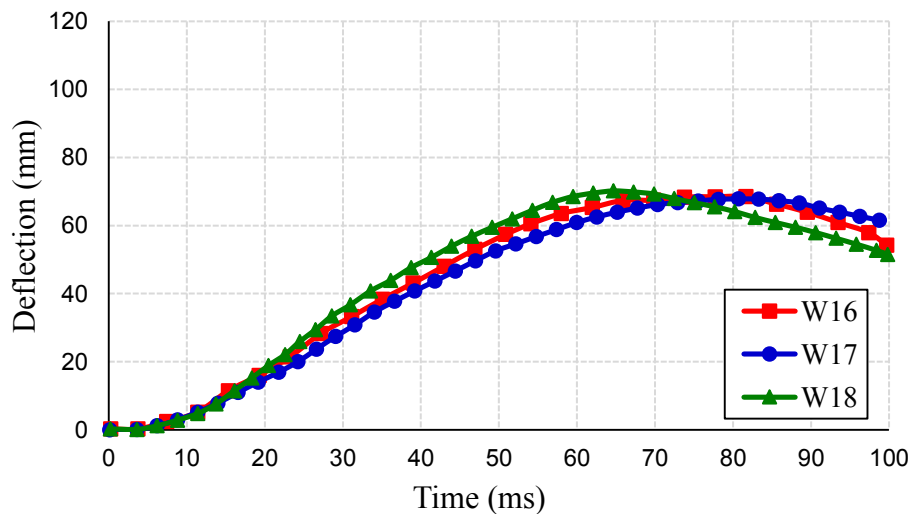
#### 4.7.1 Effect of Changing Length, Width and Height

Table 4.11 illustrates the effect of changing the layers' height ( $h$ ), wave length ( $L$ ), and the strip's width ( $W$ ) on panel's performance. Accordingly, Figures 4.26, 4.27, and 4.28 show the time history of FRP panels' central point deflection with the changed parameters. In the study, nine panels including W5 have been studied. The three different heights ( $h$ ) considered in this study are 50, 30, and 110 mm. In order to maintain the total thickness of TL and BL constant equals to 110 mm, the change in height is always associated with a change in number of layers. The increase/decrease in the material weight (% Mass) –as a result of dimensions' change– is illustrated in the table. “No. of layers” column represents the total number of layers in both TL and BL. As listed in the table, the decrease in the height leads to better performance, as the energy dissipation increases by up to 25%, and panels' peak deflection decreases by up to 13.4%. Moreover, the decrease in wave length slightly enhances the panels' performance. Comparing W17 with W16,

W20 with W19, and W23 with W22, energy dissipation increases by 2.7%, 2.9%, and 6.9%, respectively. However, the panels' peak deflection decreases by 1.5%, 3.3%, and 7.3%, respectively. The comparison between these panels is only for guidance as the nine analyzed panels have different weights of material.

**Table 4.11** Effect of length, width, and height variations

Panel	h (mm)	L (mm)	W (mm)	t (mm)	No. of layers	% Mass	ED (J)	$\Delta_{max}$ (mm)	$\theta_{max}$ (degree)	E/ $\Delta$	% E/ $\Delta$
W16	50	100	33	10	4	-	256	67	2.95	3.82	-
W17		80	24			+6.4	263	66	2.91	3.98	+4.2
W18		120	40			-6.6	249	69	3.04	3.61	-5.5
W19	30	100	33		6	+42.8	311	60	2.64	5.18	+35.6
W20		80	24			+44.2	320	58	2.56	5.52	+44.5
W21		120	40			+39.7	299	62	2.73	4.82	+26.2
W22	110	100	33		2	-37.3	203	96	4.23	2.11	-44.8
W23		80	24			-27.0	217	89	3.92	2.44	-36.1
W24		120	40			-47.5	184	103	4.54	1.79	-53.1



**Figure 4.26** Central point deflection time histories with changed parameters and h=50 mm

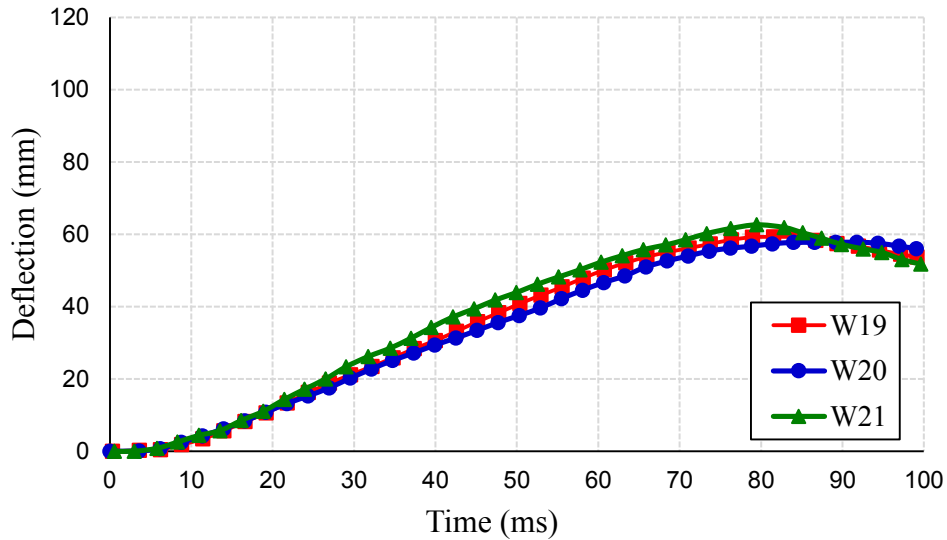


**Figure 4.27** Central point deflection time histories with changed parameters and  $h=30$  mm

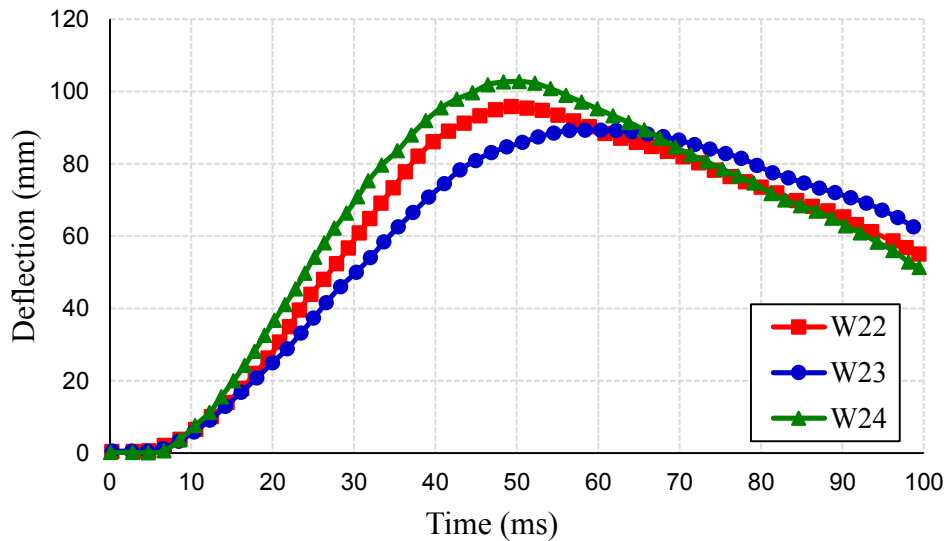


**Figure 4.28** Central point deflection time histories with changed parameters and  $h=110$  mm

#### 4.7.2 Effect of Thickness

The effect of changing layers' thickness ( $t$ ) on the panel's performance is illustrated in Table 4.12. Figures 4.29 and 4.30 show the time history of the central point deflection of W16 and W19 with different thickness. W16 and W19 panels are analyzed under four different thickness values: 10, 9, 8, and 7 mm. From the analyses, it is found that the decrease in thickness of simulated panels has no effect on energy dissipation. Upon changing each of the panel's thickness, a maximum of

0.8% variation is obtained. On the other hand, changing thickness significantly affects the panels' peak deflection, where a difference of up to 19.4% is obtained. Moreover, when comparing the material weight used in the simulated panels (% Mass) with changing energy-to-deflection ratio (% E/ $\Delta$ ), the analyses show an interesting behaviour of the panels. For instance, upon decreasing the material weight of W16 by 27.8%, the energy-to-deflection ratio decreases to 16.5% only. Regarding W19, the energy-to-deflection ratio is reduced to 13.5% upon decreasing the material weight by 28.2%. Additionally, when comparing the structural behaviour of W16 and W19 (with  $t = 7$  mm), the energy-to-deflection ratio of the latter panel is increased by 17.3%; although both panels almost have the same material weight. Therefore, decreasing thickness enhances panels' performance. This is due to the failure in the bond between FRP layers that has occurred in the simulated panels. Therefore, it could be said that the structural behaviour is not affected by decreasing the thickness of used panels the same way as much as it is affected by number of bonds contacts and number of layers.

**Table 4.12** Effect of thickness variations

Panel	h (mm)	L (mm)	W (mm)	t (mm)	No. of layers	% Mass	ED (J)	$\Delta_{max}$ (mm)	$\theta_{max}$ (degree)	E/ $\Delta$	% E/ $\Delta$
W16	50	100	33	10	4	-	256	67	2.95	3.82	-
					9	-8.8	257	72	3.17	3.57	-6.5
					8	-18.2	254	76	3.35	3.34	-12.6
					7	-27.8	255	80	3.52	3.19	-16.5
W19	30	100	33	10	6	+42.8	311	60	2.64	5.18	+35.6
					9	+29.8	309	64	2.82	4.83	+26.4
					8	+16.3	310	66	2.91	4.70	+23.0
					7	+2.5	309	69	3.04	4.48	+17.3

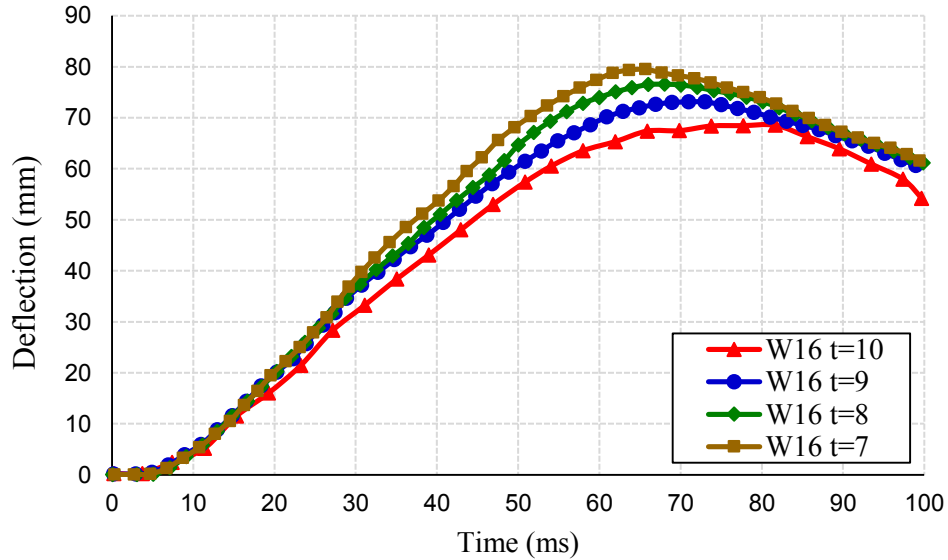


**Figure 4.29** Central point deflection time histories of W16 with different thickness

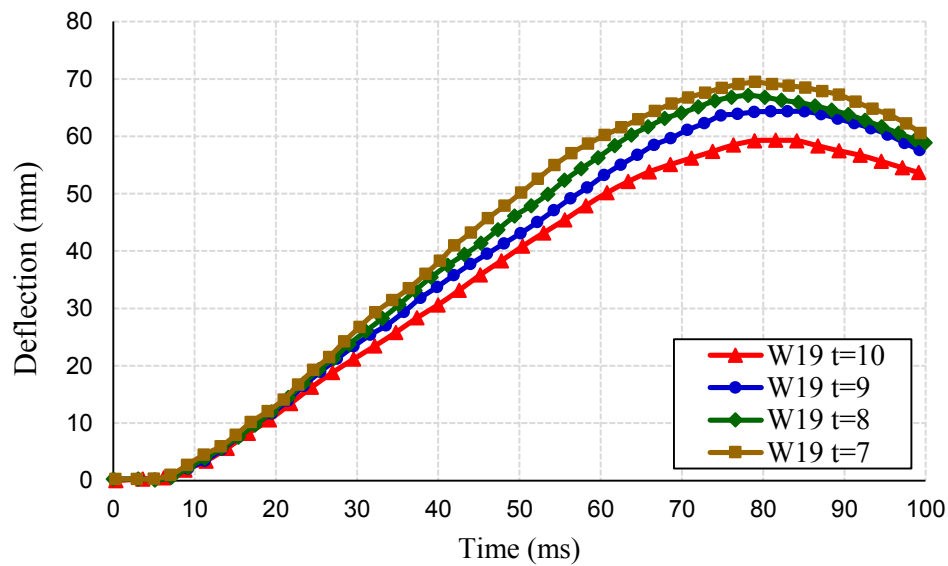


**Figure 4.30** Central point deflection time histories of W19 with different thickness

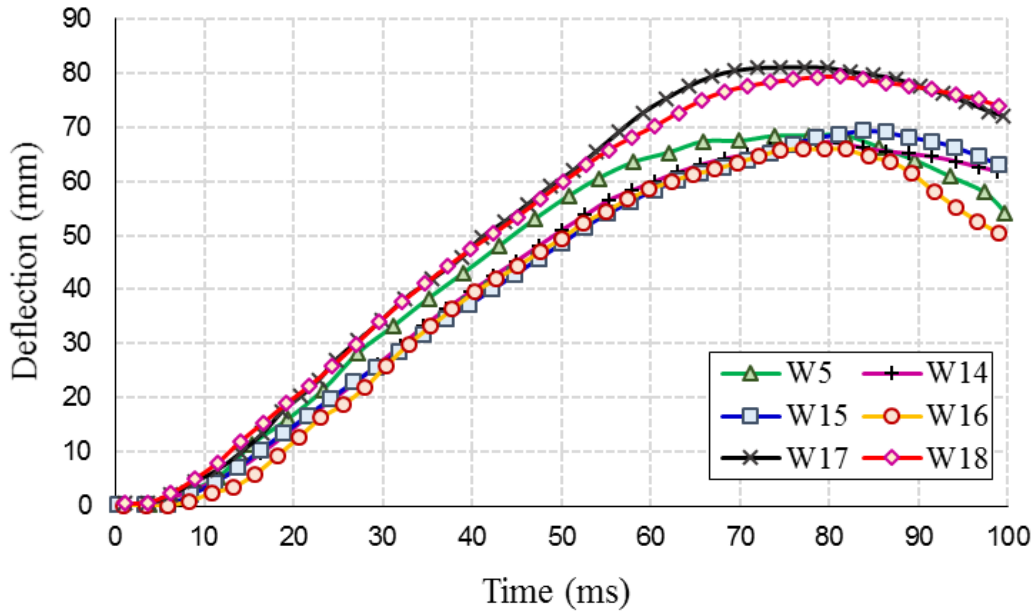
### 4.7.3 Constant Weight

Table 4.13 and Figure 4.31 illustrate the effect of changing dimensions of sinusoidal and flat layers on the panel's performance while keeping the material weight constant. Six panels including W5 have been studied. As shown in the table, three different heights ( $h$ ) have been used for each two panels. The heights used are 50, 30, and 110 mm, respectively. As for the wave lengths ( $L$ ), 100 and 80 mm are used across the three different wave heights mentioned. This means that each

two waves of the same height are once tested using a 100 mm wave length and once using an 80 mm wave length. In order to maintain the same material weight, strip width (W) and layers' thickness (t) are changeable. Panels that have been tested with 30 mm height (W26 and W27) have resulted in a superior performance compared to panel W16. Increasing number of layers while decreasing layers' thickness (t) in W26 has increased energy dissipation by 20.3% and panels' peak deflection by 2.9 %. Relatively, energy-to-deflection ratio increases by 16.7%. On the other hand, in W27, energy dissipation has increased by 24.2% and panels' peak deflection has decreased by 1.5%. Accordingly, the energy-to-deflection ratio has increased by 26.2%. This is attributed to the decrease in layers' heights that has increased number of layers and, by default, number of bonds contacts for W26 and W27. Also, the decrease in wave length (L) has resulted in increasing the number of bonds contacts when comparing W27 with W26. Therefore, W27 shows better results than W26 and all other panels.

**Table 4.13** Effect of changing sinusoidal dimensions with constant weight

Panel	h (mm)	L (mm)	W (mm)	t (mm)	No. of layers	ED (J)	$\Delta_{max}$ (mm)	$\theta_{max}$ (degree)	E/ $\Delta$	% E/ $\Delta$
W16	50	100	33	10	4	256	67	2.95	3.82	-
W25		80	23	10		261	66	2.91	3.95	+3.4
W26	30	100	33	6.8	6	308	69	3.04	4.46	+16.7
W27		80	23	6.8		318	66	2.91	4.82	+26.2
W28	110	100	36	15	2	192	81	3.57	2.37	-38.0
W29		80	25	13.8		220	79	3.48	2.78	-27.2



**Figure 4.31** Central point deflection time histories of panels with constant weight

#### 4.7.4 Effect of Wave Peak Length

Figure 4.32 shows schematics of WV2-1 strips with wave peak length  $\geq 0$ . Wave peak length represented by (b) is changed to investigate its effect on panel's performance. W16, W26, and W27 panels with the same material weight are analyzed under different wave peak length values. For W16, seven panels are studied where the wave peak length has been increased by 5 mm increments ranging in length from 0 to 30 mm; whereas for W26, five panels are studied where the wave peak length has been increased by 5 mm increments ranging in length from 0 to 20 mm. Finally, for W27, seven panels are studied where the wave peak length has been increased by 2.5 mm increments ranging in length from 0 to 15 mm. As the maximum value of wave peak length that can be reached is controlled by keeping strip layers contactless –strips are jointed only with flat layers– it is understood that the maximum peak wave length varies for each of the three studied panels. This means that maximum peak wave length for W16, W26, and W27 is 30, 20, and 15 mm, respectively.

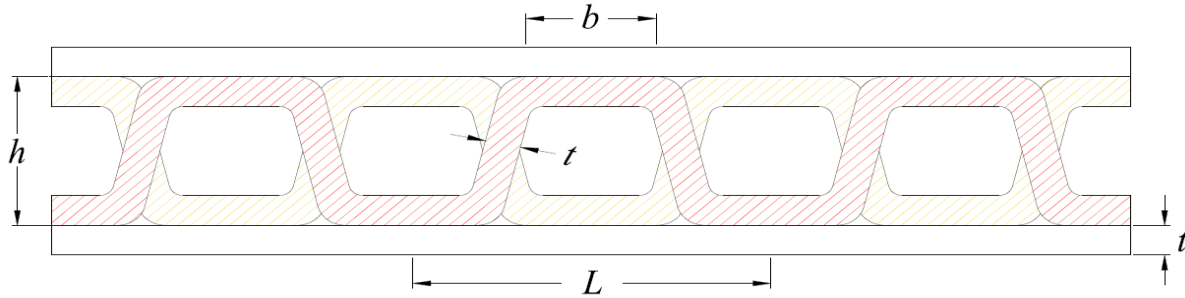


**Figure 4.32** Schematic of a woven core sandwich panel with wave peak length  $\geq 0$

Figure 4.33 and Table 4.14 demonstrates the effect of changing wave peak length on energy-to-deflection ratio for W16, W26, and W27 panels. From the figure, it is shown that on increasing wave peak length, energy-to-deflection rotation ratio increases until it reaches the peak value then decreases gradually. For the three studied panels, reaching the peak wave length differs from one panel to another. For W16, the maximum energy-to-deflection ratio is reached at wave peak length of 20 mm. Comparing the increase in  $E/\Delta$  ratio of changing the wave peak length from 0 to 20 mm, the  $E/\Delta$  ratio increases by 12.0%. As for W26, the maximum energy-to-deflection ratio is at wave peak length of 15 mm. Comparing the increase in  $E/\Delta$  ratio of changing the wave peak length from 0 to 15 mm, the  $E/\Delta$  ratio increases by 8.1%. Finally for W27, the maximum energy-to-deflection ratio is at wave peak length of 10 mm. Comparing the increase in  $E/\Delta$  ratio of changing the wave peak length from 0 to 10 mm, the  $E/\Delta$  ratio increases by 5.6%. This is attributed to the bond failure between FRP layers in simulated panels. As a result, the increase in wave peak length increases bonding area which in return increases the panels' performance. A new comparison is conducted after obtaining the best results from the above mentioned analyses. The comparison is between W16 (with  $b = 0$ ) which has the same sinusoidal and flat layers' dimensions as the experimental panels and W27 (with  $b = 10$  mm) which has obtained the best results. As a result, the  $E/\Delta$  ratio has increased by 34.3%.

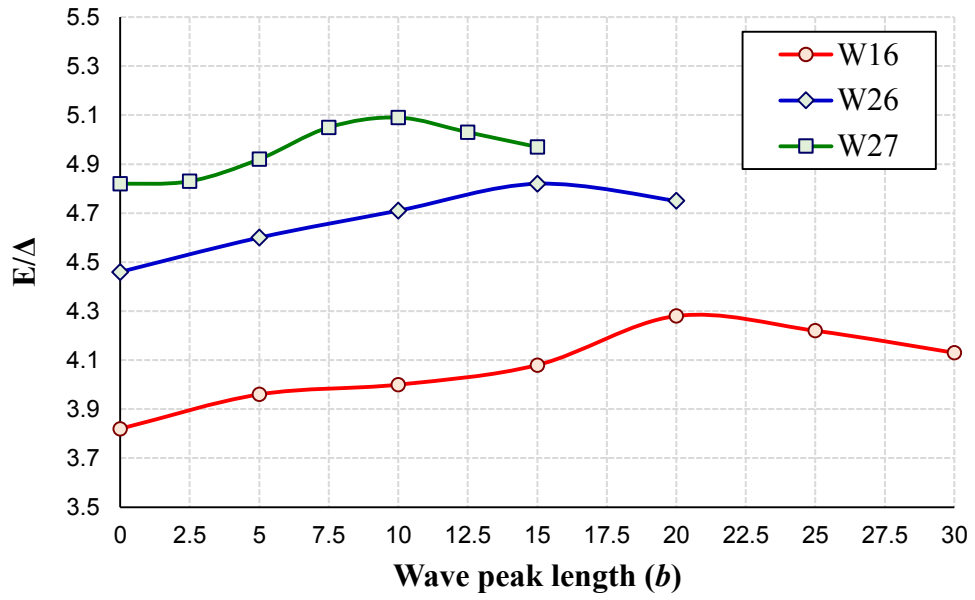


Figure 4.33 Effect of peak length variations

**Table 4.14** Effect of changing wave peak length

<b>Panel</b>	<b>h (mm)</b>	<b>L (mm)</b>	<b>W (mm)</b>	<b>t (mm)</b>	<b>b (mm)</b>	<b>No. of layers</b>	<b>ED (J)</b>	<b><math>\Delta_{\max}</math> (mm)</b>	<b><math>\theta_{\max}</math> (degree)</b>	<b>E/<math>\Delta</math></b>	<b>% E/<math>\Delta</math></b>	
W16	50	100	33	10	0	4	256	67	2.95	3.82	-	
							5	265	67	2.95	3.96	3.7
							10	264	66	2.91	4.00	4.7
							15	269	66	2.91	4.08	6.8
							20	274	64	2.82	4.28	12.0
							25	270	64	2.82	4.22	10.5
30	260	63	2.73	4.13	8.1							
W26	30	100	33	6.8	0	6	308	69	3.04	4.46	-	
							5	313	68	3.00	4.60	3.1
							10	320	68	3.00	4.71	5.6
							15	323	67	2.95	4.82	8.1
							20	318	67	2.95	4.75	6.5
W27	30	80	23	6.8	0	6	318	66	2.91	4.82	-	
							2.5	319	66	2.91	4.83	0.2
							5	325	66	2.91	4.92	2.1
							7.5	328	65	2.86	5.05	4.8
							10	331	65	2.86	5.09	5.6
							12.5	327	65	2.86	5.03	4.4
							15	323	65	2.86	4.97	3.1

## 4.8 Filling Material

Experimental panels (W1, W2, W3, and W4) and all of the proposed FRP panel are filled with sand. In this study, the mechanical properties of sand material used have been defined according to (Laine & Sandvik, 2001). Figure 4.34 shows the compaction curves for sand. In the current study, W3, W4, W16, W26, and W27 are studied once without filling material and another time while using foam as a filling material. Two types of foam are considered; polyurethane and dytherm (expanded polystyrene) foam. Material properties and compaction curves for the considered foams are defined according to (Goel et al., 2012). Figure 4.35 shows the compaction curves for polyurethane and dytherm foam, and Table 4.15 lists the mechanical properties for the two considered foam types.

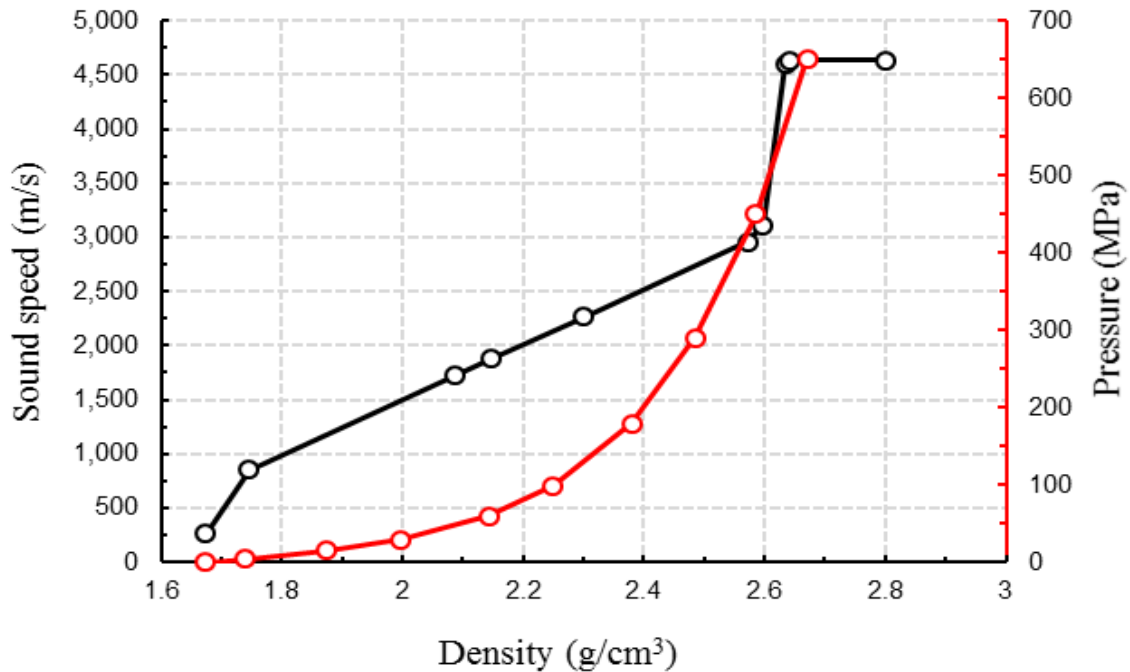
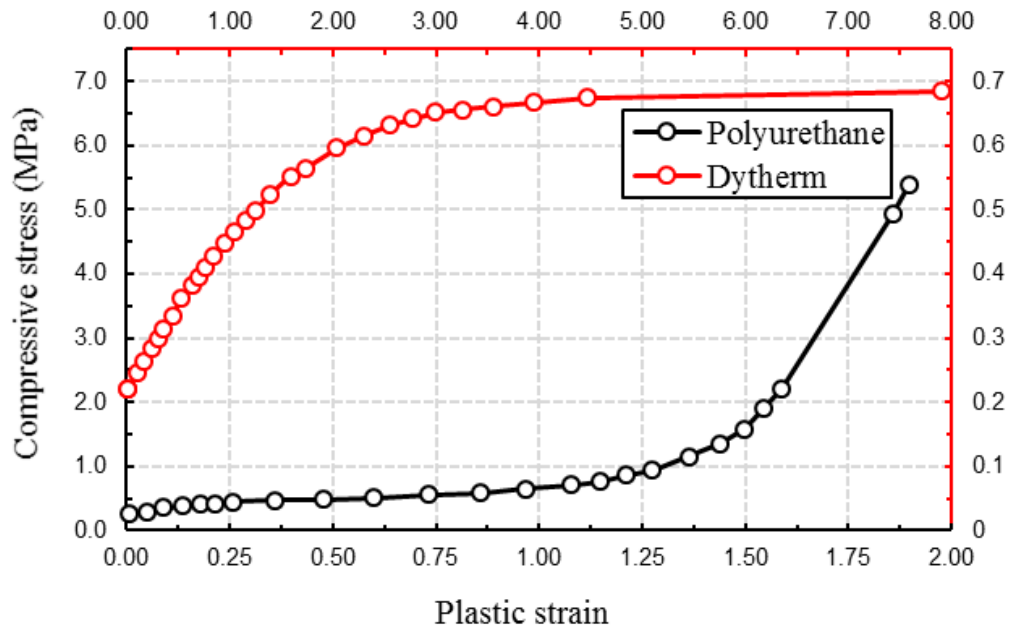


Figure 4.34 Compaction of sand



**Figure 4.35** Compaction of polyurethane and dytherm foams

**Table 4.15** Mechanical properties of polyurethane and dytherm foam

Mechanical properties	Polyurethane foam	Dytherm foam
Density, ( $kg/m^3$ )	60	100
Young's modulus, (MPa)	7.5	3.0
Shear modulus, (MPa)	6.2	4.3
Compressive strength, (MPa)	0.20	0.22
Tensile strength, (MPa)	0.02	0.02

Figures 4.36 to 4.40 represent the time history of central point deflection for W3, W4, W16, W26, and W27 with different filling materials; sand, no filling, polyurethane foam and dytherm foam. Table 4.16 illustrates the effect of changing filling material on panel's performance. Table 4.17 represents a comparison between the original panels –using sand as a filling– and other panels with different filling materials. Such comparison shows a percentage of difference in panel's deformations, energy dissipation, and  $E/\Delta$  ratio. From the figure and tables, it is found that using filling material leads to having a stiffer panel that reduces panel's maximum deformation. Energy

absorption increases by up to 49.7% and panels' deformation decreases by up to 28.8%. Comparing panels with no filling materials and others with sand, deformation increases by up to 25.4%, whereas energy absorption decreases by up to 23.5%. As a result,  $E/\Delta$  ratio decreases by up to 42.7%. On the other hand, upon using polyurethane foam, panels' maximum deflection decreases by up to 3.7%, while energy absorption increases by up to 15.7% in comparison with using sand material. Accordingly,  $E/\Delta$  ratio increases by up to 19.0%. Moreover, on using dytherm foam, the panels' maximum deflection decreases by up to 4.3%, while energy absorption increases by up to 17.4% in comparison with using sand. Therefore, this results in increasing the  $E/\Delta$  ratio by up to 20.8%. Based on the results, using foam materials significantly enhances the panel's energy dissipation and causes minor enhancement in the deformation. Finally, the usage of FRP panels with filling materials provides a damping ambulance that enhances the behaviour of FRP sandwich panels under blast loading.

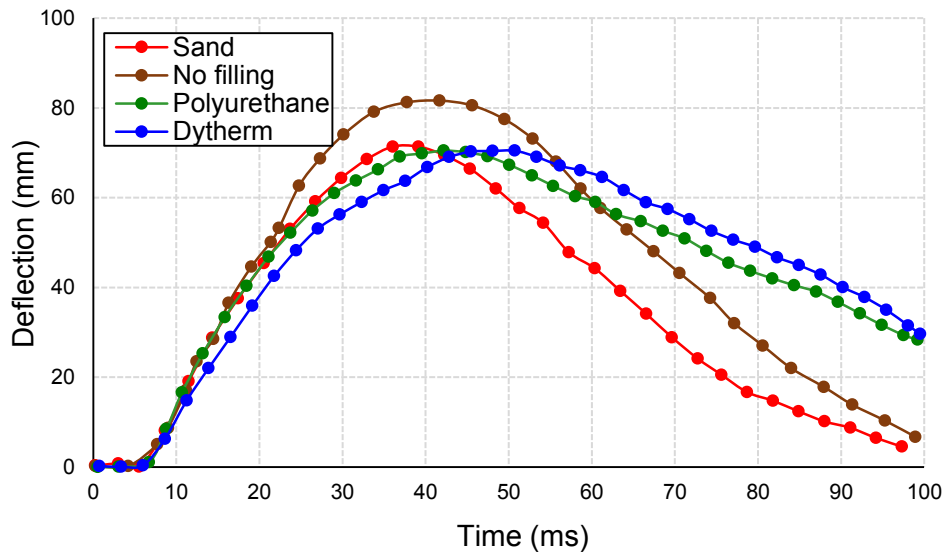


**Figure 4.36** Deflection time history of W3 with different filling materials

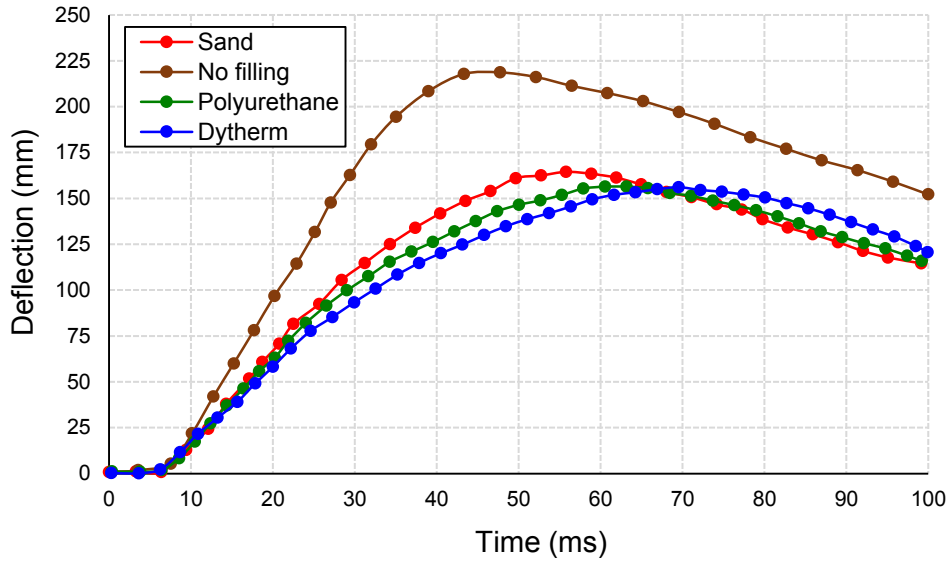


**Figure 4.37** Deflection time history of W4 with different filling materials

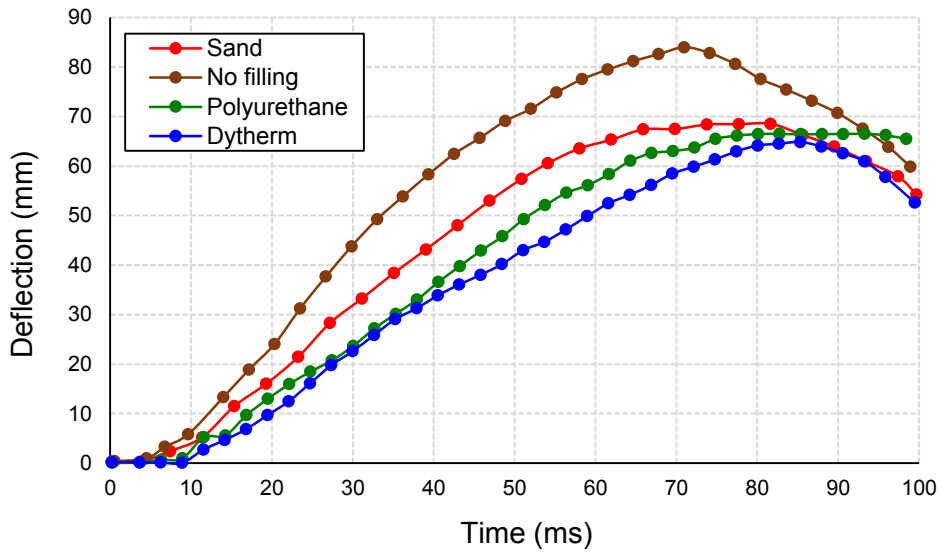


**Figure 4.38** Deflection time history of W16 with different filling materials

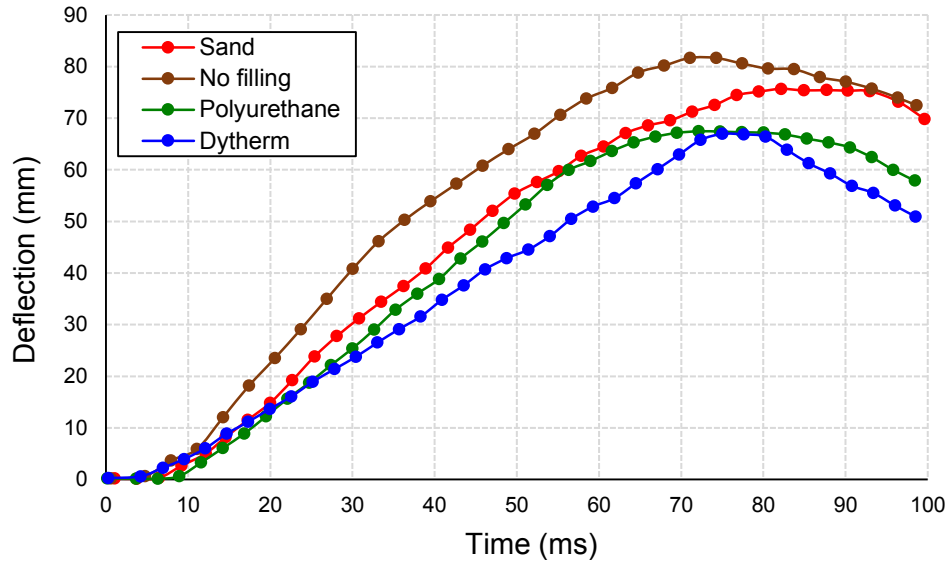


Figure 4.39 Deflection time history of W26 with different filling materials

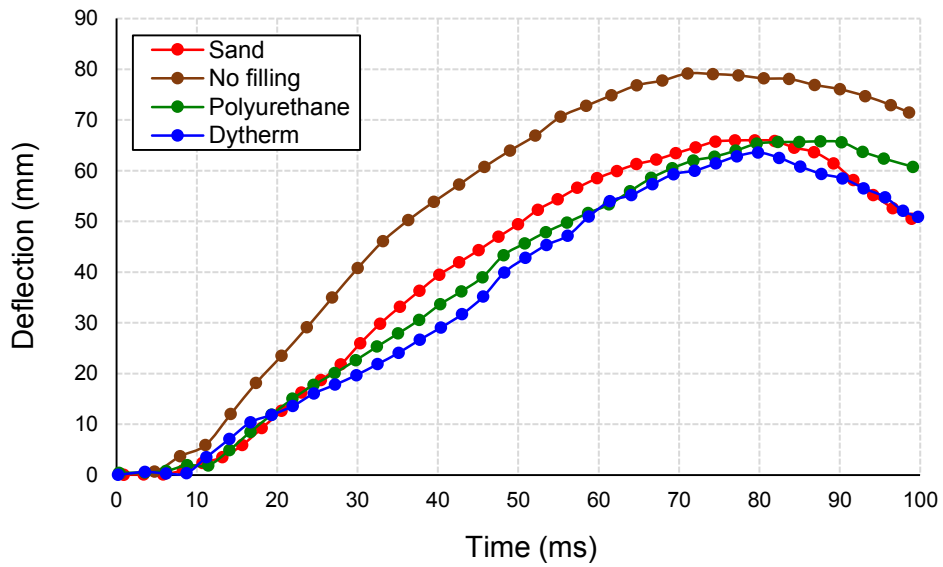


Figure 4.40 Deflection time history of W27 with different filling materials

**Table 4.16** Effect of filling materials on panels' deformations and energy dissipation

Panel	With sand			Without sand			Polyurethane			Dytherm		
	ED (J)	$\Delta_{max}$ (mm)	E/ $\Delta$	ED (J)	$\Delta_{max}$ (mm)	E/ $\Delta$	ED (J)	$\Delta_{max}$ (mm)	E/ $\Delta$	ED (J)	$\Delta_{max}$ (mm)	E/ $\Delta$
W3	121	72	1.68	103	82	1.26	140	70	2.00	142	70	2.03
W4	268	163	1.64	205	219	0.94	299	157	1.90	307	156	1.97
W16	256	67	3.82	228	84	2.71	287	66	4.35	291	65	4.48
W26	308	69	4.46	266	82	3.24	324	68	4.76	330	67	4.92
W27	318	66	4.82	282	79	3.57	335	66	5.08	339	64	5.30

**Table 4.17** Comparison between panels of different filling materials

Panel	Without sand			Polyurethane			Dytherm		
	ED (%)	$\Delta_{max}$ (%)	E/ $\Delta$ (%)	ED (%)	$\Delta_{max}$ (%)	E/ $\Delta$ (%)	ED (%)	$\Delta_{max}$ (%)	E/ $\Delta$ (%)
W3	-14.8	13.9	-25.0	15.7	-2.8	19.0	17.4	-2.8	20.8
W4	-23.5	34.4	-42.7	11.6	-3.7	15.8	14.6	-4.3	20.1
W16	-10.9	25.4	-29.1	12.1	-1.5	13.9	13.7	-3.0	17.3
W26	-13.6	18.8	-27.3	5.2	-1.4	6.7	7.1	-2.9	10.3
W27	-11.3	19.7	-25.9	5.3	0	5.4	6.6	-3.0	10.0

## 4.9 Summary

The effectiveness of sandwich panels in blast load resistance is investigated. In this chapter, FRP sandwich panel is studied using different inner core configurations, where a new core configuration that is formed from woven shape has been proposed. During this study, sandwich panels were evaluated using a nonlinear explicit finite element software *AUTODYN*. The numerical model was validated using experimental field tests conducted on four FRP honeycomb panels filled with sand when subjected to blast effects. The numerical model proved its efficiency in predicting the failure pattern of tested panels as well as their peak deflections with a maximum

deviation of 18%. The study also investigates the effect of filling FRP panels with sand on the panel's blast resistance. It is found that using sand as a filling material provides a damping environment which reduces panels' deflection by up to 26% and increases energy dissipation by up to 31%.

Twelve FRP panels with different inner core configurations were proposed, where these panels are divided into three groups. The results show that group 3 which used woven shape or a combination of woven and honeycomb shapes obtained the best blast resistance performance. Whereas among all panels, W16 can be considered to have the best performance as it has the highest energy-to-deflection ratio. Therefore, W16 was chosen to conduct a parametric study. Parametric studies were carried out to determine the effect of various parameters: thickness of layers, height of sinusoidal layer, length of sinusoidal wave, width of strip, and length of wave peak. It is found that changing wave peak length and other parameters ( $h$ ,  $L$ ,  $W$ , and  $t$ ) while keeping the material weight constant increases the energy-to-deflection ratio by about 34%. Finally, the effect of changing filling material on panel's performance against blast loads was investigated. Accordingly, dytherm foam showed the best performance where it enhances the  $E/\Delta$  ratio by up to 20.8% in comparison to using sand and by up to 4.3% in comparison to using polyurethane foam.

## Chapter

# 5

## Metallic Sandwich Panels

### 5.1 Core Topologies

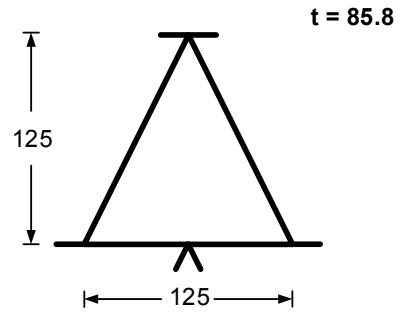
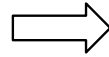
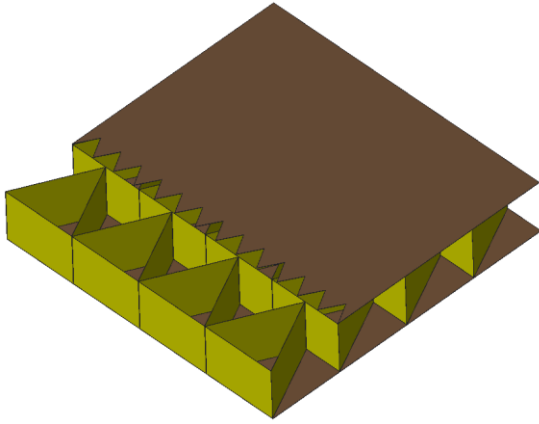
In the current study, three core topologies were studied which are honeycomb, folded, and woven shapes. Honeycomb and folded shapes have been investigated in previous studies, whereas woven shape is proposed in the current study. As for honeycomb shape, three shapes have been studied which are triangle honeycomb shape (TH), square honeycomb shape (SH), and hexagonal honeycomb shape (HH). Figure 5.1 shows the three different honeycomb topologies with the dimensions and thickness of each topology. In order to validate and compare results, the studied dimensions and thicknesses are similar to these applied by (Alberdi et al., 2013), where the thickness of TH, SH, and HH are 85.8 mm, 94.3 mm, and 96.7 mm, respectively. Regarding folded shape, five shapes have been studied which are diamond folded shape (DF), Y-frame folded shape (YF), triangle folded shape (TF), sinusoidal-corrugated folded shape (SF), and trapezoidal-corrugated folded shape (ZF). Figure 5.2 shows the five different folded topologies with the dimensions of each topology. For the diamond, Y-frame, and triangle folded shapes the used dimensions are the same as these used in (Alberdi et al., 2013) work. Whereas the sinusoidal-corrugated and trapezoidal-corrugated shapes have been proposed in this study. Finally, for woven shapes, three shapes have been studied which are triangle woven shape (TWV), sinusoidal-corrugated woven shape (SWV), and trapezoidal-corrugated woven shape (Z WV). Figure 5.3 shows the three different woven topologies. Woven shapes are made from the same triangle, sinusoidal-corrugated, and trapezoidal-corrugated folded layers but they are cut into strips and

interlaced together forming the woven shape. Triangle woven, sinusoidal-corrugated woven, and trapezoidal-corrugated woven shapes are formed from strips of 40 mm, 110 mm, and 70 mm thicknesses, respectively. All core topologies are 0.3 mm thick, while the front and back layers are of different thicknesses.

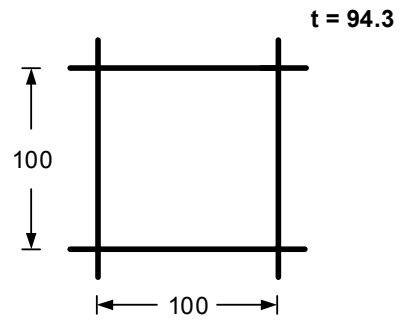
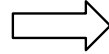
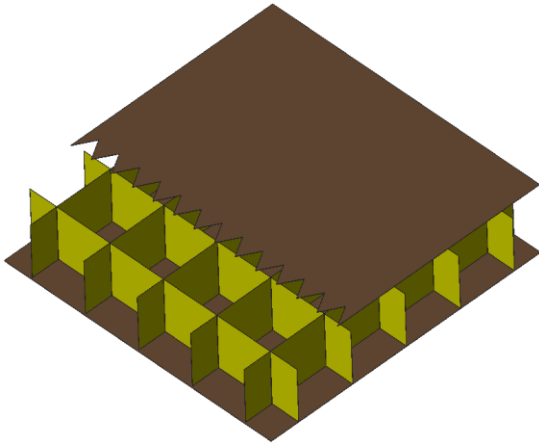
## Plan view of honeycomb configurations

All dimensions are in mm

(a) Triangle honeycomb



(b) Square honeycomb



(c) Hexagonal honeycomb

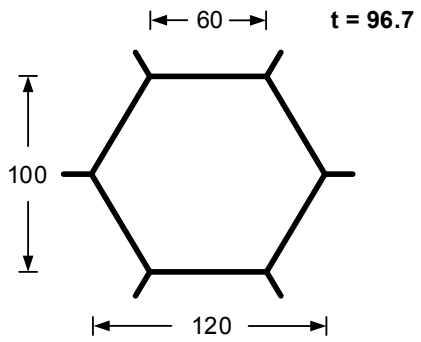
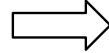
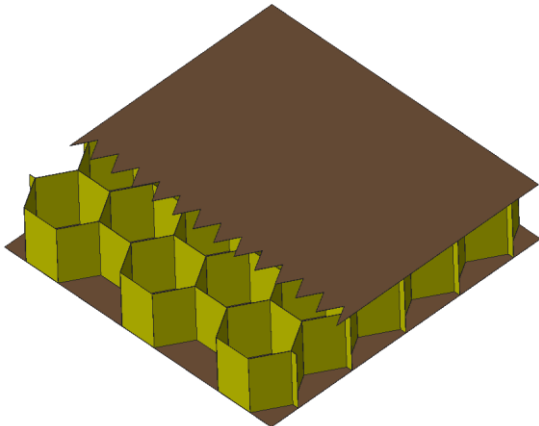
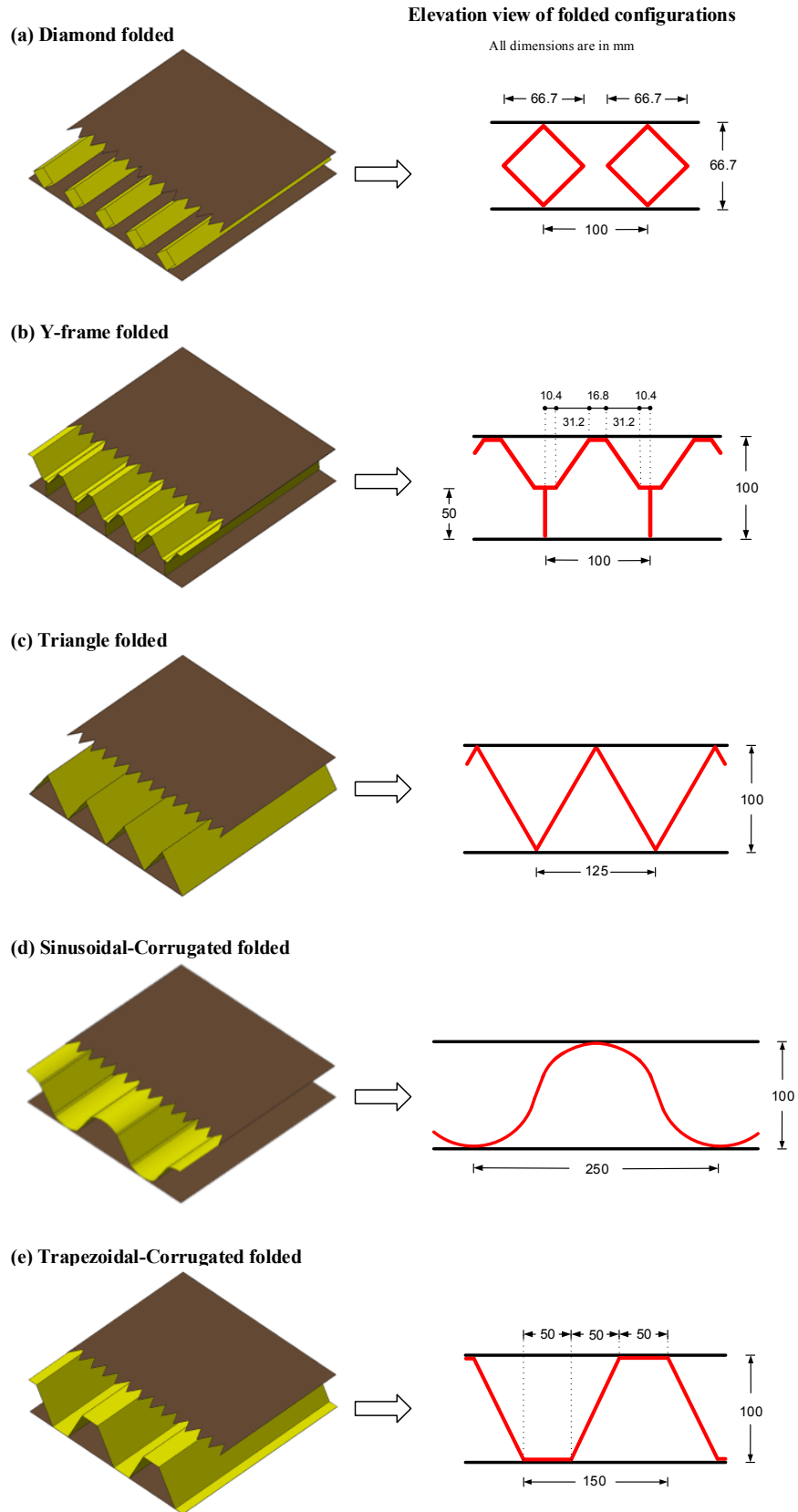
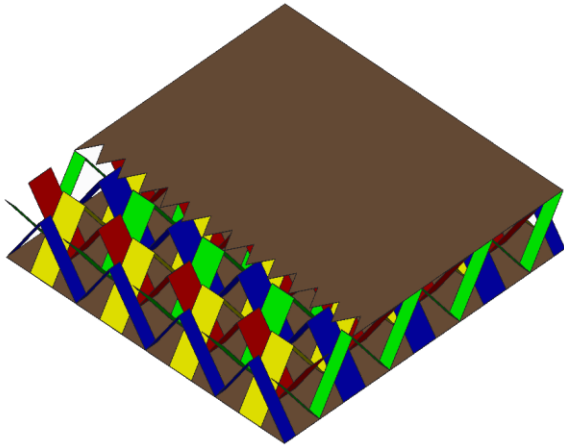


Figure 5.1 Honeycomb core topologies

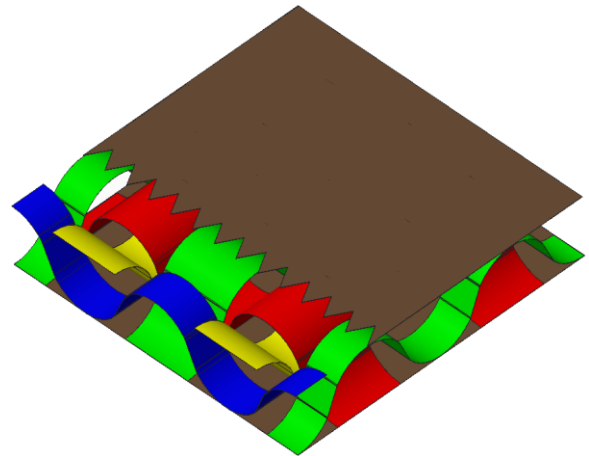


**Figure 5.2** Folded core topologies

**(a) Triangle woven**



**(b) Sinusoidal-Corrugated woven**



**(c) Trapezoidal-Corrugated woven**

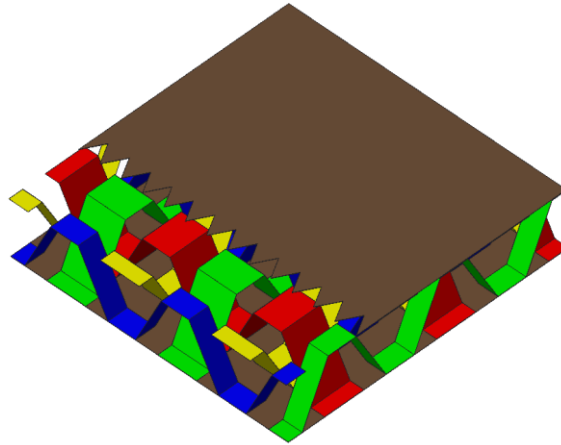


**Figure 5.3** Woven core topologies

Relative densities of each core topology were calculated by dividing the volume of material in each core by its total volume. Table 5.1 shows relative densities of different core topologies. Calculating relative densities is important to compare the amount of material needed for each core topology. Excluding SF and ZF, the small range of relative densities shows that all topologies utilize almost the same amount of material.

**Table 5.1** Relative densities of different core topologies

---

<b>Topology</b>	<b>Relative density</b>
TH	7.73e-03
SH	5.97e-03
HH	6.31e-03
DF	8.43e-03
YF	6.18e-03
TF	5.62e-03
SF	3.74e-03
ZF	4.99e-03
TW	7.01e-03
SW	6.52e-03
RW	6.83e-03

---

## 5.2 Material Properties

Following the work done by (Alberdi et al., 2013), metallic sandwich panels are modeled using AISI 304 stainless steel. Table 5.2 shows the material properties of AISI 304 stainless steel. For the purpose of material modelling using AUTODYN (2014), the parameters of material's EOS must be defined first. Then, strength and failure models are defined for the material. EOS is defined as shock, the strength model parameter is defined as Steinberg-Guinan strength, while no failure mode was defined.

**Table 5.2** Material properties of AISI 304 stainless steel

<b>Parameter</b>	<b>value</b>
Reference density	7900 kg/m <sup>3</sup>
Gruneisen coefficient	1.93
Parameter C1	4.57e+3 m/s
Parameter S1	1.49
Reference temperature	300 K
Specific heat	423 J/kgK
Shear modulus	7.7e+7 kPa
Maximum yield stress	2.5e+6 kPa
Young's modulus	2.1e+5 kPa
Poisson's ratio	0.3
Hardening constant	43
Hardening exponent	0.35
Derivative dG/dP	1.74
Derivative dG/dP	-3.504e+4 kPa/K
Derivative dG/dP	7.684e-3
Melting temperature	2.38e+3 K

### 5.3 Model Validation

The current numerical model has been validated by (Alberdi et al., 2013) work that used *LS-DYNA* software. Six sandwich panels with different core topologies have been tested under blast effects. The six sandwich panels are divided into three panels with a honeycomb shape and another three panels with folded shape. For the honeycomb shape, the three shapes that have been studied are triangle honeycomb, square honeycomb, and hexagonal honeycomb. As for the folded shape, the three shapes that have been studied are diamond folded, Y-frame folded, and triangle folded. In the current numerical model, six sandwich panels have been simulated using *AUTODYN* software with the same core topologies and dimensions as (Alberdi et al., 2013) work. Panels are 500 mm length and 500 mm height, whereas the thickness varies depending on core topologies as shown in Figures 5.1 and 5.2.

Blast load is characterized by using scaled distance,  $Z$ . It is computed by dividing the ratio of stand-off distance by the cube root of the charge weight. In this study, similar to (Alberdi et al., 2013) work, the scaled distance used is  $1.26 \text{ m/kg}^{1/3}$ . Two types of gauges are used; fixed gauges and moving gauges. Fixed gauges are attached to their coordinates and they do not move throughout the simulation, while moving ones move with the element during simulation. Fixed gauges are used for capturing the model's pressure readings, while moving gauges are used to capture deflection readings. Several pressure gauges have been assigned to track pressure change along air domain.

### 5.3.1 Varying Back Layer

The performance of the six sandwich panels have been evaluated where the thickness of core layers and front layers of each is 0.3 mm. As for back layers, the following four different thicknesses have been used: 0.3, 0.5, 0.8, and 1 mm to investigate its effect on the sandwich panel performance. Deflection of front layer, deflection of back layer, and energy dissipation were studied. Figures 5.4 and 5.5 show the effect of changing back layer thickness on front layer deflection for both; work done by (Alberdi et al., 2013) (*LS-DYNA*) and the current study (*AUTODYN*). From the figures, it is noticed that a minor change in front layer deflection has been achieved upon changing the back layer thickness. The maximum change percentage of honeycomb shape is 16.7% upon using HH shape, whereas the maximum change percentage of folded shape is 3.6% upon using YF shape. Also, it is noticed that front layer deflection for folded shapes is higher than that of honeycomb shapes. This can be attributed to the fact that folded shapes suffer from more crushing than honeycomb shapes as it is less stiff. Moreover, the figures show that the maximum deviation between *LS\_DYNA* and *AUTODYN* models for TH, SH, and HH shapes is 6.8% at 0.5 mm thickness, 3.7% at 1 mm thickness, and 2.4% at 0.3 mm thickness, respectively. Whereas the maximum deviation for DF, YF, and TF shapes is 2.9% at 0.3 mm thickness, 4.3% at 0.5 mm thickness, and 3.9% at 0.5 mm thickness, respectively. Figures 5.6 and 5.7 show the effect of changing back layer thickness on back layer deflection. From the figures, it is noticed that the back layer deflection decreases on increasing the back layer thickness. Comparing deflection upon using back layer of 1 mm thickness with the deflection upon using back layer of 0.3 mm thickness, it is found that deflection decreases by 33.75%, 39.5%, and 38.1% for TH, SH, and HH shapes, respectively. However, the deflection of DF, YF, and TF shapes decreases by 53%, 62.5%, and

25.1%, respectively. It is also shown from the figures that the maximum deviation between *LS\_DYNA* and *AUTODYN* models for TH, SH, and HH shapes is 7.9% at 0.8 mm thickness, 8.6% at 0.5 mm thickness, and 6.8% at 0.8 mm, respectively. On the other hand, the maximum deviation for DF, YF, and TF shapes is 8.5% at 0.5 mm thickness, 10.3% at 0.5 mm thickness, and 8.4% at 1 mm thickness, respectively. Figures 5.8 and 5.9 show the effect of changing back layer thickness on energy dissipation. From the figures, it is noticed that folded shapes absorb more energy than honeycomb shapes. As previously mentioned, this also can be attributed to the fact that folded shapes suffer from more crushing than honeycomb shapes as it is less stiff, and this is consistent with the front layer deformation of these panels. Also, the figures show that the maximum deviation between *LS\_DYNA* and *AUTODYN* models for TH, SH, and HH shapes is 2.7% at 0.8 mm thickness, 3.1% at 1 mm thickness, and 4.1% at 0.8 mm thickness, respectively. Whereas, the maximum deviation for DF, YF, and TF shapes is 3.6% at 0.3 mm thickness, 7.5% at 0.3 mm thickness, and 3.7% at 0.8 mm thickness, respectively. To conclude, a good agreement has been reached between the work done by (Alberdi et al., 2013) and the current work with maximum deviation of 10.3%.

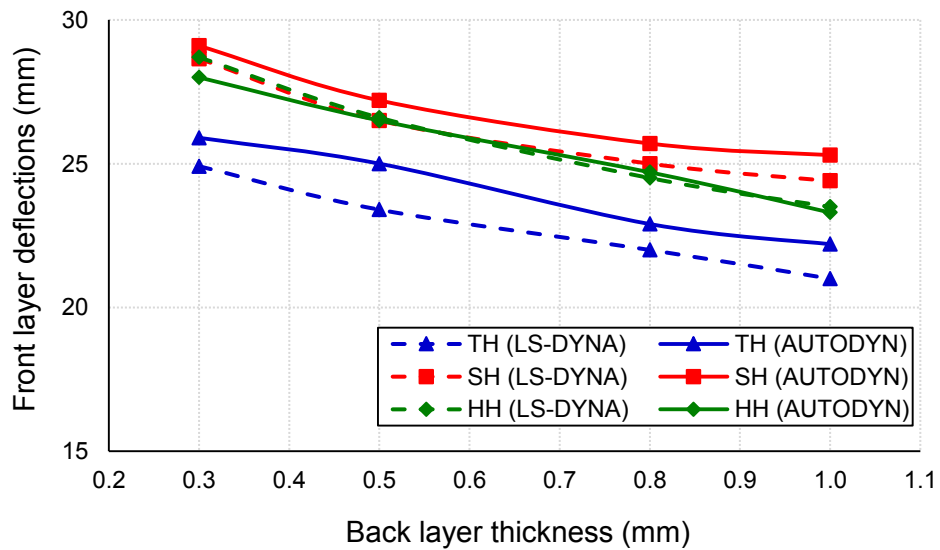


**Figure 5.4** Effect of changing back layer thickness on front layer deflection for honeycomb shape using *LS\_DYNA* (Alberdi et al., 2013) and *AUTODYN* (Current study)

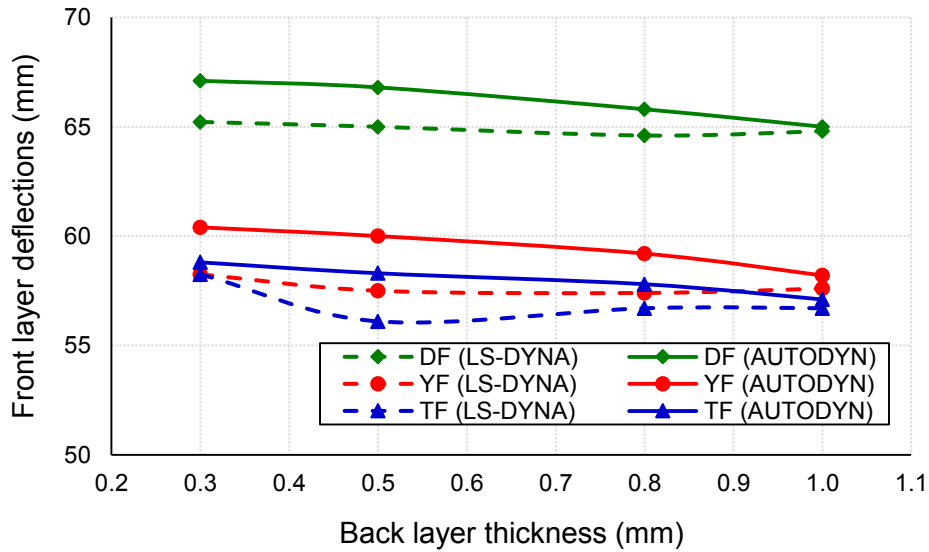


**Figure 5.5** Effect of changing back layer thickness on front layer deflection for folded shape using LS\_DYNA (Alberdi et al., 2013) and AUTODYN (Current study)

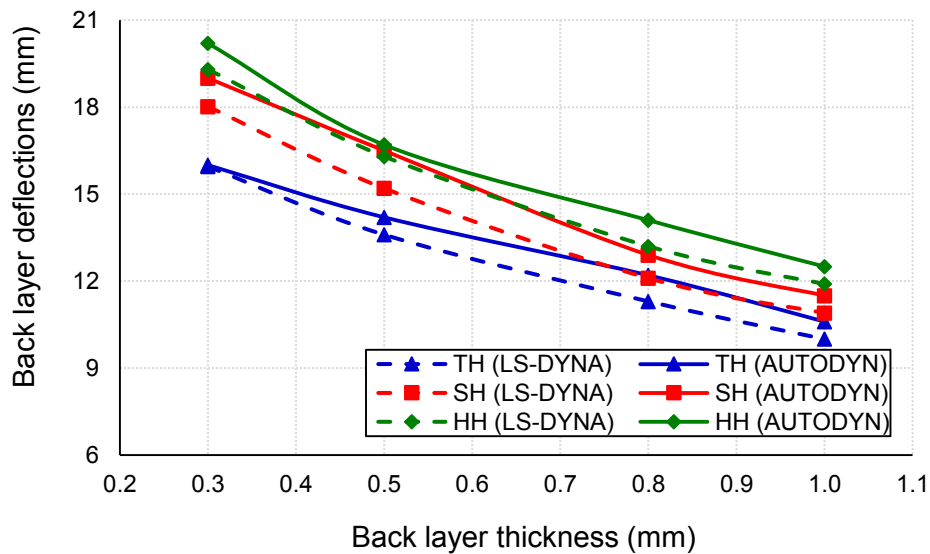


**Figure 5.6** Effect of changing back layer thickness on back layer deflection for honeycomb shape using LS\_DYNA (Alberdi et al., 2013) and AUTODYN (Current study)

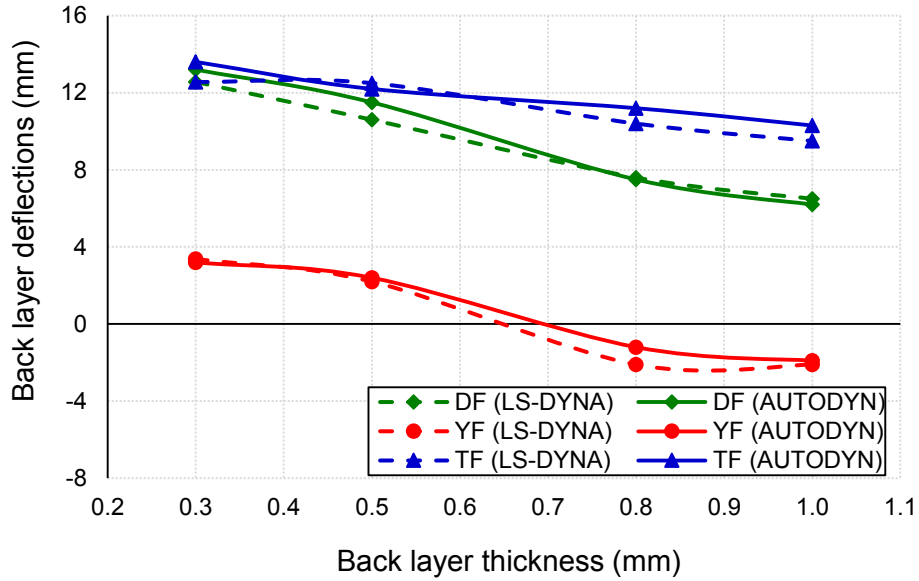


**Figure 5.7** Effect of changing back layer thickness on back layer deflection for folded shape using LS\_DYNA (Alberdi et al., 2013) and AUTODYN (Current study)

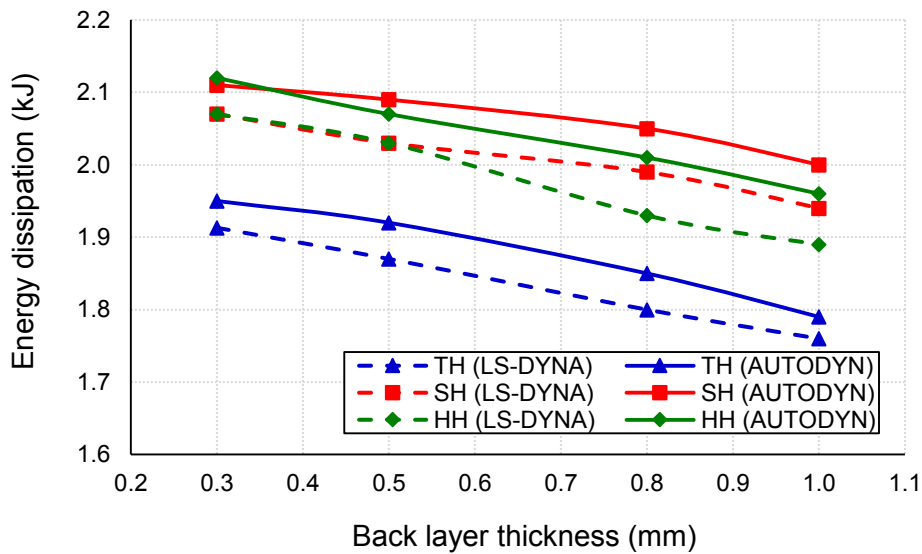


**Figure 5.8** Effect of changing back layer thickness on energy dissipation for honeycomb shape using LS\_DYNA (Alberdi et al., 2013) and AUTODYN (Current study)

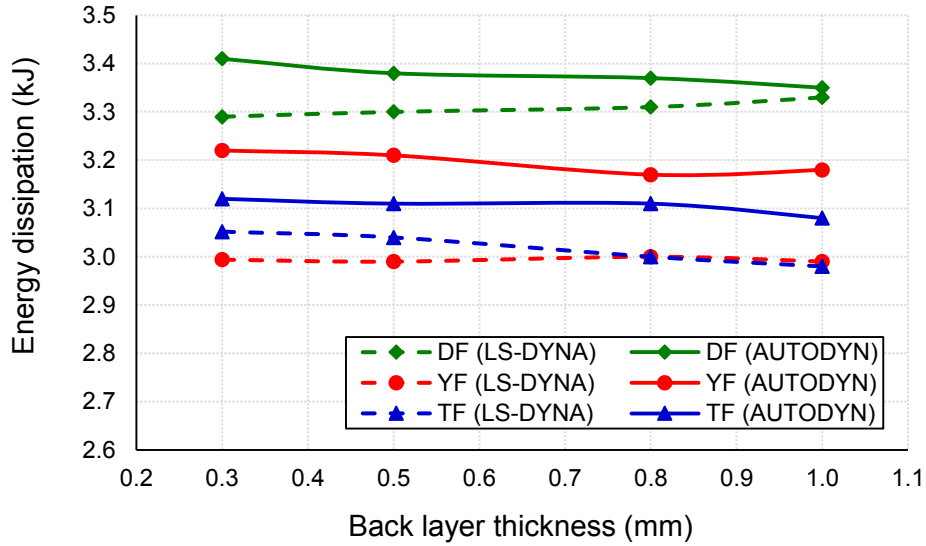


**Figure 5.9** Effect of changing back layer thickness on energy dissipation for folded shape using *LS\_DYNA* (Alberdi et al., 2013) and *AUTODYN* (Current study)

### 5.3.2 Varying Front Layer

The performance of the six sandwich panels was evaluated for the case where the thickness of core layers and back layers are 0.3 mm. As for the front layers, the following four different thicknesses have been used: 0.3 mm, 0.5 mm, 0.8 mm, and 1 mm to investigate its effect on sandwich panel performance. Front layer deflection, back layer deflection, and energy dissipation have been studied. Figures 5.10 and 5.11 show the effect of changing the front layer thickness on the front layer deflection. From the figures, it is noticed that front layer deflection decreases upon increasing the front layer thickness. Comparing the deflection when using a front layer of 1 mm thickness with the deflection when using a front layer of 0.3 mm thickness, the deflection decreases by 35.1%, 40.2%, and 43.6% for TH, SH, and HH shapes, respectively. While deflection decreases by 54.5%, 53.6%, and 49.3% for DF, YF, and TF shapes, respectively. Also, the figures show that the maximum deviation between *LS\_DYNA* and *AUTODYN* models for TH, SH, and HH shapes is 7.8% at 0.5 mm thickness, 8.6% at 1 mm thickness, and 5.9% at 0.5 mm, respectively. On the other hand, the maximum deviation for DF, YF, and TF shapes is 8.9% at 0.8 mm thickness, 7.8% at 0.5 mm thickness, and 5.4% at 0.8 mm thickness, respectively. Figures 5.12 and 5.13 show the effect of changing the front layer thickness on the back layer deflection. From the figures, it is noticed that back layer deflection decreases when increasing the front layer thickness. Comparing deflection upon using a front layer of 1 mm thickness with deflection upon using a front layer of

0.3 mm thickness, it is noticed that deflection decreases by 43.1%, 38.9%, and 37.6% for TH, SH, and HH shapes, respectively, while for TF shape the deflection decreases by 33.1%. On the other hand, the deflection of DF and YF shapes has occurred in the opposite direction to the applied blast loads due to the overall behaviour of the core elements. Also, the figures show that the maximum deviation between *LS\_DYNA* and *AUTODYN* models for TH, SH, and HH shapes is 8.7% at 0.5 mm thickness, 7.2% at 1 mm thickness, and 9.8% at 0.5 mm, respectively. Whereas the maximum deviation for DF, YF, and TF shapes is 12.1% at 0.5 mm thickness, 12.9% at 0.5 mm thickness, and 8.3% at 0.3 mm thickness, respectively. Figures 5.14 and 5.15 show the effect of changing front layer thickness on energy dissipation. The figures show that on varying back layer thickness, it is noticed that the energy dissipation for folded shapes absorb more energy than for honeycomb shapes. Also, the maximum deviation between *LS\_DYNA* and *AUTODYN* models for TH, SH, and HH shapes is 4.3% at 0.5 mm thickness, 9.5% at 1 mm thickness, and 8.4% at 0.5 mm, respectively. Whereas the maximum deviation for DF, YF, and TF shapes is 9.1% at 0.8 mm thickness, 8.3% at 0.5 mm thickness, and 5.7% at 0.8 mm thickness, respectively. To conclude, a good agreement has been reached between the work done by (Alberdi et al., 2013) and the current work with maximum deviation of 12.9%.

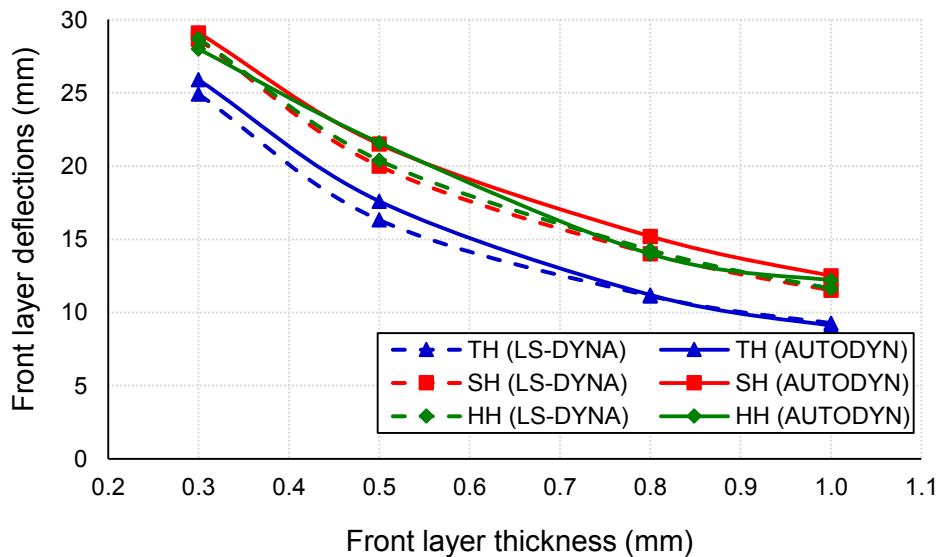


**Figure 5.10** Effect of changing front layer thickness on front layer deflection for honeycomb shape using *LS\_DYNA* (Alberdi et al., 2013) and *AUTODYN* (Current study)

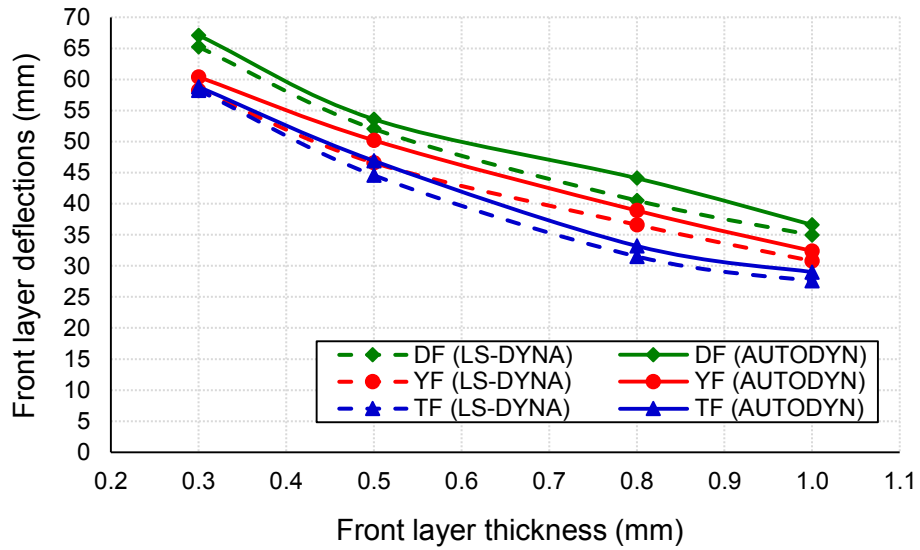


**Figure 5.11** Effect of changing front layer thickness on front layer deflection for folded shape using LS\_DYNA (Alberdi et al., 2013) and AUTODYN (Current study)

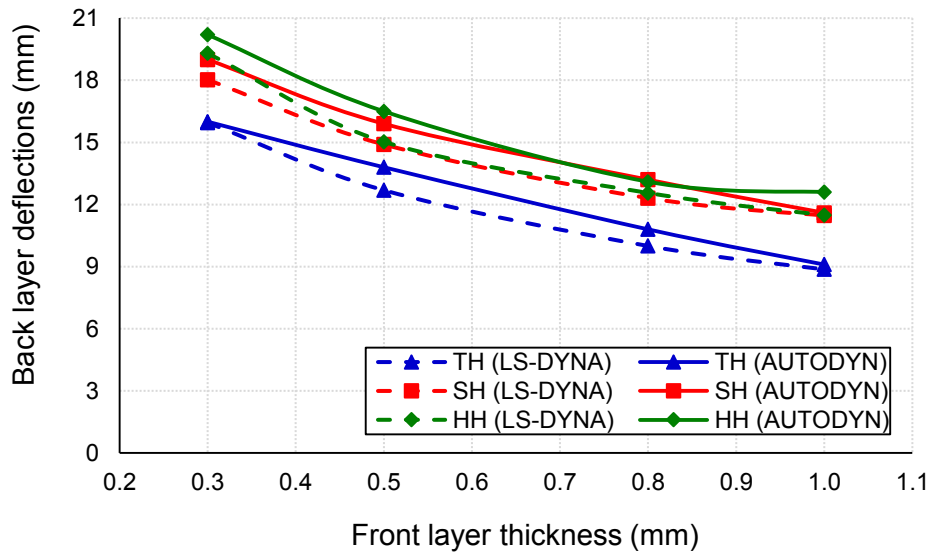


**Figure 5.12** Effect of changing front layer thickness on back layer deflection for honeycomb shape using LS\_DYNA (Alberdi et al., 2013) and AUTODYN (Current study)

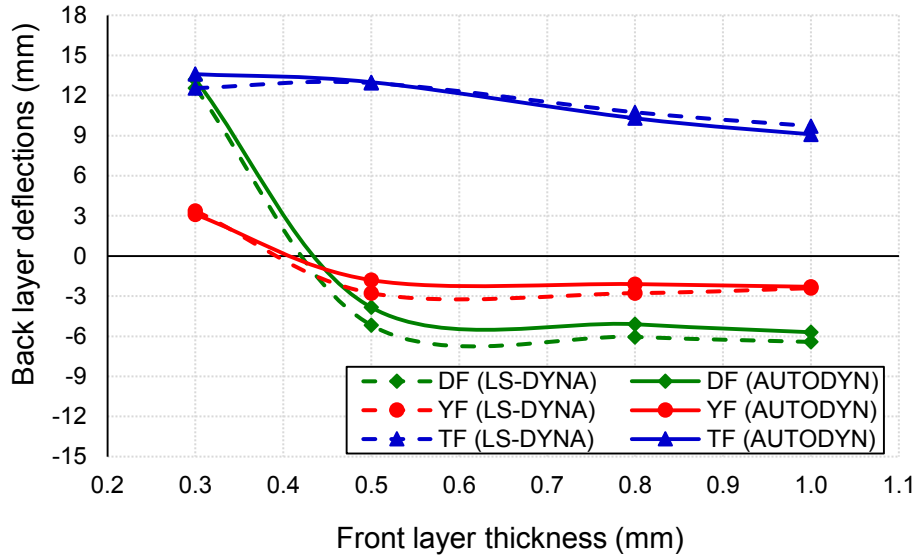


**Figure 5.13** Effect of changing front layer thickness on back layer deflection for folded shape using LS\_DYNA (Alberdi et al., 2013) and AUTODYN (Current study)

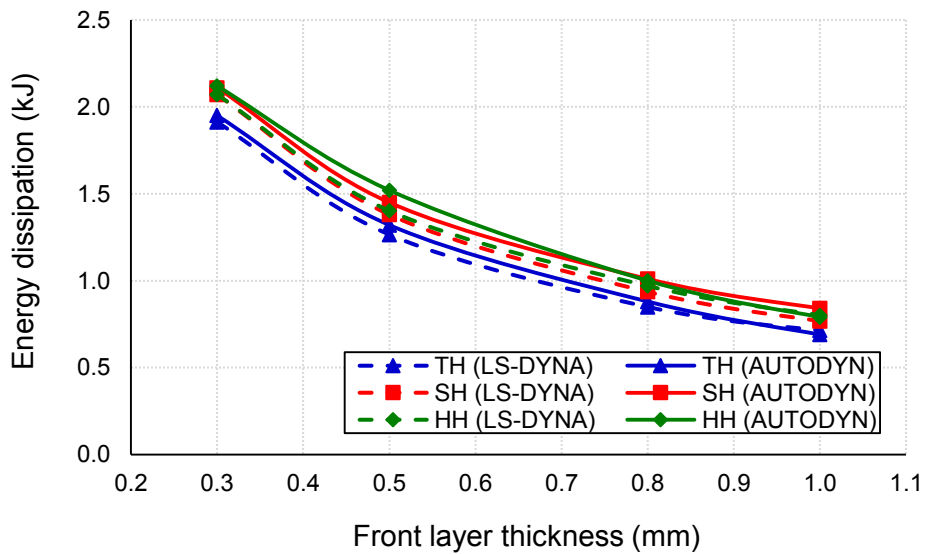


**Figure 5.14** Effect of changing front layer thickness on energy dissipation for honeycomb shape using LS\_DYNA (Alberdi et al., 2013) and AUTODYN (Current study)

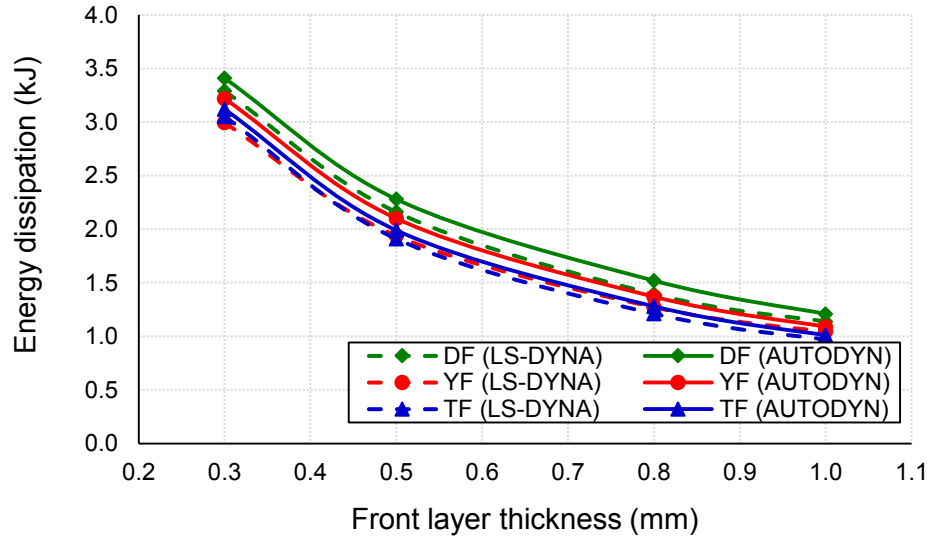


**Figure 5.15** Effect of changing front layer thickness on energy dissipation for folded shape using LS\_DYNA (Alberdi et al., 2013) and AUTODYN (Current study)

## 5.4 Proposed Core Configurations

Five sandwich panels with different core topologies have been proposed and studied under blast effects. The five sandwich panels are divided into two folded shape panels and another three woven shape panels. For the folded shape panels, the two shapes that have been studied are sinusoidal-corrugated folded shape and trapezoidal-corrugated folded shape. As for the woven shape panels, the three shapes that have been studied are triangle woven shape, sinusoidal-corrugated woven shape, and trapezoidal-corrugated woven shape. The five sandwich panels have been simulated using *AUTODYN* software. The panels are of 500 mm length, 500 mm height, and 100 mm thickness. The scaled distance that has been used is  $1.26 \text{ m/kg}^{1/3}$ . Proposed panels are modeled with the same dimensions and the same scaled distance as the panels used in the validation in order to compare results.

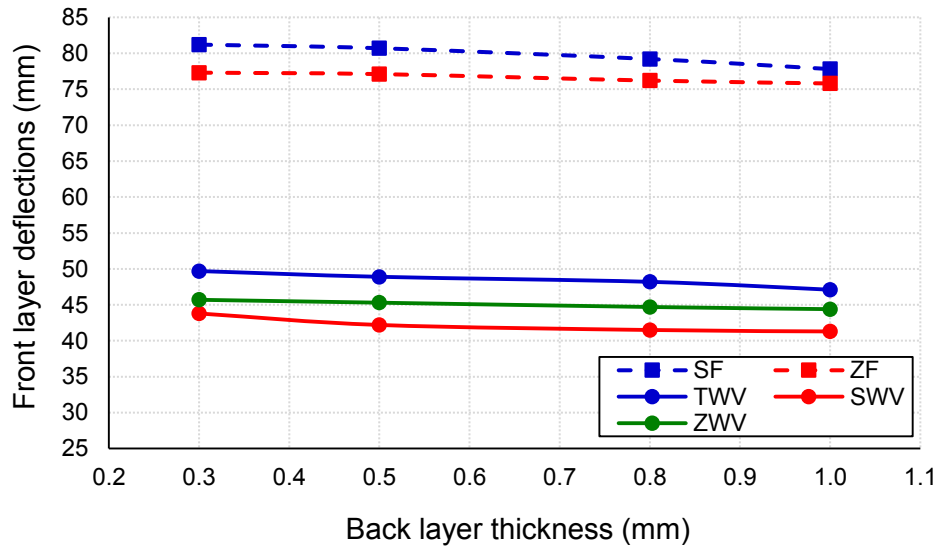
### 5.4.1 Varying Back Layer

The performance of the five sandwich panels are evaluated where the thickness of core layers and front layers are 0.3 mm. As for the back layer, the following four different thicknesses are used: 0.3 mm, 0.5 mm, 0.8 mm, and 1 mm to investigate its effect on sandwich panel performance. Front layer deflection, back layer deflection, and energy dissipation are studied. Figure 5.16 shows the effect of changing back layer thickness on front layer deflection. From the figure, it is noticed

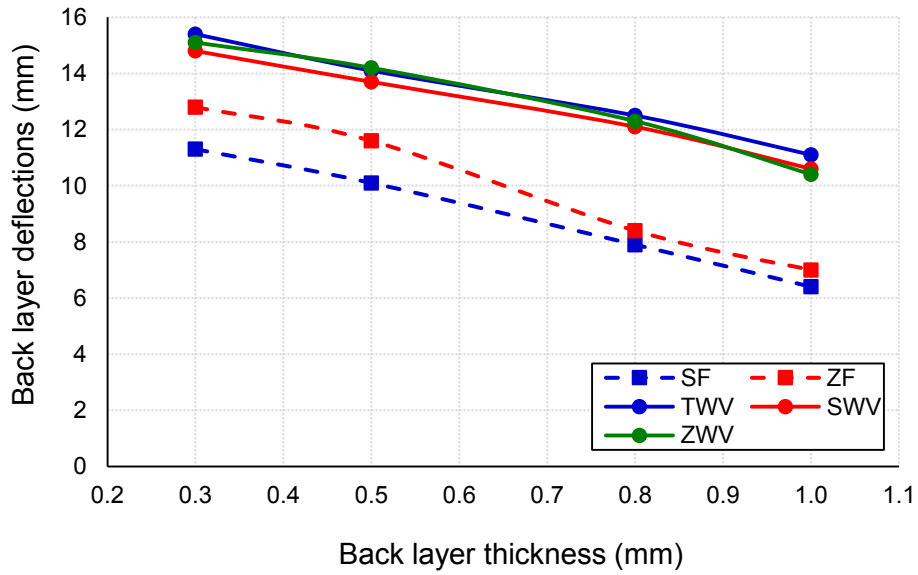
that a minor change in front layer deflection is achieved when changing back layer thickness. The average changing percentage for the considered five panels is 4%. Also comparing with validation models (Figures 5.4 and 5.5), SF and ZF shapes have gotten the highest deflection values among all panels. While for woven shape panels (TWV, SWV, and ZWV), they get less deflection values than these achieved by folded shapes and greater than the values achieved by honeycomb shapes. For the woven shapes, the front layer deflection is ranging from 50 mm to 41 mm. While for folded and honeycomb shapes, the front layer deflection is ranging from 81 mm to 57 mm and from 29 mm to 22 mm, respectively. Therefore, it could be said that woven shapes are stiffer than folded shapes and less stiff than honeycomb shapes.

Figure 5.17 shows the effect of changing back layer thickness on back layer deflection. From the figure, it is noticed that back layer deflection decreases upon increasing back layer thickness. Comparing deflection when using a back layer of 1 mm thickness with the deflection when using a back layer of 0.3 mm thickness, the deflection decreases by 43.4%, 45.3%, 27.9%, 28.4%, and 31.1% for SF, ZF, TWV, SWV, and ZWV shapes, respectively.

Figure 5.18 shows the effect of changing back layer thickness on energy dissipation. From the figure, it is noticed that, similar to the front layer deflection, a minor change in the energy dissipation is achieved upon changing the back layer thickness. The energy dissipation decreases by 3.9%, 5.2%, 5.9%, 4.8%, and 4.7% for SF, ZF, TWV, SWV, and ZWV shapes, respectively. Also comparing with validation models (Figures 5.8 and 5.9), woven shapes dissipate more energy than folded and honeycomb shapes. For woven shapes, energy dissipation ranges from 3.98 kJ to 3.66 kJ with an average of 3.82 kJ. While for the folded and honeycomb shapes, energy dissipation ranges from 3.41 kJ to 3.07 kJ with an average of 3.24 kJ and from 2.12 kJ to 1.79 kJ with an average of 1.99 kJ, respectively. Accordingly, energy dissipation increases on using woven shapes by 17.9% compared to folded shapes and by 92% compared to honeycomb shapes.



**Figure 5.16** Effect of changing back layer thickness on front layer deflection for proposed panels



**Figure 5.17** Effect of changing back layer thickness on back layer deflection for proposed panels

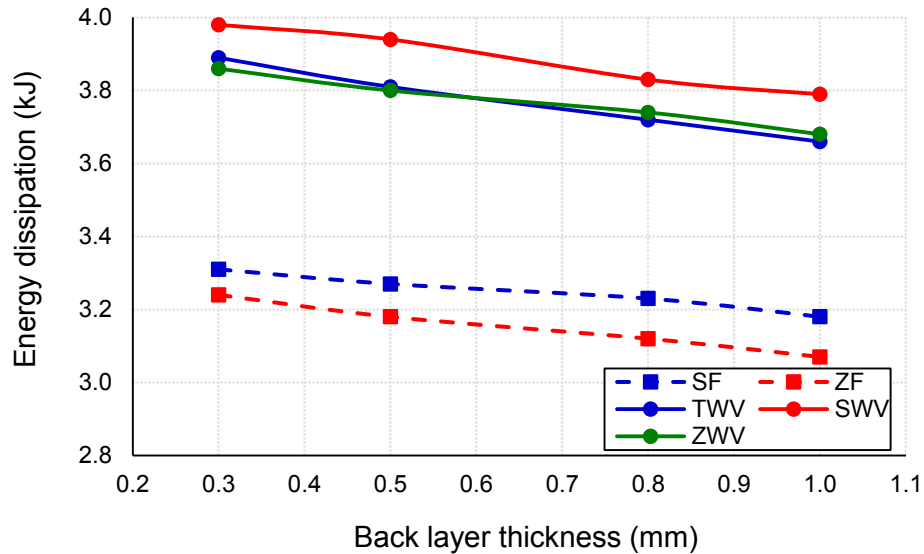


**Figure 5.18** Effect of changing back layer thickness on energy dissipation for proposed panels

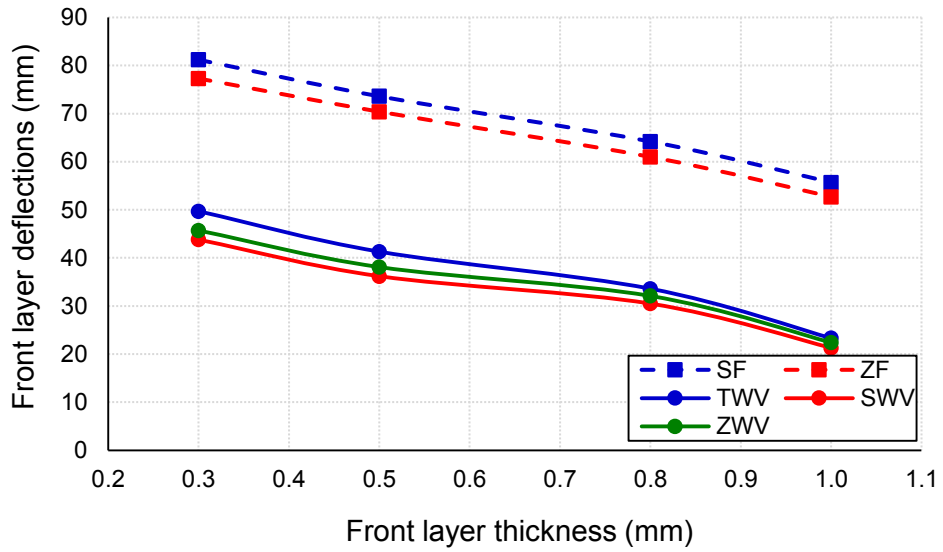
#### 5.4.2 Varying Front Layer

The performance of the five sandwich panels is evaluated when the thickness of core layers and back layers is 0.3 mm. As for the front layers, the following four different thicknesses are used: 0.3 mm, 0.5 mm, 0.8 mm, and 1 mm to investigate its effect on sandwich panel performance. Front layer deflection, back layer deflection, and energy dissipation are studied. Figure 5.19 shows the effect of changing front layer thickness on front layer deflection. From the figure, it is noticed that front layer deflection decreases upon increasing front layer thickness. Comparing deflection when using a front layer of 1 mm thickness with the deflection when using a front layer of 0.3 mm thickness, it is noticed that deflection decreases by 32.4%, 31.8%, 53.1%, 51.4%, and 51% for SF, ZF, TWV, SWV, and ZWV shapes, respectively. Again, comparing with the validation models in Figures 5.10 and 5.11, the SF and ZF shapes have gotten the highest deflection values among all panels. The average deflection value is 79.2 mm, 72 mm, 62.6 mm, and 54.2 mm for SF and ZF shapes of thickness 0.3 mm, 0.5 mm, 0.8mm, and 1 mm, respectively. Whereas for woven shape panels, they have less deflection values than these that are achieved by folded shapes and greater than the values achieved by honeycomb shapes. Accordingly, the average deflection value is 46.4 mm, 38.5 mm, 32.1 mm, and 22.3 mm for woven shapes of thickness 0.3 mm, 0.5 mm, 0.8mm, and 1 mm, respectively. While the average deflection value is 62.1 mm, 50.3 mm, 38.7 mm, and 32.6 mm for folded shapes excluding SF and ZF shapes of thickness 0.3 mm, 0.5 mm, 0.8mm, and

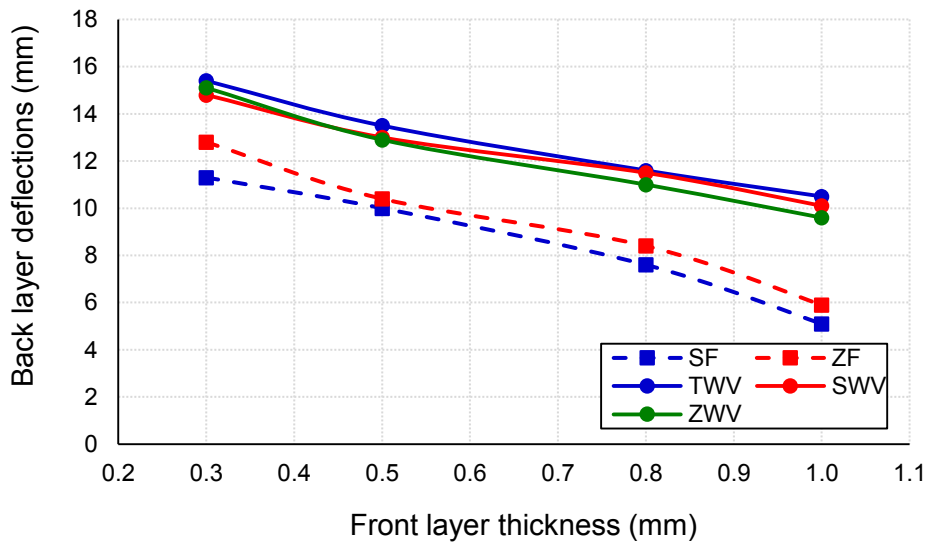
1 mm, respectively. Whereas the average deflection value is 27.7 mm, 20.2 mm, 13.5 mm, and 11.3 mm for honeycomb shapes of thickness 0.3 mm, 0.5 mm, 0.8mm, and 1 mm, respectively.

Figure 5.20 shows the effect of changing front layer thickness on back layer deflection. From the figure, it is noticed that back layer deflection decreases upon increasing front layer thickness. Comparing deflection upon using a front layer of 1 mm thickness with the deflection when using a front layer of 0.3 mm thickness, it is noticed that the deflection decreases by 54.9%, 53.9%, 31.8%, 31.7%, and 36.4% for SF, ZF, TWV, SWV, and ZWV shapes, respectively.

Figure 5.21 shows the effect of changing front layer thickness on energy dissipation. From the figure, it is noticed that the energy dissipation decreases upon increasing back layer thickness. The energy dissipation decreases by 60.4%, 66.7%, 52.4%, 48.2%, and 49% for SF, ZF, TWV, SWV, and ZWV shapes, respectively. Also comparing with validation models (Figures 5.14 and 5.15), it is noticed that, as the case when varying back layer thickness, woven shapes absorb more energy than folded and honeycomb shapes. For woven shapes, the average energy dissipation is 3.91 kJ, 3.14 kJ, 2.39 kJ, and 1.96 kJ for panels of thickness 0.3 mm, 0.5 mm, 0.8 mm, and 1 mm, respectively. While for folded, the average energy dissipation is 3.26 kJ, 2.18kJ, 1.48kJ, and 1.14 kJ, for panels of 0.3 mm, 0.5 mm, 0.8 mm, and 1 mm thickness, respectively. Finally for honeycomb shapes, the average energy dissipation is 2.06 kJ, 1.43 kJ, 0.96 kJ, and 0.77 kJ for panels of 0.3 mm, 0.5 mm, 0.8 mm, and 1 mm thickness, respectively. Accordingly, energy dissipation increases by an average of 49.3% on using woven shapes comparing to folded shapes and by an average of 128.2% comparing to honeycomb shapes. To conclude, although woven shapes have less front layer deflection than folded shapes, they are able to dissipate more energy, whereas woven shapes have more front layer deflection and energy dissipation than honeycomb shapes.



**Figure 5.19** Effect of changing front layer thickness on front layer deflection for proposed panels



**Figure 5.20** Effect of changing front layer thickness on back layer deflection for proposed panels

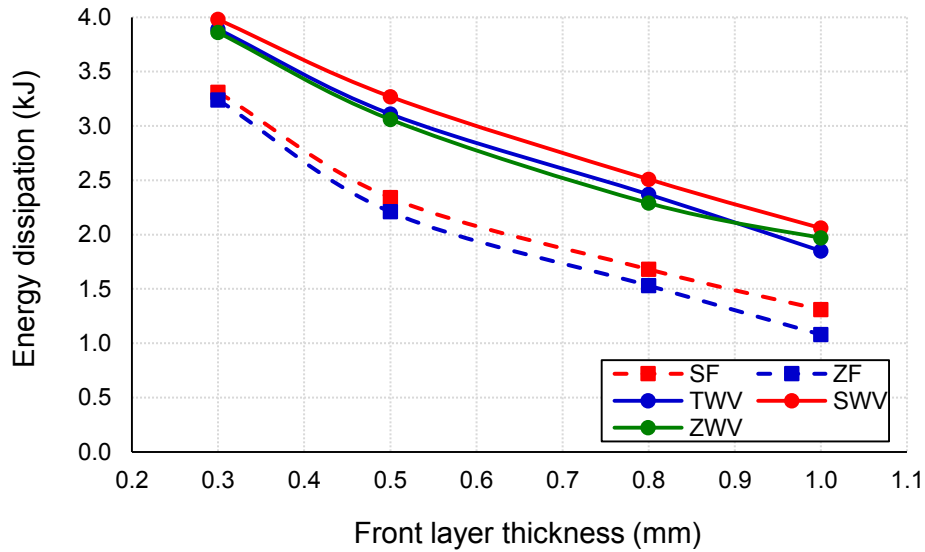


**Figure 5.21** Effect of changing front layer thickness on energy dissipation for proposed panels

## 5.5 Changing Outer Layers' Thickness

Eleven sandwich panels with different core topologies were studied under blast effects where a scaled distance of  $1.26 \text{ m/kg}^{1/3}$  is used. These eleven panels include the six panels used in the validation and the five proposed panels. Relatively, the eleven panels are divided into three honeycomb panels, five folded panels, and three woven panels. In this section, the core thickness is 0.3 mm, while both front and back layers (outer layers) have the same thickness which is changeable. The following four thicknesses are studied: 0.3 mm, 0.5 mm, 0.8 mm, and 1 mm to investigate the effect of changing thickness on the panel's performance.

### 5.5.1 Front Layer Deflection

Figures 5.22, 5.23, and 5.24 show the effect of changing the thickness of outer layers on the front layer deflection for honeycomb, folded, and woven shapes. From the figures, it is noticed that front layer deflection decreases upon increasing outer layers' thicknesses. Comparing deflection when using outer layers of 1 mm thickness with deflection when using outer layers of 0.3 mm thickness, it is noticed that, for honeycomb shape, deflection decreases by 62.2%, 53.3%, and 53.2% for TH, SH, and HH shapes, respectively. As for folded shape, the deflection decreases by 42.6%, 42.7%, 47.4%, 30.1% and 28.9% for DF, YF, TF, SF, and ZF shapes, respectively. Finally, for woven shape, deflection decreases by 48.9%, 40.7%, and 45.3% for TWV, SWV, and

ZWV shapes, respectively. Therefore, upon increasing outer layers' thicknesses, panels become stiffer which results in reducing front layer deflection.

The results of increasing the outer layers' thicknesses (Figures 5.22 to 5.24) are compared with the results of increasing only the front layer thickness for validation models (Figures 5.10 and 5.11) and proposed models (Figure 5.19). From the figures, it is noticed that the deflection of honeycomb shape is reduced by an average of 3.9% for panels of 0.5 mm thickness and is increased by an average of 5.9% and 8% for panels of 0.8 mm and 1 mm thickness, respectively. Whereas the deflection of folded shape is reduced by an average of 1.6% for panels of 0.5 mm thickness and is increased by an average of 3.6% and 5.7% for panels of 0.8 mm and 1 mm thickness, respectively. Finally, the deflection of woven shape is reduced by an average of 2.7% for panels of 0.5 mm thicknesses and is increased by an average of 4.3% and 9.8% for panels of 0.8 mm and 1 mm thickness, respectively. For all considered panels, it is noticed that deflection increases upon increasing both front and back thickness to 0.8 mm and 1 mm when compared to similar panels on increasing the thickness of front layers only to 0.8 mm and 1 mm. This is attributed to the fact that when increasing the thickness of front and back layers while keeping the core thickness as 0.3 mm, more crushing to the core is achieved resulting in more deflection to front layers.

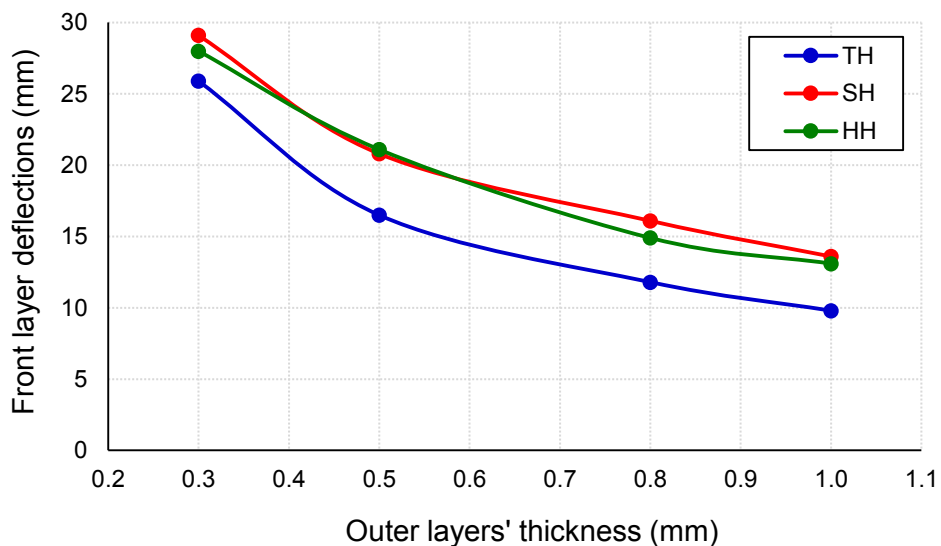


**Figure 5.22** Effect of changing outer layers' thickness on front layer deflection for honeycomb panels

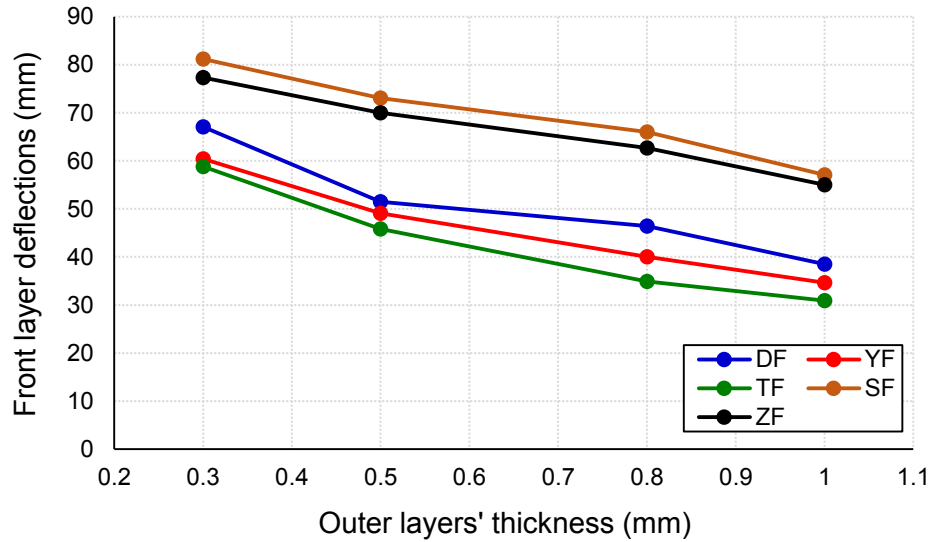


**Figure 5.23** Effect of changing outer layers' thickness on front layer deflection for folded panels

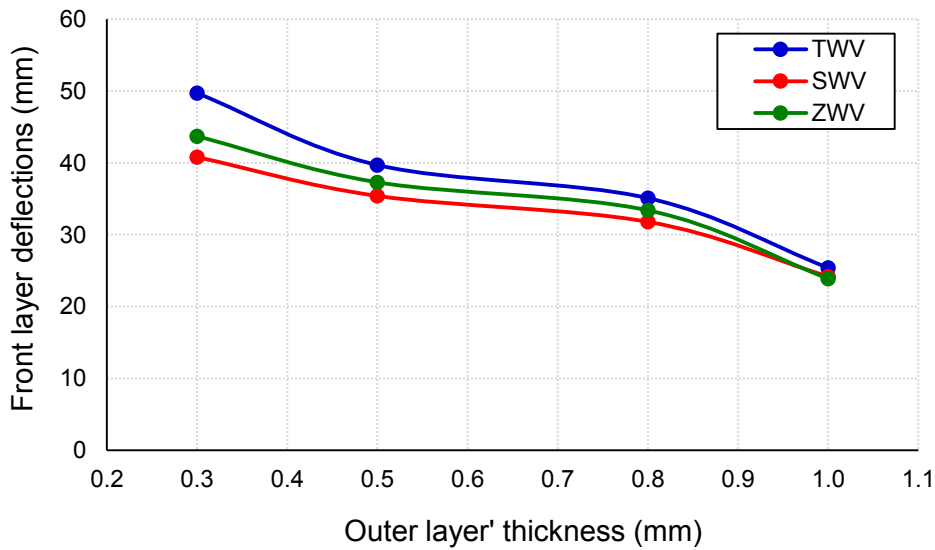


**Figure 5.24** Effect of changing outer layers' thickness on front layer deflection for woven panels

### 5.5.2 Back Layer Deflection

Figures 5.25, 5.26, and 5.27 show the effect of changing the thickness of outer layers on back layer deflection for honeycomb, folded, and woven shapes. From the figures, it is noticed that back layer deflection decreases on increasing outer layers' thicknesses. Comparing the deflection when using outer layers of 1 mm thickness with the deflection when using outer layers of 0.3 mm thickness, it is noticed that, for honeycomb shape, deflection decreases by 65%, 62.1%, and 66.8%

for TH, SH, and HH shapes, respectively. As for folded shape, deflection decreases by 54.9%, 71.7%, and 68.8% for TF, SF, and ZF shapes, respectively. Whereas the deflection of DF and YF shapes has occurred in the opposite direction to the applied blast loads due to the overall behaviour of core elements. Finally, for woven shape, deflection decreases by 55.2%, 55.5%, and 57% for TWV, SWV, and ZWV shapes, respectively. As previously mentioned, panels become stiffer when increasing outer layers' thicknesses which results in reducing back layer deflection.

The results of increasing outer layers' thicknesses (Figures 5.25 to 5.27) are compared with the results of increasing only the front layer thickness for validation models (Figures 5.12 and 5.13) and proposed models (Figure 5.20). From the comparison, the deflection of honeycomb shape is reduced by an average of 16.8%, 29.5%, and 41.1% for 0.5 mm, 0.8 mm, and 1 mm thickness, respectively. Whereas the deflection of folded shape is reduced by an average of 13.9%, 28.1%, and 37.2% for 0.5 mm, 0.8 mm, and 1 mm thickness, respectively. Finally, the deflection of woven shape is reduced by an average of 7.8%, 22.8%, and 33.7% for 0.5 mm, 0.8 mm, and 1 mm thickness, respectively. It is noticed that all the considered shapes have the same performance; the more thickness is used (0.5 mm, 0.8 mm, and 1 mm), the more average reduction in the percentage of deflection is achieved.

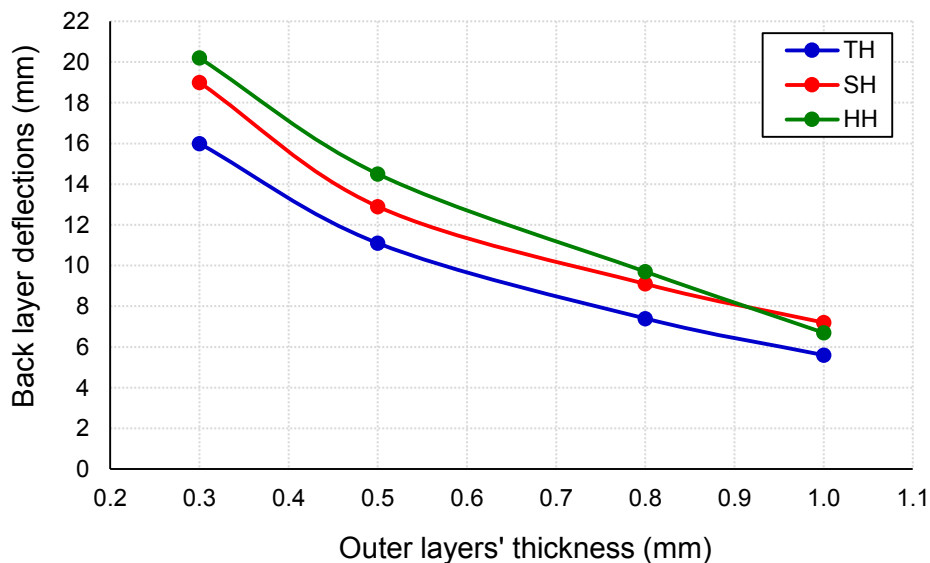


**Figure 5.25** Effect of changing outer layers' thickness on back layer deflection for honeycomb panels

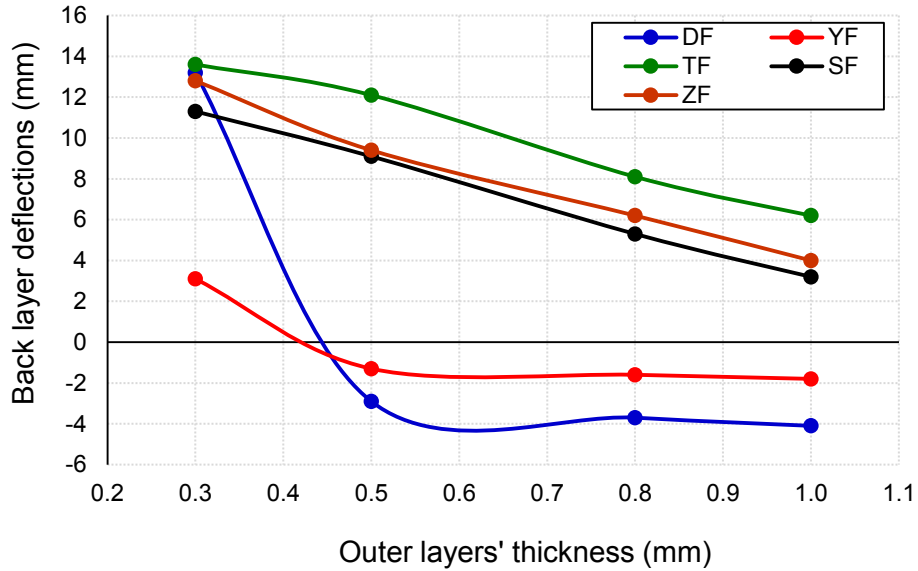


**Figure 5.26** Effect of changing outer layers' thickness on back layer deflection for folded panels

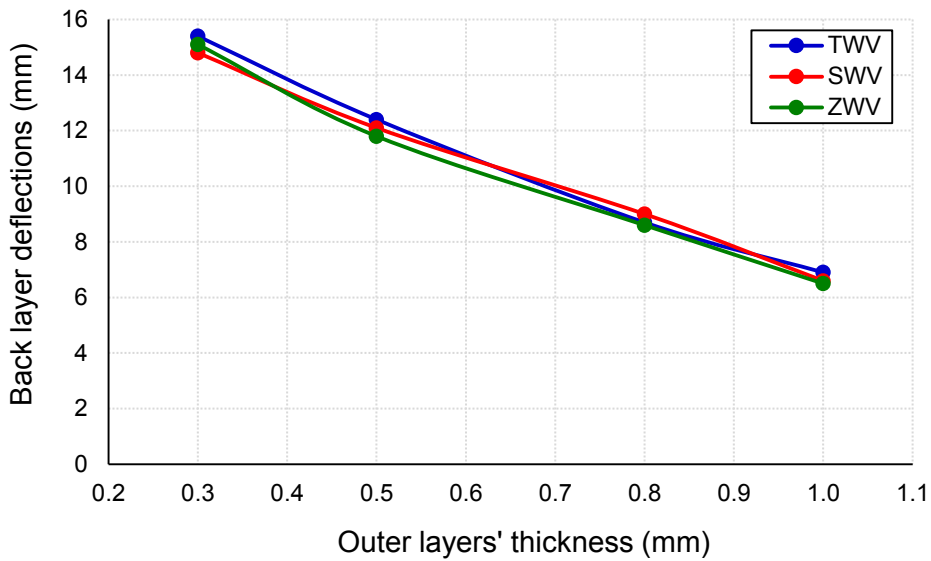


**Figure 5.27** Effect of changing outer layers' thickness on back layer deflection for woven panels

### 5.5.3 Energy Dissipation

Figures 5.28, 5.29, and 5.30 show the effect of changing outer layers' thickness on energy dissipation for honeycomb, folded, and woven shapes. From the figures, it is noticed that energy dissipation decreases upon increasing outer layers' thickness. Comparing deflection when using outer layers of 1 mm thickness with deflection when using outer layers of 0.3 mm thickness, it is noticed that, for honeycomb shape, energy dissipation decreases by 60.5%, 55.4%, and 58.5% for

TH, SH, and HH shapes, respectively. As for folded shape, energy dissipation decreases by 61.6%, 62.7%, 64.4%, 57.1%, and 63.3% for DF, YF, TF, SF, and ZF shapes, respectively. Finally, for woven shape, energy dissipation decreases by 48.3%, 44.7%, and 45.8% for TWV, SWV, and ZWV shapes, respectively. Therefore, the panels become stiffer when increasing outer layers' thickness which results in reducing the crushing in core layers, and hence reducing energy dissipation.

The results of increasing outer layers' thickness (Figures 5.28 to 5.30) are compared with the results of increasing only the front layer thickness for validation models (Figures 5.14 and 5.15) and proposed models (Figure 5.21). From comparison, the energy dissipation of honeycomb shape is reduced by an average of 7% for panels of 0.5 mm thickness and is increased by an average of 9.3% and 11.6% for panels of 0.8 mm and 1 mm thickness, respectively. Whereas the energy dissipation of folded shape is reduced by an average of 14% for panels of 0.5 mm thickness and is increased by an average of 5.1% and 9.4% for panels of 0.8 mm and 1 mm thickness, respectively. Finally, the energy dissipation of woven shape is reduced by an average of 2.2% for panels of 0.5 mm thickness and is increased by an average of 3.2% and 7.2% for panels of 0.8 mm and 1 mm thickness, respectively. Similar to the response of the front layer deflection, it is noticed that energy dissipation increases on increasing the thickness of front and back layers to 0.8 mm and 1 mm when compared to similar panels on increasing the thickness of front layers only to 0.8 mm and 1 mm. This can be attributed to the fact that when increasing the thickness of front and back layers while keeping the core thickness as 0.3 mm, more crushing to the core is achieved resulting in more energy dissipation.

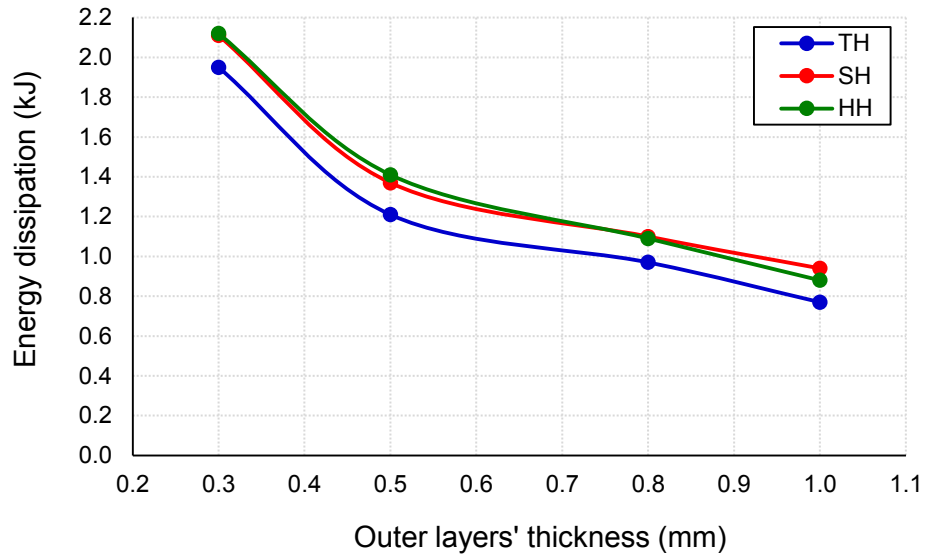


**Figure 5.28** Effect of changing outer layers' thickness on energy dissipation for honeycomb panels

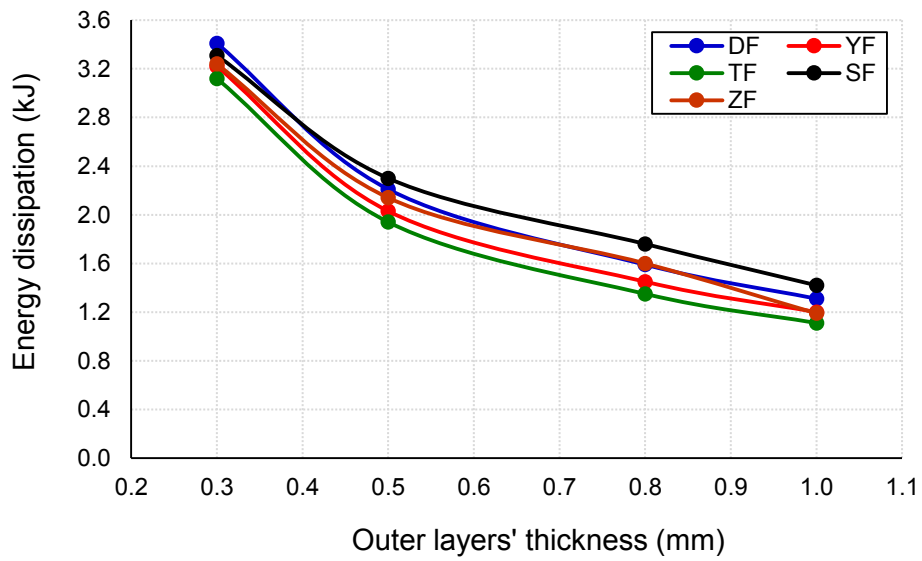


**Figure 5.29** Effect of changing outer layers' thickness on energy dissipation for folded panels

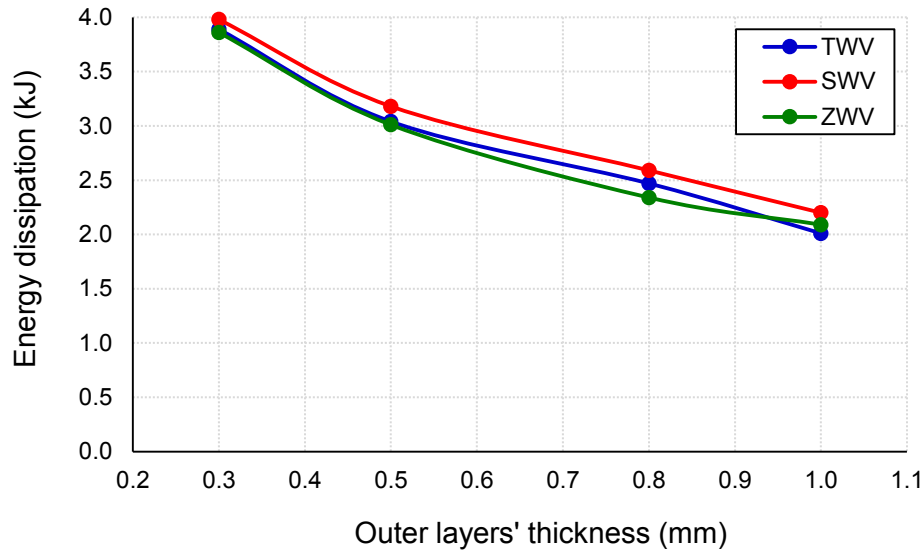


**Figure 5.30** Effect of changing outer layers' thickness on energy dissipation for woven panels

## 5.6 Successive Blast Loads on Same Sandwich Panel

This section illustrates a new scenario where the same sandwich panel is exposed to a second blast load following the first one. Usually, metallic sandwich panels when exposed to blast loads, a core crushing occurs and hence the whole panel is replaced with a new one. However, in this scenario, the two blast loads have occurred to the same sandwich panel before being replaced. Scaled distance for the first and second attacks is  $1.26 \text{ m/kg}^{1/3}$ . This scenario has been applied to the eleven panels studied in the previous section. These eleven panels include the six panels used in the validation and the five proposed panels. Relatively, these eleven panels are composed of three honeycomb panels, five folded panels, and three woven panels. For all panels, the core thickness is 0.3 mm, while both the front and back layers (outer layers) have the same thickness which is changeable. The following four thicknesses have been studied: 0.3 mm, 0.5 mm, 0.8 mm, and 1 mm to investigate the effect of changing thickness on the panel's performance.

### 5.6.1 Front Layer Deflection

Figures 5.31, 5.32, and 5.33 illustrate front layer deflection of honeycomb, folded, and woven shapes upon changing outer layers' thickness. The figures show the deflection of the panels upon being exposed to a second attack (E 2) versus panels exposed to only one attack (E 1). The front layer deflection for (E 2) is a cumulative deflection when exposed to two successive blast loads. It

is noticed that all folded panels with 0.3 mm thickness have suffered from fracture at the edges with no deflection reading. Also, it is noticed that the least front deflection value for folded shape of thickness 0.5mm, 0.8 mm, and 1 mm is obtained by DF shape. It is worth mentioning that, all the folded shapes panel thickness is 100 mm except the DF shape which is 66.7 mm thick as shown in Figure 6.2. Accordingly, the average deflection value excluding DF results is 121.6 mm, 99.8 mm, and 84.3 mm for folded shapes of thickness 0.5 mm, 0.8 mm, and 1 mm, respectively. While the deflection value is 93.1 mm, 79.2 mm, and 65.2 mm for DF shape of 0.5 mm, 0.8 mm, and 1 mm thickness, respectively. While for honeycomb and woven shapes, all panels have sustained the successive blast loads without any fracture. The average deflection value is 83.2 mm, 63.1 mm, 47.3 mm, and 40.7 mm for honeycomb shape of 0.3 mm, 0.5 mm, 0.8 mm, and 1 mm thickness, respectively. On the other hand, the average deflection value is 119.3 mm, 107 mm, 92.4 mm, and 81.5 mm for woven shape of 0.3 mm, 0.5 mm, 0.8 mm, and 1 mm thickness, respectively.

The results obtained from analyzing sandwich panels that were exposed to two successive blast loads are compared with sandwich panels that were exposed to one blast load. It is noticed that deflection increases by an average of 201.3%, 228.2%, 236.4%, and 241.2% for honeycomb shape of 0.3 mm, 0.5 mm, 0.8 mm, and 1 mm thickness, respectively. On the other hand, the deflection increases by an average of 168.6%, 186.6%, 176.9%, and 233% for woven shape of 0.3 mm, 0.5 mm, 0.8 mm, and 1 mm thickness, respectively. While for folded shape, the deflection has increased to the extent that panels have suffered from fracture upon using 0.3 mm thickness for all panels. Whereas, deflection increases by an average of 105.8%, 101.5%, and 94.9% for folded shape of 0.5 mm, 0.8 mm, and 1 mm thickness, respectively. To conclude, honeycomb and woven shapes have shown better blast resistance than folded shapes.

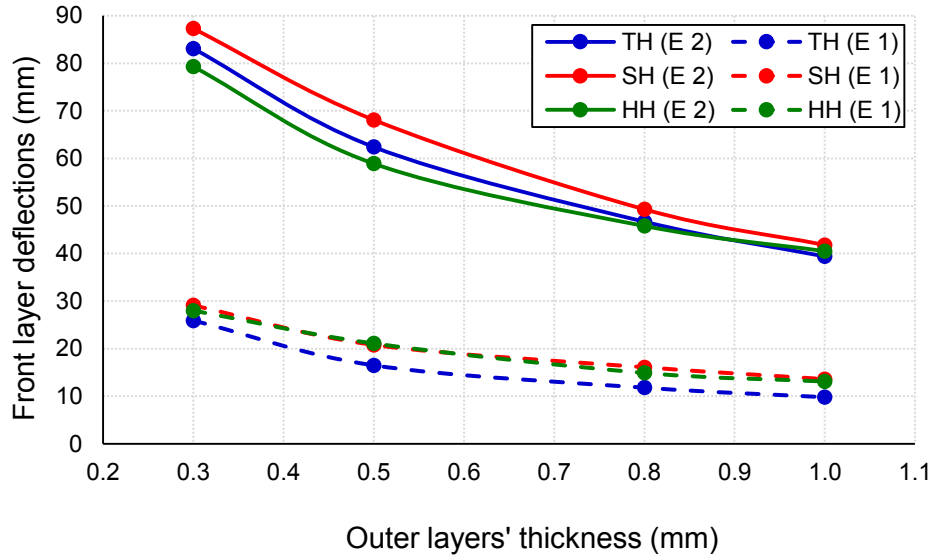


**Figure 5.31** Front layer deflection for honeycomb panels exposed to a second blast load

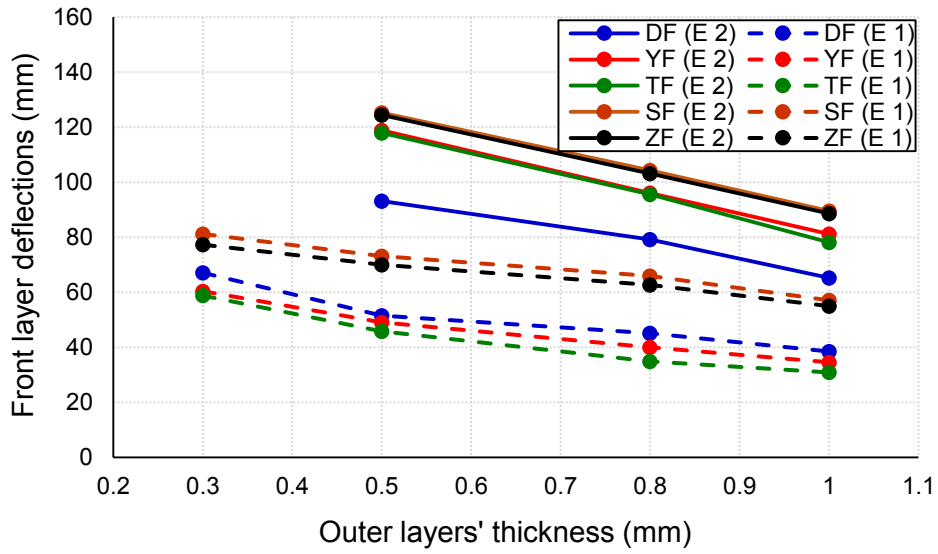


**Figure 5.32** Front layer deflection for folded panels exposed to a second blast load

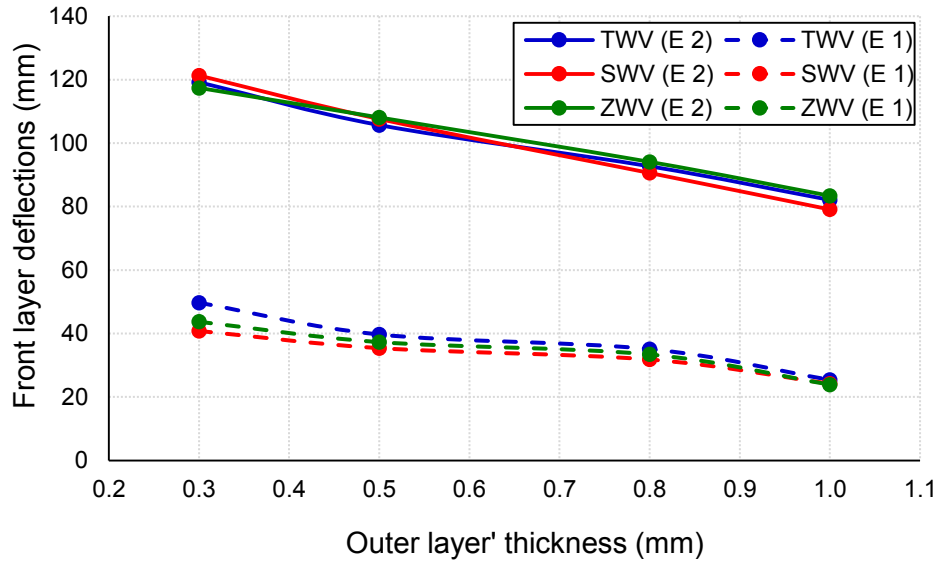


**Figure 5.33** Front layer deflection for woven panels exposed to a second blast load

### 5.6.2 Back Layer Deflection

Figures 5.34, 5.35, and 5.36 illustrate back layer deflection of honeycomb, folded, and woven shapes upon changing outer layers' thickness. The figures show the deflection of the panels upon being exposed to a second attack (E 2) versus panels exposed to only one attack (E 1). The back layer deflection is a cumulative deflection on being exposed to two successive blast loads. The average deflection value is 35.5 mm, 22.5 mm, 14.9 mm, and 10.8 mm for honeycomb shape of 0.3 mm, 0.5 mm, 0.8 mm, and 1 mm thickness, respectively. On the other hand, the average deflection value is 53.2 mm, 26.3 mm, 14.1 mm, and 9.9 mm for folded shape of 0.3 mm, 0.5 mm, 0.8 mm, and 1 mm thickness, respectively. While the average deflection value is 27.5 mm, 20.2 mm, 15.7 mm, and 11 mm for honeycomb shape of 0.3 mm, 0.5 mm, 0.8 mm, and 1 mm thickness, respectively.

The results obtained from analyzing sandwich panels that were exposed to two successive blast loads are compared with sandwich panels that were exposed to one blast load. It is noticed that for honeycomb shape, the deflection increases by an average of 95.1%, 77.1%, 71.8%, and 67.2% on using thickness of 0.3 mm, 0.5 mm, 0.8 mm, and 1 mm, respectively. Based on the comparison, the average percentage of deflection increase for honeycomb panels ranges between 201.3% and 241.2% for front layer and between 67.2% and 95.1% for back layer. Therefore, front layers are

affected more than back layers due to exposure to successive blast loads. On the other hand, and as per the mentioned comparison, the deflection of folded shape excluding DF and YF shapes increases by an average of 328.4%, 183.5%, 114.1%, and 130.8% on using thickness of 0.3 mm, 0.5 mm, 0.8 mm, and 1 mm, respectively. Such exclusion is done because the deflection of DF and YF shapes has occurred in the opposite direction when being exposed to one blast load. As the panels are at its initial stage of damage and due to the overall behaviour of the core elements, deflection has occurred in the opposite direction. Whereas upon being exposed to successive blast loads, the deflection happens in the same direction of the applied blast loads. Due to the above mentioned comparison, it is noticed that the highest average percentage of deflection increase is 328.4% on using panels of 0.3 mm thickness. This can be attributed to the fact that folded panels with 0.3 mm thickness suffer from fracture at the edges resulting in transferring more loads to back layers. Based on the above mentioned comparison, the average percentage of deflection increase for folded panels, excluding panels with 0.3 mm thickness due to its failure, ranges between 94.9% and 105.8% for front layer and between 114.1% and 183.5% for back layer. Therefore, unlike the response of honeycomb shapes, back layers of folded shapes are affected more than front layers due to the exposure to successive blast loads. Finally, as per the mentioned comparison, deflection of woven shape increases by an average of 82.5%, 66.9%, 79.5%, and 65.6% for woven shape of 0.3 mm, 0.5 mm, 0.8 mm, and 1 mm thickness, respectively. Based on the above mentioned comparison, the average percentage of deflection increase for woven panels ranges between 168.6% and 233% for front layer and between 65.6% and 82.5% for back layer. Therefore, similar to the response of honeycomb shapes and unlike the response of folded shapes, front layers of woven shapes are affected more than back layers due to the exposure to successive blast loads.

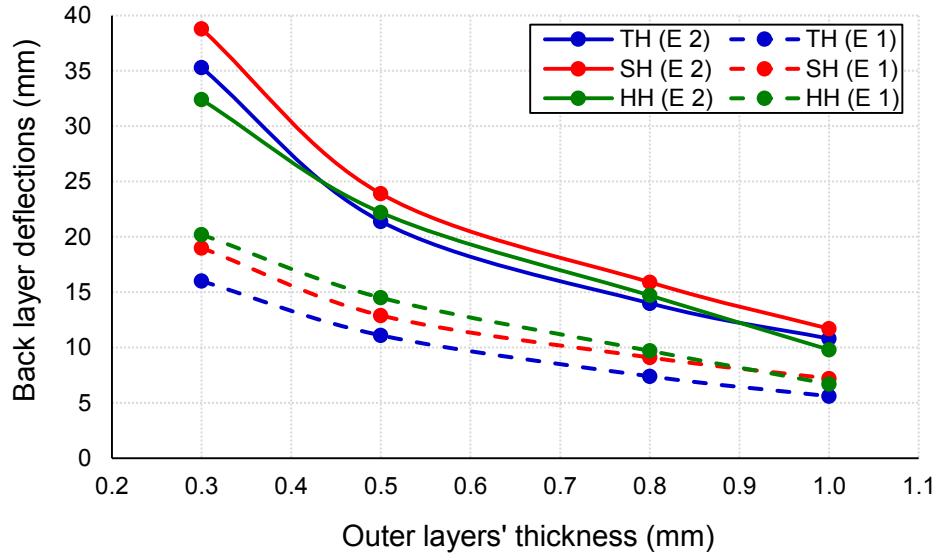


Figure 5.34 Back layer deflection for honeycomb panels exposed to a second blast load

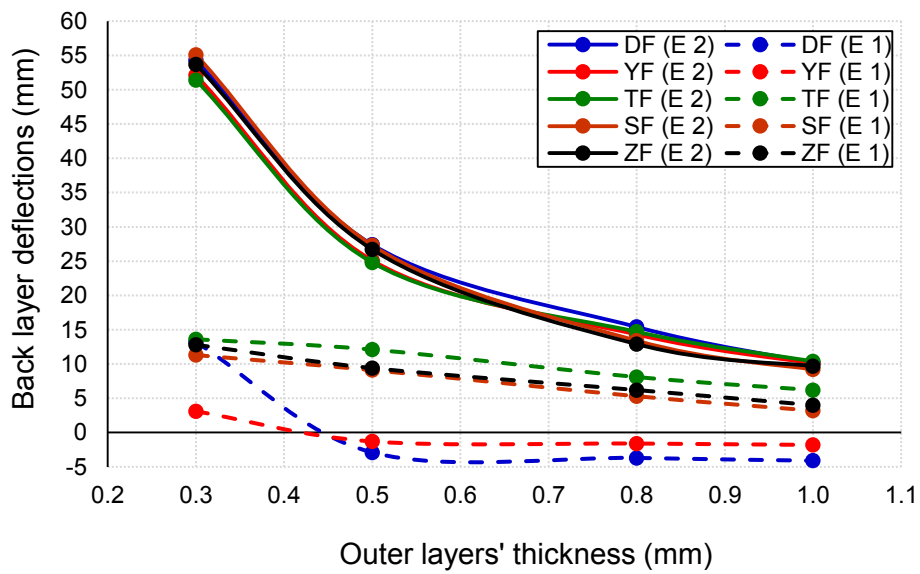
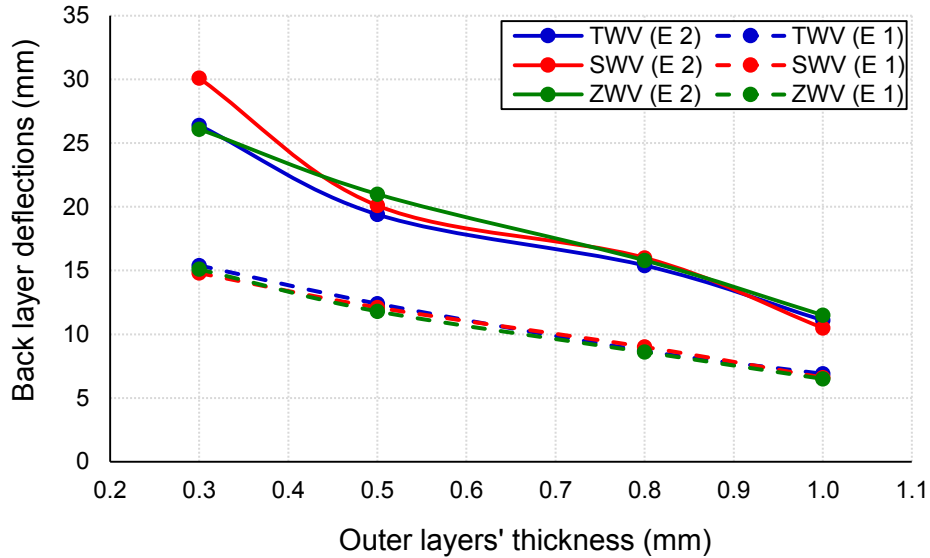


Figure 5.35 Back layer deflection for folded panels exposed to a second blast load



**Figure 5.36** Back layer deflection for woven panels exposed to a second blast load

### 5.6.3 Energy Dissipation

Figures 5.37, 5.38, and 5.39 illustrate energy dissipation of honeycomb, folded, and woven shapes upon changing outer layers' thickness. The figures show the energy dissipation of the panels upon being exposed to a second attack (E 2) versus panels exposed to only one attack (E 1). The energy dissipation is the amount of absorbed energy due to the second attack and is not the cumulative energy dissipation. From the figures, it is noticed that woven shapes have the highest energy dissipation values, followed by folded shapes, and finally honeycomb shapes obtained the least energy dissipation values. The average energy dissipation value is 7.19 kJ, 5.56 kJ, 4.3 kJ, and 3.47 kJ for woven shapes of 0.3 mm, 0.5 mm, 0.8 mm, and 1 mm thickness, respectively. While, the average energy dissipation value is 6.31 kJ, 5 kJ, 3.74 kJ, and 2.91 kJ for folded shapes of 0.3 mm, 0.5 mm, 0.8 mm, and 1 mm thickness, respectively. Finally, the average energy dissipation value is 4.53 kJ, 3.69 kJ, 3.02 kJ, and 2.48 kJ for honeycomb shapes of 0.3 mm, 0.5 mm, 0.8 mm, and 1 mm thickness, respectively. To conclude, upon being exposed to a second attack, woven shapes can dissipate an average of 14.8% more energy than folded shapes and 48% more energy than honeycomb shapes.

The results obtained from analyzing sandwich panels that were exposed to two successive blast loads are compared with sandwich panels that were exposed to one blast load. It is noticed that for honeycomb shapes, the energy dissipation increases by an average of 220.3%, 278.6%, 287.4%,

and 289.1% on using panels of 0.3 mm, 0.5 mm, 0.8 mm, and 1 mm thickness, respectively. For folded shapes, the energy dissipation increases by an average of 193.6%, 236.1%, 243.3%, and 235.6% on using panels of 0.3 mm, 0.5 mm, 0.8 mm, and 1 mm thickness, respectively. Finally for woven shapes, the energy dissipation increases by an average of 183.8%, 180.7%, 174.6%, and 165.3% on using panels of 0.3 mm, 0.5 mm, 0.8 mm, and 1 mm thickness, respectively. Therefore, energy dissipation increases by an average of 224% when exposing sandwich panels to successive blast loads compared with these that were exposed to one blast load only.

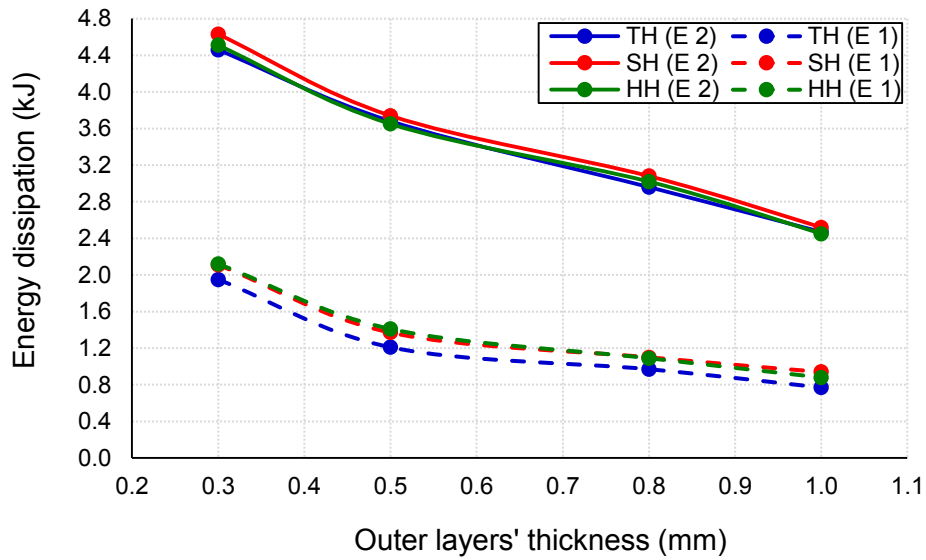


**Figure 5.37** Energy dissipation for honeycomb panels exposed to a second blast load

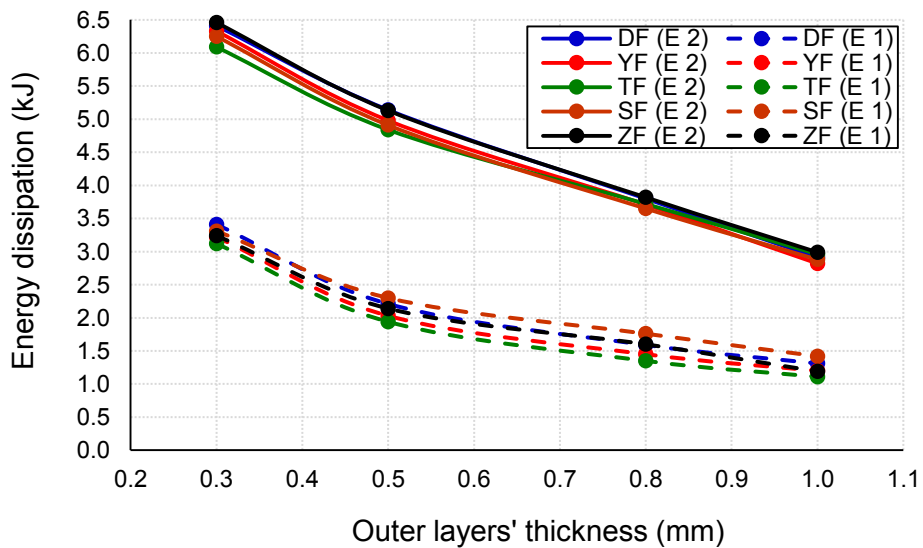


**Figure 5.38** Energy dissipation for folded panels exposed to a second blast load

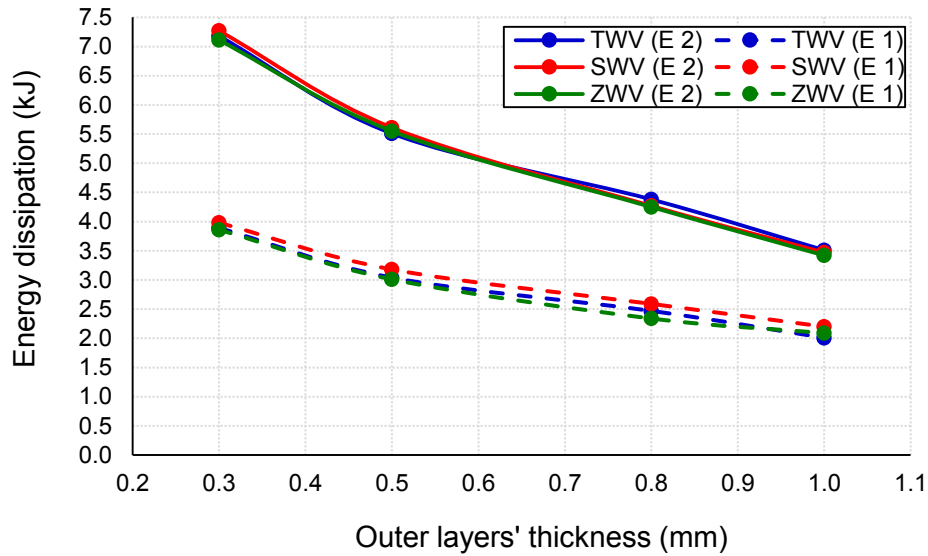


**Figure 5.39** Energy dissipation for woven panels exposed to a second blast load

## 5.7 Changing Scaled Distance

This section illustrates the different scenarios of changing scaled distance. In this study four scaled distances are investigated. Scaled distance of  $1.26 \text{ m/kg}^{1/3}$ ,  $1 \text{ m/kg}^{1/3}$ ,  $0.87 \text{ m/kg}^{1/3}$ , and  $0.79 \text{ m/kg}^{1/3}$  are studied. It is worth mentioning that scaled distance of  $1.26 \text{ m/kg}^{1/3}$  has been represented in section 6.5, while the effect of the other scaled distance will be represented in this section. This scenario was applied to the eleven panels with the eleven different core topologies. These eleven panels include the six panels used in validation and the five proposed panels. Relatively, these eleven panels are composed of three honeycomb panels, five folded panels, and three woven panels. For all panels, core thickness is 0.3 mm, while both the front and back layers (outer layers) have the same thickness which is changeable. The following four thicknesses have been studied: 0.3 mm, 0.5 mm, 0.8 mm, and 1 mm to investigate the effect of changing thickness on panel's performance.

### 5.7.1 Scaled Distance of $1 \text{ m/kg}^{1/3}$

Figures 5.40, 5.41, and 5.42 illustrate front layer deflection of honeycomb, folded, and woven shapes upon using scaled distance of  $1 \text{ m/kg}^{1/3}$  (SD 1) versus upon using scaled distance of 1.26

$\text{m/kg}^{1/3}$  (SD 1.26). It is noticed that DF, SF, and ZF panels with 0.3 mm thickness suffer from fracture at the edges with no deflection reading. The average deflection value is 124.6 mm for YF and TF panels of 0.3 mm thickness. Also, it is noticed that the least front deflection value for folded shape of 0.5mm, 0.8 mm, and 1 mm thickness is obtained by DF shape. It is worth mentioning that, all the folded shape panels thickness is 100 mm except that of DF shape which is 66.7 mm as shown in Figure 5.2. Accordingly, the average deflection value of folded shapes excluding DF results is 114.2 mm, 97.3 mm, and 82.1 mm for panels of 0.5 mm, 0.8 mm, and 1 mm thickness, respectively. Whereas the deflection value is 87.1 mm, 72.1 mm, and 60.4 mm for DF shape of 0.5 mm, 0.8 mm, and 1 mm thickness, respectively. On the other hand, for honeycomb and woven shapes, all panels have sustained the blast loads without any fracture. The average deflection value is 71.8 mm, 56.9 mm, 42.7 mm, and 32.4 mm for honeycomb shapes of 0.3 mm, 0.5 mm, 0.8 mm, and 1 mm thickness, respectively. Whereas the average deflection value is 110.5 mm, 96.4 mm, 80.1 mm, and 67.1 mm for woven shapes of 0.3 mm, 0.5 mm, 0.8 mm, and 1 mm thickness, respectively.

The results obtained for front layer deflection upon using scaled distance of  $1 \text{ m/kg}^{1/3}$  are compared with the results obtained for front layer deflection upon using scaled distance of  $1.26 \text{ m/kg}^{1/3}$ . It is noticed that, the deflection increases by an average of 160.2%, 195.5%, 203.7%, and 171.7% for honeycomb shape of 0.3 mm, 0.5 mm, 0.8 mm, and 1 mm thickness, respectively. On the other hand, the deflection increases by an average of 148.7%, 157.9%, 159.5%, and 173.9% for woven shape of 0.3 mm, 0.5 mm, 0.8 mm, and 1 mm thickness, respectively. While for folded shape, the deflection has increased to the extent that panels have suffered from fracture for DF, SF, and ZF shapes upon using panels with 0.3 mm thickness. Whereas the deflection increases by an average of 94.4%, 95.6% and 92.8% for folded shape of 0.5 mm, 0.8 mm, and 1 mm thickness, respectively. To conclude, all honeycomb and woven shapes in addition to YF and TF shapes—from folded shapes—have shown better blast resistance than DF, SF, and ZF shapes.

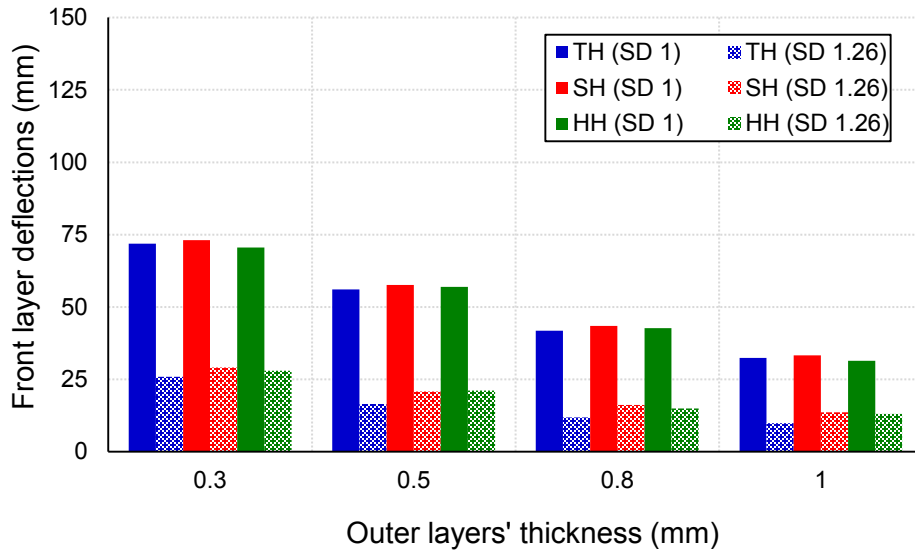


**Figure 5.40** Front layer deflection for honeycomb panels having scaled distance of  $1 \text{ m/kg}^{1/3}$

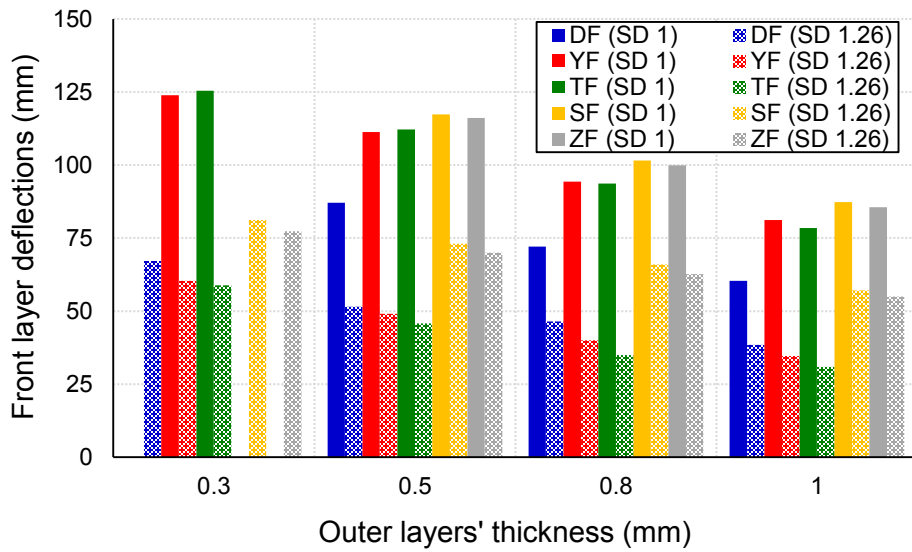


**Figure 5.41** Front layer deflection for folded panels having scaled distance of  $1 \text{ m/kg}^{1/3}$

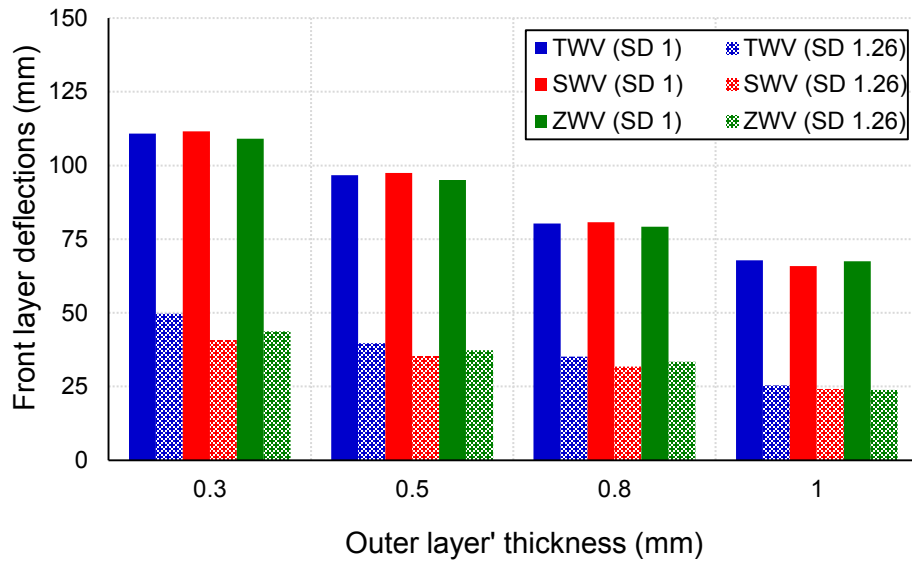


**Figure 5.42** Front layer deflection for woven panels having scaled distance of  $1 \text{ m/kg}^{1/3}$

Figures 6.43, 6.44, and 6.45 illustrate back layer deflection of honeycomb, folded, and woven shapes upon using scaled distance of  $1 \text{ m/kg}^{1/3}$  (SD 1) versus upon using scaled distance of  $1.26 \text{ m/kg}^{1/3}$  (SD 1.26). The average deflection value is 33.3 mm, 20.6 mm, 14.7 mm, and 10.6 mm for honeycomb shape of 0.3 mm, 0.5 mm, 0.8 mm, and 1 mm thickness, respectively. While for the folded shape, it is noticed that DF, SF, and ZF panels with 0.3 mm thickness get higher deflection value comparing to YF and TF shapes. This can be attributed to the fact that DF, SF, and ZF panels with 0.3 mm thickness suffer from fracture at the edges resulting in transferring more loads to back layers. The average deflection value is 40.1 mm for DF, SF, and ZF panels of 0.3 mm thickness, while it is 27.7 mm for YF and TF shapes of 0.3 mm thickness. Whereas the average deflection value is 20.2 mm, 14.3 mm, and 10.6 mm for folded shape of 0.5 mm, 0.8 mm, and 1 mm thickness, respectively. On the other hand, the average deflection value is 26.1 mm, 18.5 mm, 14.2 mm, and 10.1 mm for woven shapes of 0.3 mm, 0.5 mm, 0.8 mm, and 1 mm thickness, respectively.

The results obtained for back layer deflection upon using scaled distance of  $1 \text{ m/kg}^{1/3}$  are compared with the results obtained for back layer deflection upon using scaled distance of  $1.26 \text{ m/kg}^{1/3}$ . It is noticed that for honeycomb shape, the deflection increases by an average of 83.4%, 69.9%, 68.5%, and 65.9% on using thickness of 0.3 mm, 0.5 mm, 0.8 mm, and 1 mm, respectively. Based on the comparison, the average percentage of deflection increase for honeycomb panels ranges between 160.2% and 203.7% for front layer and between 65.9% and 83.4% for back layer.

Therefore, front layers are affected more than back layers upon increasing scaled distance similar to what has happened on the exposure to two successive blast loads. On the other hand, and as per the mentioned comparison, the deflection of folded shape excluding DF and YF shapes increases by an average of 193.4%, 100.3%, 122.5%, and 149.2% on using 0.3 mm, 0.5 mm, 0.8 mm, and 1 mm thickness, respectively. Such exclusion is done because the deflection of DF and YF shapes has occurred in the opposite direction when exposed to one blast load. As the panels are at its initial stage of damage and due to the overall behaviour of core elements, deflection has occurred in the opposite direction. While, on increasing the scaled distance, the deflection occurs in the same direction of the applied blast loads similar to what has happened on being exposed to successive blast loads. Based on the above mentioned comparison, the average percentage of deflection increase for folded panels, excluding panels with 0.3 mm thickness due to its failure, ranges between 92.8% and 95.6% for front layer and between 100.3% and 149.2% for back layer. Therefore, unlike what has happened on using honeycomb shapes, back layers of folded shapes are affected more than front layers upon increasing scaled distance. Finally, as per the mentioned comparison, the deflection of woven shape increases by an average of 73.2%, 53%, 62.4%, and 51.7% for woven shape of 0.3 mm, 0.5 mm, 0.8 mm, and 1 mm thickness, respectively. Based on the above mentioned comparison, the average percentage of deflection increase for woven panels ranges between 148.7% and 173.9% for front layer and between 51.7% and 73.2% for back layer. Therefore, as what has happened on using honeycomb shapes and unlike what has happened on using folded shapes, front layers of woven shapes are affected more than back layers upon increasing scaled distance.

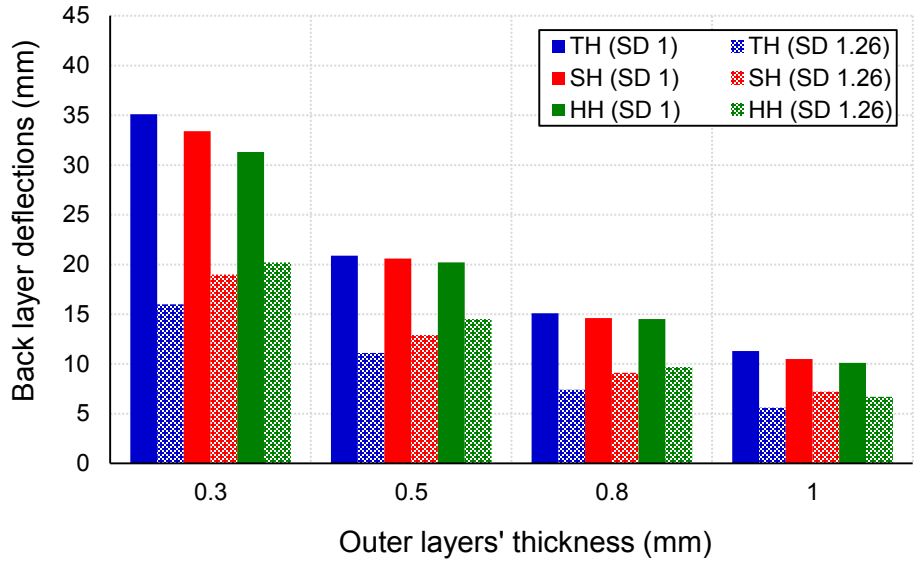


**Figure 5.43** Back layer deflection for honeycomb panels having scaled distance of  $1 \text{ m/kg}^{1/3}$

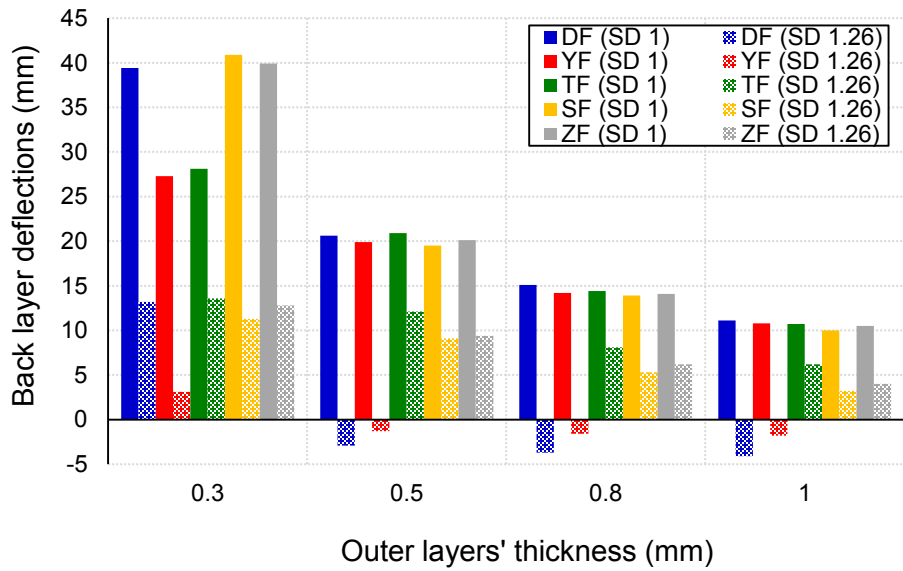


**Figure 5.44** Back layer deflection for folded panels having scaled distance of  $1 \text{ m/kg}^{1/3}$

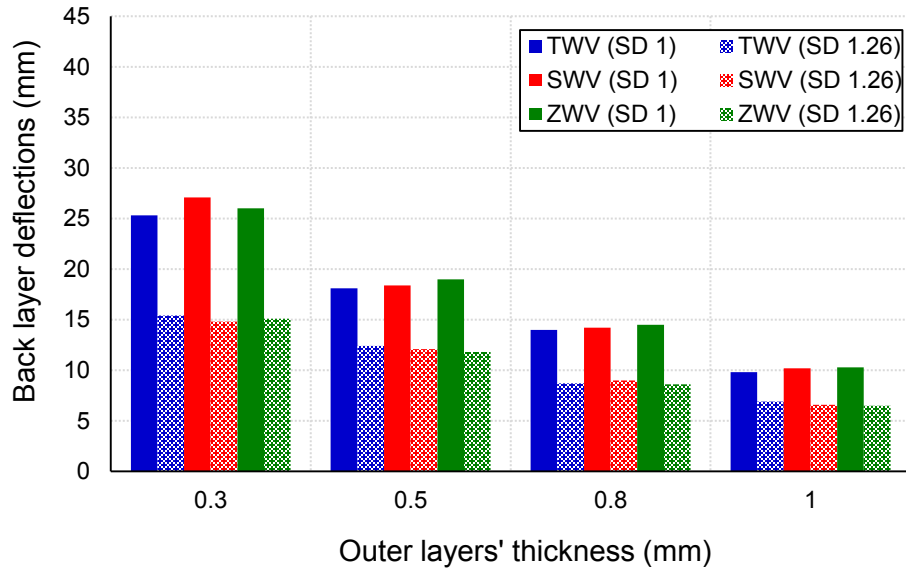


**Figure 5.45** Back layer deflection for woven panels having scaled distance of  $1 \text{ m/kg}^{1/3}$

Figures 5.46, 5.47, and 5.48 illustrate energy dissipation of honeycomb, folded, and woven shapes upon using scaled distance of  $1 \text{ m/kg}^{1/3}$  (SD 1) versus upon using scaled distance of  $1.26 \text{ m/kg}^{1/3}$  (SD 1.26). From the figures, it is noticed that woven shapes have the highest energy dissipation values, followed by folded shapes, and finally honeycomb shapes have obtained the least energy dissipation values. The average energy dissipation value is 10.02 kJ, 7.82 kJ, 5.59 kJ, and 4.10 kJ for woven shapes of 0.3 mm, 0.5 mm, 0.8 mm, and 1 mm thickness, respectively. While, the average energy dissipation value is 8.91 kJ, 6.87 kJ, 4.48 kJ, and 3.53 kJ for folded shapes of 0.3 mm, 0.5 mm, 0.8 mm, and 1 mm thickness, respectively. Finally, the average energy dissipation value is 6.16 kJ, 4.56 kJ, 3.18 kJ, and 2.18 kJ for honeycomb shapes of 0.3 mm, 0.5 mm, 0.8 mm, and 1 mm thickness, respectively. To conclude, upon using scaled distance of  $1 \text{ m/kg}^{1/3}$ , the woven shapes can dissipate an average of 16.8% more energy than folded shapes and 74.5% more energy than honeycomb shapes.

The results obtained for energy dissipation upon using scaled distance of  $1 \text{ m/kg}^{1/3}$  are compared with the results obtained for energy dissipation upon using scaled distance of  $1.26 \text{ m/kg}^{1/3}$ . It is noticed that for honeycomb shapes, the energy dissipation increases by an average of 198.1%, 243.9%, 202.6%, and 154.4% on using panels of 0.3 mm, 0.5 mm, 0.8 mm, and 1 mm thickness, respectively. For folded shapes, the energy dissipation increases by an average of 173.4%, 224.9%, 191.5%, and 185.2% on using panels of 0.3 mm, 0.5 mm, 0.8 mm, and 1 mm thickness,

respectively. Finally for woven shapes, energy dissipation increases by an average of 156.2%, 154.4%, 127.1%, and 95.6% on using panels of 0.3 mm, 0.5 mm, 0.8 mm, and 1 mm thickness, respectively. Therefore, energy dissipation increases by an average of 175.6% upon using scaled distance of  $1 \text{ m/kg}^{1/3}$  compared with scaled distance of  $1.26 \text{ m/kg}^{1/3}$ .

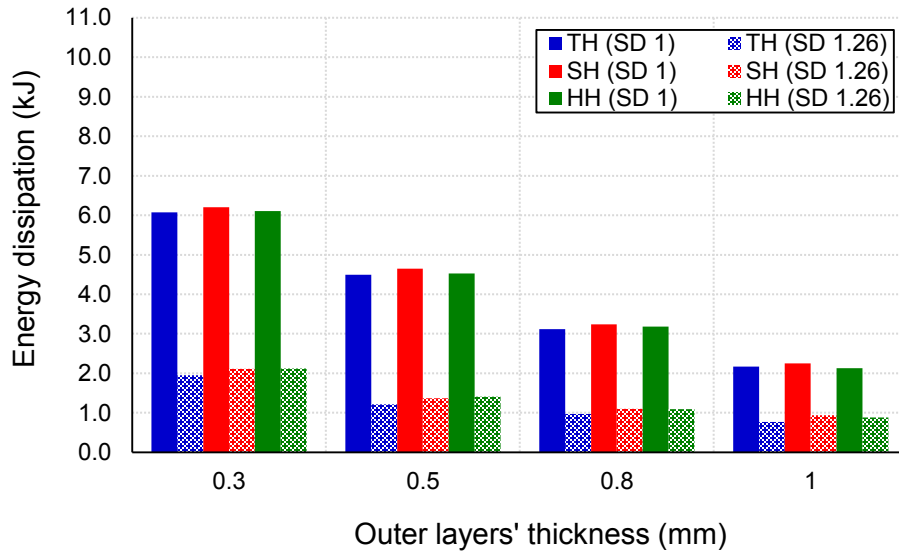


**Figure 5.46** Energy dissipation for honeycomb panels having scaled distance of  $1 \text{ m/kg}^{1/3}$

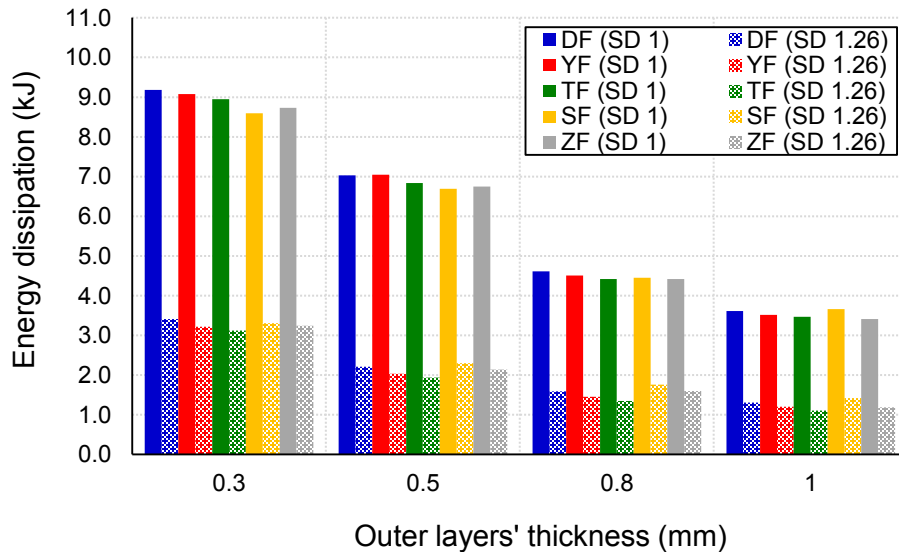


**Figure 5.47** Energy dissipation for folded panels having scaled distance of  $1 \text{ m/kg}^{1/3}$

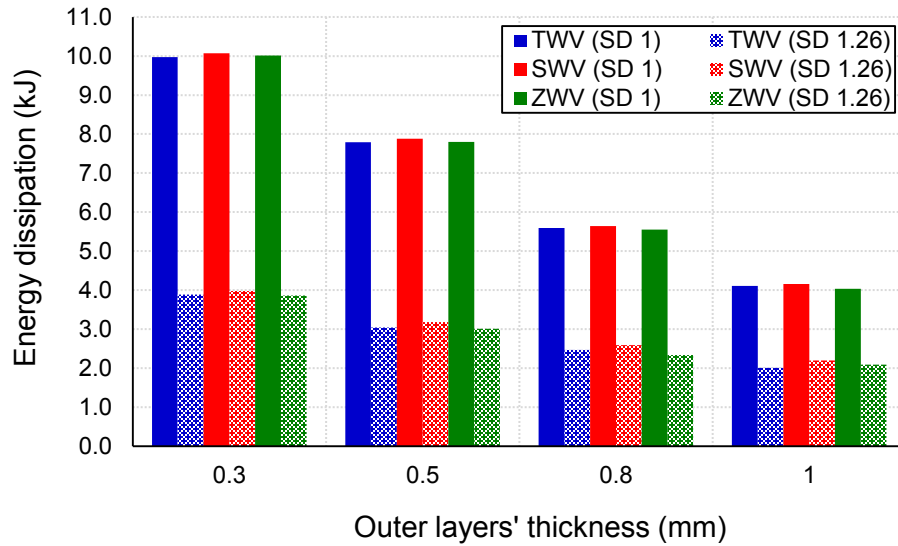


**Figure 5.48** Energy dissipation for woven panels having scaled distance of  $1 \text{ m/kg}^{1/3}$

### 5.7.2 Scaled Distance of $0.87 \text{ m/kg}^{1/3}$

Figures 5.49, 5.50, and 5.51 illustrate front layer deflection of honeycomb, folded, and woven shapes upon using scaled distance of  $0.87 \text{ m/kg}^{1/3}$  (SD 0.87) versus upon using scaled distance of  $1.26 \text{ m/kg}^{1/3}$  (SD 1.26). It is noticed that all folded panels with 0.3 mm thickness suffer from fracture at the edges with no deflection reading. Also, SF and ZF panels with 0.5 mm thickness suffer from fracture at the edges with no deflection reading. Again, it is noticed that the least front deflection value for folded shape of 0.5mm, 0.8 mm, and 1 mm thickness is obtained by DF shape. It is worth mentioning that, all the folded shape panel thickness is 100 mm except DF shape which is 66.7 mm as shown in Figures 5.2. Accordingly, the average deflection value is 132.5 mm for YF and TF panels of 0.5 mm thickness. Whereas, the average deflection value excluding DF results is 120.6 mm and 102.4 mm for folded shapes of 0.8 mm and 1 mm thickness, respectively. While, the deflection value is 100.8 mm, 92.3 mm, and 76.4 mm for DF shape of 0.5 mm, 0.8 mm, and 1 mm thickness, respectively. On the other hand, for honeycomb and woven shapes, all the panels have sustained the blast loads without any fracture. The average deflection value is 114.2 mm, 84.3 mm, 57.6 mm, and 45.6 mm for honeycomb shape of 0.3 mm, 0.5 mm, 0.8 mm, and 1 mm thickness, respectively. Whereas the average deflection value is 132.4 mm, 117.1 mm, 98.3 mm, and 84.6 mm for woven shape of 0.3 mm, 0.5 mm, 0.8 mm, and 1 mm thickness, respectively.

The results obtained for front layer deflection upon using scaled distance of  $0.87 \text{ m/kg}^{1/3}$  are compared with the results obtained for front layer deflection upon using scaled distance of  $1.26 \text{ m/kg}^{1/3}$ . It is noticed that, the deflection increases by an average of 313.9%, 339.6%, 311.4%, and 282.8% for honeycomb shape of 0.3 mm, 0.5 mm, 0.8 mm, and 1 mm thickness, respectively. On the other hand, the deflection increases by an average of 197.7%, 213%, 195.4%, and 245.4% for woven shape of 0.3 mm, 0.5 mm, 0.8 mm, and 1 mm thickness, respectively. While for folded shape, the deflection has increased to the extent that panels have suffered from fracture for all folded shapes upon using panels with 0.3 mm thickness, and for SF and ZF shapes upon using panels with 0.5 mm thickness. Whereas the deflection increases by an average of 142.7% and 135.8% for folded shape of 0.8 mm and 1 mm thickness, respectively. To conclude, honeycomb and woven shapes have shown better blast resistance than folded shapes.

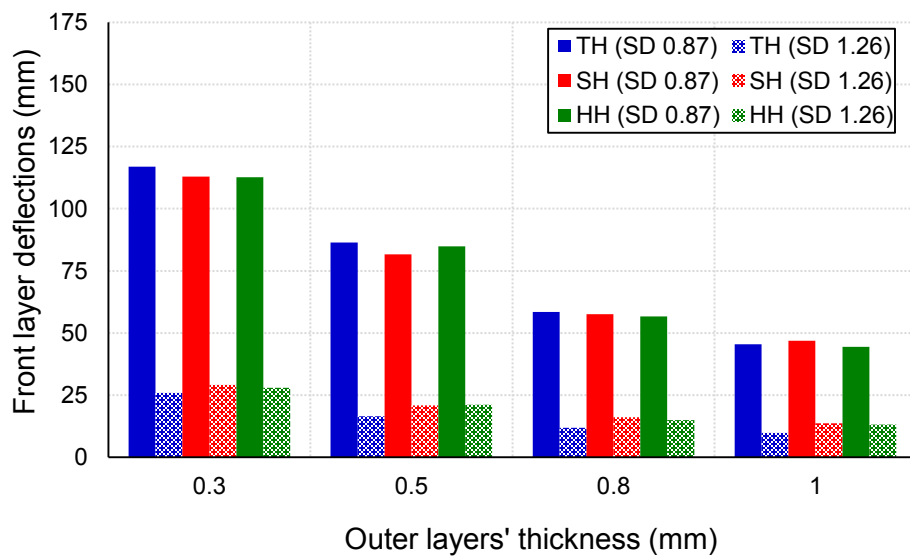


**Figure 5.49** Front layer deflection for honeycomb panels having scaled distance of  $0.87 \text{ m/kg}^{1/3}$

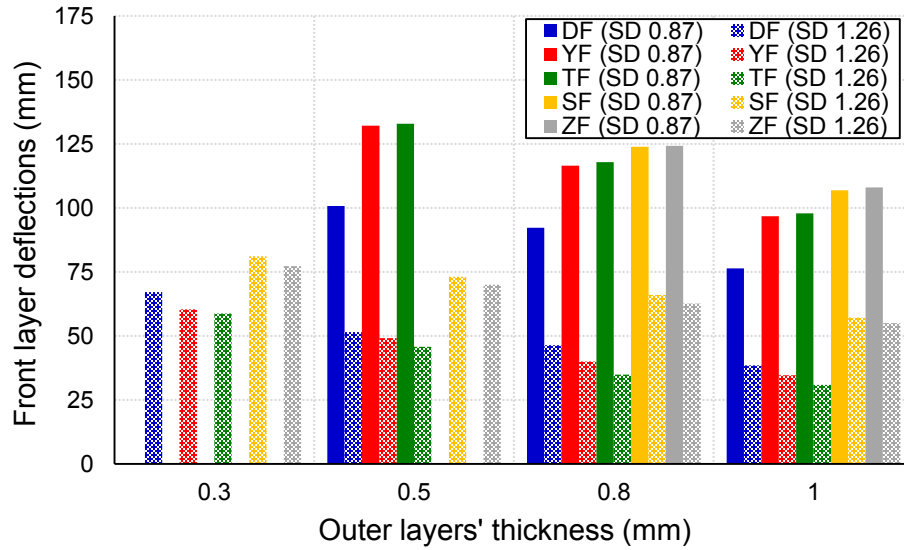


**Figure 5.50** Front layer deflection for folded panels having scaled distance of  $0.87 \text{ m/kg}^{1/3}$

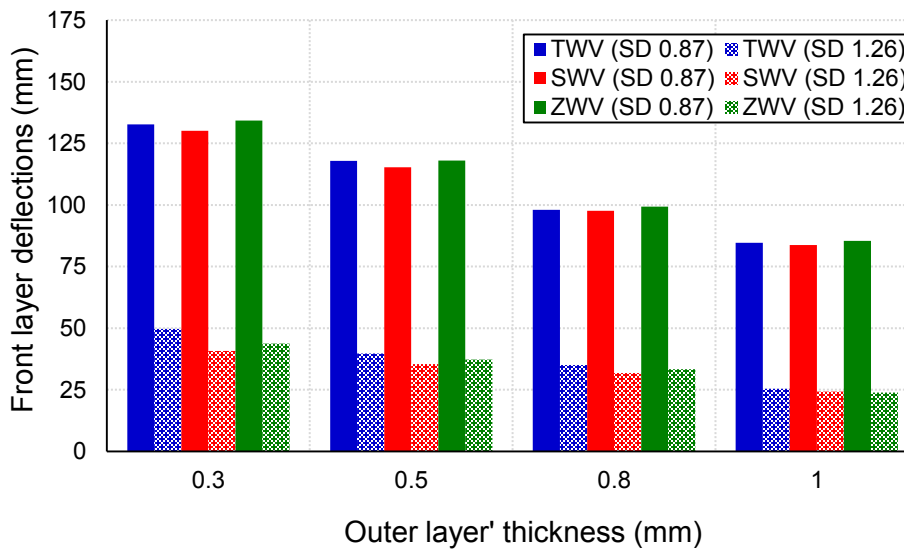


**Figure 5.51** Front layer deflection for woven panels having scaled distance of  $0.87 \text{ m/kg}^{1/3}$

Figures 5.52, 5.53, and 5.54 illustrate back layer deflection of honeycomb, folded, and woven shapes upon using scaled distance of  $0.87 \text{ m/kg}^{1/3}$  (SD 0.87) versus upon using scaled distance of  $1.26 \text{ m/kg}^{1/3}$  (SD 1.26). The average deflection value is 46.4 mm, 36.1 mm, 27.2 mm, and 19.7 mm for honeycomb shape of 0.3 mm, 0.5 mm, 0.8 mm, and 1 mm thickness, respectively. While, the average deflection value is 39.7 mm, 33.5 mm, 23.8 mm, and 16.6 mm for woven shapes of 0.3 mm, 0.5 mm, 0.8 mm, and 1 mm thickness, respectively. On the other hand, for the folded

shapes, it is noticed that all folded panels with 0.3 mm thickness and SF and ZF panels with 0.5 mm thickness get higher deflection value. This can be attributed to the fact that all folded panels with 0.3 mm thickness and SF and ZF panels with 0.5 mm thickness suffer from fracture at the edges resulting in transferring more loads to the back layers. The average deflection value is 60.6 mm for folded panels of 0.3 mm thickness. Whereas, the average deflection value is 50.3 mm for SF and ZF panels of 0.5 mm thickness, while it is 35.4 mm for DF, YF, and TF panels of 0.5 mm thickness. On the other hand, the average deflection value is 24.2 mm and 17.1 mm for folded shape of 0.8 mm and 1 mm thickness, respectively.

The results obtained for back layer deflection upon using scaled distance of  $0.87 \text{ m/kg}^{1/3}$  are compared with the results obtained for back layer deflection upon using scaled distance of  $1.26 \text{ m/kg}^{1/3}$ . It is noticed that for honeycomb shape, the deflection increases by an average of 155.1%, 176.7%, 216.6%, and 206.8% on using panels of 0.3 mm, 0.5 mm, 0.8 mm, and 1 mm thickness, respectively. Based on the comparison, the average percentage of deflection increase for honeycomb panels ranges between 282.8% and 339.6% for front layer and between 155.1% and 216.6% for back layer. Therefore, front layers are affected more than back layers upon increasing scaled distance similar to what has happened on being exposed to two successive blast loads. On the other hand, and as per the mentioned comparison, the deflection of folded shape excluding DF and YF shapes increases by an average of 384.9%, 324.7%, 279.4%, and 308.5% on using panels of 0.3 mm, 0.5 mm, 0.8 mm, and 1 mm thickness, respectively. Such exclusion is done because the deflection of DF and YF shapes has occurred in the opposite direction when exposed to one blast load. As the panels are at its initial stage of damage and due to the overall behaviour of core elements, deflection has occurred in the opposite direction. While, on increasing the scaled distance, the deflection is in the same direction of the applied blast loads similar to what has happened on being exposed to successive blast loads. Based on the above mentioned comparison, the average percentage of deflection increase for folded panels, excluding panels with 0.3 mm and 0.5 mm thickness due to its failure, ranges between 135.8% and 142.7% for front layer and between 279.4% and 308.5% for back layer. Therefore, unlike what has happened on using honeycomb shapes, back layers of folded shapes are affected more than front layers upon increasing scaled distance. Finally, as per the mentioned comparison, the deflection of woven shape increases by an average of 162.9%, 177.7%, 172%, and 148.6% for woven shape of 0.3 mm, 0.5 mm, 0.8 mm, and 1 mm thickness, respectively. Based on the above mentioned comparison, the average percentage

of deflection increase for woven panels ranges between 195.4% and 245.4% for front layer and between 148.6% and 177.7% for back layer. Therefore, as what has happened on using honeycomb shapes and unlike what has happened on using folded shapes, the front layers of woven shapes are affected more than the back layers upon increasing scaled distance.

The results obtained for back layer deflection upon using scaled distance of  $0.87 \text{ m/kg}^{1/3}$  (Figures 5.52 to 5.54) are compared with the results obtained for back layer deflection upon using scaled distance of  $1 \text{ m/kg}^{1/3}$  (Figures 5.43 to 5.45). It is noticed that for honeycomb shape, the deflection increases by an average of 39.8%, 75.4%, 84.8%, and 85.6% on using panels of 0.3 mm, 0.5 mm, 0.8 mm, and 1 mm thickness, respectively. While, the deflection of folded shape increases by an average of 78.6%, 105.4%, 68.6%, and 60.4% on using panels of 0.3 mm, 0.5 mm, 0.8 mm, and 1 mm thickness, respectively. Finally, the deflection of woven shape increases by an average of 52.1%, 81.7%, 67.5%, and 64.2% on using panels of 0.3 mm, 0.5 mm, 0.8 mm, and 1 mm thickness, respectively. To conclude, back layer deflection increases by an average of 227% upon using scaled distance of  $0.87 \text{ m/kg}^{1/3}$  compared with scaled distance of  $1.26 \text{ m/kg}^{1/3}$ . Whereas, it increases by an average of 72% upon using scaled distance of  $0.87 \text{ m/kg}^{1/3}$  compared with scaled distance of  $1 \text{ m/kg}^{1/3}$ .

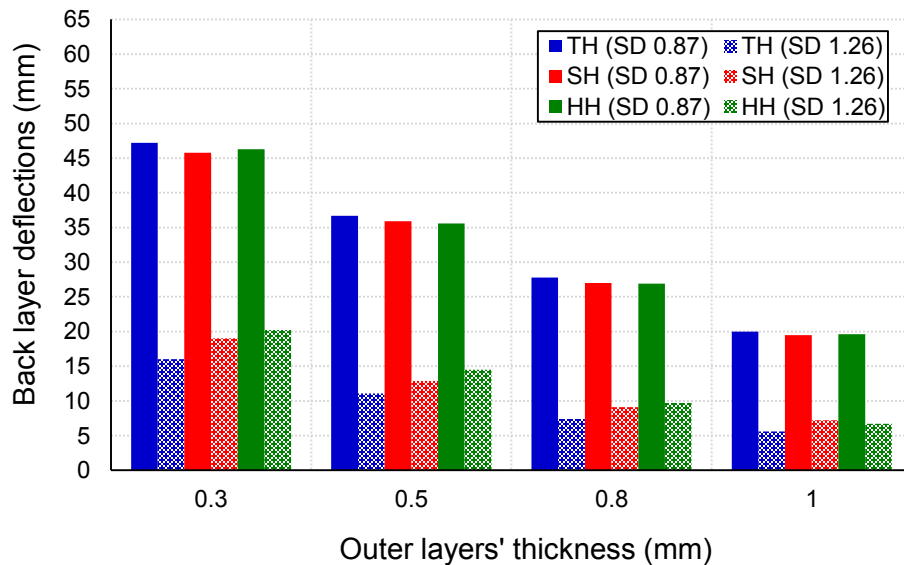


**Figure 5.52** Back layer deflection for honeycomb panels having scaled distance of  $0.87 \text{ m/kg}^{1/3}$

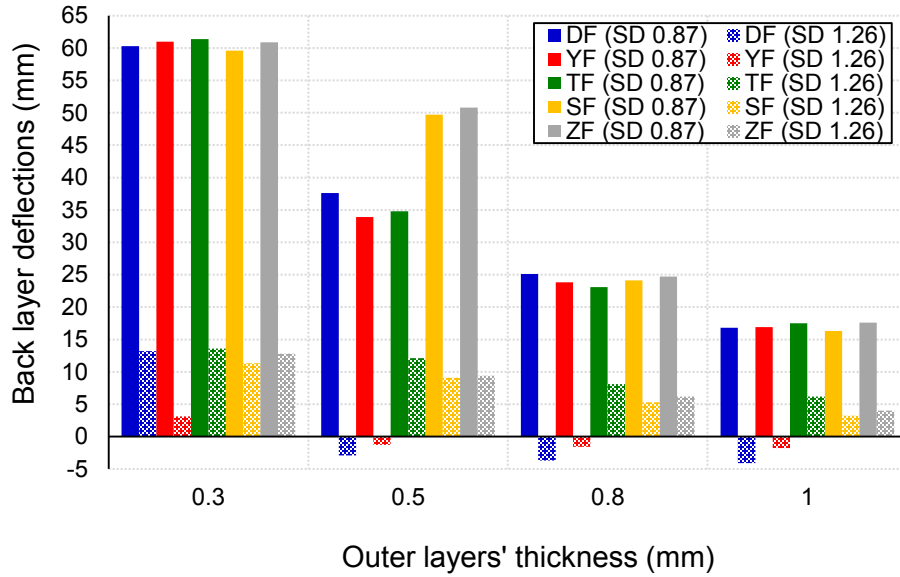


**Figure 5.53** Back layer deflection for folded panels having scaled distance of  $0.87 \text{ m/kg}^{1/3}$

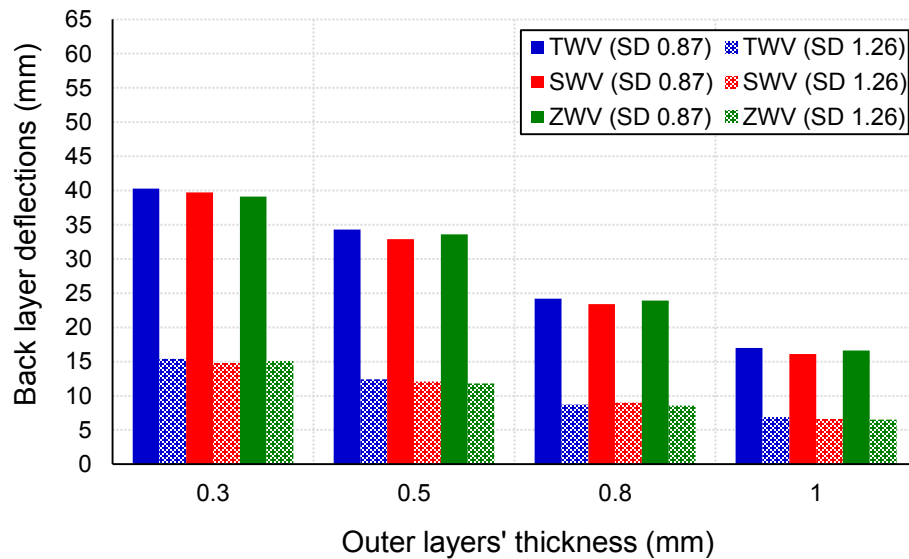


**Figure 5.54** Back layer deflection for woven panels having scaled distance of  $0.87 \text{ m/kg}^{1/3}$

Figures 5.55, 5.56, and 5.57 illustrate energy dissipation of honeycomb, folded, and woven shapes upon using scaled distance of  $0.87 \text{ m/kg}^{1/3}$  (SD 0.87) versus upon using scaled distance of  $1.26 \text{ m/kg}^{1/3}$  (SD 1.26). From the figures, it is noticed that woven shapes have the highest energy dissipation values, followed by folded shapes, and finally honeycomb shapes obtained the least energy dissipation values. The average energy dissipation value is 17.56 kJ, 12.6 kJ, 8.41 kJ, and 6.75 kJ for woven shapes of 0.3 mm, 0.5 mm, 0.8 mm, and 1 mm thickness, respectively. Whereas

the average energy dissipation value is 16.69 kJ, 11.79 kJ, 7.51 kJ, and 5.92 kJ for folded shapes of 0.3 mm, 0.5 mm, 0.8 mm, and 1 mm thickness, respectively. Finally, the average energy dissipation value is 12.5 kJ, 8.2 kJ, 5.55 kJ, and 4.27 kJ for honeycomb shapes of 0.3 mm, 0.5 mm, 0.8 mm, and 1 mm thickness, respectively. To conclude, upon using scaled distance of  $0.87 \text{ m/kg}^{1/3}$ , the woven shapes can dissipates an average of 9.5% more energy than folded shapes and 51% more energy than honeycomb shapes.

The results obtained for energy dissipation upon using scaled distance of  $0.87 \text{ m/kg}^{1/3}$  are compared with the results obtained of energy dissipation upon using scaled distance of  $1.26 \text{ m/kg}^{1/3}$ . It is noticed that for honeycomb shapes, energy dissipation increases by an average of 508.9%, 521.8%, 428.5%, and 398.1% on using panels of 0.3 mm, 0.5 mm, 0.8 mm, and 1 mm thickness, respectively. For folded shapes, the energy dissipation increases by an average of 412.3%, 457.5%, 389.2%, and 379.1% on using panels of 0.3 mm, 0.5 mm, 0.8 mm, and 1 mm thickness, respectively. Finally for woven shapes, energy dissipation increases by an average of 349.1%, 309.8%, 241.5%, and 221.8% on using panels of 0.3 mm, 0.5 mm, 0.8 mm, and 1 mm thickness, respectively. Therefore, energy dissipation increases by an average of 384.8% upon using scaled distance of  $0.87 \text{ m/kg}^{1/3}$  compared with scaled distance of  $1.26 \text{ m/kg}^{1/3}$ .

The results obtained for energy dissipation upon using scaled distance of  $0.87 \text{ m/kg}^{1/3}$  (Figures 5.55 to 5.57) are compared with the results obtained for energy dissipation upon using scaled distance of  $1 \text{ m/kg}^{1/3}$  (Figures 5.46 to 5.48). It is noticed that for honeycomb shapes, the energy dissipation increases by an average of 104.5%, 80.8%, 74.5%, and 95.7% on using panels of 0.3 mm, 0.5 mm, 0.8 mm, and 1 mm thickness, respectively. For folded shapes, energy dissipation increases by an average of 87.4%, 71.7%, 67.5%, and 67.4% on using panels of 0.3 mm, 0.5 mm, 0.8 mm, and 1 mm thickness, respectively. Finally for woven shapes, energy dissipation increases by an average of 75.3%, 61.1%, 50.4%, and 64.5% on using panels of 0.3 mm, 0.5 mm, 0.8 mm, and 1 mm thickness, respectively. Therefore, energy dissipation increases by an average of 75.1% upon using scaled distance of  $0.87 \text{ m/kg}^{1/3}$  compared with scaled distance of  $1 \text{ m/kg}^{1/3}$ .

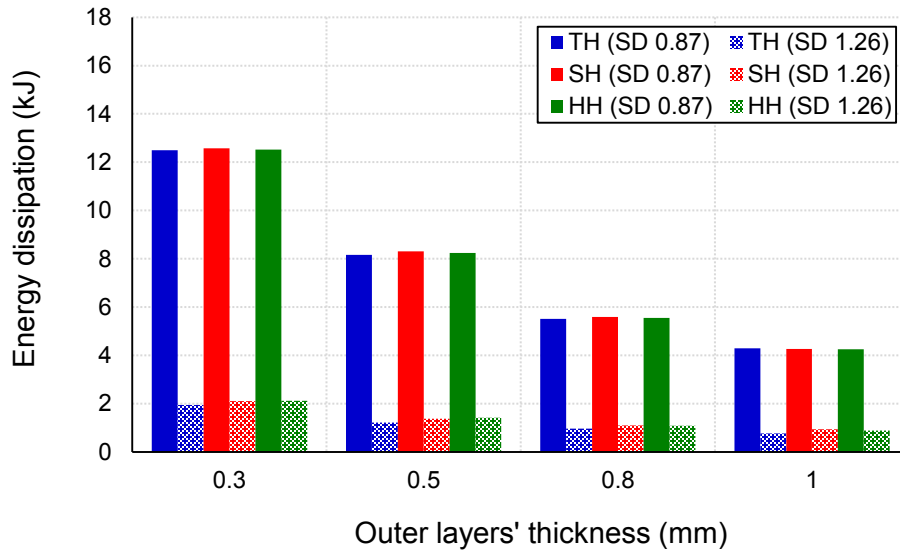


**Figure 5.55** Energy dissipation for honeycomb panels having scaled distance of  $0.87 \text{ m/kg}^{1/3}$

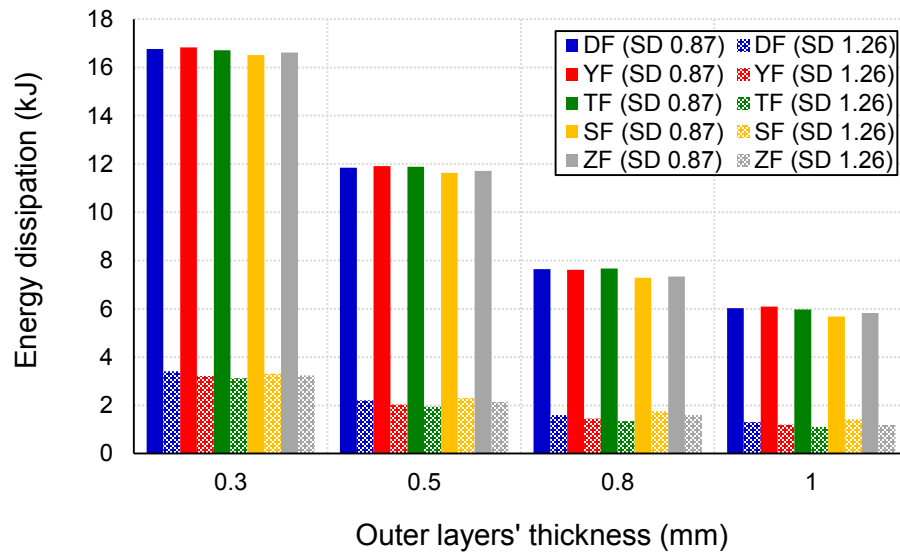


**Figure 5.56** Energy dissipation for folded panels having scaled distance of  $0.87 \text{ m/kg}^{1/3}$

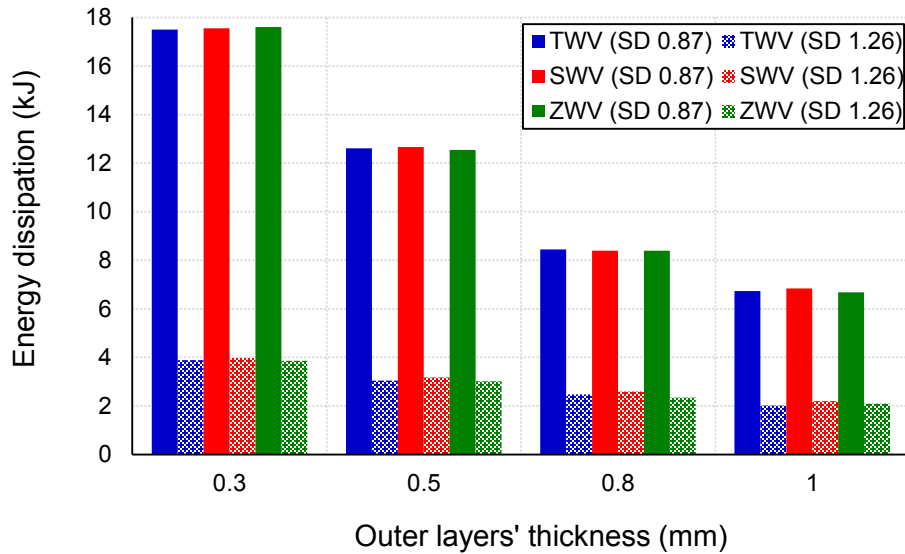


**Figure 5.57** Energy dissipation for woven panels having scaled distance of  $0.87 \text{ m/kg}^{1/3}$

### 5.7.3 Scaled Distance of $0.79 \text{ m/kg}^{1/3}$

Figures 5.58, 5.59, and 5.60 illustrate front layer deflection of honeycomb, folded, and woven shapes upon using scaled distance of  $0.79 \text{ m/kg}^{1/3}$  (SD 0.79) versus upon using scaled distance of  $1.26 \text{ m/kg}^{1/3}$  (SD 1.26). It is noticed that all folded panels in addition to TH, TWV, and ZWV—from honeycomb and woven panels—with 0.3 mm thickness suffer from fracture at the edges with no deflection reading. Also, DF, SF, and ZF panels with 0.5 mm thickness suffer from fracture at the edges with no deflection reading. For honeycomb shapes, the average deflection value is 133.4 mm for SH and HH panels of 0.3 mm thickness. While, the average deflection value is 103.9 mm, 73.2 mm, and 59.2 mm for honeycomb shape of 0.5 mm, 0.8 mm, and 1 mm thickness, respectively. For folded shapes, it is noticed that the least front deflection value for folded shape of 0.8 mm and 1 mm thickness is obtained by DF shape. It is worth mentioning that all folded shape panels are 100 mm thick except DF shape which is 66.7 mm thick as shown in Figure 5.2. Accordingly, the average deflection value is 142.5 mm for YF and TF panels of 0.5 mm thickness. Whereas, the average deflection value excluding DF results is 126.6 mm and 116 mm for folded shapes of 0.8 mm and 1 mm thickness, respectively. While, the deflection value is 102.9 mm and 89.9 mm for DF shape of 0.8 mm and 1 mm thickness, respectively. For woven shapes, the deflection value is 139.3 mm for SWV panel of 0.3 mm thickness. While, the average deflection

value is 123.3 mm, 109.7 mm, and 100 mm for honeycomb shape of 0.5 mm, 0.8 mm, and 1 mm thickness, respectively.

The results obtained for front layer deflection upon using scaled distance of  $0.79 \text{ m/kg}^{1/3}$  are compared with the results obtained for front layer deflection upon using scaled distance of  $1.26 \text{ m/kg}^{1/3}$ . For honeycomb shapes, the deflection has increased to the extent that TH panel of 0.3 mm thickness has suffered from fracture. Whereas, the deflection increases by an average of 440.4%, 421.6%, and 397.1% for honeycomb shape of 0.5 mm, 0.8 mm, and 1 mm thickness, respectively. For folded shapes, the deflection has increased to the extent that panels have suffered from fracture for all folded shapes upon using panels with 0.3 mm thickness and DF, SF, and ZF shapes upon using panels with 0.5 mm thickness. Whereas, the deflection increases by an average of 158.3% and 170.9% for folded shape of 0.8 mm and 1 mm thickness, respectively. For woven shapes the deflection has increased to the extent that TWV and ZWV panels of 0.3 mm thickness have suffered from fracture. Whereas, the deflection increases by an average of 229.8%, 228.6%, and 308.3% for woven shape of 0.5 mm, 0.8 mm, and 1 mm thickness, respectively. To conclude, SH, HH, and SWV have shown better blast resistance among all panels considered in this study.

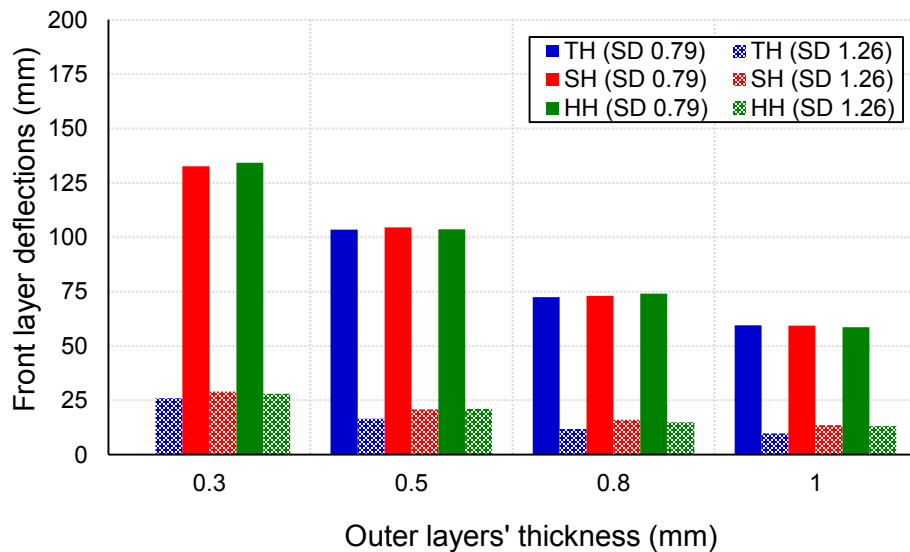


**Figure 5.58** Front layer deflection for honeycomb panels having scaled distance of  $0.79 \text{ m/kg}^{1/3}$

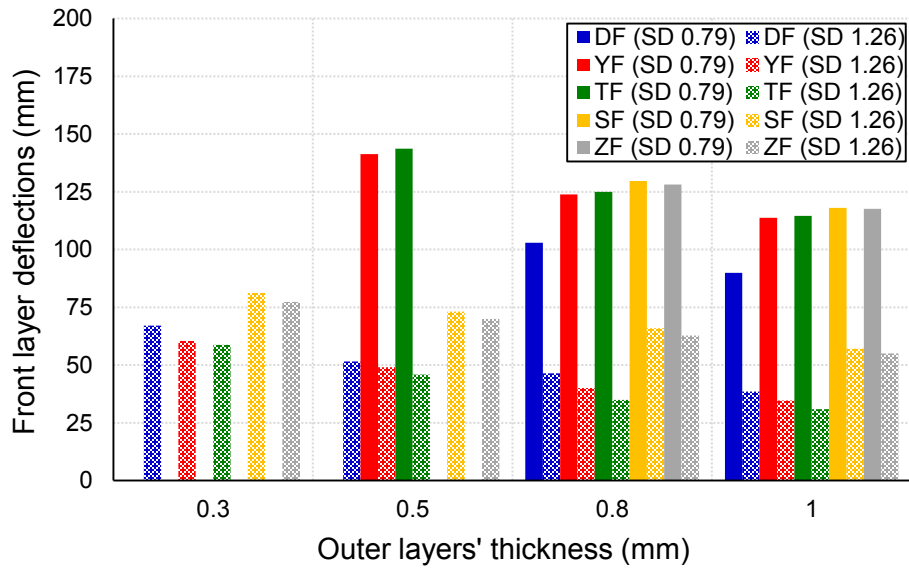


**Figure 5.59** Front layer deflection for folded panels having scaled distance of  $0.79 \text{ m/kg}^{1/3}$

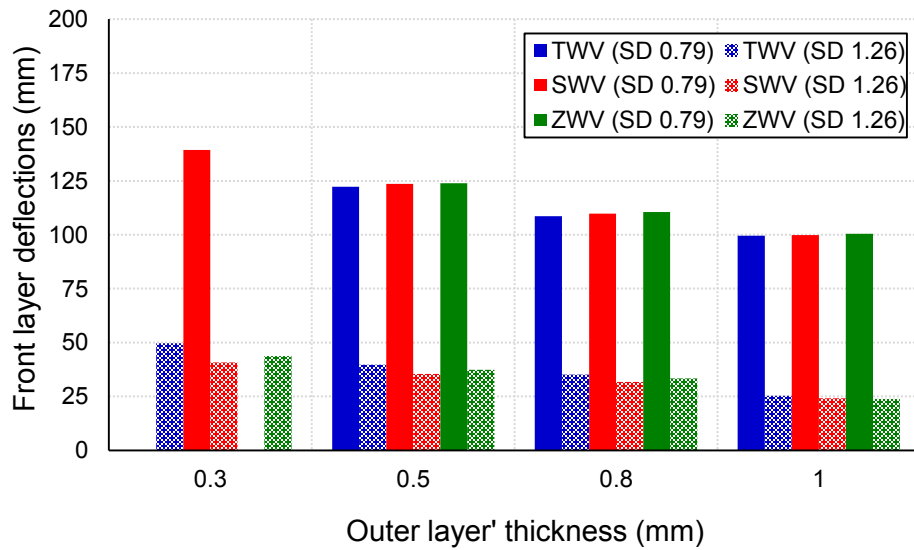


**Figure 5.60** Front layer deflection for woven panels having scaled distance of  $0.79 \text{ m/kg}^{1/3}$

Figures 5.61, 5.62, and 5.63 illustrate back layer deflection of honeycomb, folded, and woven shapes upon using scaled distance of  $0.79 \text{ m/kg}^{1/3}$  (SD 0.79) versus upon using scaled distance of  $1.26 \text{ m/kg}^{1/3}$  (SD 1.26). For honeycomb shapes, it is noticed that TH panel with 0.3 mm thickness gets higher deflection value due to the fracture that occurs at the edges of its front layer. Therefore, more loads are transferred to the back layer. However, unlike folded and woven shapes, honeycomb has high stiffness that already allows a lot of loads to be transferred to the back layers.

As a result, at 0.3 mm thickness, there is a slight deflection difference of 6.8% between TH panel—that has suffered from front layer fracture—and other honeycomb panels (SH and HH)—suffered no fracture. The deflection value is 69.1 mm for TF shape of 0.3 mm thickness, while the average deflection value is 64.7 mm of SH and HH shapes of 0.3 mm thickness. Whereas, the average deflection value is 51.4 mm, 39.3 mm, and 30 mm for honeycomb shape of 0.5 mm, 0.8 mm, and 1 mm thickness, respectively. For folded shapes, panels that suffered from fracture including all the panels with 0.3 mm thickness and DF, SF, and ZF panels with 0.5 mm thickness get high deflection value. As panels with 0.3 mm thickness get an average of 80.6 mm deflection value, also DF, SF, and ZF panels with 0.5 mm thickness get an average of 66.3 mm deflection value. While, the average deflection value is 52 mm for YF and TF of 0.5 mm thickness. Therefore, there is a noticeable deflection difference of 27.5% between panels that have suffered from front layer fracture and other panels of the same thickness and with no fracture. Whereas, the average deflection value is 36.6 mm and 25.9 mm for folded shape of 0.8 mm and 1 mm thickness, respectively. For woven shapes, TWV and ZWV panels with 0.3 mm thickness get higher deflection with an average of 69 mm due to the fracture that has happened to the front layer of these panels. On the other hand, the deflection value is 60.6 mm of SWV shape of thickness 0.3 mm. Therefore, the deflection difference is 13.9% between panels that have suffered from front layer fracture and other panels of the same thickness and with no fracture, which is lower than what has happened in honeycomb panels and higher than folded panels. Whereas, the average deflection value is 50.4 mm, 37.1 mm, and 27.1 mm for woven shape of 0.5 mm, 0.8 mm, and 1 mm thickness, respectively.

The results obtained for back layer deflection upon using scaled distance of  $0.79 \text{ m/kg}^{1/3}$  are compared with the results obtained for back layer deflection upon using scaled distance of  $1.26 \text{ m/kg}^{1/3}$ . It is noticed that for honeycomb shape, the deflection increases by an average of 263.8%, 305.5%, 355.8%, and 367% on using panels of 0.3 mm, 0.5 mm, 0.8 mm, and 1 mm thickness, respectively. Based on the comparison, the average percentage of deflection increase for honeycomb panels ranges between 397.1% and 440.4% for front layer and between 263.8% and 367% for back layer. Therefore, front layers are still affected more than back layers upon increasing scaled distance. However, it is noticed that the gap between the average percentages of increasing deflection due to comparison has decreased between back layer and front layer comparing to pervious scenarios upon using scaled distance of  $1 \text{ m/kg}^{1/3}$  and  $0.87 \text{ m/kg}^{1/3}$ , which

means that more core crushing has occurred. On the other hand, and as per the mentioned comparison, the deflection of folded shape excluding DF and YF shapes increases by an average of 543.3%, 520.3%, 469.9%, and 517.1% on using panels of 0.3 mm, 0.5 mm, 0.8 mm, and 1 mm thickness, respectively. Such exclusion is done because the deflection of DF and YF shapes has occurred in the opposite direction when exposed to one blast load. As the panels are at its initial stage of damage and due to the overall behaviour of core elements, deflection has occurred in the opposite direction. While, on increasing the scaled distance, deflection occurs in the same direction of the applied blast loads similar to what has happened on being exposed to successive blast loads. Based on the above mentioned comparison, the average percentage of deflection increase for folded panels, excluding panels with 0.3 mm and 0.5 mm thickness due to its failure, ranges between 158.3% and 170.9% for front layer and between 469.9% and 517.7% for back layer. Therefore, unlike what has happened on using honeycomb shapes, back layers of folded shapes are affected more than front layers upon increasing scaled distance. Finally, as per the mentioned comparison, the deflection of woven shape increases by an average of 338.2%, 316.4%, 323.7%, and 306.9% for woven shape of 0.3 mm, 0.5 mm, 0.8 mm, and 1 mm thickness, respectively. Based on the above mentioned comparison, the average percentage of deflection increase for woven panels ranges between 228.6% and 308.3% for front layer and between 306.9% and 338.2% for back layer. Therefore, unlike what has happened in pervious scenarios upon using scaled distance of  $1 \text{ m/kg}^{1/3}$  and  $0.87 \text{ m/kg}^{1/3}$  and unlike what has happened on using honeycomb shapes, the back layers of woven shapes are affected more than front layers upon increasing scaled distance. Accordingly, woven shapes upon using scaled distance of  $0.79 \text{ m/kg}^{1/3}$  behave similar to folded shapes.

The results obtained for back layer deflection upon using scaled distance of  $0.79 \text{ m/kg}^{1/3}$  (Figures 5.61 to 5.63) are compared with the results obtained for back layer deflection upon using scaled distance of  $1 \text{ m/kg}^{1/3}$  (Figures 5.43 to 5.45). It is noticed that for honeycomb shape, the deflection increases by an average of 98.9%, 150.1%, 166.8%, and 182.8% on using panels of 0.3 mm, 0.5 mm, 0.8 mm, and 1 mm thickness, respectively. While, the deflection of folded shape increases by an average of 137.2%, 200.3%, 155.2%, and 143.8% on using panels of 0.3 mm, 0.5 mm, 0.8 mm, and 1 mm, respectively. Finally, the deflection of woven shape increases by an average of 153.9%, 172.4%, 160.9%, and 168.4% on using panels of 0.3 mm, 0.5 mm, 0.8 mm, and 1 mm thickness, respectively.

The results obtained for back layer deflection upon using scaled distance of  $0.79 \text{ m/kg}^{1/3}$  (Figures 5.61 to 5.63) are compared with the results obtained for back layer deflection upon using scaled distance of  $0.87 \text{ m/kg}^{1/3}$  (Figures 5.52 to 5.54). It is noticed that for honeycomb shape, the deflection increases by an average of 42.1%, 42.7%, 44.3%, and 52.3% on using panels of 0.3 mm, 0.5 mm, 0.8 mm, and 1 mm thickness, respectively. While, the deflection of folded shape increases by an average of 32.9%, 48.6%, 51.5%, and 52.2% on using panels of 0.3 mm, 0.5 mm, 0.8 mm, and 1 mm thickness, respectively. Finally, the deflection of woven shape increases by an average of 66.8%, 49.9%, 55.8%, and 63.7% on using panels of 0.3 mm, 0.5 mm, 0.8 mm, and 1 mm thickness, respectively. To conclude, back layer deflection increases by an average of 385.7% upon using scaled distance of  $0.79 \text{ m/kg}^{1/3}$  compared with scaled distance of  $1.26 \text{ m/kg}^{1/3}$ . Whereas, it increases by an average of 157.6% upon using scaled distance of  $0.79 \text{ m/kg}^{1/3}$  compared with scaled distance of  $1 \text{ m/kg}^{1/3}$ . While, it increases by an average of 50.2% upon using scaled distance of  $0.79 \text{ m/kg}^{1/3}$  compared with scaled distance of  $0.87 \text{ m/kg}^{1/3}$ .

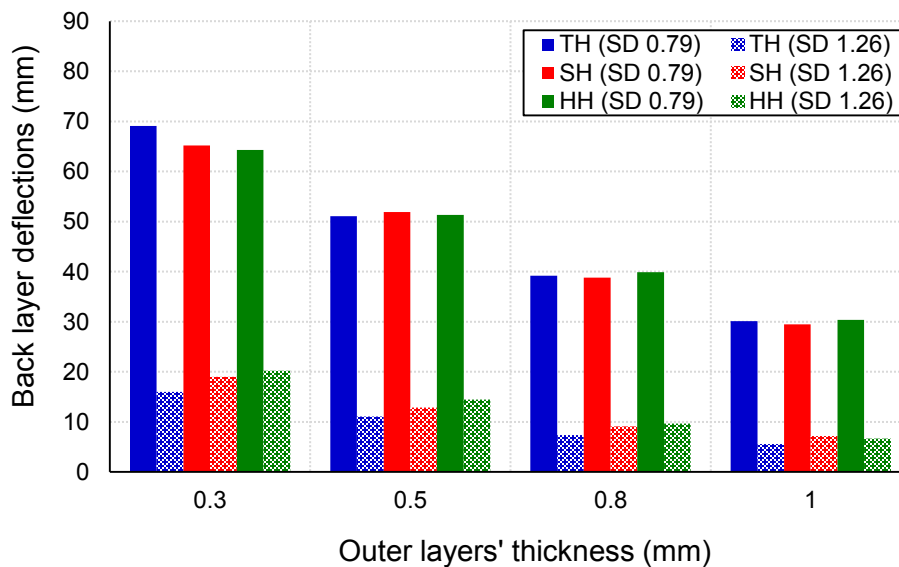


**Figure 5.61** Back layer deflection for honeycomb panels having scaled distance of  $0.79 \text{ m/kg}^{1/3}$

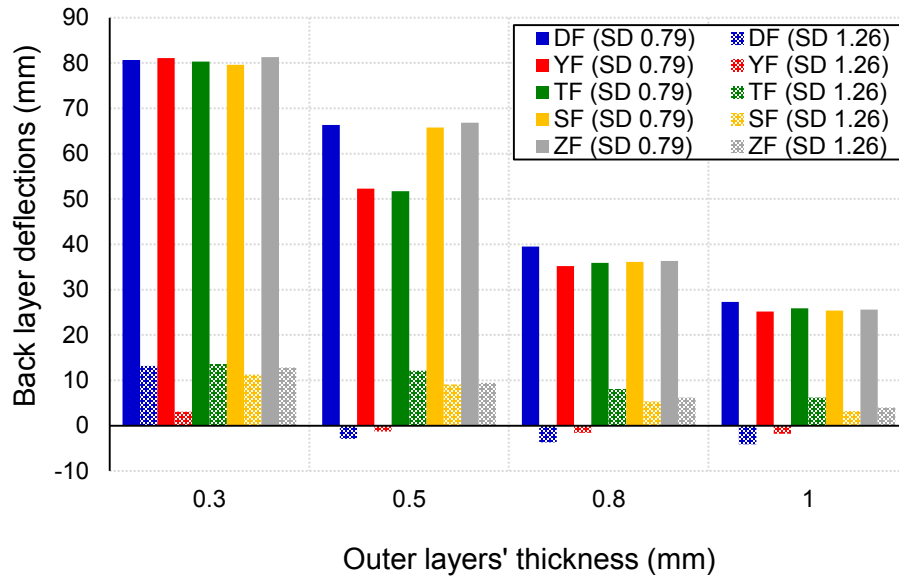


**Figure 5.62** Back layer deflection for folded panels having scaled distance of  $0.79 \text{ m/kg}^{1/3}$

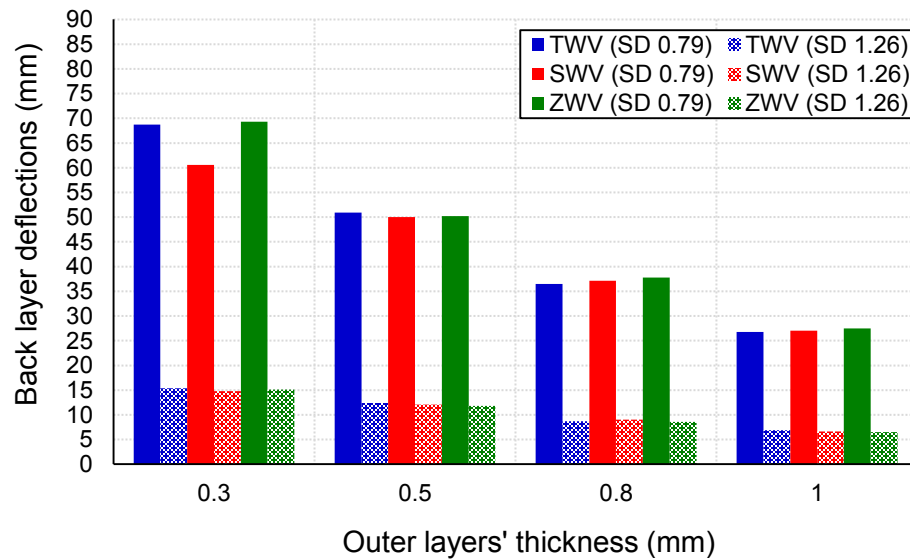


**Figure 5.63** Back layer deflection for woven panels having scaled distance of  $0.79 \text{ m/kg}^{1/3}$

Figures 5.64, 5.65, and 5.66 illustrate energy dissipation of honeycomb, folded, and woven shapes upon using scaled distance of  $0.79 \text{ m/kg}^{1/3}$  (SD 0.79) versus upon using scaled distance of  $1.26 \text{ m/kg}^{1/3}$  (SD 1.26). From the figures, it is noticed that woven shapes have the highest energy dissipation values, followed by folded shapes, and finally honeycomb shapes obtained the least energy dissipation values. The average energy dissipation value is 28.96 kJ, 20.28 kJ, 14.2 kJ, and 10.54 kJ for woven shapes of 0.3 mm, 0.5 mm, 0.8 mm, and 1 mm thickness, respectively. While,

the average energy dissipation value is 25.31 kJ, 18.51 kJ, 12.8 kJ, and 9.06 kJ for folded shapes of 0.3 mm, 0.5 mm, 0.8 mm, and 1 mm thickness, respectively. Finally, the average energy dissipation value is 20.49 kJ, 13.74 kJ, 8.97 kJ, and 6.58 kJ for honeycomb shapes of 0.3 mm, 0.5 mm, 0.8 mm, and 1 mm thickness, respectively. To conclude, upon using scaled distance of  $0.79 \text{ m/kg}^{1/3}$ , woven shapes can dissipate an average of 12.8% more energy than folded shapes and 51.8% more energy than honeycomb shapes.

The results obtained of energy dissipation upon using scaled distance of  $0.79 \text{ m/kg}^{1/3}$  are compared with the results obtained for energy dissipation upon using scaled distance of  $1.26 \text{ m/kg}^{1/3}$ . It is noticed that for honeycomb shapes, energy dissipation increases by an average of 895.7%, 937.2%, 753.8%, and 667% on using panels of 0.3 mm, 0.5 mm, 0.8 mm, and 1 mm thickness, respectively. For folded shapes, energy dissipation increases by an average of 677%, 774.4%, 732.3%, and 632.5% on using panels of 0.3 mm, 0.5 mm, 0.8 mm, and 1 mm thickness, respectively. Finally for woven shapes, energy dissipation increases by an average of 640.5%, 559.4%, 476.7%, and 402.6% on using panels of 0.3 mm, 0.5 mm, 0.8 mm, and 1 mm thickness, respectively. Therefore, the energy dissipation increases by an average of 679.1% upon using scaled distance of  $0.79 \text{ m/kg}^{1/3}$  compared with scaled distance of  $1.26 \text{ m/kg}^{1/3}$ .

The results obtained for energy dissipation upon using scaled distance of  $0.79 \text{ m/kg}^{1/3}$  (Figures 5.64 to 5.66) are compared with the results obtained for energy dissipation upon using scaled distance of  $1 \text{ m/kg}^{1/3}$  (Figures 5.46 to 5.48). It is noticed that for honeycomb shapes, energy dissipation increases by an average of 234.4%, 201.6%, 182%, and 201.8% on using panels of 0.3 mm, 0.5 mm, 0.8 mm, and 1 mm thickness, respectively. For folded shapes, energy dissipation increases by an average of 184.3%, 169.4%, 185.6%, and 156.6% on using panels of 0.3 mm, 0.5 mm, 0.8 mm, and 1 mm thickness, respectively. Finally for woven shapes, energy dissipation increases by an average of 189.2%, 159.2%, 153.9%, and 156.9% on using panels of 0.3 mm, 0.5 mm, 0.8 mm, and 1 mm thickness, respectively. Therefore, energy dissipation increases by an average of 181.2% upon using scaled distance of  $0.79 \text{ m/kg}^{1/3}$  compared with scaled distance of  $1 \text{ m/kg}^{1/3}$ .

The results obtained for energy dissipation upon using scaled distance of  $0.79 \text{ m/kg}^{1/3}$  (Figures 5.64 to 5.66) are compared with the results obtained for energy dissipation upon using scaled distance of  $0.87 \text{ m/kg}^{1/3}$  (Figures 5.55 to 5.57). It is noticed that for honeycomb shapes, energy

dissipation increases by an average of 63.5%, 66.8%, 61.5%, and 54.2% on using panels of 0.3 mm, 0.5 mm, 0.8 mm, and 1 mm thickness, respectively. For folded shapes, energy dissipation increases by an average of 51.6%, 56.9%, 70.6%, and 53.2% on using panels of 0.3 mm, 0.5 mm, 0.8 mm, and 1 mm thickness, respectively. Finally for woven shapes, energy dissipation increases by an average of 64.9%, 60.9%, 68.8%, and 56.2% on using panels of 0.3 mm, 0.5 mm, 0.8 mm, and 1 mm thickness, respectively. Therefore, energy dissipation increases by an average of 60.8% upon using scaled distance of 0.79  $\text{m/kg}^{1/3}$  compared with scaled distance of 0.87  $\text{m/kg}^{1/3}$ .

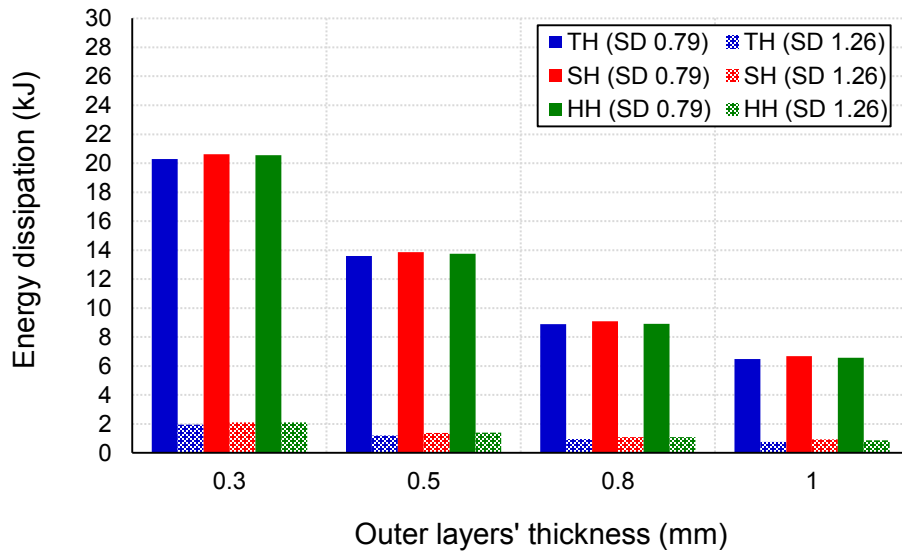


**Figure 5.64** Energy dissipation for honeycomb panels having scaled distance of 0.79  $\text{m/kg}^{1/3}$

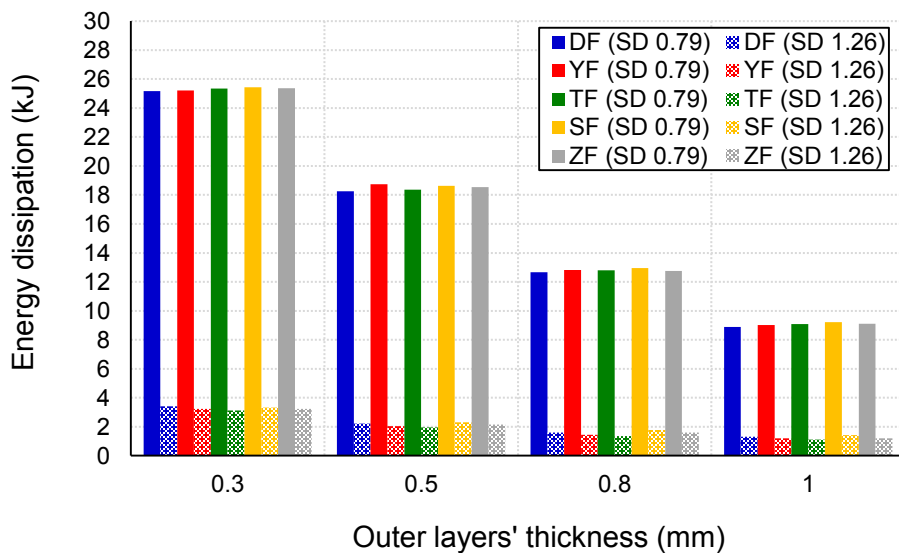


**Figure 5.65** Energy dissipation for folded panels having scaled distance of  $0.79 \text{ m/kg}^{1/3}$

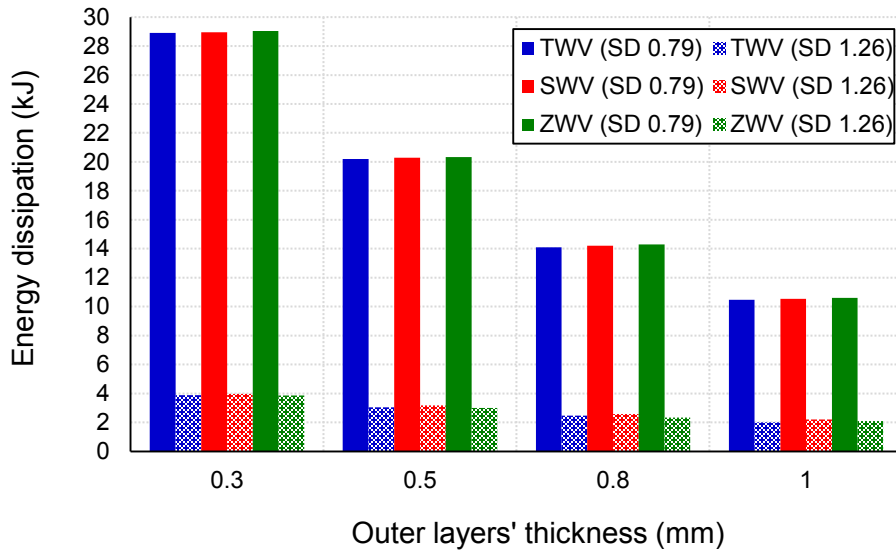


**Figure 5.66** Energy dissipation for woven panels having scaled distance of  $0.79 \text{ m/kg}^{1/3}$

## 5.8 Parameters chart of different panels topologies

Based on the four scaled distances studied in the previous section, this section provides a chart for the panels of honeycomb topology, folded topology, and woven topology. In the chart, back layer deflection ( $\Delta$ ) and energy dissipation (ED) are obtained from the scaled distance for the four thicknesses considered in this study; i.e. 0.3 mm, 0.5mm, 0.8 mm, and 1 mm. In order to increase the usefulness of the charts, another four scaled distances are studied. Therefore a total of eight scaled distances are investigated;  $1.26 \text{ m/kg}^{1/3}$ ,  $1.10 \text{ m/kg}^{1/3}$ ,  $1.00 \text{ m/kg}^{1/3}$ ,  $0.93 \text{ m/kg}^{1/3}$ ,  $0.87 \text{ m/kg}^{1/3}$ ,  $0.83 \text{ m/kg}^{1/3}$ ,  $0.79 \text{ m/kg}^{1/3}$ , and  $0.74 \text{ m/kg}^{1/3}$ . Figure 5.67 is the chart of the honeycomb topology, where the values used for plotting this chart are the average values for the three honeycomb shapes considered in this study (TH, SH, and HH). The relative standard deviation for the back layer deflection ranges between 0.6% and 11.2%, whereas the relative standard deviation for the energy dissipation ranges between 0.3% and 8.2%. From this chart and by knowing the scaled distance, the back layer deflection and energy dissipation are obtained for honeycomb topology and are valid for scaled distance ranging from  $0.7 \text{ m/kg}^{1/3}$  to  $1.3 \text{ m/kg}^{1/3}$ . Figure 5.68 is the chart of the folded topology, where the values used for plotting this chart are the average values for the five folded shapes considered in this study (DF, YF, TF, SF, and ZF). The relative standard

deviation for the back layer deflection ranges between 1.4% and 17.9%, excluding scaled distance of  $1.26 \text{ m/kg}^{1/3}$  and  $1.10 \text{ m/kg}^{1/3}$ . These two scaled distances are excluded as the deflection of DF and YF shapes has occurred in the opposite direction. As the panels are at its initial stage of damage and due to the overall behaviour of the core elements, deflection has occurred in the opposite direction. Whereas the relative standard deviation for the energy dissipation ranges between 1.1% and 9.2%. From this chart and by knowing the scaled distance, the back layer deflection and energy dissipation are obtained for folded topology and are valid for scaled distance ranging from  $0.7 \text{ m/kg}^{1/3}$  to  $1.3 \text{ m/kg}^{1/3}$ . Figure 5.9 is the chart of the woven topology, where the values used for plotting this chart are the average values for the three woven shapes considered in this study (TWV, SWV, and ZWV). The relative standard deviation for the back layer deflection ranges between 0.7% and 6.0%, whereas the relative standard deviation for the energy dissipation ranges between 0.2% and 4.1%. From this chart and by knowing the scaled distance, the back layer deflection and energy dissipation are obtained for woven topology and are valid for scaled distance ranging from  $0.7 \text{ m/kg}^{1/3}$  to  $1.3 \text{ m/kg}^{1/3}$ .

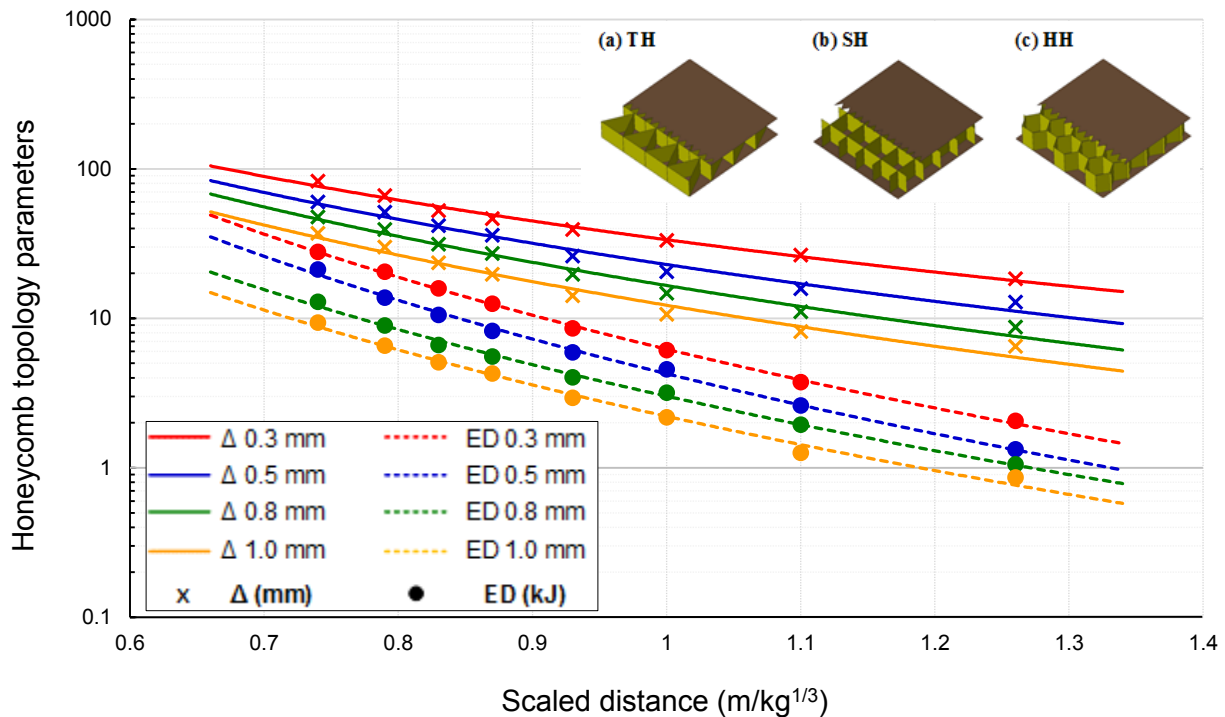


**Figure 5.67** Honeycomb topology parameters (back layer deflection,  $\Delta$ , and energy dissipation, ED) versus scaled distance

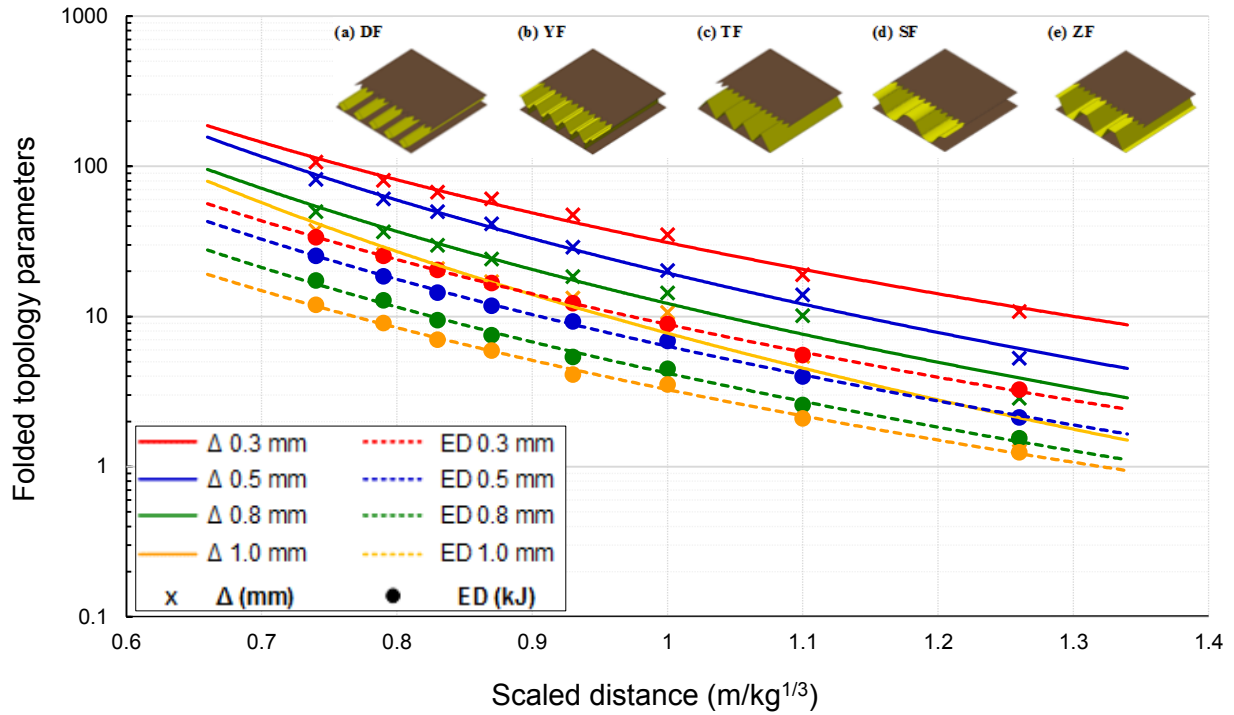


**Figure 5.68** Folded topology parameters (back layer deflection,  $\Delta$ , and energy dissipation, ED) versus scaled distance

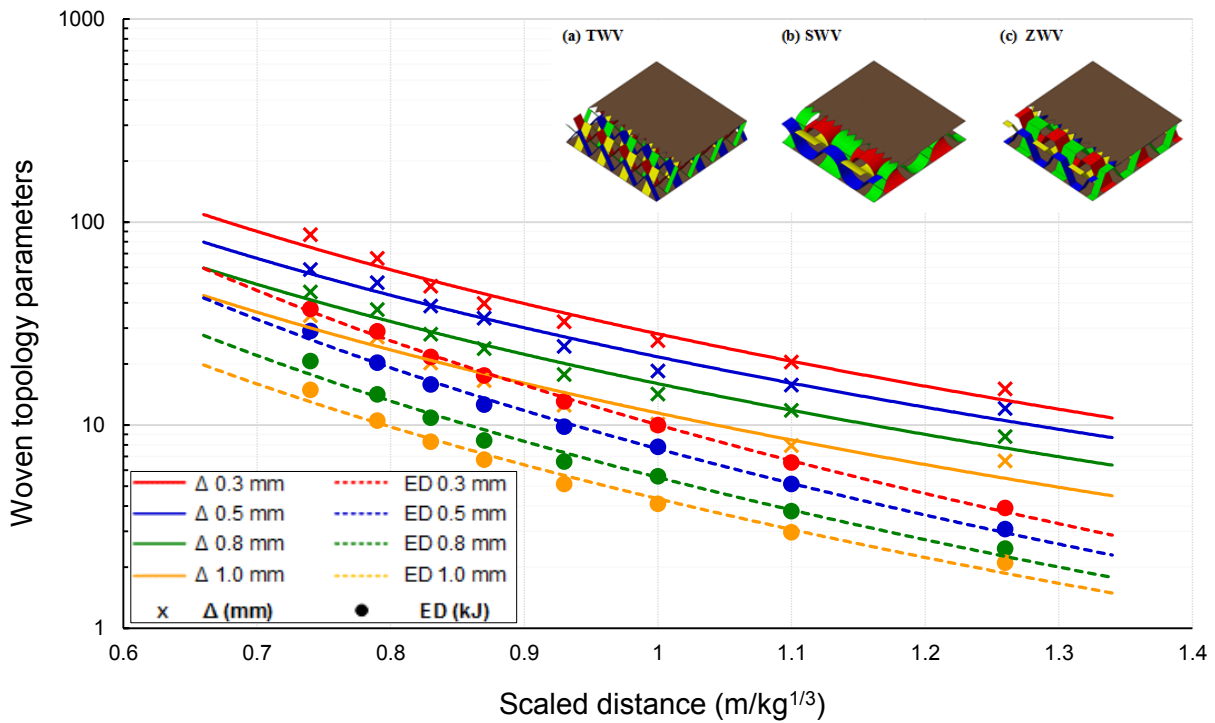


**Figure 5.69** Woven topology parameters (back layer deflection,  $\Delta$ , and energy dissipation, ED) versus scaled distance

## 5.9 Summary

The effectiveness of sandwich panels in blast load resistance is investigated in Chapter 5. In this chapter, three core topologies (honeycomb, folded, and woven) were analyzed for studying metallic sandwich panels. Honeycomb and folded topologies were introduced before in previous studies, while the woven topology is newly proposed in this study. These three topologies are divided into eleven shapes, resulting in eleven different panels that have been studied with different layers thickness (0.3 mm, 0.5 mm, 0.8 mm, and 1 mm), where the material is defined as AISI 304 stainless steel. During this study, sandwich panels were evaluated using a nonlinear explicit finite element software *AUTODYN*. The numerical model was validated with the available data in the literature. Relatively, a good agreement has been reached for the front layer deflection, back layer deflection, and energy dissipation with maximum deviation of 12.9%.

The proposed woven topology was studied under blast load and it exhibits better blast resistance compared to folded and honeycomb topologies. Accordingly, woven shapes have less front layer deflection but they dissipate up to 49.3% more energy than folded shapes. On the other hand, woven shapes have more front layer deflection and energy dissipation compared to that of honeycomb shapes. The effect of changing outer layers' thicknesses has been also studied in this chapter. It has been found that increasing outer layers' thicknesses results in having stiffer panels which leads to reducing front layer deflection, back layer deflection, and energy dissipation. Moreover, the effect of applying two successive explosions on the same panel was investigated, where the two explosions have the same scaled distance of  $1.26 \text{ m/kg}^{1/3}$ . Accordingly, honeycomb and woven shapes have sustained the successive blast loads without any fracture, whereas folded shapes of 0.3 mm thickness have suffered from fracture at the edges. Furthermore, the effect of changing scaled distance has been studied, where four scaled distances are used;  $1.26 \text{ m/kg}^{1/3}$ ,  $1.00 \text{ m/kg}^{1/3}$ ,  $0.87 \text{ m/kg}^{1/3}$ , and  $0.79 \text{ m/kg}^{1/3}$ . On changing scaled distance, it was found that SH, HH, and SWV shapes are the only panels of 0.3 mm thickness that have sustained blast loads without any fracture. Also, it was proved that woven topology can dissipate more energy than other topologies upon changing scaled distance. Finally, a chart for each of the three topologies considered in this study is developed for the scaled distance from  $0.7 \text{ m/kg}^{1/3}$  to  $1.3 \text{ m/kg}^{1/3}$ .

## Chapter

# 7

## Conclusions

### 6.1 Conclusions

The effectiveness of sandwich panels in blast load resistance is investigated. In this study, a new core configuration formed from woven shape is proposed. This core configuration is studied for both FRP and metallic sandwich panels. During this study, sandwich panels were evaluated using a nonlinear explicit finite element simulation. A convergence study was applied on the models to better choose the mesh size.

For FRP sandwich panels, twelve FRP panels with different inner core configurations and two different thicknesses were analyzed. The numerical model was validated using experimental field tests conducted on four FRP honeycomb panels filled with sand when subjected to blast effects. The numerical model is able to predict the failure pattern of tested panels as well as their peak deflections with a maximum deviation of 18%. The study also investigates the effect of filling FRP panels with sand on the panel's blast resistance. It is found that filling panels with sand provides a damping environment which reduces panels' deflection by up to 26% and increases energy dissipation by up to 31%.

The performance of the twelve proposed panels is evaluated in terms of the panel's failure mode, peak deflection, energy dissipation, and energy-to-deflection ratio ( $E/\Delta$ ). The numerical model showed a minor enhancement in the panels' behaviour when the proposed configurations were applied to thin panels. This is attributed to the fact that the proposed inner core configurations

did not change the failure mode of thin panels which was a complete bond failure. However, when the proposed configurations were applied to thick panels, the following were observed:

- The combination of RW axis and the PW axis shapes (represented by W9-W12) has shown a major enhancement in the panels' energy dissipation by up to 125% with an increase in the panels' deflection by only 31%.
- Woven shape WV2-1 has dissipated almost twice the energy at the same level of deformation.
- The combination of RW axis and woven shape WV2-1 has led to a superior performance under blast effects. This combination dissipates up to twice the energy at a reduced level of deformation.
- Despite the effectiveness of woven shape WV2-2 in dissipating blast energy at a reduced level of deformation, this configuration utilizes 33% more FRP material compared to other configurations. Moreover, the complexity of manufacturing this shape will make it less economical and practical compared to other proposed configurations.
- W16 can be considered to have the best performance among all panels considered in this study, as it has the highest energy-to-deflection ratio.

W16 was chosen for conducting a parametric study due to its performance. Accordingly, parametric studies were carried out to determine the effect of various parameters: thickness of layers, height of sinusoidal layer, length of sinusoidal wave, width of strip, and length of wave peak. The following results have been observed:

- Changing one of the parameters from  $h$ ,  $L$ ,  $W$ , and  $t$  while keeping other parameters constant have resulted in changing the material weight which makes it difficult to compare results of different panels.
- Having the same material weight, then decreasing wave length increases bonds' contacts, while decreasing layers' heights increases number of layers. Subsequently, the performance of analyzed panel is enhanced by up to 24.2% increase in energy dissipation and 1.5% decrease in panels' peak deflection.

- Changing wave peak length while keeping the material weight constant improves the performance of analyzed panel by up to 12% in energy-to-deflection due to the increase in the bonding area.
- Changing wave peak length and other parameters (h, L, W, and t) while keeping the material weight constant increases the energy-to-deflection ratio by 34.3%. To conclude, W27 (with b = 10 mm) performs the best among all other panels.

The effect of changing the filling material on the panel's performance against blast loads is investigated. It is found that using filling material provides a damping environment which reduces panels' deflection by up to 28.8% and increases panel's energy absorption by up to 49.7%. Among all the used filling materials in this study, dytherm foam showed the best performance where it enhances the  $E/\Delta$  ratio by up to 20.8% in comparison to using sand and by up to 4.3% in comparison to using polyurethane foam.

For metallic sandwich panels, three core topologies (honeycomb, folded, and woven) are analyzed. These topologies are divided into eleven shapes, resulting in eleven different panels that were studied with different layers thickness. Metallic sandwich panels are modeled using AISI 304 stainless steel. The numerical model were validated with available data in the literature. Relatively, a good agreement has been reached for the front layer deflection, back layer deflection, and energy dissipation with maximum deviation of 12.9%.

The performance of the eleven panels is evaluated in terms of front layer deflection, back layer deflection, energy dissipation, and panel's failure mode. From the evaluation the following have been observed:

- Upon changing back layer thickness, a minor change in front layer deflection and energy dissipation has been achieved. On the other hand, back layer deflection decreases upon increasing back layer thickness.
- Upon increasing front layer thickness, the front layer deflection, back layer deflection, and energy dissipation decrease.
- Upon using woven shapes, less front layer deflection occurs compared to that of folded shapes. However, woven shapes dissipate up to 49.3% more energy. On the other hand,

woven shapes have more front layer deflection and energy dissipation compared to that of honeycomb shapes.

- Upon increasing outer layers' thicknesses, the panels become stiffer which results in reducing front layer deflection, back layer deflection, and energy dissipation. However, comparing similar panels upon increasing outer layers' thicknesses with increasing front layer thicknesses only, the front layer deflection and energy dissipation increase upon using outer layers' thickness of 0.8 mm and 1 mm. This is attributed to the fact that upon increasing both front and back thickness to 0.8 mm and 1 mm while keeping the core thickness as 0.3 mm, less deflection to back layer and more crushing to the core are achieved resulting in more deflection to front layers and more energy dissipated by the panel.
- Upon applying two successive blast loads on the same panel, all folded panels with 0.3 mm thickness have suffered from fracture at the edges. On the other hand, for honeycomb and woven shapes, all the panels have sustained the successive blast loads without any fracture.
- Upon using scaled distance of  $1 \text{ m/kg}^{1/3}$ , DF, SF, and ZF panels with 0.3 mm thickness have suffered from fracture at the edges. On the other hand, YF and TF panels in addition to all honeycomb and woven panels have sustained blast loads without any fracture.
- Upon using scaled distance of  $0.87 \text{ m/kg}^{1/3}$ , all folded panels with 0.3 mm thickness in addition to SF and ZF panels with 0.5 mm thickness have suffered from fracture at the edges, whereas all honeycomb and woven panels have sustained blast loads without any fracture.
- Upon using scaled distance of  $0.79 \text{ m/kg}^{1/3}$ , all folded, TH, TWV, and ZWV panels with 0.3 mm thickness in addition to DF, SF, and ZF panels with 0.5 mm thickness have suffered from fracture at the edges. While, SH, HH, and SWV panels have sustained blast loads without any fracture.
- Upon applying two successive blast loads on the same panel, front layers are affected more than back layers for all honeycomb and woven panels, whereas back layers are affected more than front layers for all folded panels. Accordingly, energy dissipation increases by an average of 224% when sandwich panels are exposed to successive blast loads compared with being exposed to only one blast load.

- Upon applying two successive blast loads on the same panel, woven shapes can dissipate an average of 14.8% more energy than folded shapes and 48% more energy than honeycomb shapes.
- Upon increasing the scaled distance, front layers are affected more than back layers for all the panels that can sustain blast load without any fracture in the front layer. This effect is valid until the panel core crushes to a level where back layer is affected more than front layer. Accordingly, back layer of folded panels are affected more on changing scaled distance to  $1 \text{ m/kg}^{1/3}$ ,  $0.87 \text{ m/kg}^{1/3}$ , and  $0.79 \text{ m/kg}^{1/3}$ . Also, back layer of woven panels are affected more on changing scaled distance to  $0.79 \text{ m/kg}^{1/3}$ .
- Upon increasing the scaled distance, energy dissipation increases by an average of 175.6%, 384.8%, and 679.1% upon using scaled distance of  $1 \text{ m/kg}^{1/3}$ ,  $0.87 \text{ m/kg}^{1/3}$ , and  $0.79 \text{ m/kg}^{1/3}$ , relatively, compared with scaled distance of  $1.26 \text{ m/kg}^{1/3}$ .
- Upon increasing the scaled distance, woven shapes have the highest energy dissipation capacity, as it can dissipate an average of 16.8% more energy than folded shapes and 74.5% more energy than honeycomb shapes upon using scaled distance of  $1 \text{ m/kg}^{1/3}$ . Whereas woven shapes can dissipate an average of 9.5% more energy than folded shapes and 51% more energy than honeycomb shapes on using scaled distance of  $0.87 \text{ m/kg}^{1/3}$ . Finally, woven shapes can dissipate an average of 12.8% more energy than folded shapes and 51.8% more energy than honeycomb shapes on using scaled distance of  $0.79 \text{ m/kg}^{1/3}$ .

Finally, a chart for each of the three topologies of metallic sandwich panels considered in this study is developed for the scaled distance from  $0.7 \text{ m/kg}^{1/3}$  to  $1.3 \text{ m/kg}^{1/3}$ .

## 6.2 Future Work

The results presented here have demonstrated the effectiveness of using woven shapes in both FRP and metallic sandwich panels against blast loads. This research provides a solid starting point for several future lines of research that can arise from this work. The following topics could be pursued:

- Despite the fact that applying numerical simulations helps reducing experimental work in terms of effort, time, and resources particularly under impulsive loadings such as that

caused by a blast, the woven shapes need to be examined experimentally as it is a new shape.

- In this study, for metallic sandwich panels, woven topologies are compared with honeycomb and folded topologies. Similar study is needed to compare those topologies with lattice truss topologies.
- The effect of using filling material in the metallic sandwich panels needs to be investigated.
- In this study, woven panels are studied against blast loads, where similar study needs to be done to examine the effectiveness of using this shape against fragmentation.
- In this study, woven panels are studied against blast loads, where similar studies need to be done to examine the effectiveness of using woven shape in other applications such as bridge decking, flooring, and roofing. Also, the effectiveness of using woven shapes in mechanical engineering field can be investigated (i.e., especially for the automotive, aerospace, and transportation applications).

## References

---

- Alagusundaramoorthy, P., Harik, I., & Choo, C. (2006). Structural behavior of FRP composite bridge deck panels. *Journal of Bridge Engineering*, 11(4), 384-393.
- Alberdi, R., Przywara, J., & Khandelwal, K. (2013). Performance evaluation of sandwich panel systems for blast mitigation. *Engineering Structures*, 56, 2119-2130.
- Allen, H. (1969). *Analysis and design of structural sandwich panels*: Pergamon Press, Oxford, London, England
- Army, T. (1990). TM 5-1300. *Structures to Resist the Effects of Accidental Explosions*.
- Arora, H., Hooper, P., & Dear, J. (2012). The effects of air and underwater blast on composite sandwich panels and tubular laminate structures. *Experimental mechanics*, 52(1), 59-81.
- AUTODYN, A. (2014). Interactive Non-Linear Dynamic Analysis Software, Version 15, User's Manual. SAS IP Inc.
- Aviles, F., & Carlsson, L. A. (2006). Three-dimensional finite element buckling analysis of debonded sandwich panels. *Journal of composite materials*, 40(11), 993-1008.
- Bahei-El-Din, Y. A., Dvorak, G. J., & Fredricksen, O. J. (2006). A blast-tolerant sandwich plate design with a polyurea interlayer. *International Journal of Solids and Structures*, 43(25), 7644-7658.
- Baker W.E., C. P. A., Westine P.S., Kulesz J.J., Strehlow R.A. (1983). *Explosion Hazards and Valuation*. New York, USA: Elsevier Scientific Publishing Company.
- Baker, W. E. (1973). *Explosions in air*: University of Texas Press.
- Birnbaum, N. K., Francis, N. J., & Gerber, B. I. (1999). Coupled techniques for the simulation of fluid-structure and impact problems. *Computer Assisted Mechanics and Engineering Sciences*, 6(3-4), 295-311.
- Boni, T. L., & de Almeida, S. F. M. (2008). Laterally supported sandwich panels subjected to large deflections—Part 1: Test apparatus design and experimental results. *Thin-walled structures*, 46(4), 413-422.
- Boni, T. L., & de Almeida, S. F. M. (2008). Laterally supported sandwich panels subjected to large deflections: Part 2: FE analyses and model validation. *Thin-walled structures*, 46(4), 423-434.
- Børvik, T., Burbach, A., Langberg, H., & Langseth, M. (2008). On the ballistic and blast load response of a 20ft ISO container protected with aluminium panels filled with a local mass—Phase II: Validation of protective system. *Engineering Structures*, 30(6), 1621-1631.
- Bulson, P. S. (2002). *Explosive loading of engineering structures*: CRC Press.
- Century Dynamics, I. (2005). SPH User Manual and Tutorial for AUTODYN Interactive Nonlinear Dynamic Analysis Software. San Ramon, California, U.S.A.
- Chang, W.-S., Ventsel, E., Krauthammer, T., & John, J. (2005). Bending behavior of corrugated-core sandwich plates. *Composite structures*, 70(1), 81-89.
- Chen, A., & Davalos, J. (2003). *Bending strength of honeycomb FRP sandwich beams with sinusoidal core geometry*. Paper presented at the Proceedings of the fourth Canadian-International Composites Conference, CANCOM 2003.

- Conrath, E. J., Krauthammer, T., Marchand, K., A., Mlakar, P., F. and Structural Engineering Institute. (1999). *Structural Design for Physical Security*: American Society of Civil Engineers.
- Cui, X., Zhao, L., Wang, Z., Zhao, H., & Fang, D. (2012). Dynamic response of metallic lattice sandwich structures to impulsive loading. *International Journal of Impact Engineering*, 43, 1-5.
- Cytec. (2016). Material Specification FM 300 Epoxy Film Adhesive Data Sheet.
- Davalos, J. F., Qiao, P., Xu, X. F., Robinson, J., & Barth, K. E. (2001). Modeling and characterization of fiber-reinforced plastic honeycomb sandwich panels for highway bridge applications. *Composite structures*, 52(3), 441-452.
- Davidson, J. S., Dawson, H., Fisher, J., Gasulla, E., Ghosh, S. K., Hoemann, J., ... & Schroder, J. W. (2014). PCI Design Handbook: Appendix A: Blast-resistant design of precast, prestressed concrete components. *PCI Journal*.
- Davies, J. (1993). Sandwich panels. *Thin-walled structures*, 16(1), 179-198.
- Dharmasena, K., Queheillalt, D., Wadley, H., Dudt, P., Chen, Y., Knight, D., . . . Deshpande, V. (2010). Dynamic compression of metallic sandwich structures during planar impulsive loading in water. *European Journal of Mechanics-A/Solids*, 29(1), 56-67.
- DoD, U. (2002). Design and analysis of hardened structures to conventional weapons effects: UFC 3-340-01.
- DoD, U. (2008). Structures to Resist the Effects of Accidental Explosions. US DoD, Washington, DC, USA: UFC 3-340-02.
- Dusenberry, D. O. (Ed.). (2010). *Handbook for blast-resistant design of buildings*. J. Wiley.
- Dvorak, G. J., & Bahei-El-Din, Y. A. (2005). Enhancement of blast resistance of sandwich plates *Sandwich Structures 7: Advancing with Sandwich Structures and Materials* (pp. 107-116): Springer.
- Fan, H., Meng, F., & Yang, W. (2007). Sandwich panels with Kagome lattice cores reinforced by carbon fibers. *Composite structures*, 81(4), 533-539.
- Fleck, N., & Deshpande, V. (2004). The resistance of clamped sandwich beams to shock loading. *Journal of Applied Mechanics*, 71(3), 386-401.
- Gibson, L. J., & Ashby, M. F. (1997). *Cellular solids: structure and properties*: Cambridge university press.
- Goel, M. D., Matsagar, V. A., Marburg, S., & Gupta, A. K. (2012). Comparative performance of stiffened sandwich foam panels under impulsive loading. *Journal of Performance of Constructed Facilities*, 27(5), 540-549.
- Hahn, Y., & Kikuchi, N. (2005). Mixed shell element for seven-parameter formulation. *International journal for numerical methods in engineering*, 64(1), 95-124.
- Hahn, Y. (2005). *Development of a mixed shell element for 7-parameter formulation and identification methods of lowest eigenvalues*. University of Michigan.
- Hayhurst, C. J., Clegg, R. A., Livingstone, I., & Francis, N. J. (1996). The application of {SPH} techniques in {AUTODYN-2D} to ballistic impact problems.
- He, M., & Hu, W. (2008). A study on composite honeycomb sandwich panel structure. *Materials & Design*, 29(3), 709-713.
- Hoemann, J. M. (2007). *Experimental evaluation of structural composites for blast resistant design*. University of Missouri--Columbia.
- Hyde, D. (1992). *ConWep - Application of TM 5-1300*. Paper presented at the U.S Army Engineer Waterways Experiment Station, Vicksburg, MA, USA.

- Jackson, M., & Shukla, A. (2011). Performance of sandwich composites subjected to sequential impact and air blast loading. *Composites Part B: Engineering*, 42(2), 155-166.
- Jacob, G. C., Fellers, J. F., Simunovic, S., & Starbuck, J. M. (2002). Energy absorption in polymer composites for automotive crashworthiness. *Journal of composite materials*, 36(7), 813-850.
- Ji, H. S., Song, W., & Ma, Z. J. (2010). Design, test and field application of a GFRP corrugated-core sandwich bridge. *Engineering Structures*, 32(9), 2814-2824.
- Kalny, O., & Peterman, R. J. (2005). Performance investigation of a fiber reinforced composite honeycomb deck for bridge applications.
- Karagiozova, D., Nurick, G., & Langdon, G. (2009). Behaviour of sandwich panels subject to intense air blasts—Part 2: Numerical simulation. *Composite structures*, 91(4), 442-450.
- Kingery, C. N., & Bulmash, G. (1984). *Air blast parameters from TNT spherical air burst and hemispherical surface burst*: Ballistic Research Laboratories.
- Kujala, P., & Klanac, A. (2005). Steel sandwich panels in marine applications. *Brodogradnja*, 56(4), 305-314.
- Laine, L., & Sandvik, A. (2001). *Derivation of mechanical properties for sand*. Paper presented at the Proceedings of the 4th Asia-Pacific Conference on Shock and impact loads on structures, CI-Premier PTE LTD, Singapore.
- Langdon, G., Karagiozova, D., von Klemperer, C., Nurick, G., Ozinsky, A., & Pickering, E. (2013). The air-blast response of sandwich panels with composite face sheets and polymer foam cores: experiments and predictions. *International Journal of Impact Engineering*, 54, 64-82.
- Langdon, G., von Klemperer, C., Rowland, B., & Nurick, G. (2012). The response of sandwich structures with composite face sheets and polymer foam cores to air-blast loading: preliminary experiments. *Engineering Structures*, 36, 104-112.
- Lee, D. K., & O'Toole, B. J. (2004). Energy absorbing sandwich structures under blast loading. In *8th International LS-DYNA Users Conference*. Pgs (pp. 8-13).
- Li, X., Wang, Z., Zhu, F., Wu, G., & Zhao, L. (2014). Response of aluminium corrugated sandwich panels under air blast loadings: Experiment and numerical simulation. *International Journal of Impact Engineering*, 65, 79-88.
- Liang, Y., Spuskanyuk, A. V., Flores, S. E., Hayhurst, D. R., Hutchinson, J. W., McMeeking, R. M., & Evans, A. G. (2007). The response of metallic sandwich panels to water blast. *Journal of Applied Mechanics*, 74(1), 81-99.
- Liu, T., Deng, Z., & Lu, T. (2006). Design optimization of truss-cored sandwiches with homogenization. *International Journal of Solids and Structures*, 43(25), 7891-7918.
- Meraghni, F., Desrumaux, F., & Benzeggagh, M. (1999). Mechanical behaviour of cellular core for structural sandwich panels. *Composites Part A: Applied Science and Manufacturing*, 30(6), 767-779.
- Mori, L., Queheillalt, D., Wadley, H., & Espinosa, H. (2009). Deformation and failure modes of I-core sandwich structures subjected to underwater impulsive loads. *Experimental mechanics*, 49(2), 257-275.
- Nayak, S., Singh, A., Belegundu, A., & Yen, C. (2013). Process for design optimization of honeycomb core sandwich panels for blast load mitigation. *Structural and Multidisciplinary Optimization*, 47(5), 749-763.
- Pamla, V. (2007). *The pioneer phase of building with glass-fibre reinforced plastics (GFRP) 1942 to 1980*. Thesis submitted to Architectural history institute, Design Faculty, Germany.

- Petras, A., & Sutcliffe, M. (1999). Indentation resistance of sandwich beams. *Composite structures*, 46(4), 413-424.
- Petras, A., & Sutcliffe, M. (2000). Indentation failure analysis of sandwich beams. *Composite structures*, 50(3), 311-318.
- Plantema, F. J. (1966). Sandwich construction: Wiley, New York.
- Rathbun, H., Radford, D., Xue, Z., He, M., Yang, J., Deshpande, V., . . . Evans, A. (2006). Performance of metallic honeycomb-core sandwich beams under shock loading. *International Journal of Solids and Structures*, 43(6), 1746-1763.
- Reis, E. M., & Rizkalla, S. H. (2008). Material characteristics of 3-D FRP sandwich panels. *Construction and Building Materials*, 22(6), 1009-1018.
- Shukla, A., Ravichandran, G., & Rajapakse, Y. (2010). *Dynamic failure of materials and structures*: Springer.
- Smith, P. D., & Hetherington, J. G. (1994). *Blast and ballistic loading of structures*: Digital Press.
- Solomos, V. K. a. G. (2013). Calculation of Blast Loads for Application to Structural Components: European Commission Joint Research Centre Institute for the Protection and Security of the Citizen.
- Steeves, C. A., & Fleck, N. A. (2004). Material selection in sandwich beam construction. *Scripta materialia*, 50(10), 1335-1339.
- Su, H., & McConnell, J. (2011). Influences of Material Properties on Energy Absorption of Composite Sandwich Panels under Blast Loads. *Journal of Composites for Construction*.
- Tekalur, S. A., Bogdanovich, A. E., & Shukla, A. (2009). Shock loading response of sandwich panels with 3-D woven E-glass composite skins and stitched foam core. *Composites Science and Technology*, 69(6), 736-753.
- Theobald, M., Langdon, G., Nurick, G., Pillay, S., Heyns, A., & Merrett, R. (2010). Large inelastic response of unbonded metallic foam and honeycomb core sandwich panels to blast loading. *Composite structures*, 92(10), 2465-2475.
- Thompsett, D., Walker, A., Radley, R., & Grieveson, B. (1995). Design and construction of expanded polystyrene embankments: practical design methods as used in the United Kingdom. *Construction and Building Materials*, 9(6), 403-411.
- Thomsen, O. T., & Frostig, Y. (1997). Localized bending effects in sandwich panels: photoelastic investigation versus high-order sandwich theory results. *Composite structures*, 37(1), 97-108.
- Vinson, J. R. (2001). Sandwich structures. *Applied Mechanics Reviews*, 54(3), 201-214.
- Wadley, H., Dharmasena, K., Chen, Y., Dudt, P., Knight, D., Charette, R., & Kiddy, K. (2008). Compressive response of multilayered pyramidal lattices during underwater shock loading. *International Journal of Impact Engineering*, 35(9), 1102-1114.
- Wadley, H. N. (2006). Multifunctional periodic cellular metals. *Philosophical Transactions of the Royal Society of London A: Mathematical, Physical and Engineering Sciences*, 364(1838), 31-68.
- Xue, Z., & Hutchinson, J. W. (2003). Preliminary assessment of sandwich plates subject to blast loads. *International Journal of Mechanical Sciences*, 45(4), 687-705.
- Xue, Z., & Hutchinson, J. W. (2004). A comparative study of impulse-resistant metal sandwich plates. *International Journal of Impact Engineering*, 30(10), 1283-1305.
- Yan, L., Han, B., Yu, B., Chen, C., Zhang, Q., & Lu, T. (2014). Three-point bending of sandwich beams with aluminum foam-filled corrugated cores. *Materials & Design*, 60, 510-519.

- Yang, Y., Fallah, A., Saunders, M., & Louca, L. (2011). On the dynamic response of sandwich panels with different core set-ups subject to global and local blast loads. *Engineering Structures*, 33(10), 2781-2793.
- Yazici, M., Wright, J., Bertin, D., & Shukla, A. (2014). Experimental and numerical study of foam filled corrugated core steel sandwich structures subjected to blast loading. *Composite structures*, 110, 98-109.
- Yun, S.-H., & Park, T. (2013). Multi-physics blast analysis of reinforced high strength concrete. *KSCE Journal of Civil Engineering*, 17(4), 777-788.
- Zhang, J., Qin, Q., & Wang, T. (2013). Compressive strengths and dynamic response of corrugated metal sandwich plates with unfilled and foam-filled sinusoidal plate cores. *Acta Mechanica*, 224(4), 759-775.
- Zhang, P., Liu, J., Cheng, Y., Hou, H., Wang, C., & Li, Y. (2015). Dynamic response of metallic trapezoidal corrugated-core sandwich panels subjected to air blast loading—An experimental study. *Materials & Design*, 65, 221-230.
- Zhou, G., Hill, M., & Hookham, N. (2007). Investigation of parameters governing the damage and energy absorption characteristics of honeycomb sandwich panels. *Journal of Sandwich Structures and Materials*, 9(4), 309-342.
- Zhou, X., & Hao, H. (2008). Prediction of airblast loads on structures behind a protective barrier. *International Journal of Impact Engineering*, 35(5), 363-375.
- Zukas, J. (2004). *Introduction to hydrocodes*: Elsevier.